PARTICLE IMAGE VELOCIMETRY INVESTIGATION OF THE WAKE FIELDS OF A LONG FLEXIBLE RISER

JIE XU

Particle Image Velocimetry Investigation of the Wake Fields of a Long Flexible Riser

by

© Jie Xu

A thesis submitted to the School of Graduate Studies in partial fulfillment of the requirements for the degree of Master of Engineering

Faculty of Engineering and Applied Science
Memorial University of Newfoundland

April 2006

St.John's Newfoundland Canada

Your file Votre référence
ISBN: 978-0-494-30519-5
Our file Notre référence
ISBN: 978-0-494-30519-5

ABSTRACT

Vortex-Induced Vibration of marine risers has been receiving increasing interest from both industry and academics as offshore oil and gas exploration moves into deeper water regions. A regular vortex pattern is formed in the wake of cylindrical risers that interacts with the cylinder motion and is the main source that causes elastically mounted cylinders to vibrate. Wake field studies of Vortex-Induced Vibration (VIV) for a long flexible cylinder can help to better understand the physical mechanisms of the interaction between the body response and the wake vortex.

The presented work consists of two major parts: some preliminary tests for the Digital Particle Image Velocimetry (DPIV) system of the Memorial University of Newfoundland (MUN) and the Vortex-Induced Vibration (VIV) wake field research using DPIV. These preliminary tests were conducted in small water tanks and the MUN towing tank. Some essential parameters and techniques using PIV were also investigated through these preliminary tests. The VIV wake field measurement experiments were performed in the ice tank, Institute for Ocean Technology (IOT). Vibration responses in both in-line and cross-flow directions of a long flexible cylinder, with a diameter of 47mm and length to diameter ratio of 181, in a free stream, were investigated at moderate Reynolds number in the range of 9400-47000. The DPIV system was employed to measure the wake velocity field and vorticity field behind the cylinder, simultaneously with acceleration measurements of the cylinder.

The experimental results show VIV responses in both in-line and cross-flow directions at the span location z/L=0.43, and with a mix of vibration frequencies and amplitudes. With the increase of the flow speeds, vibration frequencies became higher in both in-line and

cross-flow directions. The vibration frequencies of the cylinder were in a range of 0.64 Hz to 10.38 Hz over the range of Reynolds numbers. The amplitude did not obviously increase with an increase of Reynolds number. The amplitude to diameter ratio in the in-line and cross-flow directions covered a range of 0.10 - 0.41 and 0.24-0.95, respectively.

The flow field measurement results reveal that for a certain value of the vibration frequency, *f*, the Reynolds number, *Re,* and the amplitude to diameter ratio, *A/D*, three vortex modes '2S', '2P' and 'P+S' are observed in the near wake of the cylinder. At the lower Reynolds number, *Re*=9400, and with lower response frequencies from 0.61 Hz to 1.28 Hz, only '2S' vortex modes were observed in the experiments, and the '2S' vortex modes presented were stable. With an increase of the Reynolds number, at *Re*=14100 and with frequencies from 0.95 Hz to 2.74 Hz, two vortex modes, '2P' and 'P+S', were observed in the near wake at different times. The '2P' mode was dominant at this Reynolds number. Vortex modes '2S' and '2P' were observed at different times when the Reynolds number further increased, to Re=18800 and 23500 and with frequencies from 1.34 Hz to 4.79 Hz. The vortex pattern '2S' played a main role in the wake at the two speeds. At higher Reynolds number, Re>23500, and with frequencies from 1.86 Hz to 10.38 Hz, '2S' and '2P' vortex modes were also observed at different times and the vortex patterns presented were unstable due to velocity fluctuation and quick diffusion of vortices in the wake. The percentage of the vortex pattern '2P' increases at higher speeds. The results also showed that the vortex modes '2S' and '2P' were repeatable with the same vibration responses of displacements and accelerations.

List of Table

List of Figures

Acknowledgments

There are many people who have contributed in some way to the research in this thesis. I would like to take this chance to express my sincere gratitude to them. I would like to thank my supervisor, Dr. Neil Bose, for his invaluable comments in this experiment and thesis work, and for his trust on me to be responsible for the expensive PIV system. Mr. David Molyneux has been very helpful in exploring experimental techniques and developing secondary system components for the PIV experiments. Dr. Wayne Raman-Nair and Mr. Andy Wallace were very supportive in coordinating the experiments in Ice tank, IOT. Mr. Don Spencer provided the useful documents relative VIV apparatus and previous PIV experiments in the towing tank, IOT.

I appreciate Mr. Jim Gosse, Mr. Ronald O'Driscoll, Mr. Austin Bugden, Mr. James Williams, Mr. Christ Meadus, Mr. Brian Hill, Mr. Peter Hackett, for the assistance in conducting the experiments in MUN towing tank and Ice tank. I would also like to say thanks to Mr. Xiangqun Li and Ms. Lin Zhu for the discussions about VIV experiments and data process. Those practical suggestions from all of them were always appreciated.

I thank the Canada Foundation for Innovation and the Department of Innovation, Trade and Rural Development (IRIF Award) for financial support of the purchase of the PIV system and the National Sciences and Engineering Research Council and the National Research Council for financial support of the NRC/NSERC partnership program project "Vortex Induce Vibration Response for Deepwater Risers".

Finally, but certainly not the least, I want to thank my son, Roger, and my husband, Moqin, for their support and help both in daily life and academia. Thanks to my parents for their love and supports.

Table of Contents

Chapter 1 Introduction

1.1 Introduction

Since ancient times, it has been known that the wind may cause vortex-induced vibration of the taut wire of the Aeolian harp. According to Rabbinic records, King David hung his Kithara, a stringed instrument, over his bed at night, where it sounded in the midnight breeze. In the fifteenth century, Leonardo da Vinci sketched a row of vortices in the wake of a bluff body in a stream (Marris, 1964). The first scientific experiment on Aeolian tones was carried out by Strouhal in 1878. He found that the Aeolian tones generated by a wire were proportional to the wind speed divided by the wire thickness. Since then, vortex-induced vibration of structures has been of practical interest to many fields of engineering: for example, it can cause vibrations in heat exchanger tubes (Blevin 1990); it influences the dynamics of riser tubes bringing oil from the seabed to the surface in offshore oil installations (Chen 1987); power transmission lines vibrate when subjected to cross-winds (Brike & Laneville 1993); it is important to the design of civil engineering structures such as bridges and chimney stacks, as well as marine and land vehicles. Vortex-induced vibration can also cause large-amplitude vibrations of tethered structures in the ocean (Panton 1996).

Vortex-Induced Vibration (VIV) of marine risers has been receiving increasing interest from both industry and academics. Due to the large demand for crude oil in the world, offshore oil and gas exploration has been moving into deeper water regions. This requires the extension of marine risers. As a result, they encounter a complex environment of high speed and non-uniform current, large and non-uniform tension forces and vortex-induced vibration caused by the current forces and high tension (DiMarco *et al.* 2001; Robinson

2002). VIV is a common phenomenon in marine engineering structures and often causes the fatigue damage of marine risers. In addition, VIV of a structure is one of the most important dynamic responses caused by the flow through it and results in very rich dynamic behaviors (Panton 1996). VIV is a complex interaction between body motion and vortex motion, not only involving the structural response phenomena induced by the wake vortex, but also the vortex dynamic modes leading to the response. This underlines the importance of understanding which vortex dynamics give rise to the different body responses.

Regular vortices are formed in the wake, which interact with the cylinder motion and are the main sources causing elastically mounted cylinders to vibrate due to the vortex dynamics when shed from the cylinder. The interest in VIV and the interaction between body responses and wake vortex pattern have led to a large number of fundamental studies, are summarized in the comprehensive reviews of Griffin & Ramberg (1982), Bearman (1984), Parkinson (1989), Blevins (1990), Sarpkaya 1995 and Williamson & Govardhan (2004). The flow around a circular cylinder has become the prevalent problem of current around a marine riser. Many researchers have focused on the VIV problem of a rigid, oscillating cylinder using experiments that were conducted at low and moderate Reynolds number (e.g. 10^2-10^4) (Ongoren & Rockwell 1988, Williamson & Roshko 1988, Gu & Rockwell 1994 and Techet et al. 1998). A few have investigated VIV of a long flexible and freely vibrating cylinder, because testing this kind of model needs a large facility and relatively complicated measurement technique (Brika & Laneville 1993, 1995 and Govardhan & Williamson 2000). However, the vortex shedding modes behind a flexible cylinder are not expected to take the same form as those of a rigid cylinder, since its vibrating modes vary along its length (Allen & Henning 2001, Li 2005). Moreover, although an assumption has been made by Williamson & Roshko (1988) that the map of vortex patterns is representative of those patterns to be found over a large range of Reynolds number, it is necessary to carry out work to confirm this and determine how these patterns are affected by a variation in Reynolds number. It is also necessary to investigate what is the predominant vortex mode behind a long flexible cylinder, and how it affects the response of the cylinder.

1.2 Methodology

The wake formation near an oscillating cylinder is always unsteady, i.e. the flow field changes with time (Toebes 1968, Griffin 1971). Obtaining an instantaneous velocity distribution across an extended area of a VIV flow field may help us to better understand the physical mechanisms of vibration response. A velocity field can be measured by several methods, such as Pitot Tubes (PT), Hot Wire anemometers (HWA) and Laser Doppler Velocimeters (LDV) (Adrian 1983, Fingerson & Freymuth 1983). However, in the intrusive measurement methods, such as PT and HWA, the probe disturbs the flow measured, therefore it often causes additional error in the results. Also, the experimental results based on these point measurement technologies lack instantaneous flow field information. Although they are relatively reliable methods, because information for a velocity field has to be achieved by scanning the points of a velocity probe across the flow, the instantaneous structure is lost and only the average flow field is obtained. Traditional flow visualizations, on the other hand, do not quantify the flow field and can only be carried out at low Reynolds numbers (Smits & Lim 2000).

Particle Imaging Velocimetry (PIV) has found widespread application in the study of unsteady flow (Gu & Rockwell 1994, Sheridan *et al.* 1998, Techet *et al.* 1998 and Govardhan & Williamson 2000), because of its instantaneous whole-field and non-intrusive measurement features. The recent literature has showed that flow visualization and Particle Imaging Velocimetry (PIV) techniques have been widely utilized to study the interaction between fluid and motion body, especially the flow structure around an oscillating cylinder.

In the present work, PIV technology was applied to measure the flow field behind a long flexible cylinder in a tow tank and to analyze the flow field by calculating the cross-correlation of particle images (Xu *et al.* 2005).

1.3 Objectives

The aims of this present work are:

- To measure the flow field behind a long flexible cylinder over a range of Reynolds numbers and to get the details of the unsteady flow fields around the cylinder using 2D Particle Image Velocimetry;
- To investigate the vortex modes from the data of the flow field;
- To analyze the relationship between the vortex modes and the vibration responses of the cylinder.

1.4 Thesis overview

There are seven chapters in this thesis. Chapter One provides the background information on vortex-induced vibration of cylinders and vortex modes. Different measurement methodologies for flow fields are also compared in this chapter. In Chapter Two, some important phenomena encountered in vortex induced vibration and wake vortex modes behind vibrating cylinders are reviewed and previous pertinent works are summarized. Chapter Three introduces the fundamental principal of Particle Image Velocimetry and the MUN PIV system. In Chapter Four some preliminary tests with the PIV system conducted in small tanks and in the MUN towing tank are presented. The experiments included the comparison of different tracking particles, seeding methods, field of view of borescopes and the 3D flow field measurement around a very small propeller and a tug model. The test model, the experimental setup, and the measurement approach for VIV of a long flexible riser model and its wake field using PIV are described in Chapter Five. Chapter Six details the results and presents a discussion about the experiments for both vortex-induced vibration measurement and wake field measurement. Finally, in Chapter Seven, conclusions are drawn and recommendations are made for further study.

Chapter 2 Vortex Induced Vibration

2.1 Introduction

In this chapter, based on a literature review, an overview of the important phenomena encountered in vortex induced vibration will be presented mainly focusing on the forced and free vibration of elastically mounted cylinders. A number of previous studies have shown many important features of vortex induced vibration, and have been very helpful for the understanding of the near-wake structure of a vibrating cylinder.

2.2 Equation of Motion and Parameters

If a cylinder is placed in a flow, it experiences a fluctuating lift force (transverse to the flow) caused by the asymmetric formation of vortices, which can cause the structure to vibrate. The equation of motion for a body with a single-degree-of-freedom which is generally used to represent the vortex-induced vibrations of a cylinder in the transverse direction (perpendicular to the free stream) may be written as follows (Govardhan & Williamson 2000):

$$m\ddot{y} + c\dot{y} + ky = F(t)$$

where m is the total oscillating mass which includes the oscillating structural mass and the fluid added mass; c is the structural damping; k is the spring constant; and F is the total fluid force in the transverse direction.

When the cylinder oscillation frequency is synchronized with the periodic vortex wake mode, good approximations to the force, $F(t)$, and the response displacement $y(t)$, are given by

$$F(t) = F_0 \sin(\omega t + \phi)$$

$$y(t) = A \sin(\omega t)$$

where F_0 is the magnitude of the total fluid force, $\omega=2\pi f$, where f is the oscillation frequency; ϕ is the phase angle between the total fluid force and the displacement of the cylinder; A is the oscillation amplitude.

The left-hand side of the equation of motion consists of inertia force, damping force and restoring force terms, while the right-hand side is the total fluid force which can be split into the vortex force component, F_{vortex}, that is due to the dynamics of all the shed vorticity, and the potential force component, $F_{\text{potential}}$, given by the potential added mass force (Lighthill 1986). The equation of motion shows the interaction between the structure and the external fluid force, which causes the vortex-induced vibration.

In order to discuss VIV response and the near-wake vortices, a set of relevant non-dimensional parameters are usually selected, as in Table 2-1 (Khalak & Williamson 1999).

Table 2-1 Dimensionless parameter list

Mass ratio	m^*	$\dfrac{m}{\pi\rho D^2 L/4}$
Damping ratio	ζ	$\dfrac{c}{2\sqrt{k(m+m_A)}}$
Velocity ratio (reduced velocity)	U^*	$\dfrac{U}{f_n D}$
Amplitude ratio	A^*	$\dfrac{A}{D}$
Frequency ratio	f^*	$\dfrac{f}{f_n}$
Transverse force coefficient	C_y	$\dfrac{F}{1/2\rho U^2 DL}$
Reynolds number	Re	$\dfrac{UD}{\nu}$
Strouhal number	S	$\dfrac{f_s D}{U}$

In this table f is the oscillation frequency; f_n is the natural frequency in still water by decay test; and f_s is the vortex-shedding frequency, the same as f at resonance. The added mass, m_A, is given by $m_A = C_A\ m_d$, where m_d is the displaced fluid mass and C_A is the potential added-mass coefficient, $C_A \approx 1.0$.

2.3 Flow Pattern across Circular Cylinders

The periodic wake of a still, smooth, circular cylinder is a function of the Reynolds number for incompressible fluids. The major regimes of fluid flow across a circular cylinder vary with the increase of the Reynolds number (Blevins 1977). A rich variety of flow patterns has been observed when flow passes a circular cylinder (Panton 1996).

At very low Reynolds numbers, $Re < 4$, based on the cylinder diameter, the flow is symmetric and does not separate. As Reynolds number is increased, $4 < Re < 40$, the flow separates on the downstream side and a pair of fixed vortices are formed immediately behind the cylinder. These eddies are stable and remain attached to the body. As Reynolds number is further increased, $40 < Re < 60\text{-}100$, the vortices elongate until one of the vortices breaks away and a periodic wake and staggered vortex street is formed. This trail of vortices in the wake is known as the *von Karman vortex street*. The vortices travel downstream at a speed slightly less than the flow speed. They are still laminar, and the flow near the cylinder remains steady with two attached eddies. Up to a Reynolds number of approximately 150, the vortex street is laminar. In the Reynolds number range $200 < Re < 400$, the vortex street becomes unstable and it degenerates into fully turbulent flow beyond more than 50 diameters downstream of the cylinder (Lienhard 1966). At a Reynolds number of approximately 400 the vortices themselves become turbulent. The turbulence within the vortices gives them a different velocity profile from that at $Re < 400$.

From a Reynolds number of 400 to approximately 3×10^5, the boundary layer on the cylinder is laminar and separates from the front half of the cylinder at an angle of approximately 80° from the upstream direction. The critical Reynolds number 3×10^5 marks the point where the laminar boundary layer itself becomes unstable just after it separates. At the transition Reynolds number, $3\times10^5 < Re < 3.5\times10^6$, the laminar boundary layer undergoes turbulent transition and wake is narrower and disorganized (with a broad band of shedding frequencies), and the cylinder drag drops sharply Roshko (1961). At higher, supercritical Reynolds number ranges, Roshko (1961) also found that the vortex street re-establishes itself.

2.4 Modes of Vortex Formation

When a cylinder is placed in a free stream, flow separation occurs from the surface; and this gives rise to vortices shedding into the near wake downstream. The major vortex patterns near the fundamental lock-in region, i.e. an amplitude-wavelength (A-λ) plane (defining the body trajectory) up to amplitudes of five diameters, are '2S', '2P' and 'P+S', as shown in Figure 2-1 (Williamson & Govardhan 2004). The '2S' mode means the formation of two single, opposite-sign vortices each cycle, like Von Karman vortex shedding; while the '2P' mode means the formation of two pairs of counter-rotating vortices per cycle; and the 'P+S' mode is the formation of a pair and a single vortex each cycle, an asymmetric version of the 2P mode. These modes were found in the wake of a cylinder forced or freely vibrating in the in-line or the cross-flow direction by previous studies (Griffin & Ramberg 1974, 1976, Ongoren & Rockwell 1988b, Williamson & Roshko 1988, Brika & Laneville 1993, Techet et al. 1998, Evangelinos & Karniadakis 1999, Khalak & Williamson 1999, and Govardhan &Williamson 2000).

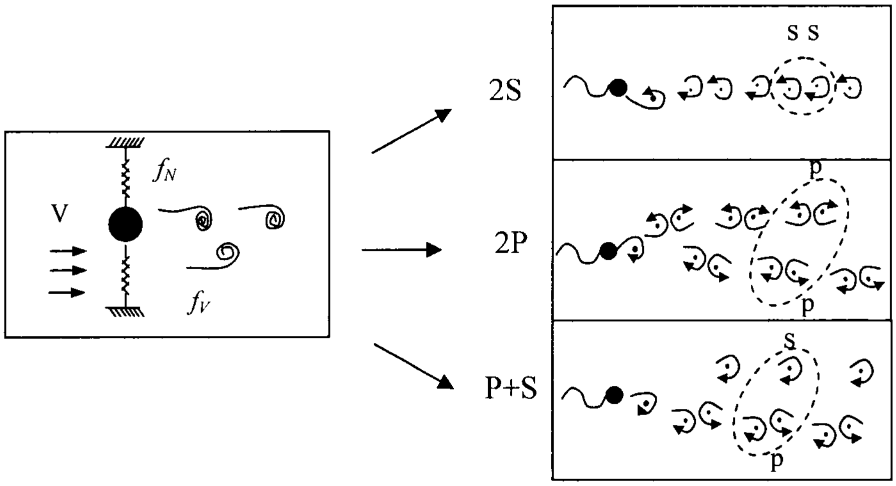

Figure 2-1 Three major vortex patterns

Williamson & Roshko (1988) defined a whole set of different regimes for the wake vortex patterns by flow visualization for a forced vibrating cylinder, in the plane of amplitude-wavelength (A/D, λ/D). In addition to the vortex patterns '2S', '2P' and 'P+S', they also described some other patterns, such as those by coalescence of small vortices, C(2S) and C(P+S), or from more vortices each cycle, 2P+2S, as shown in Figure 2-2. The map of regimes for wake vortex modes has been confirmed in many different studies. Techet et al. (1998) studied the vortical pattern behind a tapered cylinder oscillating transversely to a uniform flow and observed a 2S-2P hybrid mode along the spanwise direction of the tapered cylinder. The location of pattern transition along the cylinder was very sensitive to the Reynolds number, reduced frequency, fD/U, and amplitude to diameter ratio, A/D. The importance of these modes from controlled vibration is that they provide a map of regimes within which VIV vibration responses may be predicted by those corresponding vortex modes observed from certain branches of free vibration. Brika & Laneville (1993, 1995) were the first to show the evidence of the 2S and 2P vortex wake mode from free vibration of a long flexible circular cylinder in a wind tunnel by smoke visualization. Khalak & Williamson (1999) and Govardhan &Williamson (2000) also showed an excellent correlation and prediction of these modes from the result of free transverse vibrating rigid cylinders in the framework of the Williamson & Roshko (1988) map of modes. Evangelinos & Karniadakis (1999) found transient mixtures of (P+S) and 2P modes in the near wake, with possible formation of 2S mode, or 'general wake instability', as the flow travels downstream, from their simulation results of a flexible cylinder with prescribed cross-flow vibration.

2.5 Vibration Response and Hysteresis

The near-wake vortices cause the cylinder to synchronically respond or vibrate. Two types of response exist in an elastically mounted rigid cylinder, depending on whether the combined mass-damping parameter ($m^*\zeta$) is high or low. In the high mass damping case, an "initial" branch and "lower" branch are separated by a discontinuous mode transition;

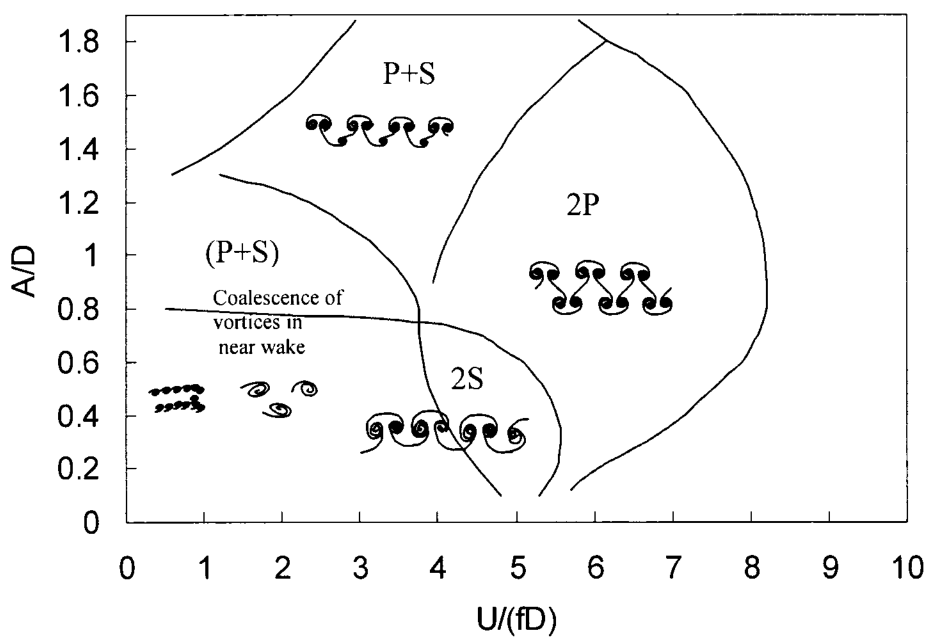

Figure 2-2 Map of vortex synchronization patterns near the fundament lock-in region (Williamson & Roshko 1988)

whereas in the case of low mass damping, in addition to the 'initial' and 'lower' branches, a further higher-amplitude 'upper' branch of response appears, and there exist two mode transitions. Govardhan &Williamson (2000) showed schematically the two types of amplitude response by summarizing the studies of Feng (1968) and Khalak & Williamson (1999) in Figure 2-3. A hysteresis loop accompanies the transitions, and the precise position of the transitions depends on whether the wavelength $\lambda=U/f$, is increased or decreased. For the high mass-damping ($m^*\zeta$) case, Feng (1968) and Brika & Laneville (1993) found a hysteresis between the initial and lower response branches. Khalak & Williamson (1999) showed the case of low mass-damping ($m^*\zeta$), that the transition between the initial and the upper branches involves a hysteresis, while the transition between the upper and the lower branches presents an intermittent switching of modes.

The relation between the branches of the response and the wake modes was proved by several previous studies. Both Brika & Laneville (1993) and Williamson & Roshko (1988) found by flow visualization that 2S corresponds to the initial branch and 2P agrees with lower branch. Hover et al. (1998) provide the same suggestion after comparing the results of a free vibration experiment with the map of vortex modes from Williamson & Roshko (1988). By analyzing the wake modes of a low mass damping case for a free vibrating cylinder, using PIV, Govardhan &Williamson (2000) proposed that the vorticity field of the initial branch exhibit the classical 2S vortex formation mode and the upper and lower branch sequence show the 2P mode, as shown in Figure 2-4.

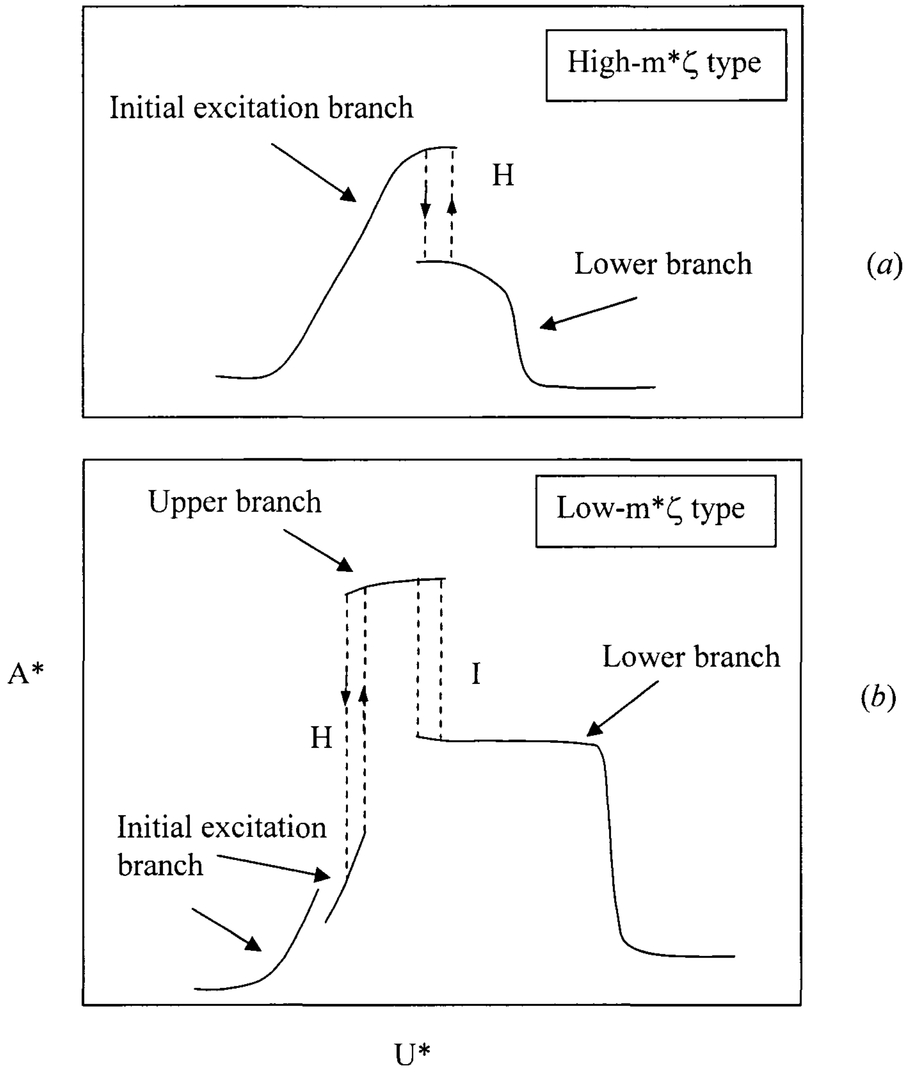

Figure 2-3. The schematic diagram of the two distinct types of amplitudes response. (Vertical axes represent A* and horizontal axes represent *U**.) (a) Feng-type of high-($m^*\zeta$) response exhibits two branches (initial and lower); (b) Khalak & Williamson-type of low- -($m^*\zeta$) response exhibits three branches (initial, upper and lower) (Khalak & Williamson 1999).

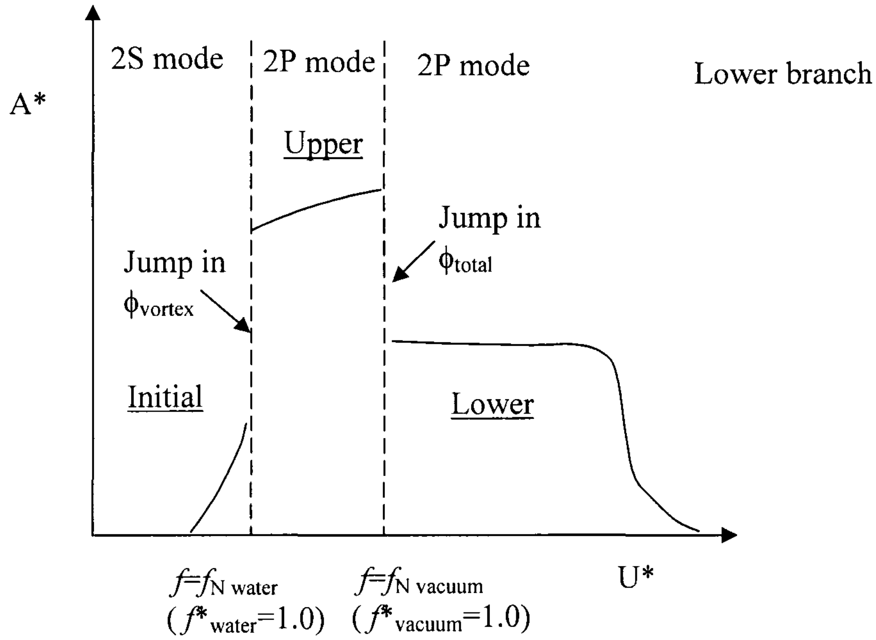

Figure 2-4 Schematic diagram of the low-($m^*\zeta$) type of response showing the three principal branches and correspondingly the two jump phenomena (Govardhan &Williamson 2000).

2.6 Lock-in Phenomenon

One of important features of vortex-induced vibration is "lock-in" or synchronization. The importance of the lock-in in the VIV problem lies in the fact that the near-wake structure can be phase-locked, i.e. synchronized, with the cylinder motion. The definition of "synchronization" or "lock-in" has led to some discussions in the literature. According to Blevins (1990) and Sumer & Fredsoe (1997), the phenomenon of "lock-in" or synchronization means that the vortex shedding frequency at a certain speed becomes close to the natural frequency of the structure and the two frequencies synchronize. When the fluid velocity is increased further, the shedding frequency and the oscillation frequency remain close to the natural frequency, i.e. the frequency ratio $f^*=f/f_N$ remains close to unity over a range of velocity. The definition is correct in the classic scenario for large mass ratio, m^*; however, it is very clearly seen that the frequency ratio, f^*, rises to

1.4 over the synchronization range, at low mass ratios, m^*, as shown in Figure 2-5 by Khalak & Williamson (1997b). The phenomenon has also been observed by Moe & Wu (1990) and Gharib et al. (1998), and is pointed out clearly in Bearman's (1984) review. Khalak & Williamson (1999) considered that it is not suitable to define that the shedding frequency necessarily matches the oscillation frequency, because the wake mode might involve more than two vortices per cycle. They hence suggest a more useful definition of synchronization as the matching of the frequency of the periodic wake vortex mode with the body oscillation frequency, which is also the definition of lock-in now used by Sarpkaya (1995).

Synchronization usually occurs in a region in the plane of (λ/D, A/D), called the fundamental synchronization region. The region is approximately over the range of reduced velocity U^* from 4 to 11, and might vary slightly, depending on the Reynolds number and the mass-damping parameter, $m^*\zeta$ (Khalak & Williamson 1999). Govardhan &Williamson (2000) observed that the synchronization regime is from 5.5 to 10, and the wake becomes desynchronized at higher than $U^*=10$.

2.7 Phase Jump

Phase jump, between the transverse force F (total force or lift force) and the cylinder displacement, y, over a small range of U^*, is another important feature of the dynamics of an elastically mounted cylinder system. When the lift force drops sharply at a point, the phase also changes abruptly by almost 180° , as shown in Figure 2-6 (Bishop & Hassan 1964 and Feng 1968). Phase jumps occur when the vibrating response of the cylinder changes from one branch to another, i.e. from initial branches to upper branches or upper branches to lower branches. Zdravkovich (1982), Ongoren & Rockwell (1988a), Gu &

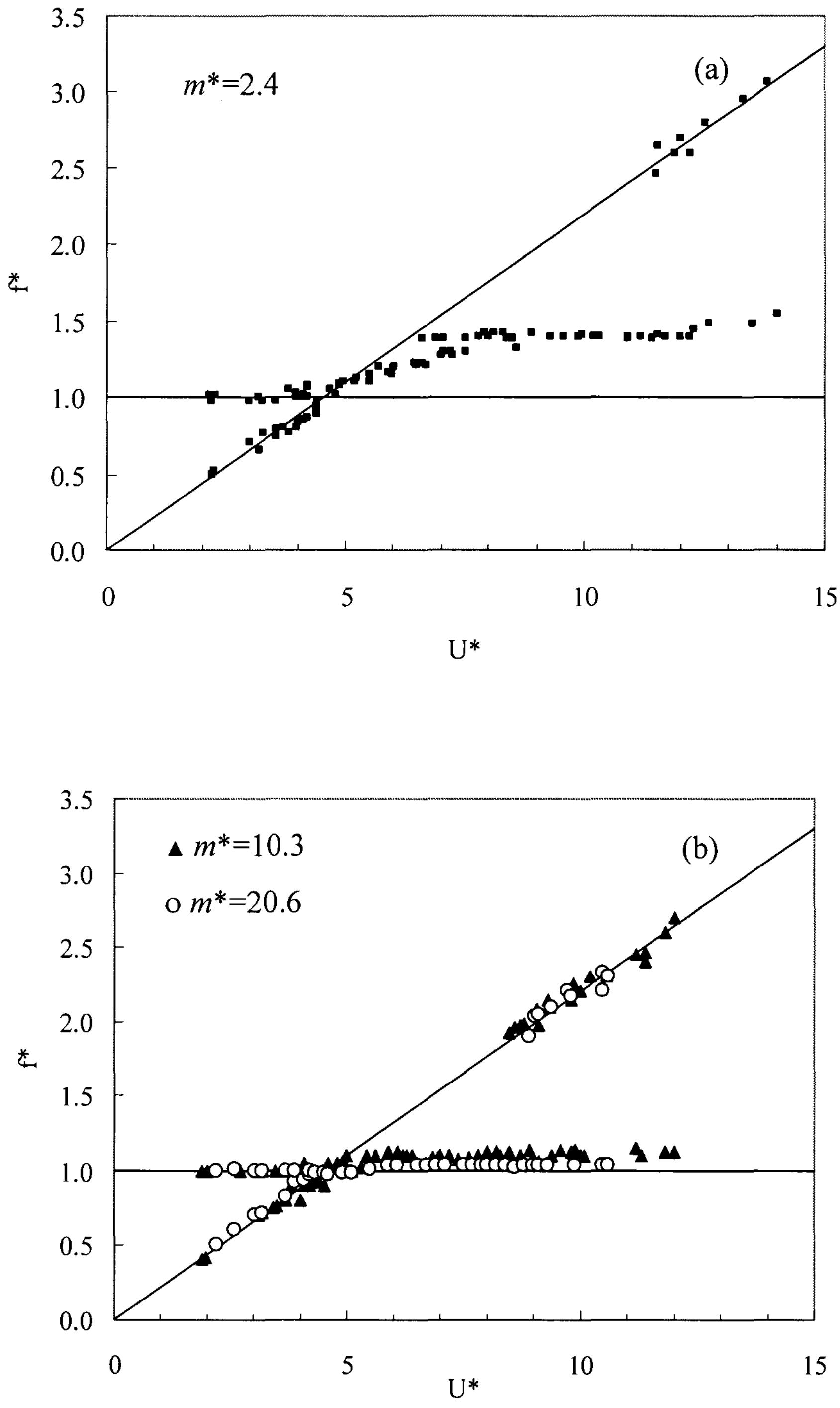

Figure 2-5 Frequency response for a range of mass ratios, m^*, through the synchronization regime. (a) frequency ratio rising to 1.4 at lower mass ratio; (b) frequency ratio close to 1 at higher mass ratios (Khalak & Williamson 1997b).

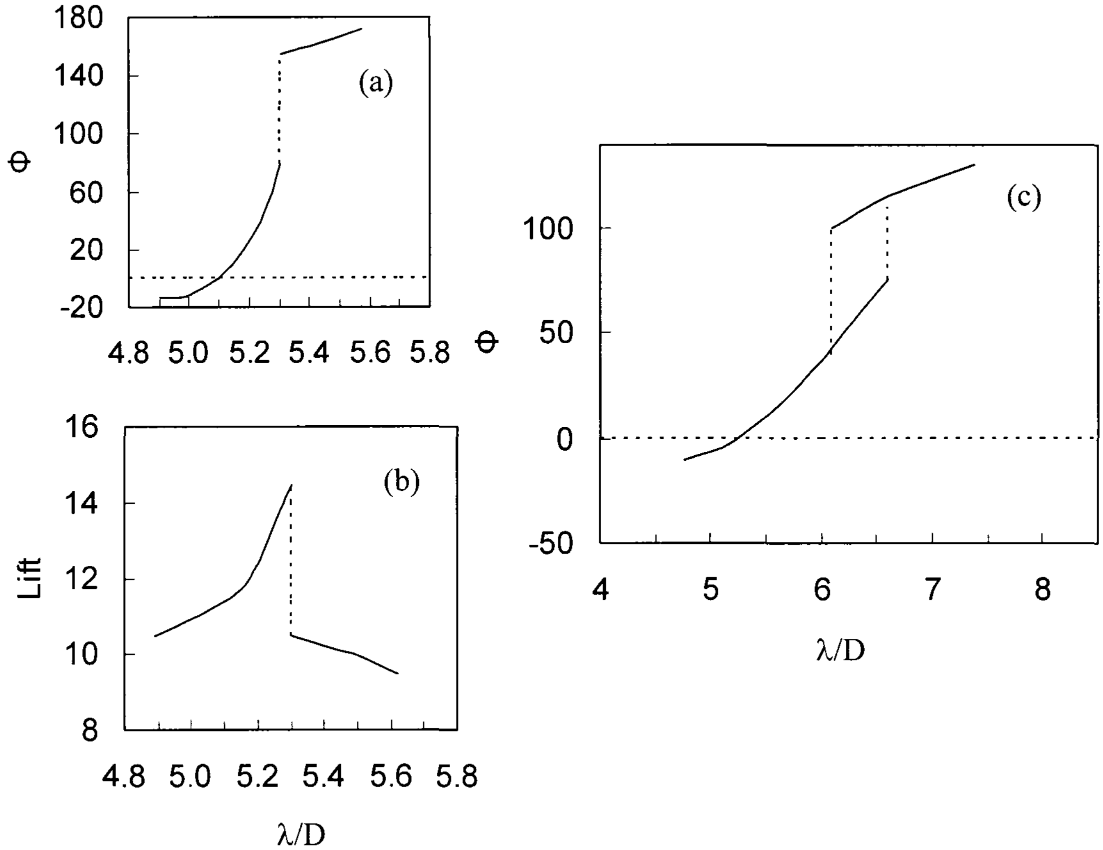

Figure 2-6 Variation of lift force and its phase as wavelength is varied. (a) and (b) are for a cylinder forced to oscillate, from Bishop and Hassan (1964); (c) is for an elastically mounted cylinder from Feng (1964)

Rockwell (1994), and Krishnamoorthy et al.(2001) showed using flow visualization and PIV that a jump in phase angle is matched by a switch in the timing of vortex shedding. The previous studies have shown that the phase jump reflects the sharp changeover of the wake modes. Brika & Laneville (1993,1995), and Khalak & Williamson (1999) showed by flow visualization in the free vibration case of a high mass- damping cylinder that the jump from the initial branch to the lower branch corresponds with a mode change from ‘2S’ to ‘2P’. Williamson & Roshko (1988) observed by flow visualization in forced vibration the occurrence of the phase jump with the abrupt mode jump as the flow is just precritical and is perturbed by a slight increase of wavelength. In Figure 2-7, a schematic variation of ϕ with λ demonstrates a kind of the hysteresis reported by Bishop and Hassan (1964). The lower curve can be associated with the 2S mode and the upper curve with the 2P mode.

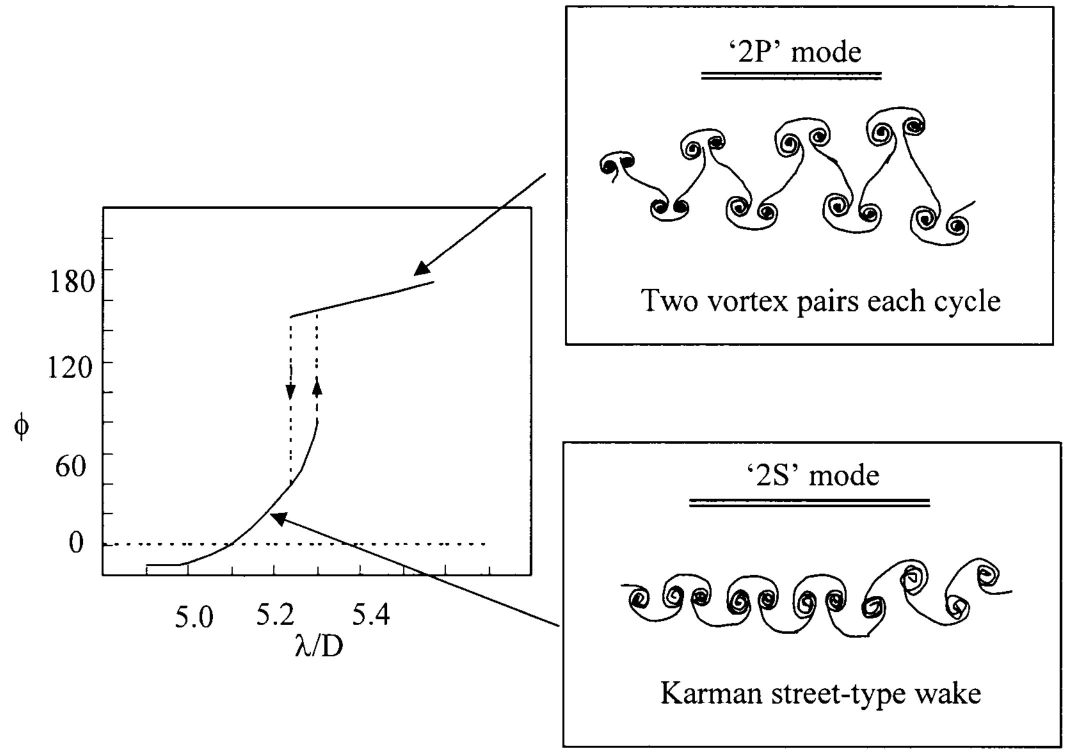

Figure 2-7 A schematic variation of lift force phase with wavelength, to demonstrate the possibility of hystersis being caused by an overlap of the regions where the '2S' and '2P' modes occur (Williamson & Roshko 1988)

Govardhan &Williamson (2000) shows that the first mode transition, from the initial branches to upper branches is associated with the jump in the vortex phase between vortex force and displacement, while the second mode (upper-lower) transition corresponded to the jump in the total phase between total transverse force and displacement. They also suggested that the jump in the vortex phase is principally associated with the switch of wake modes and provided the evidence that the jump in vortex phase for the transition between the initial branches and upper branches was consistent with the jump between the vortex modes '2S' and '2P'; therefore, the wake modes across the transition between the upper branches and lower branch were similar due to the absence of a large jump in vortex phase, see Figure 2-4.

2.8 Vortex-Induced Vibration of A Long Flexible Cylinder

In the ocean, many cylindrical structures are potentially subject to VIV from ocean currents. These structures include risers, tendons, mooring lines and the hull of a spar-type structure. Due to the increased water depth, risers on a deep water system will encounter more technological challenges than a shallow-water riser. In some deepwater areas, current velocities are not only very high (up to 2m/s) but also they are usually non-uniform over water depth (DiMarco *et al.* 2001). Deepwater risers are also subjected to extremely large and non-uniform tension forces due to their long length and complex structural nature. They can experience very high modes of vibration and can also experience more than one mode of vibration simultaneously (Allen & Henning 2001). The multi-modal VIV responses consist of a number of modal natural frequencies, modal damping, mode mass and modal stiffness, corresponding to different modal shapes along the riser span.

One of the most important parameters affecting VIV is the Reynolds number. Since the Reynolds number is proportional to both diameter and velocity, performing tests at Reynolds numbers that correspond to those of offshore risers and tendons experiencing high ocean currents is quite difficult because both the current velocity and the length to diameter ratio of the structure are often large. Another important parameter affecting VIV is the number of vibration modes, which causes the fatigue damage of the structure. For long cylindrical structures, the phenomenon of VIV is quite complicated because the structure tends to respond at a variety of frequencies over its entire length (in the multi modal case). A long flexible cylinder vibrates in both in-line and transverse directions. Unlike a rigid cylinder with only transverse vibration, there can be significant effects from the in-line vibration on the transverse oscillations for a flexible cylinder (Sarpkaya 1995).

With the demands of offshore oil and gas pushing exploration and production into deepwater, the investigation of VIV around a long flexible cylinder has become a popular and important area of research in marine hydrodynamics. However, physical model experiments for long flexible cylinders are difficult to perform because of the scaling from model to full scale and due to the limited size of testing facilities. Although some studies have focused on the investigation of VIV responses of long flexible risers (Willis *et al.*1999, Allen & Henning 2001, Triantafyllou *et al.* 2003), multi modal VIV responses are still not fully understood. The prediction of VIV remains based on data from relatively short cylinders tested in laboratory environments (Vandiver & Marcollo 2003, Newman & Karniadakis 1996). The most successful VIV prediction programs for long cylindrical marine structures are empirically based and make use of the data from these laboratory models. Many assumptions are required to extend the simplified experimental results to the prediction of vibration of long cylinders in ocean currents. Model tests with long flexible cylinders, responding at high mode number are highly desirable and are needed to help validate the predictions.

2.9 Summary

Many studies have investigated the near wake around an oscillating cylinder using PIV or flow visualization as discussed in the previous sections. To comprehend the details of the experimental methods in the previous work is very helpful in our experimental design for the wake measurement of the long flexible cylinder. Table 2-2 provides a list of detailed information of the VIV flow field measurement by PIV or flow visualization from some previous studies. Most of these experiments were conducted in water or wind tunnels, while a few experiments in tow tanks, and with forced and free vibrating cylinders. In the experiments for free vibration of a cylinder, the frequency and amplitude were obtained by different methods, one method was to computed them with the use of Hilbert transformation and Fast Fourier Transformation methods (Khalak & Williamson 1999, Govardhan & Williamson 2000, and Xu *et al.* 2005). Another method was to measure the frequencies and amplitudes with hot wire anemometer and accelerometer (Brike &Laneville 1993). Most test systems allowed a transverse motion of the cylinder but prevented the motion in the streamwise flow direction. The long flexible freely vibrating cylinder in the present study allowed motion in both in-line and cross-flow directions (Xu *et al.* 2005). From Table 2-2, we can see that these research program covered a range of low and moderate Reynolds number from 10^2 to 2×10^4. The diameters of cylinders were from 10mm to 51mm and the aspect ratios were from 9.5 to 99. The size of the field of view (FOV) in these measurements was at least 3.4d by 3.4d and up to 14d by 10d in the in-line and the transverse direction. The amplitude to diameter ratio was in a range of 0.2 to 5.0. Govardhan & Williamson (2000) were the first to simultaneously measure force, displacement and wake vorticity in free vibration.

Table 2-2 Summary of experiment parameters in some previous studies

Investigators	Re	d (mm)	Aspect ratio	FOV	A*	VIV type	Facility
Krishnamoorthy *et al.*(2001)	1500	15.9	16.4	14d×7d	0.22	forced, rigid	water tunnel
Govardhan & Williamson (2000)	2,900-19,000	38, 12.7	10, 20	10d×10d	1.19	free, rigid	water tunnel
Khalak & Williamson (1999)	5,000-16,000	38, 51	10, 8.5	4.3d×2.8d	1.18	free, rigid	water tunnel
Sheridan *et al.* (1998)	517	12.7		3.9d×3.3d	1.0	forced, rigid	water tunnel
Techet *et al.* (1998)	400 & 1,500	24	27.5	5.3d×3.4d	0.25-1.0	forced, rigid	tow tank
Lin & Rockwell (1996)	0	50.8	9.5	5.5d×3.6d	1.59	forced, rigid	water tunnel
Gu *et al.* (1994)	185 &5,000	9.5, 25.4	59, 20	3.4d×3.4d	0.2	forced, rigid	water tunnel
Brike &Laneville (1993)	3400-11800	33.4	99		0.52	free, flexible	wind tunnel
Willamson & Roshko (1988)	275, 392 & 600			13d×6d	5.0	forced, rigid	tow tank
Ongoren & Rockwell (1988)	855-3,000	12.7	28.6	5.3d×4.2d	0.13	forced, rigid	water tunnel
Xu *et al.* (2005)	4700-47000	47	184	10d × 4d	0.24-0.95	free, flexible	tow tank

Chapter 3 Particle Image Velocimetry

3.1 Introduction

This chapter introduces the fundamental principals of Particle Image Velocimetry and compares different measurement and processing techniques relative to this method. The MUN PIV measurement system and specifications of its components also are presented. The system set-ups in different measurement conditions are discussed.

3.2 Principal of Particle Image Velocimetry

Particle Image Velocimetry (PIV) is an optical, non-intrusive flow field measurement method and has been developped over the last 20 years. PIV technology originates from both Laser Speckle Velocimetry (LSV) and Particle-Tracking Velocimetry (PTV). LSV has its roots in solid mechanics, where coherent light scattered from solid surfaces naturally forms speckle patterns (Erf 1980). LSV is a technique to measure velocity by measuring speckle displacement and operation in a mode with very high concentration of scattering particles in the fluid. PTV is a flow-visualization technique to measure displacements by tracking individual particles and operation in a mode with low image density. The high-image-density PIV technique operates when particle concentrations lie between those of LSV and PTV (Adrian 1986b, 1991).

Although conventional two-dimensional particle tracking methods have been available to provide qualitative or semiquantitative results for decades, they suffer from complications that arise from the tracking of individual particles when obtaining velocity field information. PIV technology based on flow visualization makes a breakthrough from qualitative visualization to quantitative measurement. This method does not require the tracking of individual particles, hence offers a higher temporal and spatial resolution of the instantaneous flow field. This technology provides an accurate quantitative measure of the instantaneous flow velocity field across a planar area of a flow field. PIV techniques have been applied in numerous fluid experiments such as jets in water (Adrian 1986a), the flow behind an impulsively started airfoil (Lourenco et al. 1986), the turbulent wake of a cylinder (Kompenhans and Reichmuth 1987), the flow around cavitation bubbles (Yogel & Lauterborn 1988), flow structure on a ship model (Dong et al. 1997), and more lately, the wake vortex behind a forced or freely vibrating cylinder as discussed in the Chapter 2.

In order to use PIV techniques, the flow should be evenly seeded with tiny, neutrally buoyant particles. The particles in the flow are illuminated twice within a short time interval using a light sheet, formed by passing a double pulsed laser beam through an optical device including cylindrical lenses. The particles at each instant of which the light sheet is pulsed are recorded as either a single image exposed twice on a film camera or as a pair of two single exposure images on digital Charge Coupled Device (CCD) cameras. Tracer particle images in the flow are used as raw data for the PIV analysis and the direction and displacement of the particle movements are directly related to the flow velocity. The data processing determines either the average displacement of the particles over a small interrogation region in the image or the individual particle displacements between pulses of the light sheet, depending on particle concentration in the image. Knowledge of the time interval between light sheet pulses then permits computation of the flow velocity.

Figure 3-1 below shows the configuration of a typical PIV setup where a pair of pulsed lasers are used to provide the light sheet illumination (LaVision 2003). The position of particles in the flow is recorded by a CCD camera, which is oriented at 90 degrees to the plane of the light sheet. Depending on the type of a CCD camera and the particle concentration either particle tracking or correlation processing can be used to produce the processed velocity vector map. In low particle concentration cases the individual particle displacement can be determined. In high particle concentration cases, correlation processing is usually applied to statistically determine particle displacement in each sub-window.

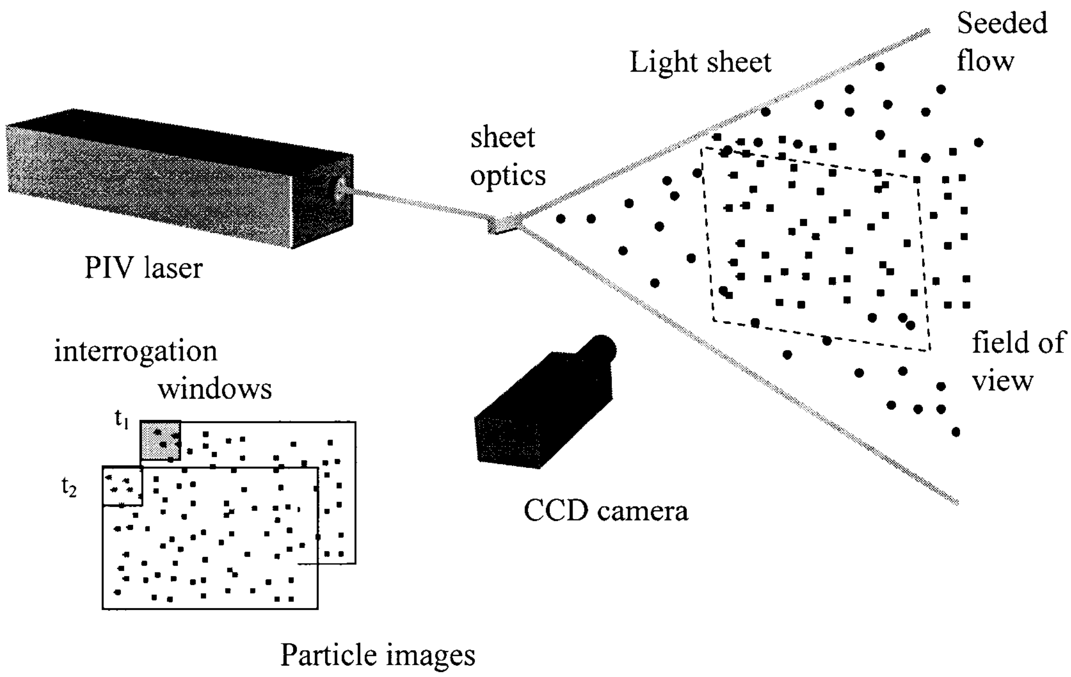

Figure 3-1 Scheme of a typical 2D PIV measurement

Basically, there are three types of data reduction techniques used in PIV: auto-correlation, cross-correlation and particle tracking. The choice of a processing technique depends primarily on the available equipment used to record the particle image data and the seed particle concentration. The correlation based processing techniques produces spatially averaged velocity estimates. The recorded image frame is divided into a number of small subregions, each containing several particles. The mean displacement is determined by computing the auto-correlation or cross-correlation function of the intensity distribution, $C\,(m,n)$, defined as (Willert &Gharib, 1991):

$$C_A(m,n) = \sum_i \sum_j G(i,j) \cdot G(i-m, j-n)$$

$$C_C(m,n) = \sum_i \sum_j G_1(i,j) \cdot G_2(i-m, j-n)$$

where $C_A(m,\ n)$ is a auto-correlation function; $G(i,\ j)$ is level of greyscale of the pixel located at coordinate i and j; $G(\text{i-}m,j\text{-}n)$ is level of greyscale of the pixel located at coordinate i-m and j-n; $G(i,\ j)$ and $G(\text{i-}m,j\text{-}n)$ are in the same subwindow of the same image. $C_C(m,\ n)$ is a cross-correlation function, $G_1(i,\ j)$ and $G_2(i\text{-}m,\ j\text{-}n)$ are level of greyscale of the pixel located at i,j in image 1 and i-m, j-n in image 2. The values of $G(i,\ j)$ vary between 0 and the maximum gray level, which correspond to black and white. The maximum gray level depends on the data type of the CCD. The gray levels are given a value from 0 to 255 for an 8bit CCD, while from 0 to 4096 for a 12bit CCD. A correlation function is calculated to search the correlation peak and the distance between particle pairs.

The early PIV based on the auto-correlation technique because the record medium was film. In this technique an image frame is exposed multiple times (≥2) to produce a multiple exposure particle image in the single frame (Adrian & Yao 1984, Dong et al. 1992). The average displacement of the recorded particle image pairs is determined by computing the auto-correlation within a small enough interrogation window. The 2-D auto-correlation is a symmetric function having a characteristic dc peak at the origin of the correlation plane and two satellite peaks, oriented symmetrically about the dc peak. Figure 3-2 shows the sample of a double exposure window and the resulting auto-

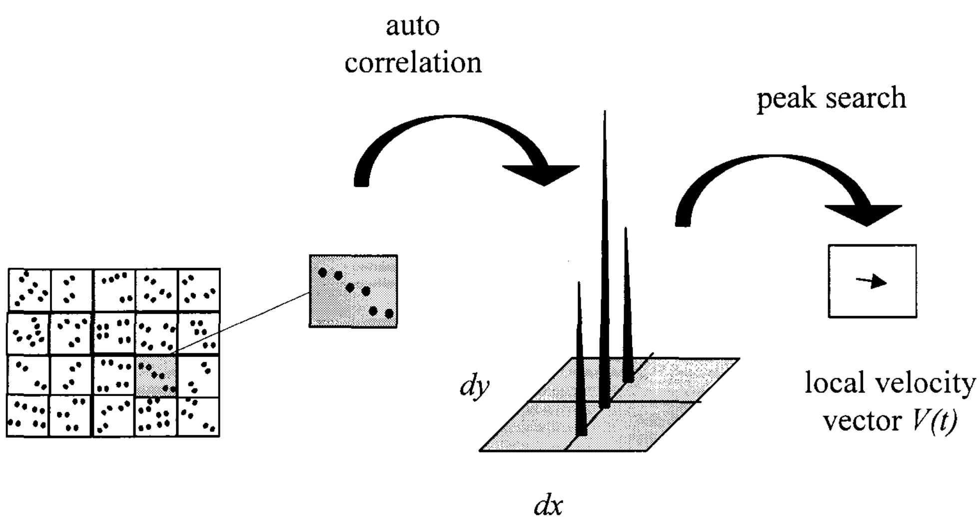

Figure 3-2 Velocity evaluation for PIV particle image using Auto-correlation

correlation plane output (LaVision 2003). The dc peak originates from the correlation of all particle images in the window; hence the size of the dc peak is related to both the total number and size of the particles in the window. The satellite peaks originate from the average displacement of the particle image pairs between two exposures. In order to discern the displacement peaks from the peak, the particle displacements must be greater than the average particle diameters across the window. This requirement places a dynamic range limitation on the auto-correlation technique. Another shortcoming is in the symmetry of the auto-correlation function. Since auto-correlation PIV relies on a single image for the flow velocity measurements, phase information is lost. This causes the existence of two diametrically opposed displacement peaks about the dc peak which yields a 180 degree directional ambiguity in the velocity vector direction (Dong et al. 1992, Wernet 1999). Although the directionally ambiguity can be eliminated by imposing a dc offset on the particle image records, that is, the particle images are mechanically shifted between laser pulse firings, image shifting introduces extra complexity in the experimental setup and also additional errors due to optical path differences resulting from the image shift (Adrian 1986a, Landreth & Adrian 1988).

In the cross-correlation technique, so called Digital PIV (DPIV), two image frames are respectively exposed once by two light pulses to produce two single exposure particle images which are stored in two successive video frames of a CCD camera (Smits & Lim, 2000). The cross-correlation process also is operated in a small window. Each of them corresponds to the same spatial position in two successive frames as shown in figure 3-3 (LaVision 2003). The resulting output on the correlation plane is a single peaked function, where the peak represents the average displacement of the particles across the window. The direction of the displacement is determined unambiguously because the images from two exposures are recorded separately. Since there is no self-correlation peak, even zero particle displacement can be measured, hence, the cross-correlation technique provides a higher dynamic range measurement capability than the auto-correlation technique (Willert & Gharib 1991, Wernet 1999).

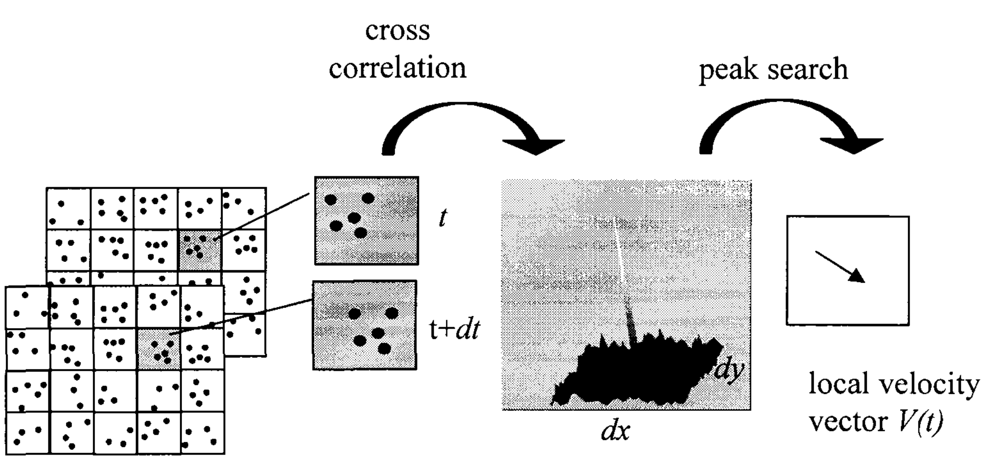

Figure 3-3 Velocity evaluation for PIV particle image using cross-correlation

In contrast to the spatially averaged correlation techniques discussed above, Particle Tracking Velocimetry (PTV) techniques attempt to identify the displacement of individual particles. Typically, particle tracking techniques require lower particle concentration than that is used for correlation based processing. The images with lower particle concentration yield randomly distributed velocity vector maps with lower accuracy and fewer vectors than correlation processed vector maps. Both single and double exposure image can be used in particle tracking algorithms. Single frame with multiple exposures is preferred since knowledge of the particle time history adds direction information, which aids in the tracking process. Most particle tracking techniques require more than two single exposures image frames in order to perform efficiently (Adrian 1991, Wernet 1999).

Alternatively, combining correlation and particle tracking techniques has been proposed to create a PIV data processing system which can cover a wide range of flow seeding conditions and offers the potential for "super-resolution" PIV measurement. As mentioned above, particle tracking by itself is typically not capable of successfully tracking particles at the high-seed particle density normally used for auto- or cross-correlation analysis. Conversely, correlation techniques must use large interrogation windows, with a concomitant reduction in spatial resolution, in order to perform adequately in the low-seed particle density regimes where particle tracking techniques are normally applied. In the combined technique, correlation analysis is used first to obtain a benchmark velocity vector map, which then serves as a guide for the particle tracking operation. Hence, high-seeded flow field images can be processed with small correlation windows, and then the spatial resolution of the measurements improved by following with particle tracking. For moderate-seeded flow field images, the correlation window is increased so that a good velocity vector map is obtained, and then this is followed by particle tracking in order to obtain high spatial resolution measurements. For low-seed particle concentration cases, the standard particle tracking technique can be used alone. By processing the image over a regular grid of small subregions, a velocity vector map is generated. The optimum number of particles per interrogation region is about 10-20 particle (Dong et al. 1992, Willert &Gharib 1991) and should not be less 8 particles.

3.3 MUN PIV System

Based on the principal of Particle Image Velocimetry, a basic 2D DPIV system consists of at least a laser, a CCD camera, and a computer for operation control, image acquisition, and data analysis. The types of PIV system can be different, depending on the demands of measurement tasks and test facilities. Memorial University of Newfoundland has recently purchased a 3D PIV system from LaVision Inc. The system consists of the following main elements:

- Twin-head Nd:YAG laser and controller
- Light guide arm and light sheet optics
- Two Charge Coupled Device (CCD) cameras
- Two borescopes
- Programmable Timing Unit (PTU)

A photograph of the complete system, assembled in air, is shown in Figure 3-4. The unique feature of this system was that there were two borescopes shown as the long tubes in the both sides of the set-up in Figure 3-4; therefore, the camera was mounted in air at the top of a borescope, through the borescope and the prism in the end of the borescope, providing the capability to obtain underwater views. The advantage of this arrangement was to keep delicate components well above the water surface, removing the need for expensive watertight housings. A similar arrangement was provided for the laser, and the light sheet optics, shown as the vertical parts in the middle of the set-up. The pulsed laser beams from a dual head Nd:Yag laser are directed downwards through a stainless connecting tube to a waterproof light sheet optics housing and are spread into light sheets .

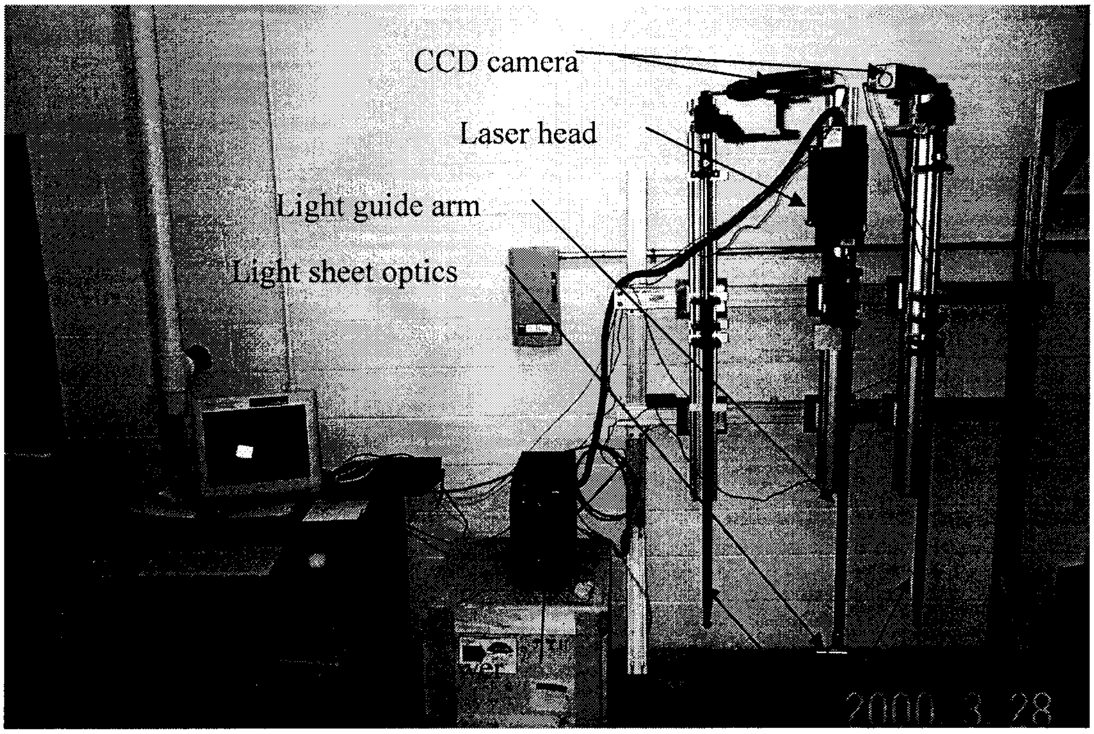

Figure 3-4 PIV System. view of complete system.

The borescopes, the cameras, the laser, and the light guide arm were fitted to an adjustable frame, which provided flexibility when setting up the equipment, allowing for variation of the spacing between the elements and the depth at which the flow measurements were made.

3.3.1 Laser and Light Sheet Optics

The laser used is a Solo 120 model supplied by New Wave Inc, which is a dual head Nd:Yag laser with maximum energy output of 120 mJ/pulse and a maximum pulse repetition rate of 15 Hz for each laser. The time between two exposures can be adjusted from 0 μs to 67000 μs. Figure 3-5 shows the layout of a dual oscillator Nd:Yag laser. Both laser beams are combined using a beam combining polarizer. The two Nd:Yag lasers output infrared light, or invisible light with wavelength 1064 nm. For PIV use, the fundamental wavelength is frequency doubled using a nonlinear crystal as second harmonic generator (SHG) which converts the IR light to visible green light of 532 nm. The crystal axis has to be orientated in a certain angle to the laser beam (phase matching). Approximately one-third of the original light energy is available in green. Dichroic mirrors that have maximum reflectivity for one given wavelength can be used to separated the green light from the fundamental wavelength (New Wave 2002).

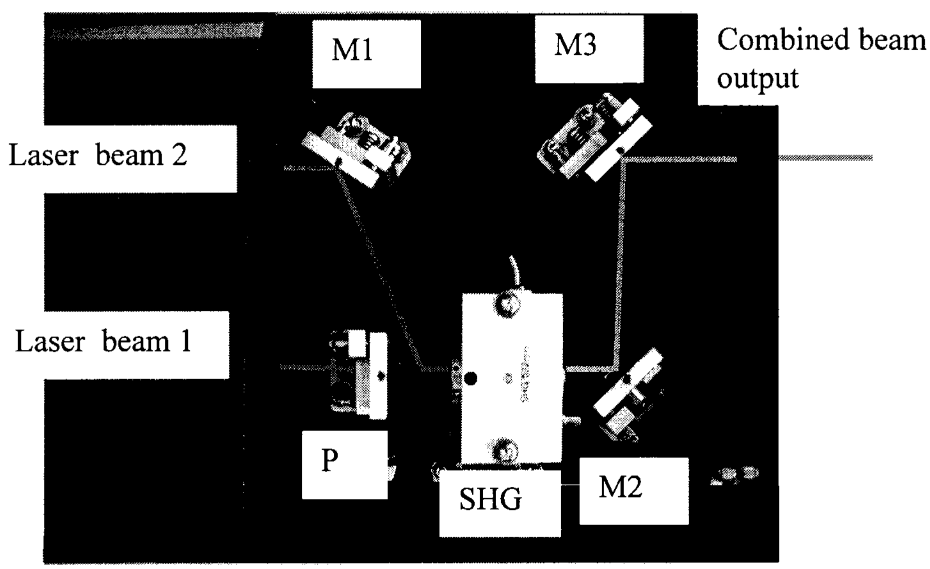

Figure 3-5 Layout of a dual oscillator Nd:Yag. M1, M2, M3: mirrors, P: beam combining polarizer, SHG: second harmonic generator.

The pulsed laser beams are directed downwards through a stainless steel connecting tube to a waterproof housing containing the light sheet optics. The specification of the light sheet optics is given in table 3-1. The light sheet optics inside the housing have a 45 degree mirror to turn the beam from vertical to horizontal and a fixed focal length cylindrical lens controls the divergence angle of the light sheet. A second 45° mirror can be used to change the direction of the laser beam. With the mirror in place, the beam is normal to the direction of the flow. This mirror can be removed so that the light sheet housing can be placed downstream of the model to illuminate a vertical plane parallel to the mean flow. At the top of the tube is a telescope with an infinitely adjustable focal length from 400 to 2500 mm (in water), which can be adjusted without disassembly of the water proof housing and is used to adjust the diameter of the laser beam to change the thickness of the light sheet. The downstream side of the light sheet housing and connecting tube was fitted with a tapered trailing edge to minimize wakes and vortex-induced vibration in the support tube.

Table 3-1 Specification of light sheet optics

Parameter	Specification
Light sheet housing diameter	40 mm
Connecting tube diameter	25 mm
Weight	5 Kg
Focal length	400-2500 mm (in water)
Divergence angle (for 4.5 mm beam diam.)	20°,30° and 60° (in water)
Material (housing and tube)	Stainless steel
Water proof	yes
Vortex shedding frequency (no taper)	80 Hz

3.3.2 Charged Coupled Device (CCD) Camera

A pair of single exposure image frames with a very short interval between the image frames, in a range of 0 μs to 67000 μs , is required to enable cross-correlation PIV data processing. The cross-correlation camera is a key element of a Digital PIV system. The digital image recording is done via a CCD camera which converts light to electric charge based on the photoelectric effect. A CCD camera contains an array of photosensitive pixels that are sensitive to light. Standard CCD video cameras are capable of acquiring video at 30 frames /s. The full-frame CCD cameras read out pixel values sequentially in a row-by-row manner, requiring almost one full frame time (1/30s) to read out completely (Smits & Lim, 2000). This presented a severe limitation, as this type of CCD necessitated the light source to be pulsed at exactly the same location within each frame. Therefore, initial applications of DPIV were limited to slow flows, since sequential images could only be pulsed synchronously at 1/30s time difference. To overcome this limitation, Dabiri & Roesgen (1991) suggested exposing each frame asynchronously. The standard convention is to use a cross-correlation camera which utilizes the "frame-straddling" or the frame transfer technique in which the CCD is exactly the same as a full frame CCD, except that the lower half is masked off and used only for storage. Using the frame transfer CCD it takes about 2 ms to shift the image from the exposed section to the masked-off section. Most recently, the full-frame interline transfer CCD has allowed even shorter pulse separations to be implemented for DPIV. This CCD placed the masked storage area adjacent to the pixel itself, making the total image shift time into storage approximately 1 microsecond (Raffel *et al.* 1998).

Two identical ImageIntense cameras were used in the MUN PIV system in order to obtain a 3D measurement. The detailed information for ImageIntense camera is given in Table 3-2. Each camera has a standard C-Mount and an adapter to Nikon F mount so that it can be used with standard Nikon C-mount or F-mount lenses (LaVision 2003). The cameras are progressive scan interline transfer CCDs. They can operate in a special double-shuttered (frame straddling) mode. A part of each pixel is masked off and can not be exposed by incoming light. This area is used as on-chip storage which allows two successive frames to be captured with a very short time delay. The recording of a PIV

Table 3-2 Image Intense Camera System Specification

Parameter	Specification
Resolution (pixels)	1376*1040
Dynamic Range, Digitization	12 bits
Cooling	2-stage thermo electric
Quantum Efficiency	65% at 500 nm
Readout noise	4e
Readout Rate	16 MHz
Date Rate(Vector Fields/sec)	5Hz
Capture Sequence Capacity to RAM	2GB
Capture Sequence Duration to RAM	34 sec
Camera Interface	High Speed Serial, PCI bus

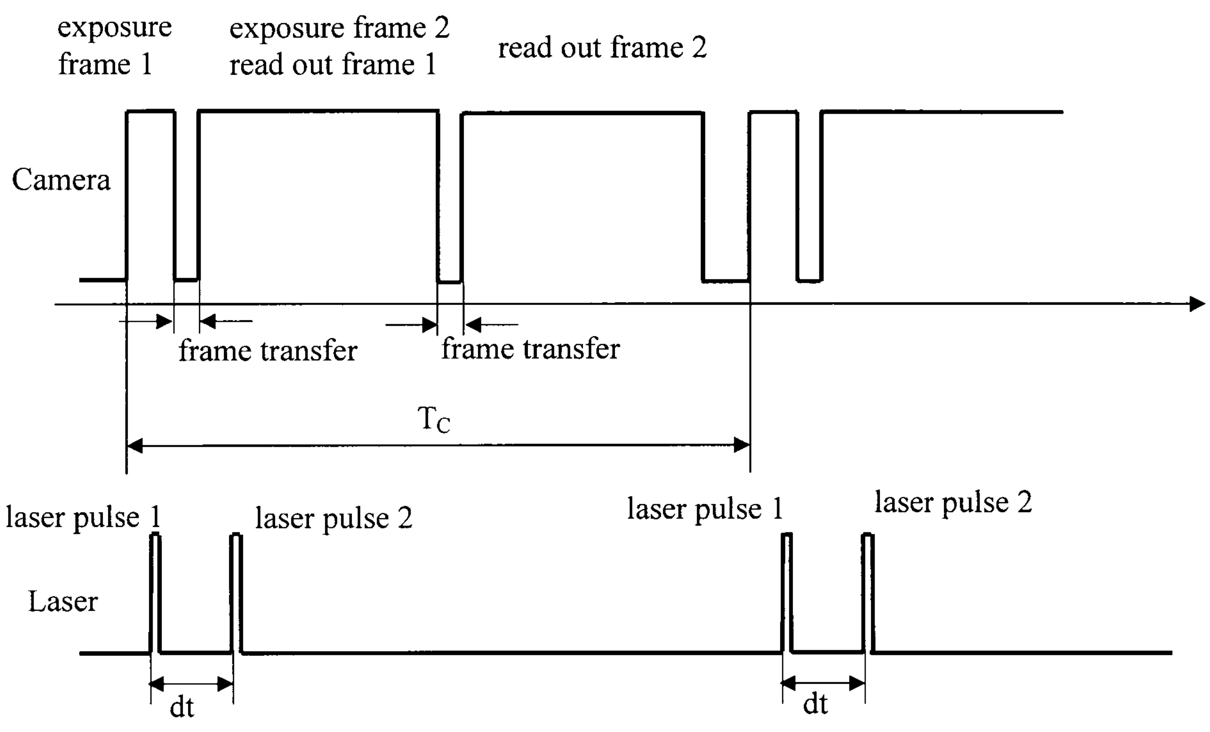

Figure 3-6 Timing scheme for a PIV recording

image is done in two steps. The optical sensitive area of a CCD is exposed and the accumulated charge for each pixel is shifted rapidly to the masked area (interframe time < $1\mu s$). For the read out of the first exposure the charge is shifted down vertically row by row in a masked off analog shift register. Then each row is clocked pixel by pixel through a charge-to-voltage converter that finally produces the analog video signal. While the first exposure is read out the second exposure is recorded on the light sensitive area. After the read out of the first exposure is completed the second image is shifted to the storage area and is also read out. Figure 3-6 shows the timing scheme between laser pulses and camera exposures. In order to follow the procedure, the exposure times for the two exposures in a double frame mode are quite different. Usually the exposure time for the first frame is in the range of some microseconds, while the time for the second exposure is determined by the time needed for the read out of the first exposure that corresponds to the camera repetition rate. Typically this is in the order of hundred milliseconds (LaVision 2003).

3.3.3 Borescopes

Borescopes were used instead of an underwater camera housing and this reduced the intrusiveness of the system in the flow. Having the submerged part of the system independent from the camera dimensions makes the system far more flexible and easy to handle. However, the small aperture of the borescopes and the lenses inside the borescopes potentially cause too much loss for the laser energy. This necessitated higher energy for the laser to obtain a good quality of images.

The detailed information about the borescope is given in table 3-3. The length of the present borescopes is 1.9 m. The collection cone angle of the borescopes and the viewing angle with respect to the borescope body are **35°** and **90°**, respectively (LaVision 2003). The viewing angle can be changed by adjusting the prism in the borescope head. A standard F-mount lens is mounted between the camera and the borescope. The image can be focused by adjusting the lens of the telescope on the borescope. This adjustment can be easily done after the all components of PIV system are installed on site. The downstream side of the borescopes is fitted with a tapered trailing edge to minimize wakes. The borescopes are optimized for the PIV system and have a maximum collection angle of 20° resulting in minimized distortion and increased light collection in Figure 3-7. A standard F-mount lens is mounted between the camera and the borescope.

Table 3-3 Specifications for borescope

Parameter	Specification
Diameter (outer)	24 mm
Length	2m
Weight (for 2m length)	4 Kg
Acceptance cone angle	35 °, 25° (in water)
Viewing angle	90°
Material	Stainless steel
Water proof	Yes
Vortex shedding frequency (no taper)	130 Hz

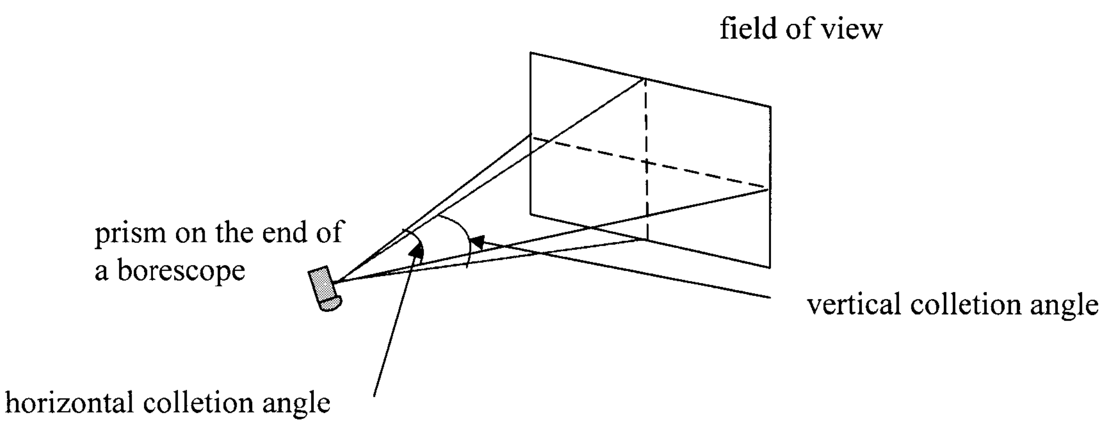

Figure 3-7 Skitch of the borescope collection angle

3.3.4 Programmable Timing Unit (PTU)

A PC-Interface (PCI)-Board and the Programmable Timing Unit-Board were installed in the computer to control the setting of the laser and cameras. There is serial data transfer between the camera and the PCI-Board. A Programmable Time Unit (PTU) controls the triggering of the camera and the synchronization with the laser. The exposure time of the camera, the laser power, and the interval between two laser pulses can also be adjusted by the PTU. The cameras and the laser can work under three modes, Single Frame/Single Exposure, Single Frame/ Double Exposure, and Double Frame/ Double exposure. The modes of particle images recorded by the different combination of two cameras and two laser pulses can be analyzed with either the auto-correlation or cross-correlation method.

3.4 PIV system setup

The CCD cameras and the laser sheet can be configured in various ways for the needs of different 2 dimensional and 3 dimensional measurement situations. Arranging a proper orientation for different measurements is also important in order to obtain a reliable result.

3.4.1 Stereoscopic PIV

The conventional 2D PIV method is only capable of recording the projection of a velocity vector in the plane of the light sheet as shown in Figure 3-8 (a). In the case of 2D PIV the out of plane velocity can not be measured which means that there are usually two velocity components measured in a two dimensional domain (2 dimensional domain and 2 velocity component, 2D-2C). However, the unknown third velocity component can also affect the measurement of the in plane components with an unrecoverable error. Because of this the light sheet is arranged according to the main flow direction, but for highly three dimensional flows this can cause significant errors. One approach to recover the complete set of velocity components is an additional PIV recording from a different viewing axis using a second camera, which is generally called Stereo PIV, as shown in Figure 3-8 (b). It can been seen that, from Figure 3-8 (b), the projections of the velocity vector in two planes can be obtained using the two different viewing angles. Therefore, it is possible to determine the viewing directions of both cameras with respect to the orientation light sheet position by a calibration. If the arrangement of both cameras is known it is possible to calculate all three velocity components from the two projections. Using stereo PIV all three velocity components can be measured on a two dimensional domain (2D-3C).

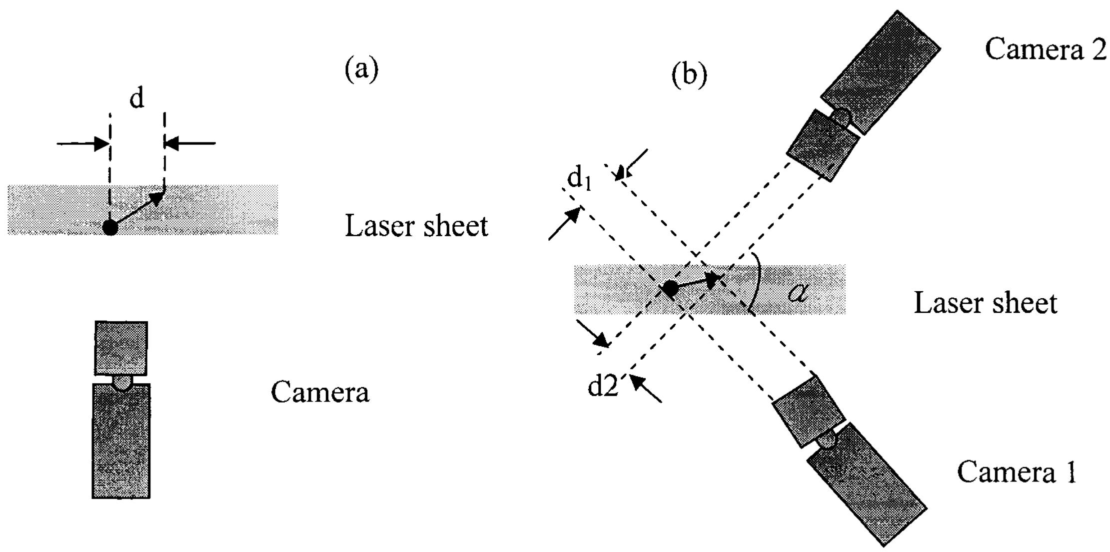

Figure 3-8 Sketch of 2D PIV in (a) and 3D PIV in (b)

3.4.2 Symmetric set up

Two cameras can symmetrically lie on the two sides of the laser sheet. The backward-backward and the forward-forward setup shown in Figure 3-9 are two symmetric orientations. The symmetric set up is the most efficient in terms of spatial resolution because the overlap of the two fields of view can be maximized. The distortion and light condition of images from two cameras is similar in this symmetric arrangement, hence better image resolution can be obtained.

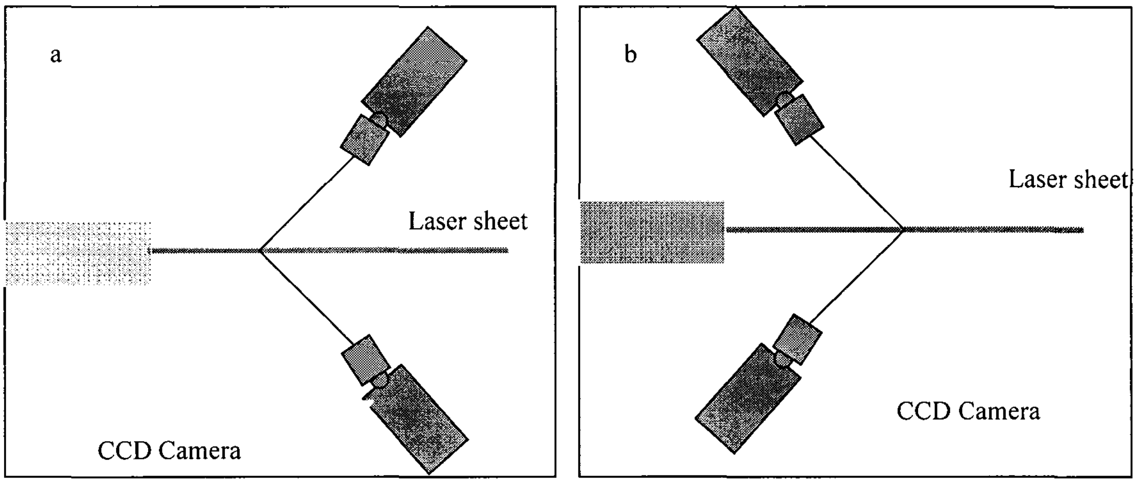

Figure 3-9 Symmetric PIV system setup, a: forward-forward scattering setup, b: backward-backward scattering setup

3.4.3 Asymmetric set up

Another possible arrangement for two cameras and the light sheet is that two cameras are on the same side of the laser sheet as shown in Figure 3-10. For this arrangement, one camera is recording the light scattered in forward direction while the second camera is recording the scattered light in backward direction. The intensities detected with both camera with the same f-number of the camera lens is different, so usually the camera viewing in backward scattering direction needs a larger aperture.

Both of the two arrangements can be used for measurements in three planes, i.e. a vertical plane normal to the flow direction, a vertical plane along the flow direction, and a horizontal plane.

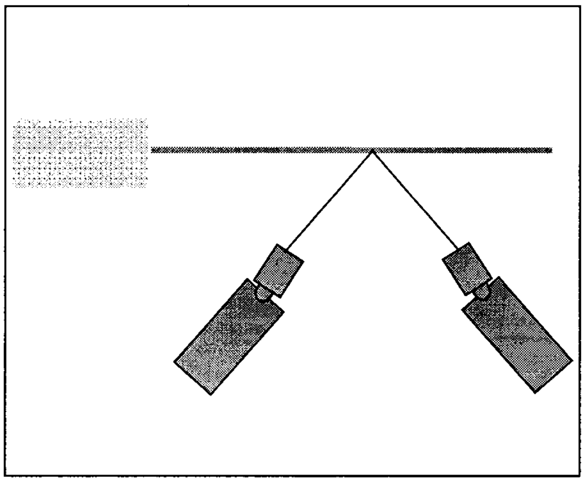

Figure 3-10 Asymmetric PIV system setup: Backward-forward scattering setup

3.5 System Accuracy

For a PIV system, the system accuracy includes two parts, processing accuracy and measurement accuracy. The processing accuracy depends on the software of particle image processing and velocity field processing. The measurement accuracy depends on the resolution of a camera, laser light sheet thickness and orientations of system set-up.

For the DaVis software in the MUN PIV system, the processing accuracy was 0.4 %, which is based on an average particle displacement of 5 pixels (LaVision 2003). The measurement accuracy of the MUN PIV system was estimated by LaVision from the flow including three components of velocity and shown in Table 4-1. It was assumed that the V_x and V_y velocity components are approximately $1/10^{th}$ of the V_z velocity component, where, the laser sheet is across the flow direction, x and y are in the plane of the laser sheet, z is normal to the laser sheet. The accuracy estimates in Table 4-1 are based on the largest field of view of 200×150 mm^2 and a speed of 1.5 m/s in the flow direction. Table 4-1 also shows the effect of the light sheet thickness on measurement accuracy. Since the measurement plane is normal to the free stream, seeding particle residence time is directly proportional to the light sheet thickness. For overlapped light sheets with a thickness of 1 mm, accuracy in the V and W velocity components will be affected due to the limited time between laser pulses and corresponding limited pixel displacements. The accuracy improves significantly as the light sheet thickness increases.

Table 3-4 System measurement accuracy estimates

Light Sheet Thickness (mm)	Max. Δt (μsec)	Max. Δz (pixels)	Max. Δx (pixels)	Max. Δx (pixels)	Error in V_z	Error in V_x & V_y
1	667	6.9	0.7	0.7	0.51%	3.6%
2	1,333	13.8	1.4	1.4	0.25%	1.8%
3	2,000	20.7	2.1	2.1	0.17%	1.2%
4	2,667	27.6	2.8	2.8	0.13%	0.9%
5	3,333	34.5	3.4	3.4	0.10%	0.7%

Chapter 4 Preliminary Tests

4.1 Introduction

Access to the Ocean Engineering Research Center (OERC) towing tank is often limited by other projects and it is extremely helpful to have the system set up and functioning prior to allocating time in the main tank, so that some simple experiments can be carried out in order to train ourselves on data collection and analysis methods. Water tanks can be used for PIV system development but provide little movement of the model for flow field measurement. Two different sized tanks were used for PIV system set up and training. The dimension for the smallest one was 1m × 0.6m × 0.6m. This tank was soon replaced by a larger tank, since it had insufficient structural strength when filled with water. The larger tank was a commercial fish-handling box, and was much larger and stronger. The larger tank had internal dimensions 1.8m × 0.9m × 0.8m. Both tanks held enough water to immerse the underwater components of the PIV system. It allowed studying the fundamental behavior of the seeding particles and developing secondary system components, such as the seeding rake, without having to use the much larger towing tank.

In this chapter, some preliminary tests with PIV system conducted in small tanks and in the MUN towing tank before the system was applied to a formal experiment are presented. The experiments included the comparison of different tracking particles, field of view of borescopes and the 3D flow field measurement around a very small propeller and different seeding method (Molyneux & Xu 2005a, 2005b, and Xu *et al.* 2005).

4.2 Comparison of Different Seeding Particles

As PIV method involves measuring the motion of microscopic particles within a flow field, it needs the seeding particles to fill the whole area with a fair density and that means a high consumption of particles during the experiment. Since the fluid velocity is inferred from the velocity of particles, it is important to select markers that will follow the flow within acceptable uncertainties without affecting the fluid properties to be measured. This implies that the fluid marker must be small enough to minimize velocity differences across its dimensions, and to have a density as close as possible to the density of the fluid being measured. The specific particles recommended for PIV are silver coated hollow glass spheres, which are very expensive; especially as a large amount of particles are needed when doing the PIV test in a towing tank.

The particles which can be used as seeding particles in PIV measurement should have features as below (Adrian 1984, Adrian & Yao 1985, Smits & Lim, 2000):

1) to follow the fluid without significant slip
2) to be as small as possible
3) to be neutrally buoyant or to be suspended in water
4) to make enough laser light reflection for taking the particle images
5) finally, for an economic reason, to be cheap

Usually, all these features can not be satisfied with only one type of particles. For example, the smaller the particles are, the easier they follow the fluid flow; however, the harder it is for them to be detected clearly by a camera. If the particles were absolutely neutrally buoyant in the water, they could be pre-seeded into the place where the measurement takes place. This would make the particle seeding easier during a test, especially in a towing tank. In fact, it is difficult to find particles with all the above properties. For the same kind of particles, the bigger their sizes are, the brighter their images are, because a bigger particle can reflect more light than a smaller one. A tiny particle often will be suspended in the water longer than a bigger one but this can only result in cloudy fluid sometimes, which in turn results in poor quality images. Meanwhile, the random motion of tiny particles due to Brownian motion may limit the accuracy of PIV measurement (Olsen & Adrian 2000).

Tests for the comparison of different particles were done in the fish box in early June, 2004. The purpose of this test was to try some substitutes for the expensive silver particles for PIV measurement. Four particles were selected for the comparison test. They were silver-coated hollow glass spheres (SHGS), Diatomite powder, flour, and toothpaste. The SHGS are commonly used in PIV measurements in water. The mean particle size is 17 microns, and the true density is 1.7 g/cc. Diatomite powder is a type of white powder normally used for cleaning water and can be found in the most water process shops. The flour and the toothpaste are the cheapest products and they can be easily found from most supermarkets.


(a)


(b)

Figure 4-1 Particle image of SHGS, (a) image taken immediately after seeding, (b) after 5 minutes

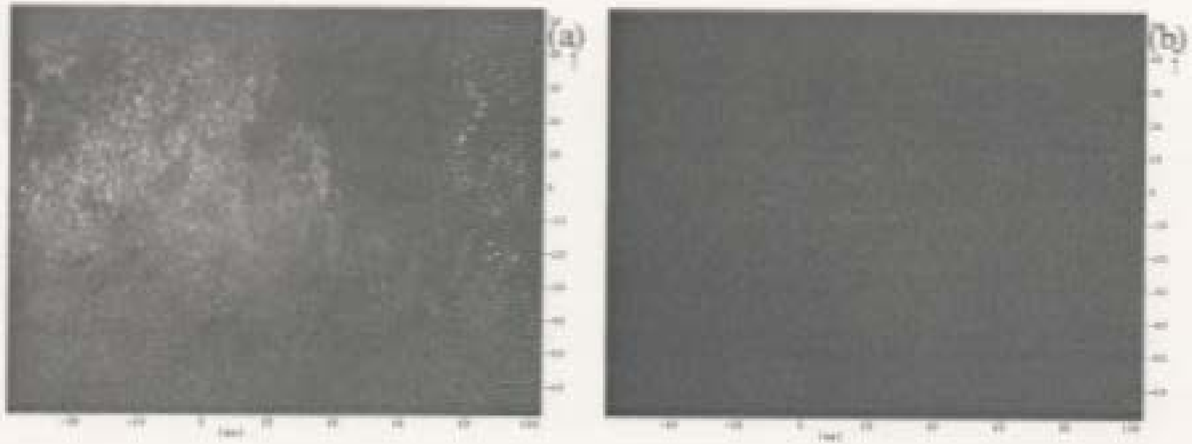

Figure 4-2 Particle image of flour, (a) image taken immediately after seeding, (b) after 5 minutes

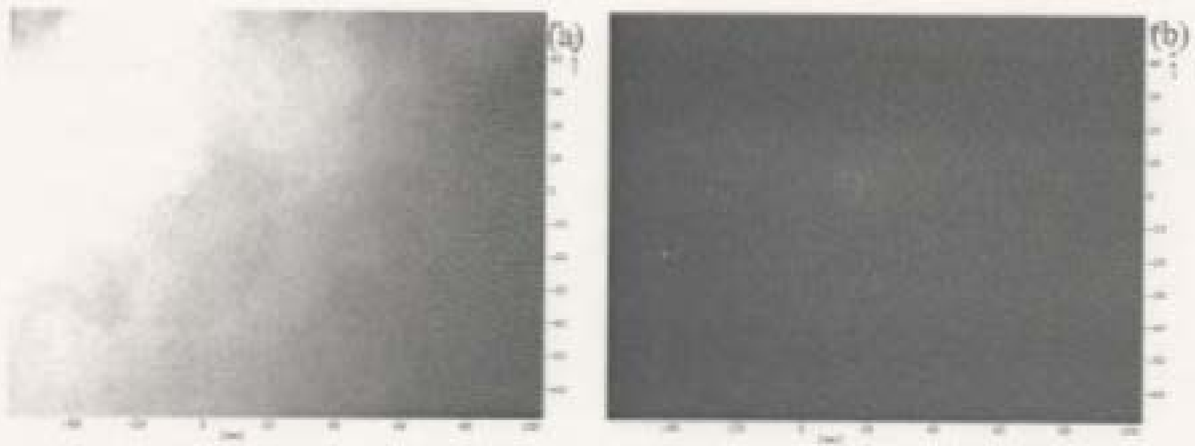

Figure 4-3 Particle image of diatomite powder, (a) image taken immediately after seeding, (b) after 5 minutes

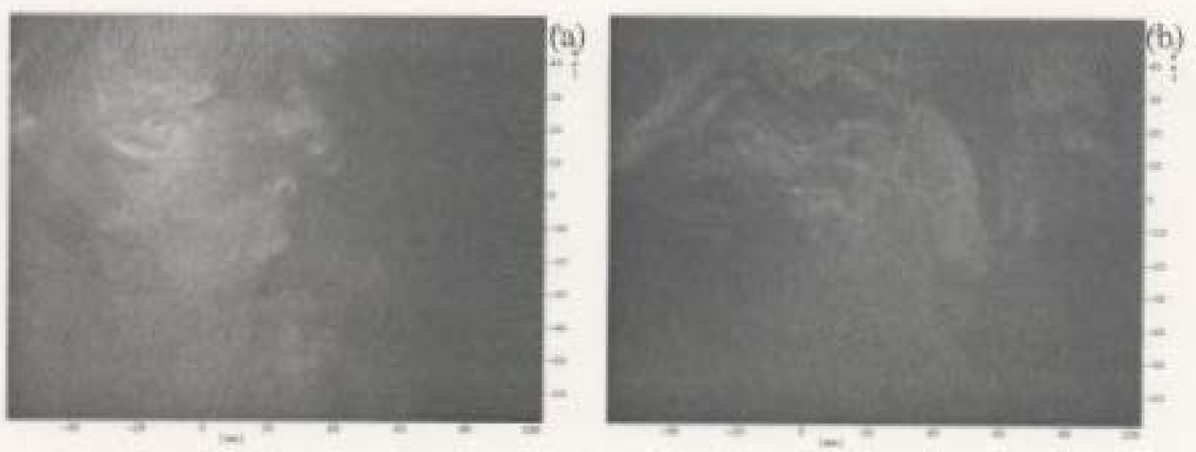

Figure 4-4 Particle image of toothpaste, (a) image taken immediately after seeding, (b) after 5 minutes

The images for the tests were taken using the 2D PIV system, i.e. one camera system, with the image mode of 'single frame single exposure', in the big tank. The experiments were done with the same field of view, 221mm by 168mm for the 4 types of particles. Fluid mixed with one type of particle was poured into fresh water in the tank. In order to observe the buoyant status of particles, particle images were taken at three different times, immediately, 5 minutes, and 10 minutes after seeding. After each test each type of particles, the tank was drained and filled again with fresh water for next test.

Figure 4-1 shows the particle image of the SHGS. In Figure 4-1(a) and (b), the particle image was respectively taken immediately and 5 minutes later after the particle fluid was poured into the water. From the image in Figure 4-1(a), it can been seen a mass of dense and bright particles in the filed of view. Although only very small amount of SHGS was added to the fluid, the concentration of the particles was quite high. After 5 minutes, as shown in Figure 4-1(b), a quite large amount of SHGS was still suspended in the water and individual particles were clearly visible, although the concentration of the particles decreased. The SHGS are quite even and can be buoyant in the water for 5-10 minutes after seeding.

Figure 4-2 shows the image of flour particles in the water. Some large individual particles were very clear just after the fluid was poured into the water, as shown in Figure 4-2(a). Flour sank fast. After 5 minutes, in Figure 4-2(b), only a few particles were left in the field of view. In fact, in addition to these discernible larger particles, there are lots of micro-particles in flour. When too much flour was put into the water, those small flour particles formed thick background noise which affected the visibility in the water and caused poor image quality. The amount of the large particles contained in flour was obviously not enough for a good PIV particle image.

The diatomite powder mainly consists of lots of very small particles which can not be discerned as individual particles by the camera. Figure 4-3 shows the image of diatomite powder. We can only see a mass of dense fog in the field of view when the fluid was just poured into water in Figure 4-3(a). The material kept sinking in the water. After 5 minutes, all of them had disappeared from the field of view, as shown in Figure 4-3(b).

Similarly to the Diatomite Powder, toothpaste also consists of very tiny particles which look like a cloud, not individual particles in the field of view, as shown in Figure 4-4(a). Unlike the Diatomite Powder, the specific gravity of toothpaste is the same as the water, the particles still suspended in the water after 5 minutes in Figure 4-4(b).

From the comparison tests, we can conclude that SHGS are high quality tracking particles with even size, good suspension ability and reflection effect. Although the tracking ability of flour was far worse than that of SHGS, it is a good cheap option. Flour can be used prior to a formal experiment to check the seeding system and condition, especially if seeding in real time is needed. This can reduce the test cost.

The size of the field of view also affects the quality of the particle image for one particular camera with the same resolution. The SHGS can have a good image effect for a measurement area of about 220 mm by 160 mm. The image effect for the same type of the particles could be different for a different field of view. Figure 4-5 shows the particle image of SHGS in two different sizes of the field of view. In Figure 4-5 (a), the particles in the image are clear and visible as individual particles. The measurement area was about 220mm by 160 mm. Figure 4-5 (b) shows an image with a measurement area of

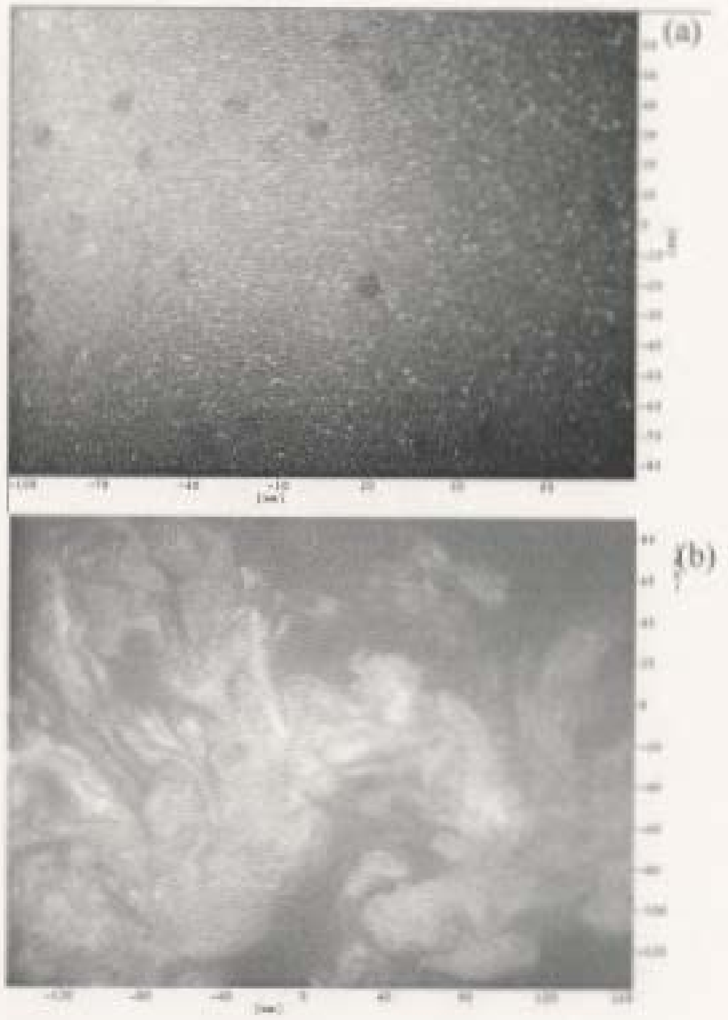

Figure 4-5 Particle image of SHGS in two different field of view, (a) 220mm by 160 mm; (b) 300mm by 220 mm

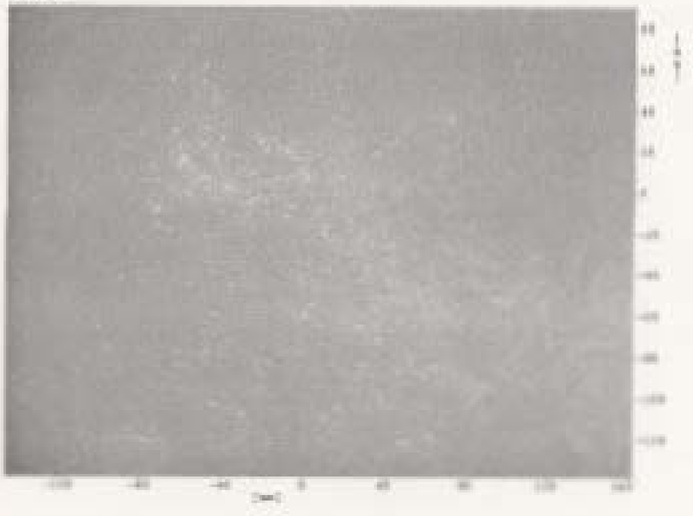

Figure 4-6 Particle image of SHCS in the field of view of 300mm by 220 mm

300mm × 220mm. These particles in the image can not be discerned as individual particles, and they look like a cloud. The particles, therefore, are not suitable for this size of a measurement area. Larger particles have to be used, in order to achieve a larger measurement area with an acceptable image quality. The silver coated hollow ceramic spheres (SHCS) are suitable substitutes of SHGS for a larger field of view. The mean size of the SHCS is 95 micros and the true density is 1.1 g/cc. Figure 4-6 shows the particle image of the SHCS with a measurement area about 300 mm by 220 mm. These individual particles can be seen in this image. Although the contrast of the image was not very good, the particle image was much better than that in Figure 4-5 (b). The SHCS sank faster than the SHGS, hence a bigger amount of SHCS is needed for the same test.

4.3 Seeding Rakes

Tracing particles play an important role in PIV measurement because the movement of the particles provides the flow field data. Seeding the flow is an essential element of PIV measurements. There are a few different seeding methods to be used in different PIV system set-ups and test facilities. If both the PIV system and the fluid are stationary, i.e. models moving, then it is only necessary to seed the volume of fluid close to the laser sheet. This option would be feasible for a stationary PIV system in a towing tank, where the ship model passes through the measurement volume. The movement of the model ship through the seeded fluid will cause a disturbance and the movement of the seed particles can be observed.

If the fluid is moving relative to the PIV system then one option is for the complete volume of the fluid to be seeded. This option may be feasible for a circulating water tunnel but is not practical in a towing tank, which has a very large volume of fluid, requiring a large number of particles. Eventually almost all of the seed particles will either sink to the bottom or float on the top because the particle density cannot be exactly the same as the water density. The large amount of particles consumed would increase the experiment cost.

A practical alternative is to introduce seed particles to the flow so that seeding is present only in the measurement volume for the duration of the measurements. This should allow for a controlled use of the seeding particles, and should provide high quality PIV images, since the seeding density is correct for the volume of fluid being studied, and the parts of the flow that are of no interest to the study are ignored. The disadvantage of this approach is that the seeding delivery system may affect the momentum of the seeding particles, which will influence the results. This was the option chosen for the MUN PIV system test in the towing tanks.

The system worked using hydrostatic pressure to deliver the seeded flow from the holding tank to the measurement volume. The seeding particles were mixed into clean water in the holding tank. The mixture was stirred prior to carrying out an experiment, to keep the seeding concentrations constant. The prototype system was constructed from readily available plumbing parts and included:

- Holding tank and drain;
- Connectors and pipes;
- Tap;
- Seeding rake

The seeding rake was made from a 22.2 mm ($^7/_8$ inches) diameter copper pipe and plumbing connectors. Two versions of the seeding rake were made. The first version had holes 6.35 mm ($^{1}/_{4}$ inches) diameter drilled at 41.3 mm ($1^{5}/_{8}$ inches) spacing and the second version had holes 1.58 mm ($^{3}/_{16}$ inches) diameter drilled at 19.1 mm ($^{3}/_{4}$ inches) spacing. Figure 4-8 shows the seeding rakes and Figure 4-9 shows the prototype system installed on the carriage.

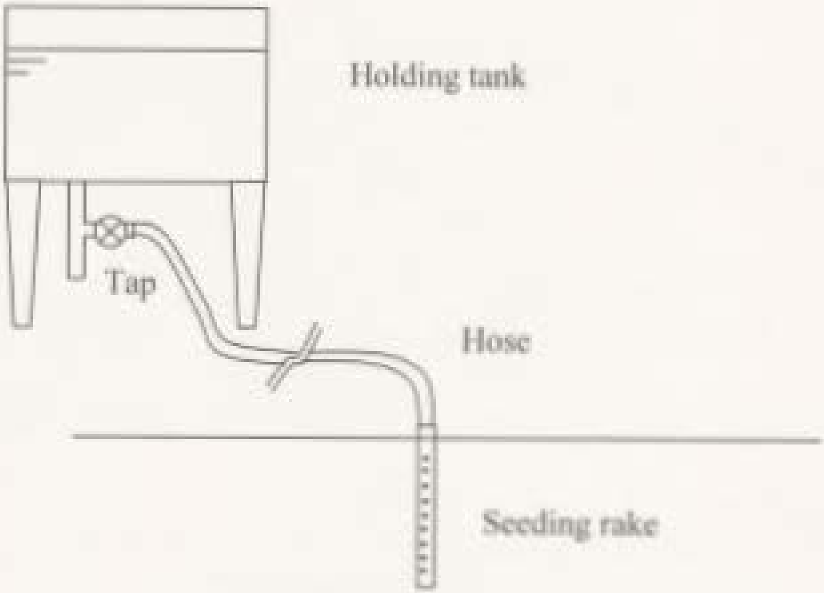

4-7 Sketch for seeding system

Figure 4-8 Seeding rakes (rake with large diameter holes on right)

Figure 4-9 PIV seeding tank installed on OERC towing tank carriage

Each rake was tested in the small tank with stationary fluid to examine the quality of the flow. The PIV system was set up in the fish box, with the laser sheet along the long axis of the tank. The seeding rake was placed upright in the laser sheet, at the edge of the field of view. PIV measurements were made with flow through the system. Examples of the particle images for each rake are given in Figures 4-10 and Figure 4-11.

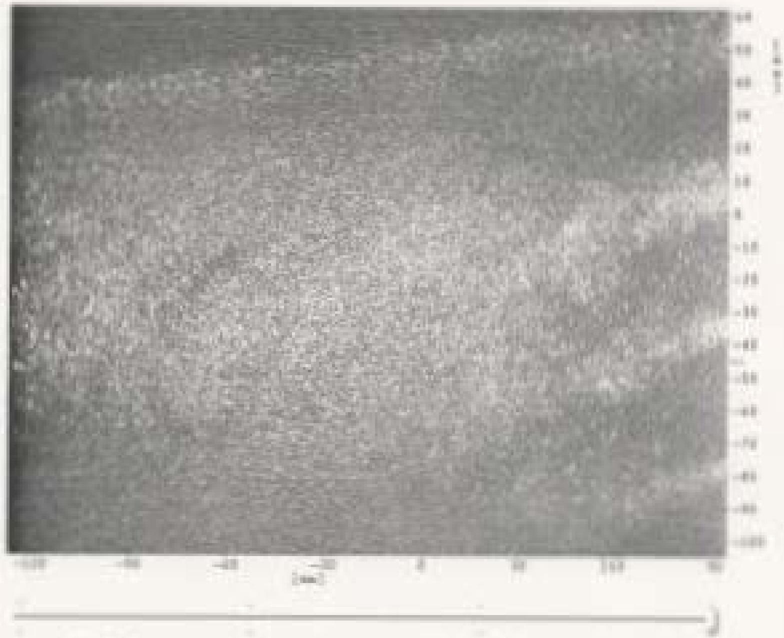

Figure 4-10 Image of seeding particles from rake with large holes

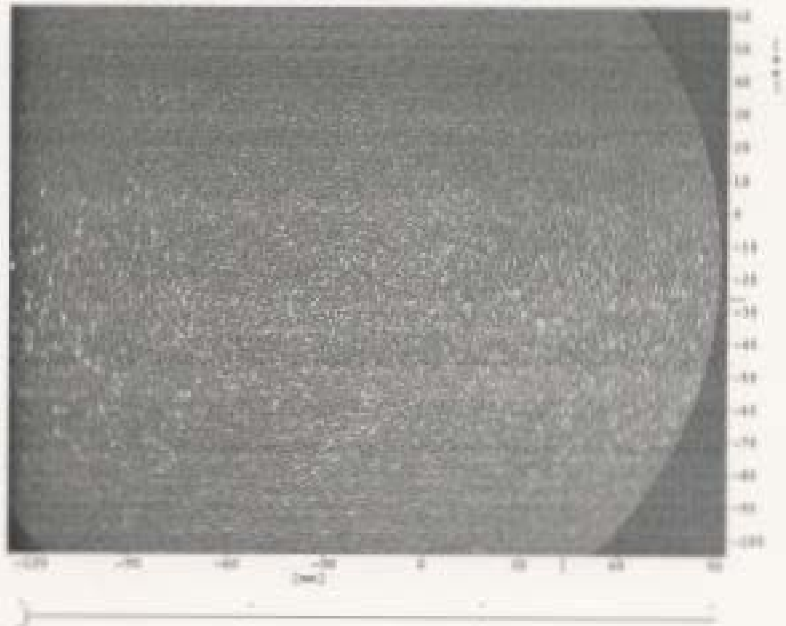

Figure 4-11 Image of seeding particles from rake with small holes

It can be seen from the seeding particle images in Figure 4-10 and Figure 4-11 that at zero flow speed, the seeding rake with large holes shows distinct jets of particles in the flow (at the right hand side of the image), but the rake with small holes has an even distribution of particles. Based on the results of these experiments, the rake with small holes was initially selected for the experiments in the towing tank. However, the rake with small holes did not give satisfactory images for the experiments with forward carriage speed, and so the rake with larger holes was used in the preliminary experiments in the MUN towing tank.

4.4 Calibration for 3D Measurement

3D-PIV measurements require two different viewing angles of the same measurement space. From the two views projections of the velocity vector can be obtained in two planes (one for each camera). It is possible to determine the viewing directions of both cameras in relation to the measurement space by using a calibration procedure. Since the arrangement of both cameras is fixed it is possible to calculate all three velocity components from the two projections, by calibrating the measurement space against a matrix of points with known spacing in three dimensions.

A proper calibration is an important step when making PIV measurements, especially for 3D measurement. Calibration of the PIV system can be carried out using a calibration plate shown in Figure 4-12. The calibration plate is a thin board of 300mm^2 area and 12mm in thickness, supplied by LaVision. Both surfaces of the plate consist of two levels with 2 mm difference in height and are marked by a black background with white dots. The spacing between two successive vertical or horizontal dots is the same. Once the PIV system was set up and fixed on the test site, the calibration plate was placed in the measurement region and must be parallel to the laser sheet to do the calibration. The calibration plate image was recorded by the two cameras and evaluated by the software in order to calculate the mapping function between the two images of the plate as shown in

Figure 4-12 Two level calibration plate

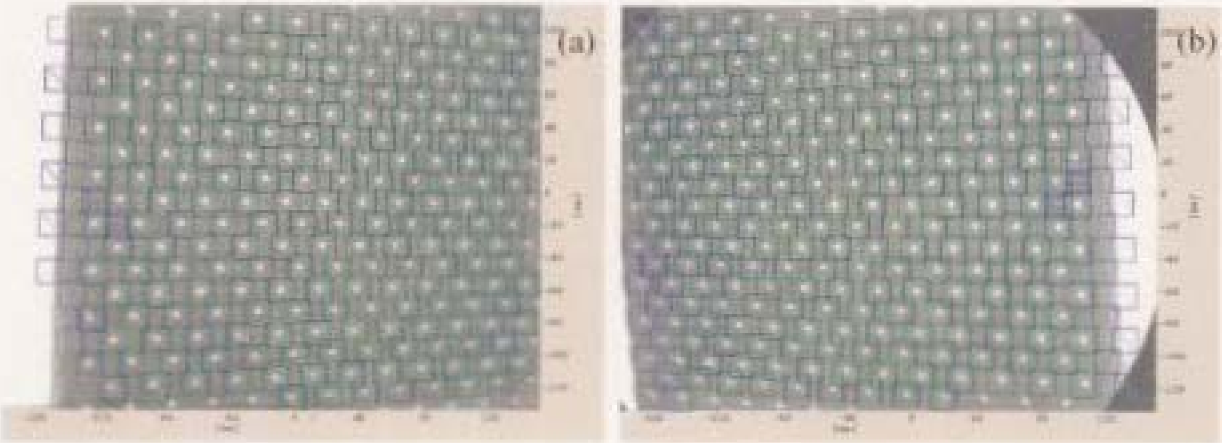

Figure 4-13 Evaluation of mapping function (a): image of calibration plate from camera 1, (b): image of calibration plat from camera 2

Figure 4-13. Parameters, such as the type of calibration plate, distance between marks in xy plane, displacement in the z plane (dz), size of dots (in pixels), etc. must be entered into the software during the calibration. The image of the calibration plate taken on site also provided information about the field of view of the camera. For evaluation of the mapping function, the software displays results of the search for dots and the least-square fit, which shows if the calibration was successful. A sufficient number of dots must have been detected to be able to compute 20 mapping coefficients. The minimum number is 20 dots, but, about 40 to 100 dots should be included to determine the mapping function with sufficient accuracy. In Figure 4-13, these squares show the result of evaluation of the mapping function. The red squares are displayed at all positions where dots are searched for (do not show in the image) and a green square is displayed when the search for a dot was successful.

4.5 Preliminary PIV experiment for 3-D Flow Field

In order to be familiar with the system and its operation, some preliminary experiments were carried out in the small tank and MUN towing tank (Xu *et al.* 2005). These included the flow field measurement for a small propeller in the small water tank, for uniform flow measurement and different seeding method test in the MUN towing tank.

4.5.1 Flow Field Measurement for a Small Propeller

The experiment of the flow field measurement for a model propeller was conducted in the small tank (Xu *et al.* 2005). The support frame for the PIV components was mounted on the ground. The light sheet optics and the two borescope ends were immersed in the water. The two-bladed propeller was submerged right under the water surface. A three dimensional flow was produced when the propeller rotated. The laser sheet with a thickness of around 2.5 mm illuminated the axial plane of the propeller. The layout of the experiment set-up is shown in Figure 4-14.

The propeller had two blades and was installed vertically under the water surface. Particles, silver coated hollow glass spheres with the average size of 18 μm in diameter, were seeded into the water. When the propeller was rotating, a flow was created around it. The measurement plane was located on the plane of the axis below the propeller. Two pulsed laser sheets successively illuminated the plane within a very short interval of 2 ms; meanwhile, the cameras took the particle images from both sides of the plane to obtain the particle movement in the volume of the light sheet. Figure 4-15 shows the four images recording the positions of the particles from the two cameras at the two instants. The left two images were taken by camera 1 at the time t1 (the upper image) and t2=t1+3ms (the lower one). The right two images were from camera 2. In figure 4-16,

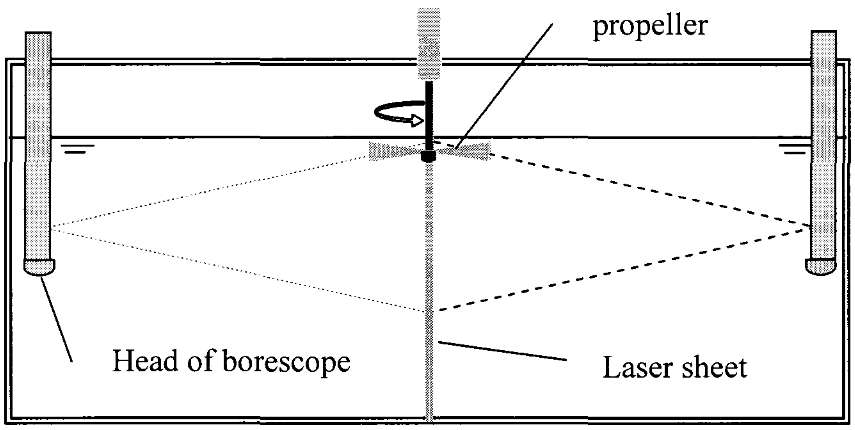

Figure 4-14 Sketch of the test set-up for the propeller

the propeller can be seen at top centre of each image frame. The velocity vectors of the whole field in the measurement area were obtained by a cross-correlation function of the particle images and the mapping function of 3D calibration images taken in the volume measured from both cameras.

In the vector analysis process, 64×64 pixel interrogation windows were used for the first correlation followed by 32×32 pixel sub-windows for the second correlation. All velocity vectors of flow within the plane of the light sheet were averaged over 30 successive frames, shown in Figure 4-16. The velocity in the z-direction, which is through the measurement plane, is displayed with contours. The V_y and V_x vectors show increasing strength as they approach the propeller and well defined flow patterns in all

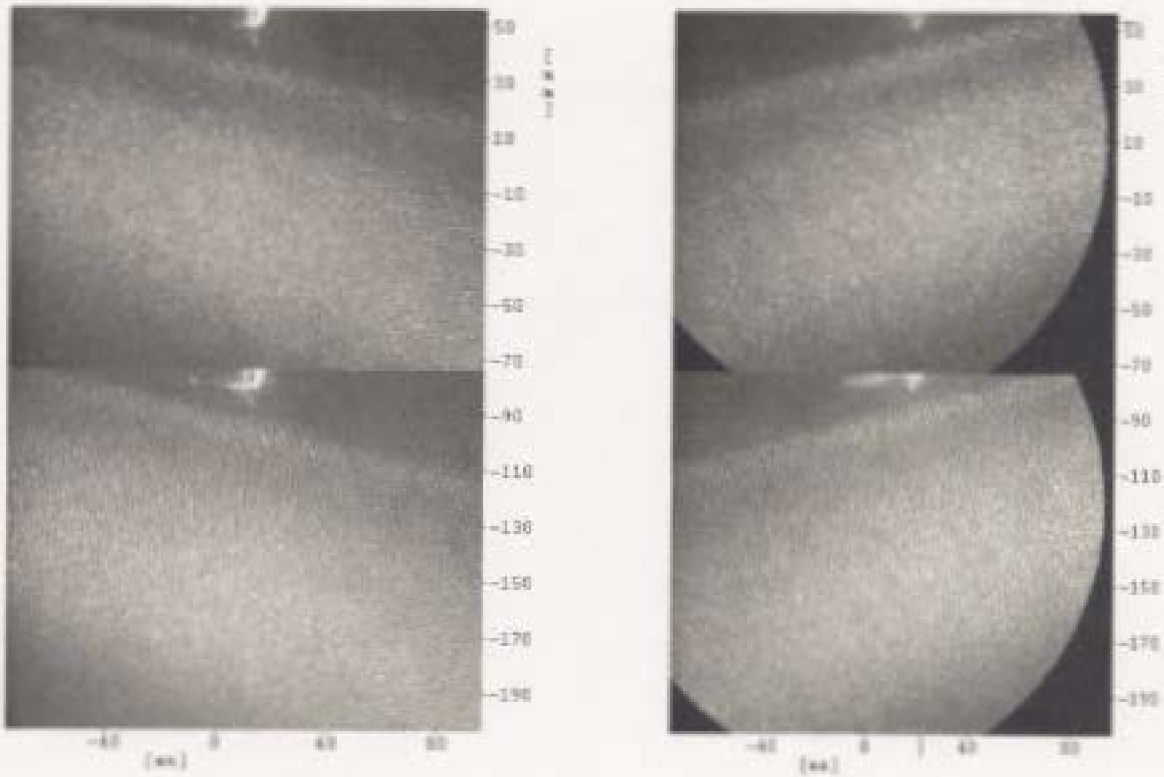

Figure 4-15 Double frame, double exposure particle images of propeller wash measurement

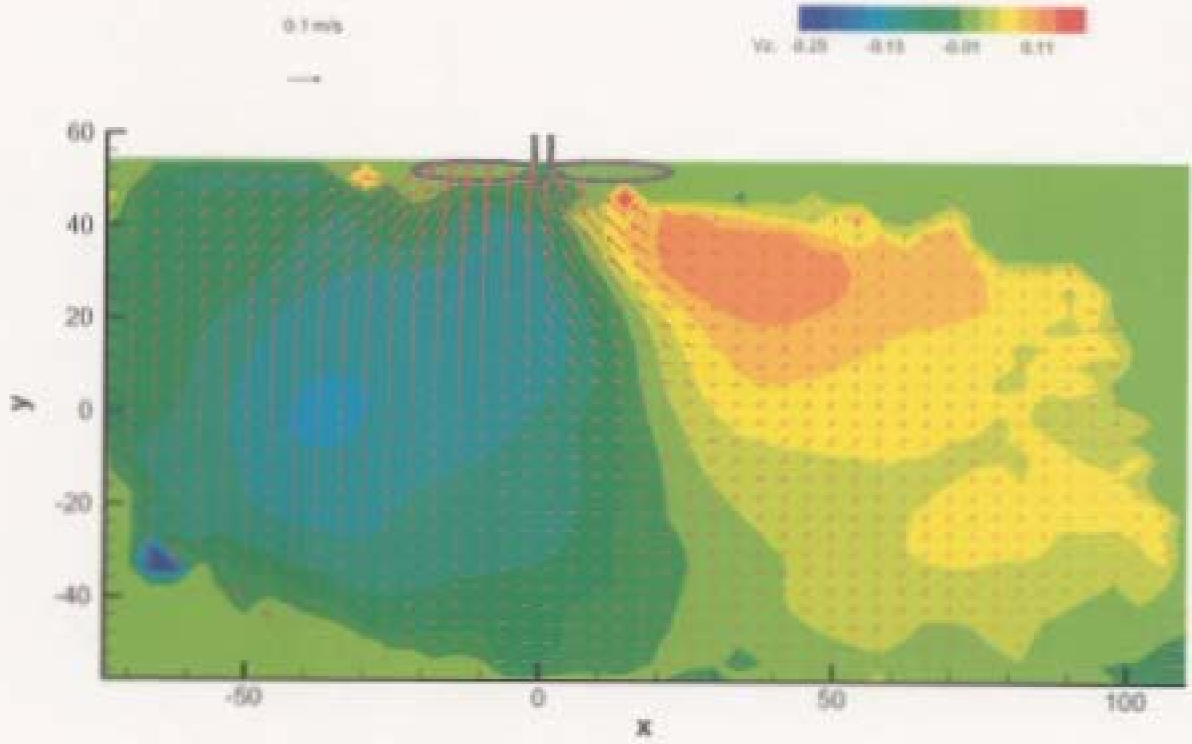

Figure 4-16 Velocity field of the propeller

regions of the measurement volume. The contour colors show the velocities through the measurement plane, V_z, were symmetrically distributed and the direction of the vectors are opposite on the either side of the propeller axis.

4.5.2 Uniform Flow Measurement and Seeding Methods

A uniform flow field was measured in the vertical measurement plane along the flow direction in the OERC towing tank. The results of uniform flow can be used to examine the effectiveness of the PIV system and seeding system. Some experiments were carried out with particles introduced to the flow using alternative seeding systems and some were carried out using only particles left in the fluid from previous runs. When the seeding system was used, it was located upstream of the measurement area, just out of the field of view of the cameras. The seeding rake can discharge the particle fluid in two ways, the side holes and the end hole. For the side discharge version, the rake extended across the depth of the field of view as shown in Figure 4-17 (a). For the end discharge version, particles entered the flow through the open end at the bottom of the cylindrical rake, and the bottom of the rake was ahead and above the field of view as shown in Figure 4-17 (b).

Particle images were analyzed using interrogation windows of 64×64 pixels with a subwindow of 32×32 pixels, with 50% overlap of each window. The resulting vector field was further processed to remove spurious vectors and the vector field smoothed. Each sequence of calculated vector fields was examined to make sure that the flow was approximately steady, and then the flow vectors were averaged over twenty frames. The calculated mean speeds over the complete vector field are given in Table 4-2.

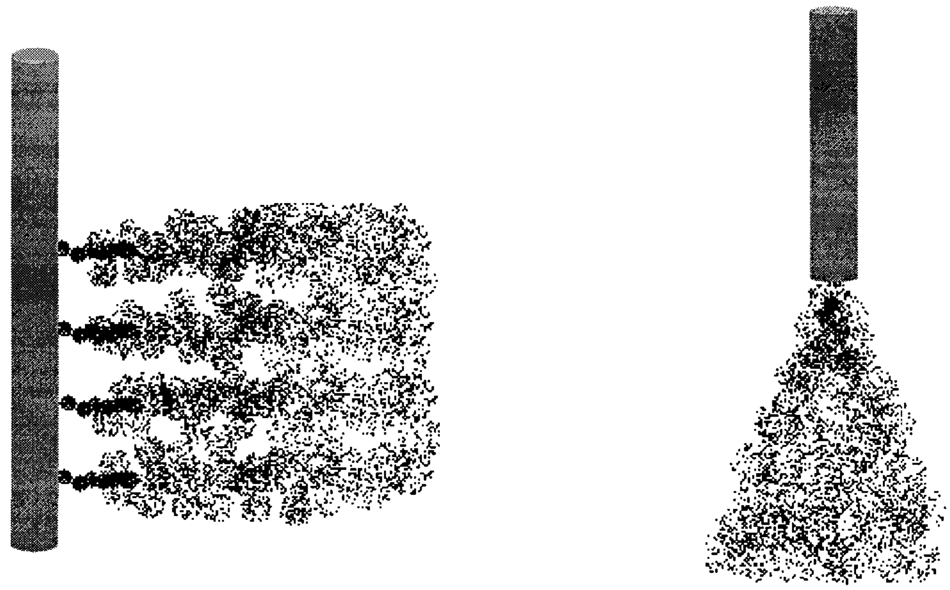

a. side hole discharge b. end hole discharge

Figure 4-17 Sketch of two discharge methods of the seeding rake

An effective wake fraction for the seeding system was defined as $w=(V_c-V_x)/V_c$, and calculated values for each experiment are given in Table 4-2. Here, V_c was the speed of the free stream and V_x, V_y, and V_z were the mean values of 20 frames calculated from the PIV for a whole measurement field, where, the x-axis was in the same direction of the carriage motion, y-axis was normal to the flow direction and vertical, z-axis was normal to the flow direction and horizontal. These results in Table 4-2 show that the best speed measurement was for Test_24 at a carriage speed of 0.75 m/s, which was made with the residual seeding left in the tank from previous runs. This case showed good agreement between the measurement value, V_x=-0.778, and the free stream, V_c=-0.75, in the flow direction. The measured velocity in the flow direction was within 3% of the free stream speed for this case. In all other cases, the flow was affected by the presence of the seeding rake in the water. For the side discharge seeding system, at the lowest speed of 0.1 m/s (Test_05), the measured velocity is within 14% of the free stream speed, but in all other cases for Test_06-Test_09, at speeds of 0.3, 0.5 and 0.75 m/s, the effective wake fraction is between 50% and 60% as shown in Table 4-2. The effect of the seeding rake on the wake became bigger with the increase of the carriage speeds for the side discharge method. There is a significant improvement between the side discharge version (Test_09) and the end discharge version (Test_23), at a speed of 0.75 m/s, but even the end discharge version has a significant effect on the flow. As shown in Table 4-2, the wake fraction for the end hole seeding is about 30%.

The example of the flow velocity distribution is given in Figure 4-18, which shows in-plane velocity vectors V_x and V_y for residual seeding at a speed of 0.75 m/s. Flow was moving from left to right. The expected result was to have a constant velocity in the x direction with the same magnitude as the carriage speed and zero velocity components in the y direction. In this case, the measurement was carried out without an active seeding system, only using the seeding left in the tank after a few experiments had been completed. This figure shows an almost constant vector field of V_x, which is represented by the black vectors, with flow vectors parallel to the x-axis and of the correct magnitude. Some vectors at the corners of the plot show the incorrect magnitude in the x direction and the velocity components in the y direction. These errors were mainly caused by the different apertures of the two borescopes as shown in Figure 4-13 and Figure 4-15.

The preliminary tests were very helpful for learning the set-up, operation, calibration of the PIV system, as well as different seeding technics. Seeding in a towing tank is a challenge especially when a test model with a larger size is on site. Further exploration is needed for future tests where even large sizes are anticipated.

Table 4-1 Summary of seeding method and wake estimate of PIV preliminary test in MUN towing tank

File	Seeding	Free stream m/s	Mean value calculated from PIV, m/s					Wake fraction
		Vc	Vx	Vy	Vz	|V|	Rms (V)	w
Test_05	Rake, side holes	0.10	0.114	0.010	0.008	0.122	0.031	-0.140
Test_06		0.30	0.148	0.013	0.037	0.174	0.056	0.507
Test_07		0.50	0.244	0.015	0.064	0.299	0.010	0.512
Test_08		0.50	0.198	0.020	0.062	0.278	0.166	0.604
Test_09		0.75	0.410	0.021	0.006	0.454	0.094	0.535
Test_23	End holes	0.75	0.635	0.043	-0.026	0.647	0.045	0.291
Test_24	Residual	0.75	0.778	0.032	-0.221	0.843	0.170	0.037

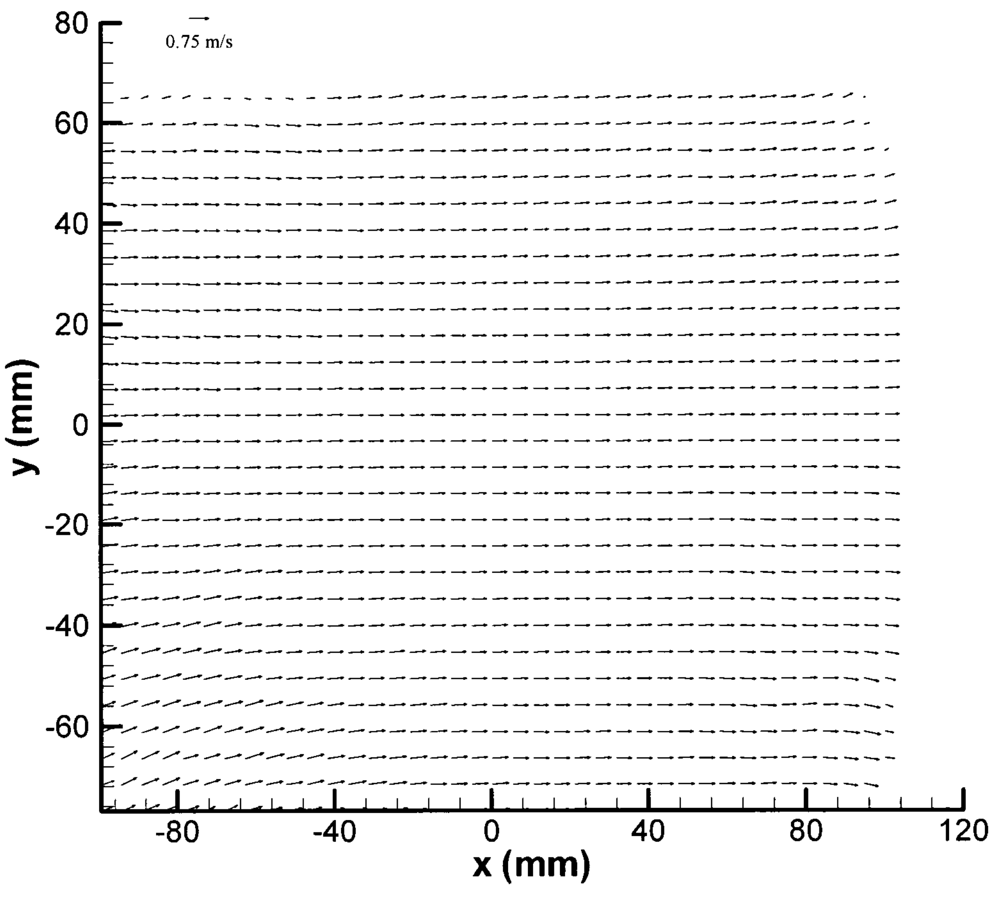

Figure 4-18 Velocity field of uniform flow at a speed of 0.75 m/s

Chapter 5 Experiment Method

5.1 Introduction

A VIV flow field experiment was performed at the IOT Ice Tank. A flexible riser model was towed horizontally at steady forward speed while it oscillated in both transverse and inline directions due to VIV. Digital Particle Image Velocimetry (DPIV) provided quantitative data of the instantaneous velocity field. The test model, the experimental setup, and the measurement approach are described in this chapter.

5.2 Ice Tank

The VIV experiment was conducted in the Ice Tank that has dimensions of 90m in length, 12m in width, and 3 m in depth, as shown in Figure 5-1. The carriage has a 4 wheel synchronous motor drive and two test frames for mounting models. The two test frames are about 10 m long, 0.6m wide and 0.8m high, aligned with the flow direction. Both frames can move vertically and horizontally to fit different demands of the model installation. The speed range is from 0.0002 m/s to 4.0 m/s. Data Acquisition is performed by a VMS and Windows NT based distributed client/server system using one or more IOtech DagBoards, each with 256 channel capability at 100 kHz. The Ice tank was used as a water tank and no ice sheet was used in this experiment.

Figure 5-1 Overview of the ice tank

5.3 VIV Test Apparatus

5.3.1 Riser Model and Installation

The VIV apparatus consisted of a riser model, a support frame and instrumentation, as shown in Figure 5-2. A length-distorted riser model, i.e. length was not similar to the prototype riser, was used in this experiment. The riser model was designed based on a linear analytical model and similarity theory (Li *et al.* 2005). Three assumptions were applied in order to design the length-distorted model riser:

i. Hydrodynamic loads acting on the riser are frequency-independent;

ii. Hydrodynamic and structural loads acting on the riser are location-independent;

iii. Hydrodynamic damping can be linearized

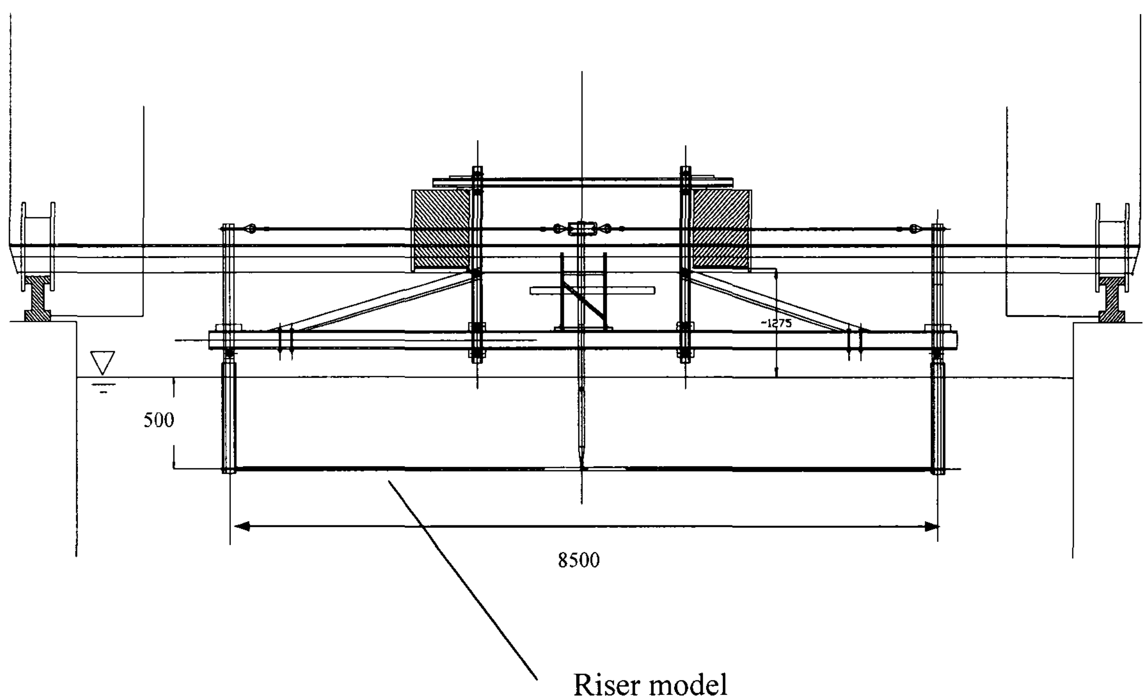

Figure 5-2 Sketch of the riser and the support frame

The length and the diameter of the riser model depended mainly on the test facility and the instruments. The parameters of the model are given in table 5-1.

Table 5-1 Properties of the riser

Property	model
Length	8.5 m
Diameter	0.047m
Weight per unit length	16.8N/m
Bending stiffness	1.52 N.m^2
Pre-tension	420 N

The riser model was made of two coaxial rubber hoses and a steel cable went through the inner hose to withstand the tension. The pre-tension acting on the riser was adjusted by a turn-buckle in the middle of the tension cable and measured using a load cell. The pre-tension for the experiments was 420 N. The tension of the riser changed with the current speeds. Two aluminum connectors, as shown in Figure 5-3, were respectively fixed at the two ends of the cylinder so that the model could be fixed to the steel frames. In order to avoid leaking, the gap between the inner and outer hoses was filled with silicone sealant, and latex tape wrapped on the cylinder surface to make it smooth. The dimension of the outer hose, D, was 0.047m, and the overall length, L was 8.5 m.

Figure 5-3 End connector of the riser

The riser was horizontally mounted under the water around 0.6m deep by a set of steel support frames and normal to the flow direction as shown in Figure 5-4. Both ends of the riser were rigidly connected to two vertical steel frames one of which played the role of a lever when the pretension was loaded. The two vertical frames were fixed to the ends of a 9m long crossbeam which was rigidly mounted with two L-frames and two vertical holding frames connected with a horizontal frame clamped on the main test frames of the carriage. In order to avoid the test apparatus tilting at high speeds, other two L-frames were used to support the whole VIV test apparatus along the flow direction.

Figure 5-4 Installation of the riser test apparatus ① Holding frame, ②Tension cable, ③ L-frame1; ④ Vertical lever; ⑤ Crossbeam; ⑥ L-frame2 ; ⑦ Riser

The riser was instrumented with 16 accelerometer pairs which were inside the inner hose and evenly distributed along its length to measure in-line and cross-flow motions. For this set of experiments, eight sets of data from four pairs of accelerometers which were close the measurement plane were acquired. The four pairs of accelerometers located at the middle of the riser and the position and the node number of each accelerometer are given in Table 5-2. The two accelerometers at node 8 were the closest to the PIV measurement plane and the data was analyzed to determine the riser vibration response associated with the wake vortex.

Table 5-2 List of accelerometers and corresponding position installed in the riser

Node	1	2	3	4	5	6	7	8
Accel.No	5#, 6#	7#, 8#	9#, 10#	11#,12#	13#,14#	15#,16#	17#,18#	19#,20#
Position (m)	0.81	1.214	1.619	2.024	2.429	2.833	3.238	3.643
z/l	0.095	0.143	0.190	0.238	0.286	0.333	0.381	0.429
Number	9	10	11	12	13	14	15	16
Accel.No	21#,22#	23#,24#	25#,26#	27#,28#	29#,30#	31#,32#	33#,34#	35#,36#
Position (m)	4.048	4.452	4.857	5.262	6.476	6.881	7.286	7.691
z/l	0.476	0.524	0.571	0.619	0.762	0.810	0.857	0.905

In Table 5-2, the odd numbers represent accelerometers for the in-line direction; the even numbers are for the cross-flow direction.

5.3.2 Calibration of Accelerometers

The calibration of accelerometers is the key step in order to obtain accurate vibration acceleration data. To calibrate the accelerometer, the riser was turned around its rotatory axis from 0° to 360° with an increment of 30° and the output voltage of the accelerometers was acquired at each angle. This was done as the riser was mounted on the test frame on site and stationary. The calibration coefficient and the orientation of each accelerometer were estimated by a sinusoidal curve fitted to the calibration data. The relationship between the sinusoidal curve and the calibration coefficient as well as the orientation for each accelerometer is given as below:

$$s_i = g / A_i$$

$$\theta_i = \phi_i$$

where, s_i and θ_i are the calibration coefficient and the orientation angle of the ith accelerometer, respectively; g is the gravity acceleration; A_i and ϕ_i are the amplitude and the phase angle of the sinusoidal curve, respectively.

The calibration data and the fitted sinusoidal curve for eight accelerometers are given in Figure 5-5 to Figure 5-8. The dots show the data points and the line is the sinusoidal curve. Table 5-3 shows the calibration coefficient and the orientation angle of these accelerometers.

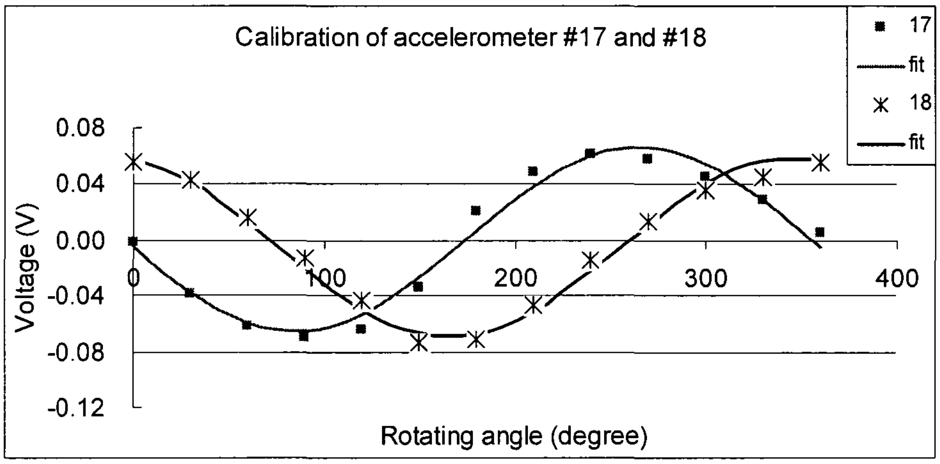

Figure 5-5 Calibration curve of accelerometer No.17 and No.18

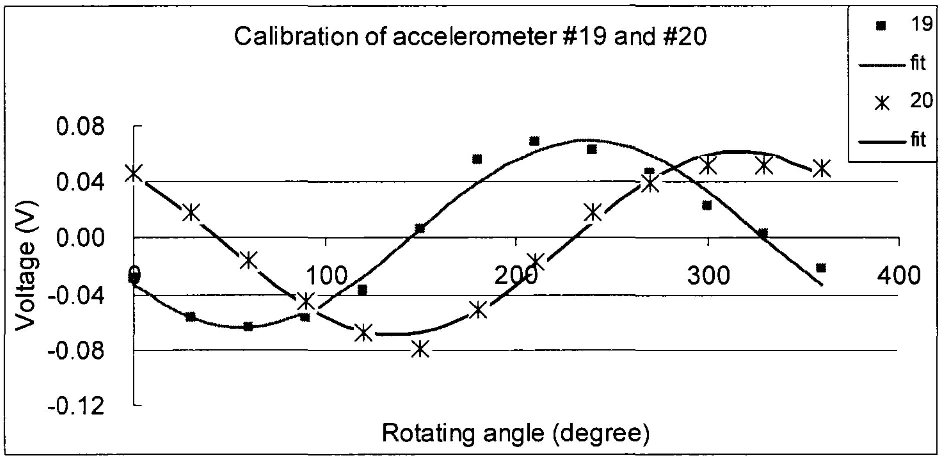

Figure 5-6 Calibration curve of accelerometer No.19 and No.20

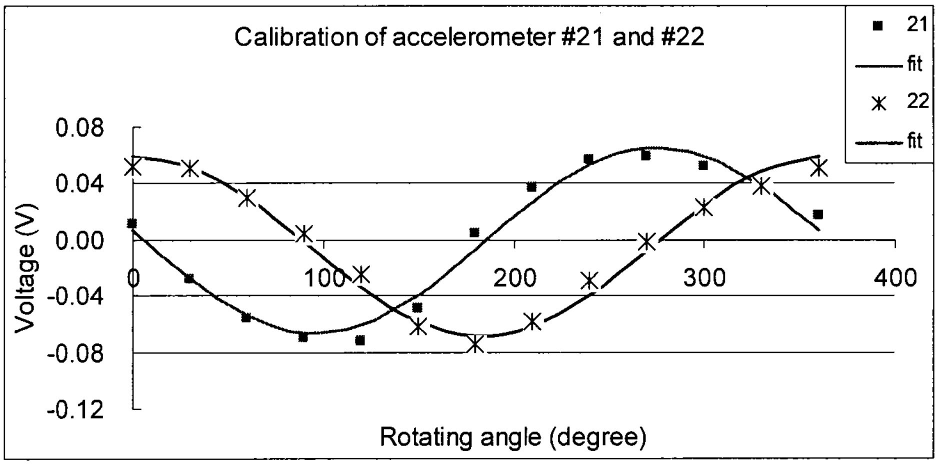

Figure 5-7 Calibration curve of accelerometer No.21 and No.22

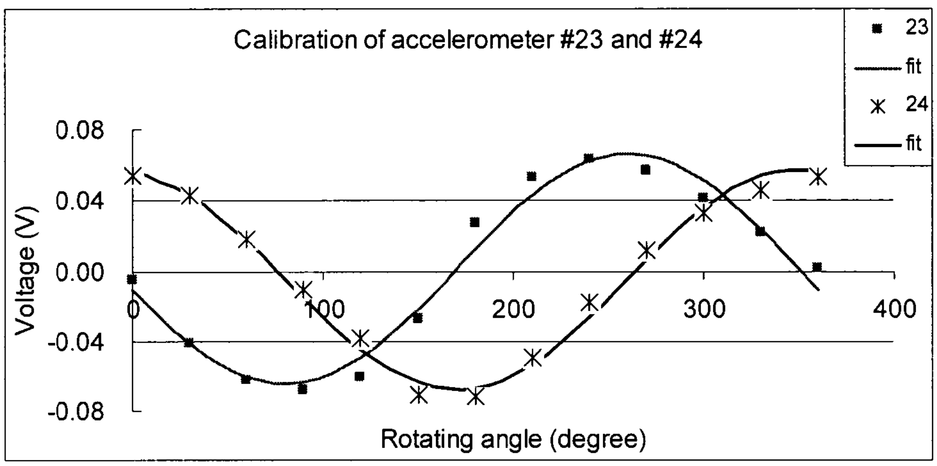

Figure 5-8 Calibration curve of accelerometer No.23 and No.24

Table 5-3 Calibration coefficient and phase angle for four pairs of accelerometers

Node	Accel.No	Coefficient (g/V)	Angle	
			degree	rad.
8	17	15.1538	5	0.0873
	18	15.4895	14	0.2443
9	19	15.0852	33	0.576
	20	15.2161	43	0.7505
10	21	15.1941	-6	-0.1047
	22	15.6937	-3	-0.0524
11	23	15.2416	10	0.1745
	24	15.9160	10	0.1745

Since in general there was an angle misalignment between the accelerometers, the riser vibration acceleration measured by each accelerometer needed to be converted into the in-line and cross-flow directions. The acceleration components in the in-line and cross-flow direction, a_x and a_y, were combined by the acceleration magnitude acquired from each pair of accelerometers.

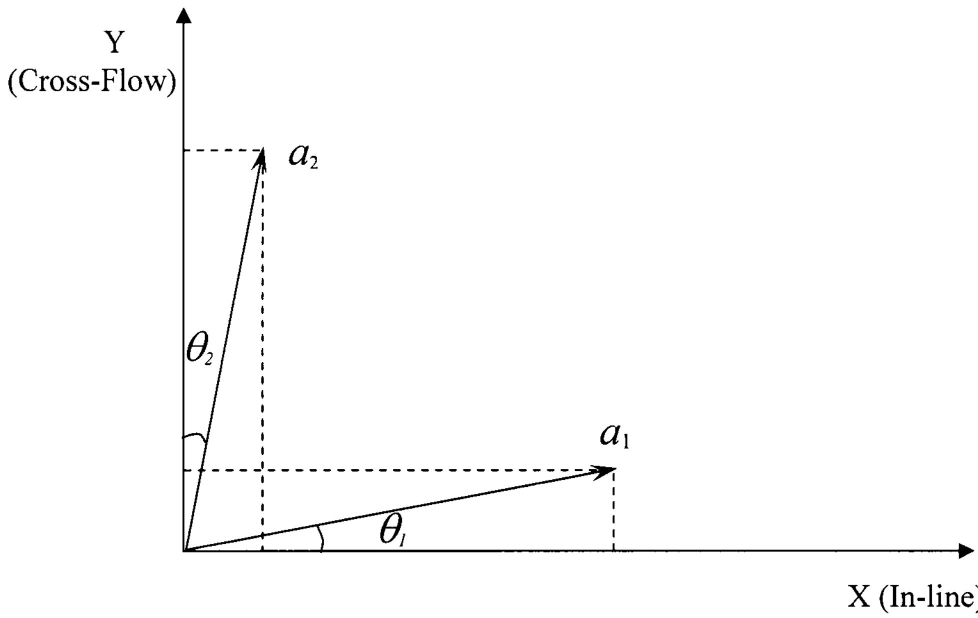

Figure 5-9 Diagram of decomposition of acceleration

The diagram in Figure 5-9 shows the decomposition and composition of a pair of accelerations. In Figure 5-9, a_1 and a_2 are the accelerations acquired from a pair of accelerometers; θ_l and θ_2 are the orientation angle of the acceleration a_1 and a_2, respectively. The parameter a_1 can be decomposed into two components, $a_1\sin\theta_l$ and $a_1\cos\theta_l$, and the parameter a_2 can be decomposed into two components, $a_2\sin\theta_2$ and $a_2\cos\theta_2$. The in-line and cross-flow accelerations for a pair of accelerometers can be written as:

$$a_x = a_1 \cos\theta_1 + a_2 \sin\theta_2$$
$$a_y = a_1 \sin\theta_1 + a_2 \cos\theta_2$$

From the two formulae, the in-line and cross-flow accelerations at each node location, a_x and a_y, can be determined by the acceleration magnitudes a_1 and a_2, as well as the orientation angles θ_1 and θ_2 at the same location. With a_x and a_y, the vibration frequencies and displacements of the riser can be determined, as discussed later.

5.4 PIV Measurement System

The PIV system was installed downstream of the riser in order to measure the wake vortex shed from the vibrating riser. Two borescopes were arranged side by side to obtain an extended viewing area in this test. The laser sheet illuminated the measured area along the flow direction forwards. Figure 5-10 shows the experimental set up.

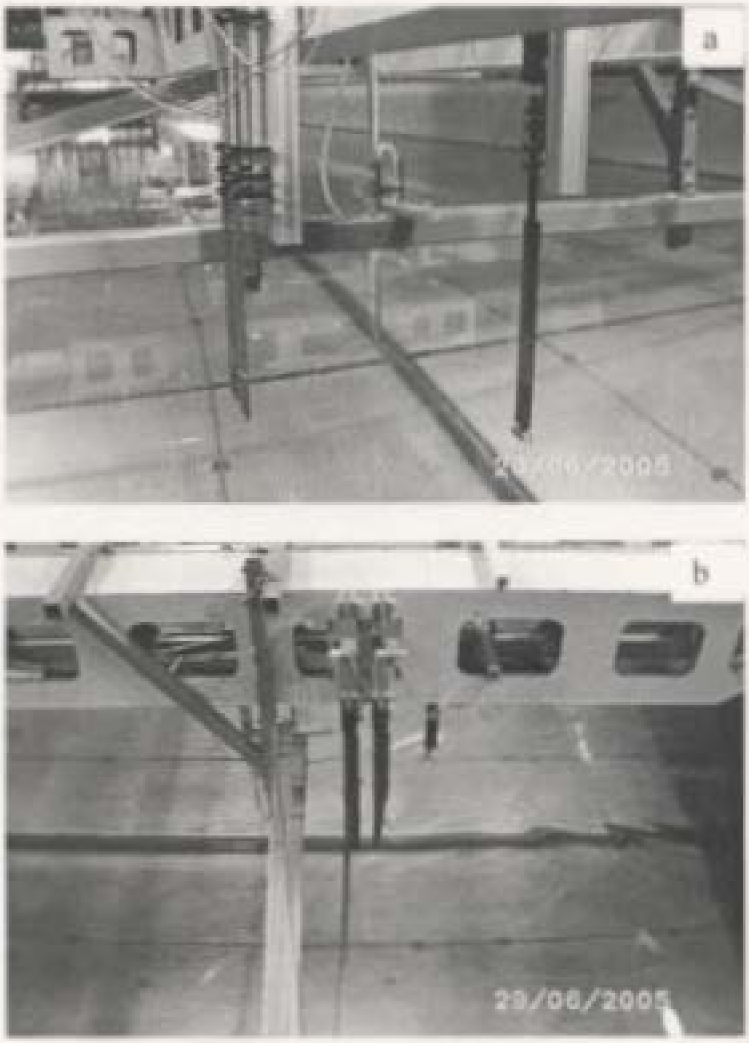

Figure 5-10 Overview of the experimental set up. a. stern view; b side view

5.4.1 PIV System Set-up

In order to provide a rigid connection between the support frame of the laser and the carriage, two 2m long extruded aluminium bars were clamped across the two crossbeams of the carriage. An upright X-section bar was fixed to the two horizontal bars by two brackets. The mounting brackets for the laser transformation arm were clamped to the vertical X-section. Moving the X-section along the two horizontal bars provided location adjustment in the horizontal direction and moving the base of the laser transformation component provided vertical adjustment. Figure 5-11 shows the installation of the laser and beam delivery arm.

Figure 5-11 Installation of the laser and the light arm

In order to install the two borescopes, four square section bars were fixed on the inside of a window in the main beam as shown in Figure 5-12. Four brackets provided rigid connection between the square section bars and the X section bar for the base of the borescopes. Similarly to the configuration of the laser component, the mounting brackets for the borescopes clamped to the vertical X-section.

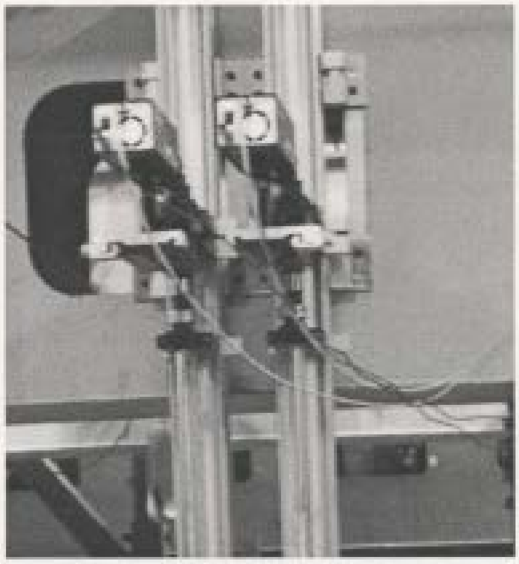

Figure 5-12 Installation of two borescopes and cameras

The borescopes and CCD were about 0.8m away from the measurement area or the laser plane and on the downstream side from the riser. The PIV system computer and laser power supply were placed on the test frame due to limited length of the cable. The monitor, the keyboard and the mouse were placed inside the control room by using a transfer cable so that acquisition and analysis operation could be done inside.

The PIV system set-up mainly depends on the viewing area, the measurement location, and the numbers of velocity components measured. The wake dimension of the riser is a key factor to determine the measured area. As discussed in Chapter 2, the wake dimension behind a vibrating cylinder could grow to immense proportions downstream of the cylinder. This means a large measured area is needed so that it could include an all of the wake field for investigation of the vortex pattern. The maximum viewing area that a measurement system can measure mainly depends on the feature of the components composing the system, especially the camera and the laser, as well as the visibility of the tracing particles. The measurement location determined the installation location of the measurement system, while the measured velocity components determined the orientation of the system set-up.

Figure 5-13 shows a sketch of the bird's eye view of the PIV system set-up on the carriage. The distance between the two main test frames on the carriage was fixed in order to clamp two horizontal holding frames of the riser test apparatus. The space between the two main frames was not enough to set up both the borescopes and the laser with 0.8 m distance between; therefore, the laser and the borescopes cannot be mounted together between the two test frames. As shown in Figure 5-13, the laser and the beam guide arm was mounted between the frames in the carriage, while the borescopes were mounted using the windows on the outside of one test frame so that the distance between the laser plane and the CCD camera was suitable for obtaining clear particle images. Two borescopes were mounted on two adjacent vertical bars so that two fields of view downstream of the riser were obtained along the flow direction. The measurement plane was located at z/l=0.44, i.e., 3.733 m from one end of the riser.

The sketch of the field of view of two CCD cameras is showed in Figure 5-14. The laser beam is spread into a vertical sheet along the flow direction to illuminate the measurement plane in the flow field. The two fields of view of the two CCD cameras were arranged side by side with a 74 mm overlap. The combined viewing area was about 448 mm by 195 mm.

Due to the effect of the drag, as the carriage started moving, the riser moved backwards and upwards by an amount, called an initial shift, which increased with the increase of the speed. When the carriage was stationary the riser was out of the front field of view. When the carriage was moving the riser just moved into the field of view at the low carriage speed. Thus, the effective measurement area can be increased.

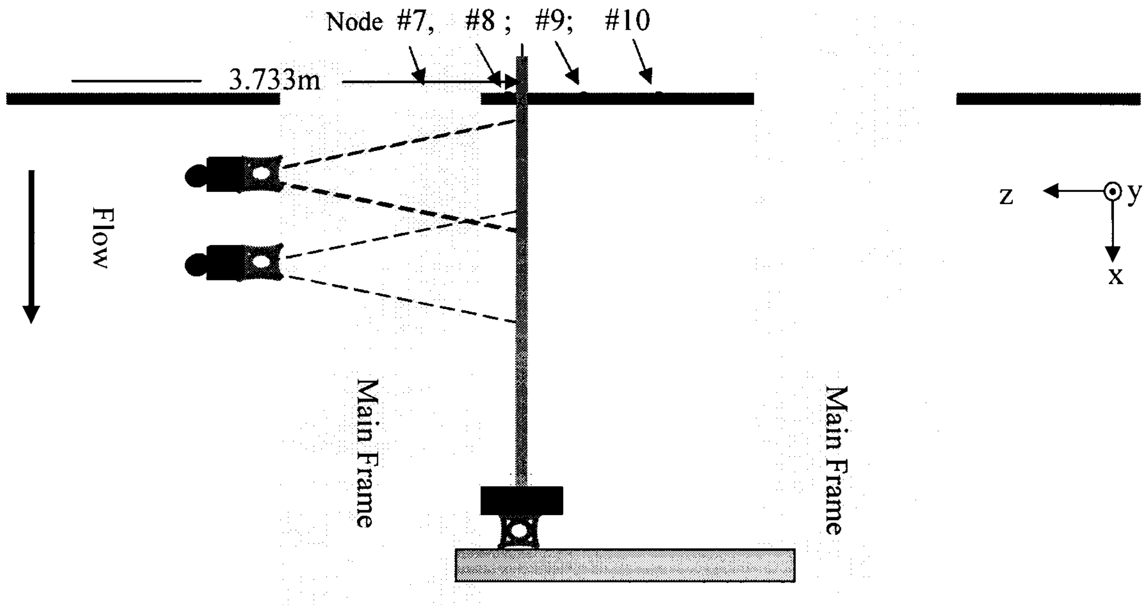

Figure 5-13 Sketch of PIV system set up

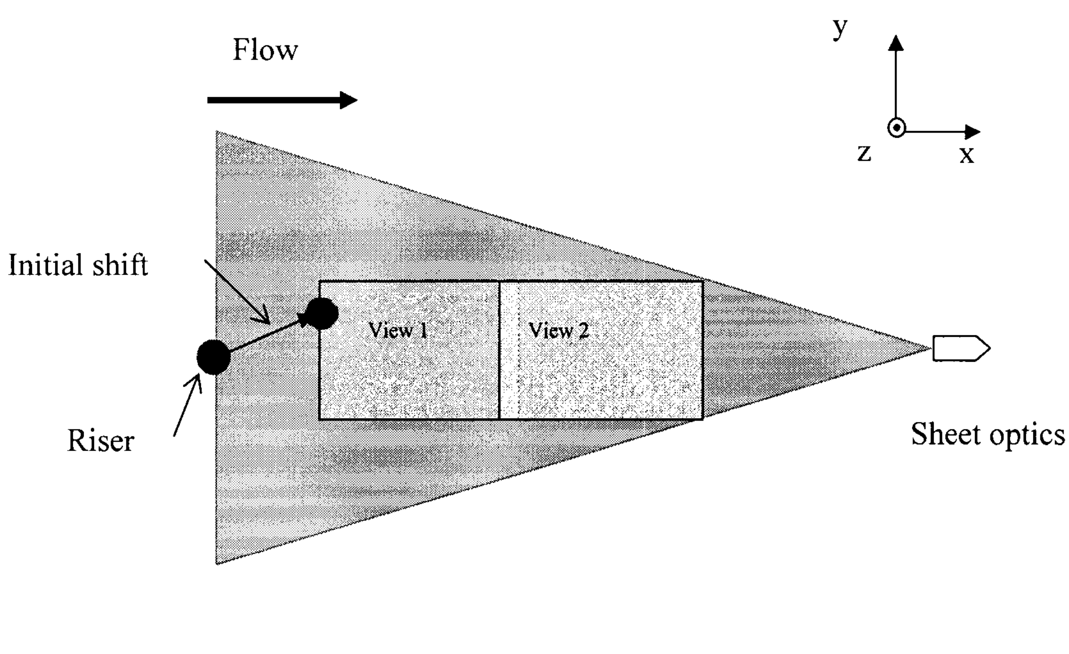

Figure 5-14 Sketch of arrangement of two fields of view relative to the riser

The coordinate system was defined as shown in Figure 5-11 and 5-12. The x–axis was downstream (defined as in-line), the y-axis was normal to the flow direction and to the cylinder axis (defined as cross-flow), and the z-axis lay along the axis of the cylinder (defined as spanwise).

5.4.2 Seeding Delivery System

The seeding system used in this experiment is shown in Figure 5-15. The system consisted mainly of two parts: a holding tank and a seeding rake. The system used hydrostatic pressure to deliver the seeded flow from the holding tank to the measurement volume. Adjusting the height of the holding tank, relative to the water level, controlled the static head and a tap was used to control flow rate. The seeding particles were mixed with clean water in the holding tank and discharged through a long hose and a rake. The rake for this set of experiments was a single pipe of 12 mm inner diameter, which had side holes with 2mm diameter drilled at 20mm spacing. The rake was placed upstream of the required measurement area and the seeded fluid was discharged from the downstream of the pipe through those side holes. The advantage of this system was that the seeding particles were more evenly distributed, but the disadvantage was that the rake was close to the path of fluid entering the measurement area, and the wake of the seeding rake can affect the measurements. The effect of the rake on the wake was shown and discussed in the Chapter 4.

The particles used in the experiments were silver coated hollow ceramic spheres, 95 microns in diameter and 1.1 g/cc in density. Most particles eventually sunk to the bottom of the tank after seeding. The holding tank was placed on the front walkway of the carriage. The seeding rake was fixed on a long wood board which was clamped on the test frame, located about 1 m upstream from the riser. A submersible pump was used to fill the holding tank by pumping water from the tank.

(a)

(b)

Figure 5-15 Seeding delivery system
(a) Particle fluid holding tank (b) seeding discharge rake

5.4.3 Signal Acquisition

In this experiment, thirteen channels of the data acquisition system were used to acquire signals, including carriage speed, test frame vibration, accelerometers, laser synchronization output and time. A list of format for all raw data files is given in Table 5-4.

The PIV measurement system was independent from the acquisition system for the accelerometer signals. The reference time was needed to link the two acquisition systems and provide a synchronous measurement between the two sets of signals. To do this, a series of pulse signals from the laser was inputted to a data acquisition channel and was recorded in the time series (see the column 2 in Table 5-4).

Table 5-4 Data acquisition channel list

Column	Data description	Channel	Data unit
1	Time		Second (s)
2	PIV trigger pulse signal	15	Voltage (V)
3	Accelerometer signal #17	17	Voltage (V)
4	Accelerometer signal #18	18	Voltage (V)
5	Accelerometer signal #19	19	Voltage (V)
6	Accelerometer signal #20	20	Voltage (V)
7	Accelerometer signal #21	21	Voltage (V)
8	Accelerometer signal #22	22	Voltage (V)
9	Accelerometer signal #23	23	Voltage (V)
10	Accelerometer signal #24	24	Voltage (V)
11	Test frame acceleration-Z		Acceleration
12	Test frame acceleration-X		Acceleration
13	Carriage speed		m/s

A TTL pulse signal with 5 volts and 110 microseconds from the Q-Switch synchronic output signal port relative to each laser pulse was inputted to Channel 15 of the data acquisition system. A positive transition from 0 volts to +5 volts occurs when the Q-Switch was energized. A laser pulse will give off from the laser head approximately 60 nanoseconds after this signal. The relationship between the synchronization pulse and the laser pulse are shown in Figure 5-16.

A sample rate with 5kHz was applied for all data channels in the experiments so that narrow synchronous signals of the laser pulses could be captured. However, the pulse width of the laser synchronous signal, 110μs, is still too narrow to be captured by the acquisition system at the acquisition rate of 5kHz. As a result, a signal generator was introduced to provide signals with wider pulse to data acquisition system. The laser synchronous signals were inputted to the signal generator. After receiving each laser synchronous signal pulse, a delay signal pulse, 5 volt and 5 ms duration was generated by the signal generator and inputted to the data acquisition system. The delay time between each laser signal pulse and relative delay pulse was 2.5 ms. Figure 5-17 shows the time relationship between the two signals.

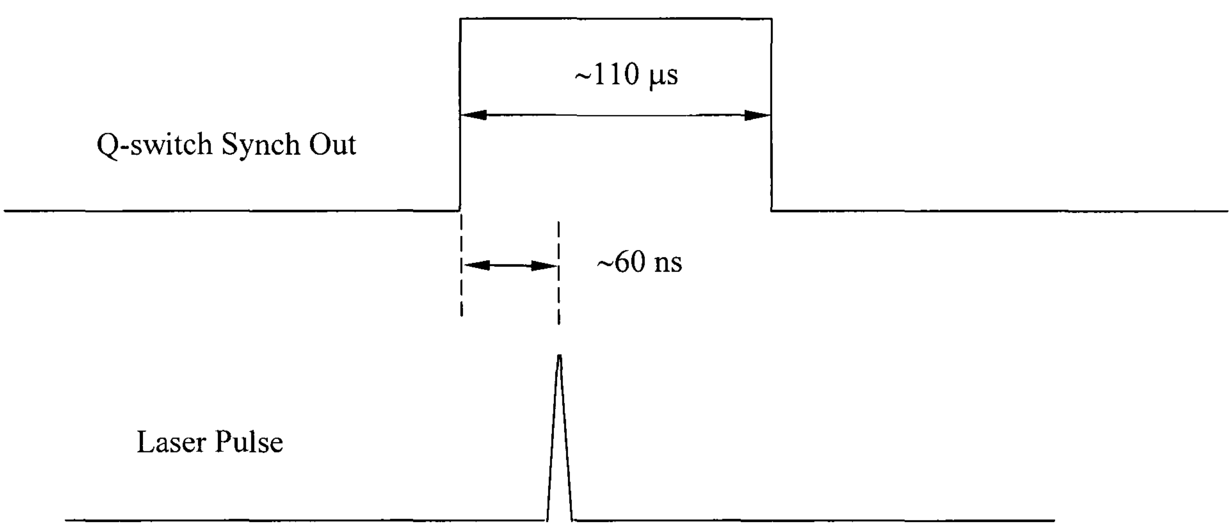

Figure 5-16 Sketch of time delay between laser pulse and Q-switch synchronization signal

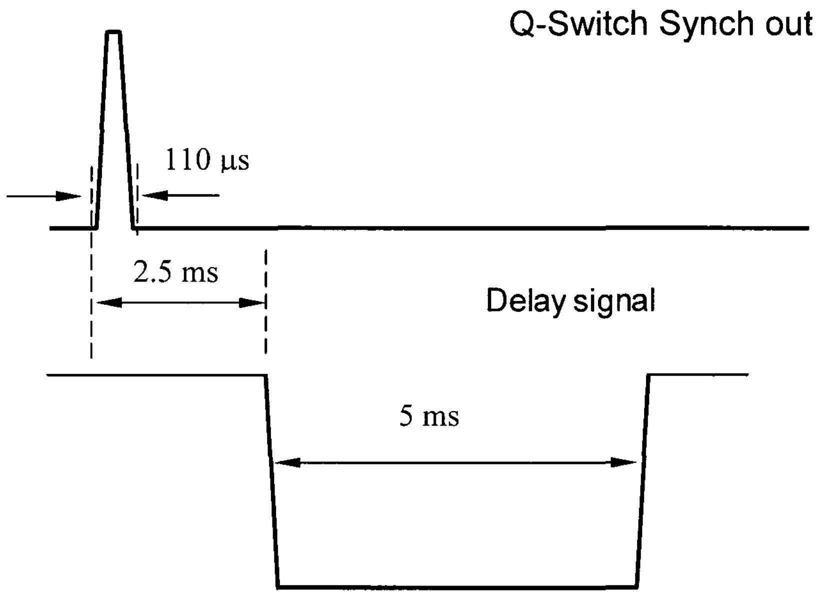

Figure 5-17 Sketch of time delay between Q-switch synchronization output and signal generator

Figure 5-18 provides samples of raw data from the acquisition channels 15, 19 and 20 at the carriage speed of 0.5 m/s. The channel 15 gives the delay pulse signal against the time series, which provided the reference time of delay signal. The time of each laser synchronous pulse, i.e. the time at which each image was taken, was 2.5 ms prior to the reference time. The channels 19 and 20 are the voltage signal from accelerometers 19 and 20 at node 8. With the same time coordinate, each image can be linked to the riser motion by the accelerometer signal relative to the image moment. The velocity field and wake vortex pattern, therefore, can be connected to the riser's movement at that moment.

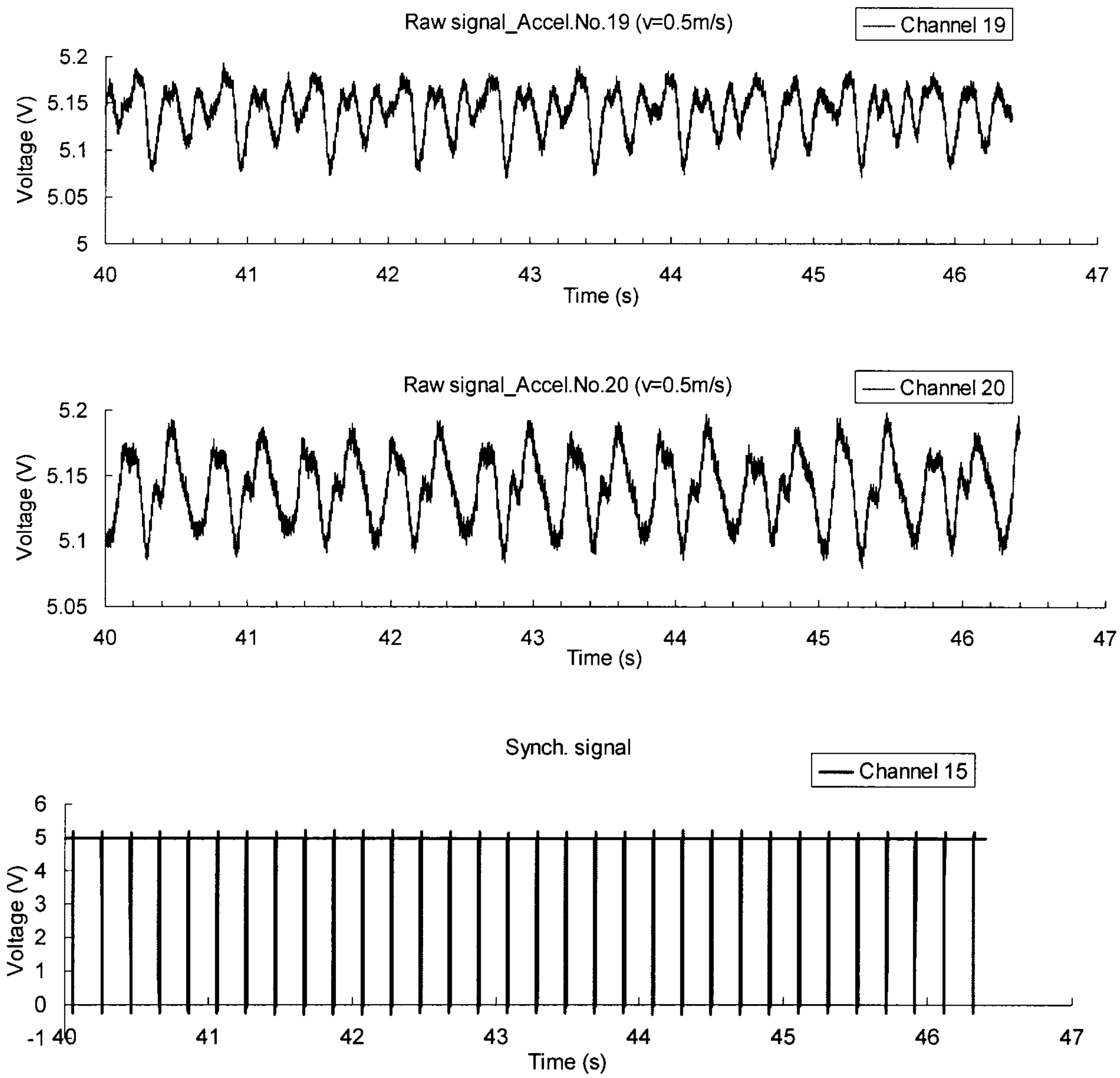

Figure 5-18 Sample of data signal acquisition. channel 19: riser acceleration in in-line direction at node 8; channel 20: riser acceleration in cross-flow direction at node 8; channel 15: synchronic signal from laser

5.4.4 Field of View of Cameras

In this experiment, two fields of view were respectively obtained from two cameras. The relative position of the two fields of view had to be determined during the experiment in order to combine them for the analysis of velocity fields. The calibration plate was placed at the measurement plane on the laser sheet and its image was taken by both cameras, as shown in Figure 5-19. The upper image was from camera 1 and lower image from camera 2. The same reference dots (marked with the oval in Figure 5-19) on the plate can be found from the two images, and then the relative position between the two fields can be determined by the coordinate of their reference point. From Figure 5-19, we can see there is almost no distortion in the image of the plate, because the lens of the borescopes was normal to the field of view.

5.4.5 Measurement Procedures

The PIV system and VIV apparatus were two independent measurement systems, as discussed above, which needed to work together to obtain both of the velocity field data and accelerometer data in the same time series. For PIV measurement, a few operational procedures must be performed before images were recorded in order to obtain good quality seeding. A well organized procedure for the measurement process was very helpful to effectively obtain the experimental data within a short run time.

Figure 5-20 shows the flow chart of the measurement procedure for both PIV system and VIV system at each carriage run. Each run was at one carriage speed so that there was enough time for the PIV measurement. The seeding tap was turned on just after the carriage started moving. The data acquisition system began to acquire the data from all data channels. Meanwhile, the laser and the cameras were set to “adjust” and “grab” to look at seeding quality in a image. If the seeding density was not correct, the tap was adjusted to change the seeding volume until the number of the particles was around 10 in each interrogation window. Once the seeding quality looked correct, the laser and the cameras were switched to test status and the system began to record images. When the set amount of image frames had been recorded, the PIV software system automatically finished. The carriage and the data acquisition system were then manually stopped. The particle image could be analyzed to check the velocity field measured just after the image acquisition finished. The same test could be repeated if necessary.

(a)

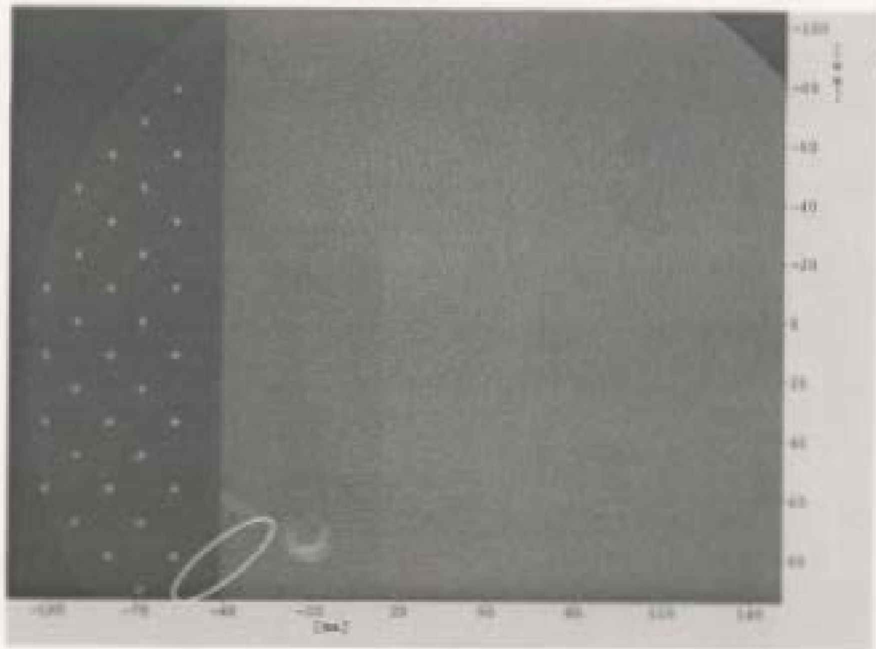

(b)

Figure 5-19 Images of calibration plate from two cameras:

(a) for camera 1, (b) for camera 2

5.4.6 Image Acquisition and Processing

5.4.6.1 Image Acquisition

During each carriage run, 150 images were record in order to obtain as much information as possible on the unsteady wake. The images were collected in double frame-double exposure mode, which means that each image consisted of two frames recording the movement of all particles in the field of view within two exposures, respectively. The interval between two successive images was 0.2 seconds based on a repeat rate of 5 Hz for the CCD cameras. The interval of two laser pulses was determined based on the flow speed, the measurement area, the size of the interrogation window and the resolution of the system. In this experiment, the intervals mainly depended on the flow speeds, because other factors were the same in each test. Table 5-5 shows the intervals set in the experiment.

The laser intensity and the particle density affect the image quality, which is essential to make accurate measurement. Due to the relatively large field of view in this experiment, the laser power was set at 115mj, 95% of the maximum energy, in order to obtain a clear particle image. The particle density was monitored at the beginning of each test and adjusted by the tap connected to the seeding hose and the fluid holding tank, as discussed above.

Table 5-5 Interval setting between two lasers in experiments

Speed (m/s)	Interval (μs)
0.1-0.3	3000
0.4-0.6	1000
0.7-1.0	600

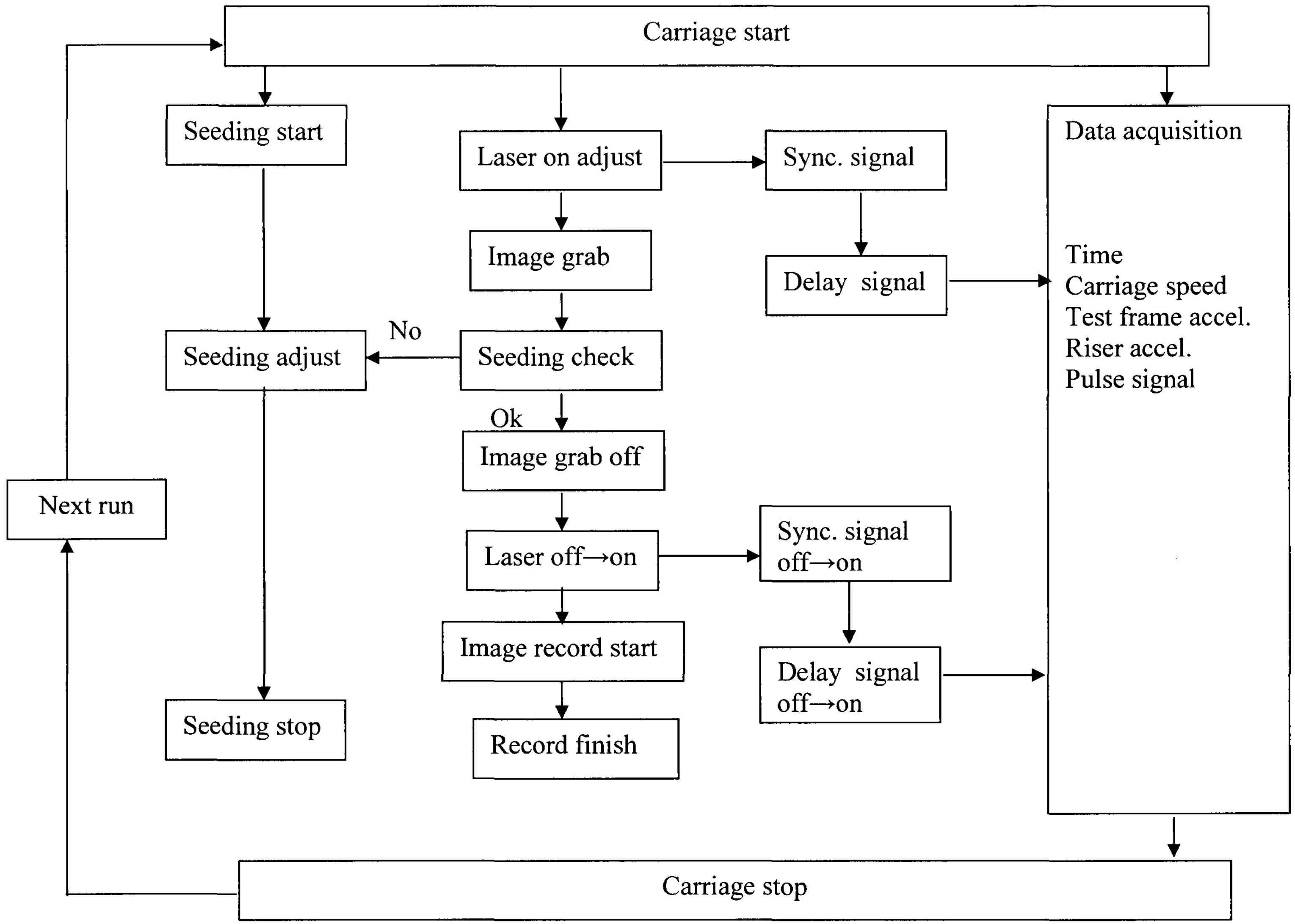

Figure 5-20 Flow Chart of the measurement procedure

Figure 5-21 shows two pairs of particle images which were taken by the two cameras with two exposures, respectively. The upper two images are from the camera 1 with an interval of 1 millisecond, while the lower two are from the camera 2 with the same interval.

Figure 5-22 shows four particle images of camera 1 at the first exposure time at a carriage speed of 0.2m/s. These images were taken at different times in the same run. Due to the free vibration, the position of the riser in each image changed during the run. At this speed, the riser just moved into the field of view of the camera 1. In Figure 5-22 a, b, and d, a small partial riser section displayed on the left edge of the images and its location in three images was different, while in Figure 5-22 c, the riser was completely out of the image. From these images, we can see the change of the position of the riser was quite big, especially in the vertical direction. This means that the vibration of the riser was obvious and unsteady. At the lower speed, vortices easily were formed and developed. The wake vortices were obviously observed in the images and the vortex pattern was different. It also can be seen in the images that the vortices rolled up, and this meant that the particles were gathered toward the cores of the vortices and caused dark regions, i.e. the regions without particles, formed.

Figure 5-23 shows four particle images taken by camera 1 at the first exposure time at the carriage speed of 0.3 m/s. It is obvious that the initial shift of the riser was bigger than that at the speed of 0.2 m/s and the position of the riser changed a lot from image to image. In Figure 5-24 and 5-25, each shows four particle images taken by camera 1 at the first exposure at the

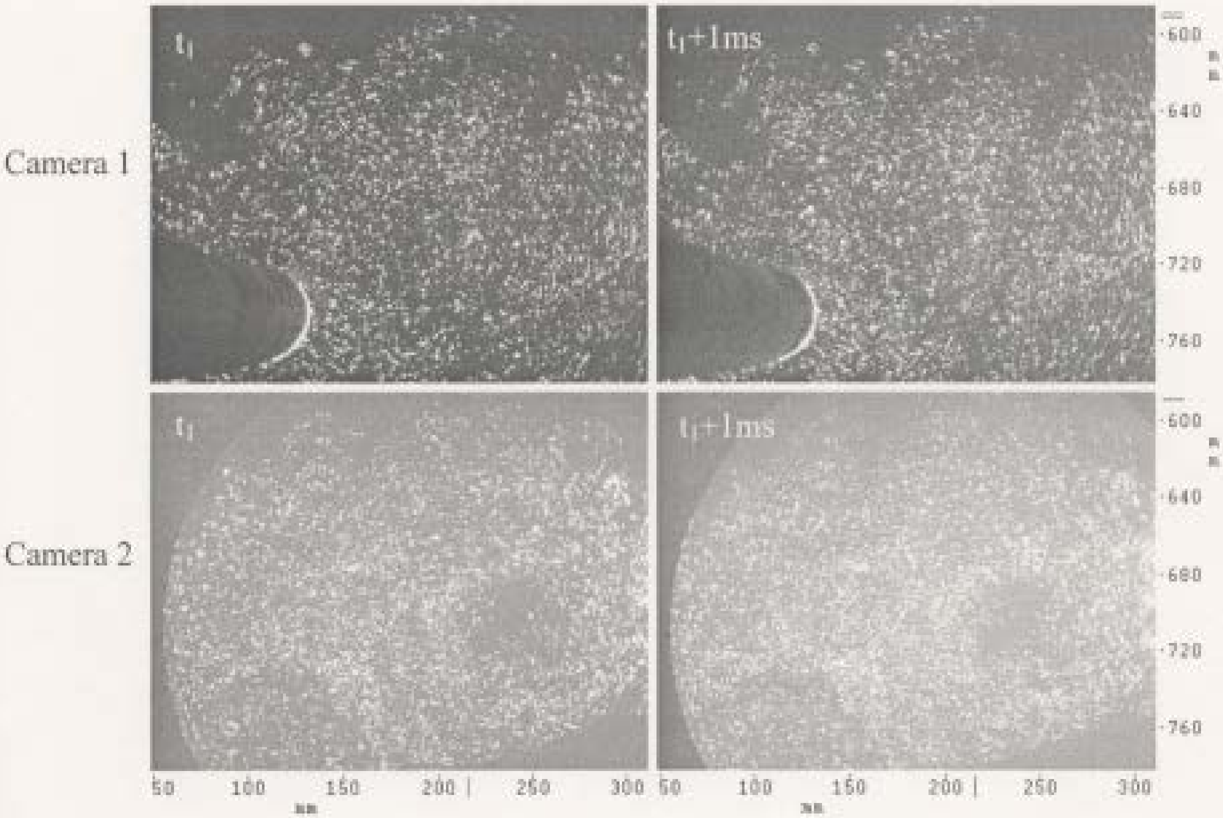

Figure 5-21 Particle images taken by two cameras at time t_1 and t_1+1ms
(upper from camera 1, lower from camera 2, left at t_1, right at t_2)

carriage speed of 0.5 m/s and 0.8m/s, respectively. With the increase of the carriage speed, the initial shift of the riser also increased obviously. Figure 5-26 and Figure 5-27 show two images in the speed of 0.9 m/s and 1.0 m/s. The riser almost reached to the middle on the bottom of the image at these speeds. The wake vortices are not very obvious from the particle images at these higher speeds and can only be obtained by the velocity field process. With the increase of the speed, the extent of vibration of the riser also increased. The riser strongly stirred the fluids and caused a larger dark region on the top of the images because the seeding area was not big enough. The image obtained for the set up in this experiment is a vertical mirror image of the real field, i.e. the bottom in the image is the top of the real field. Figure 5-28 shows the diagram of the relative position between the still riser and the combining field of view of two cameras.

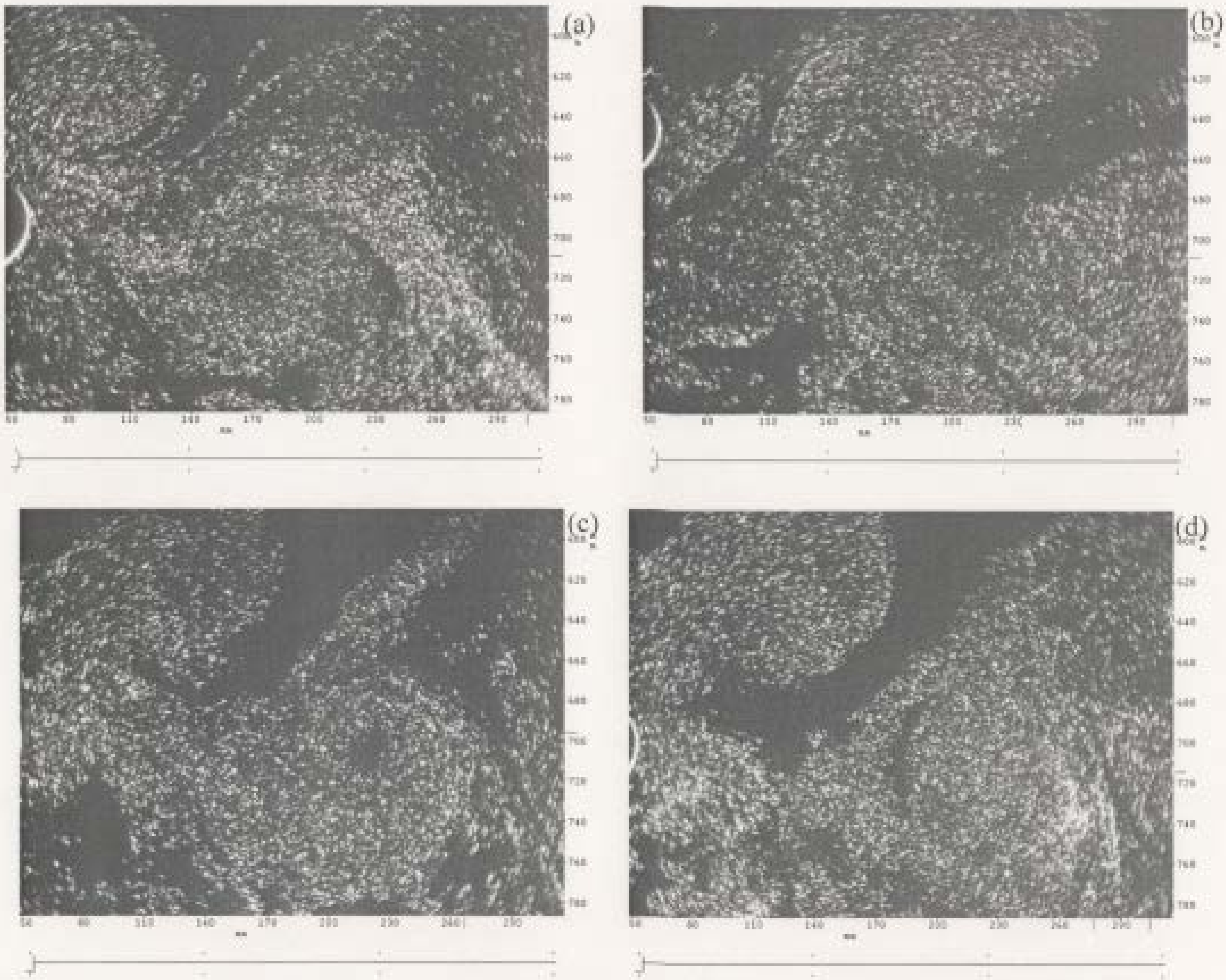

Figure 5-22 Particle images at four different instants at a carriage speed of 0.2 m/s (Image frame #3, #7, #28, #106)

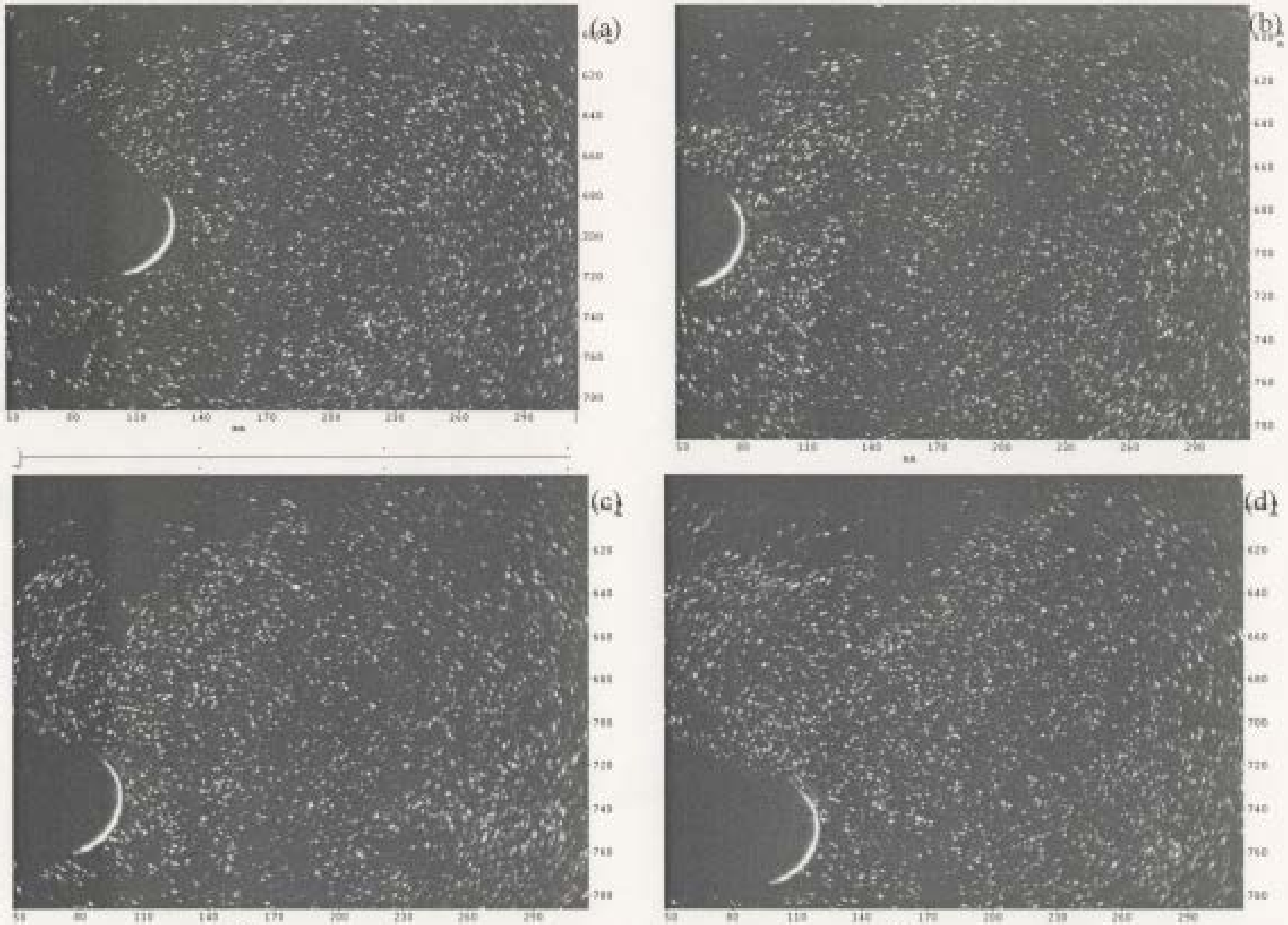

Figure 5-23 Particle images at four different instants at a carriage speed of 0.3 m/s (Image frame #1, #2, #3, # 4)

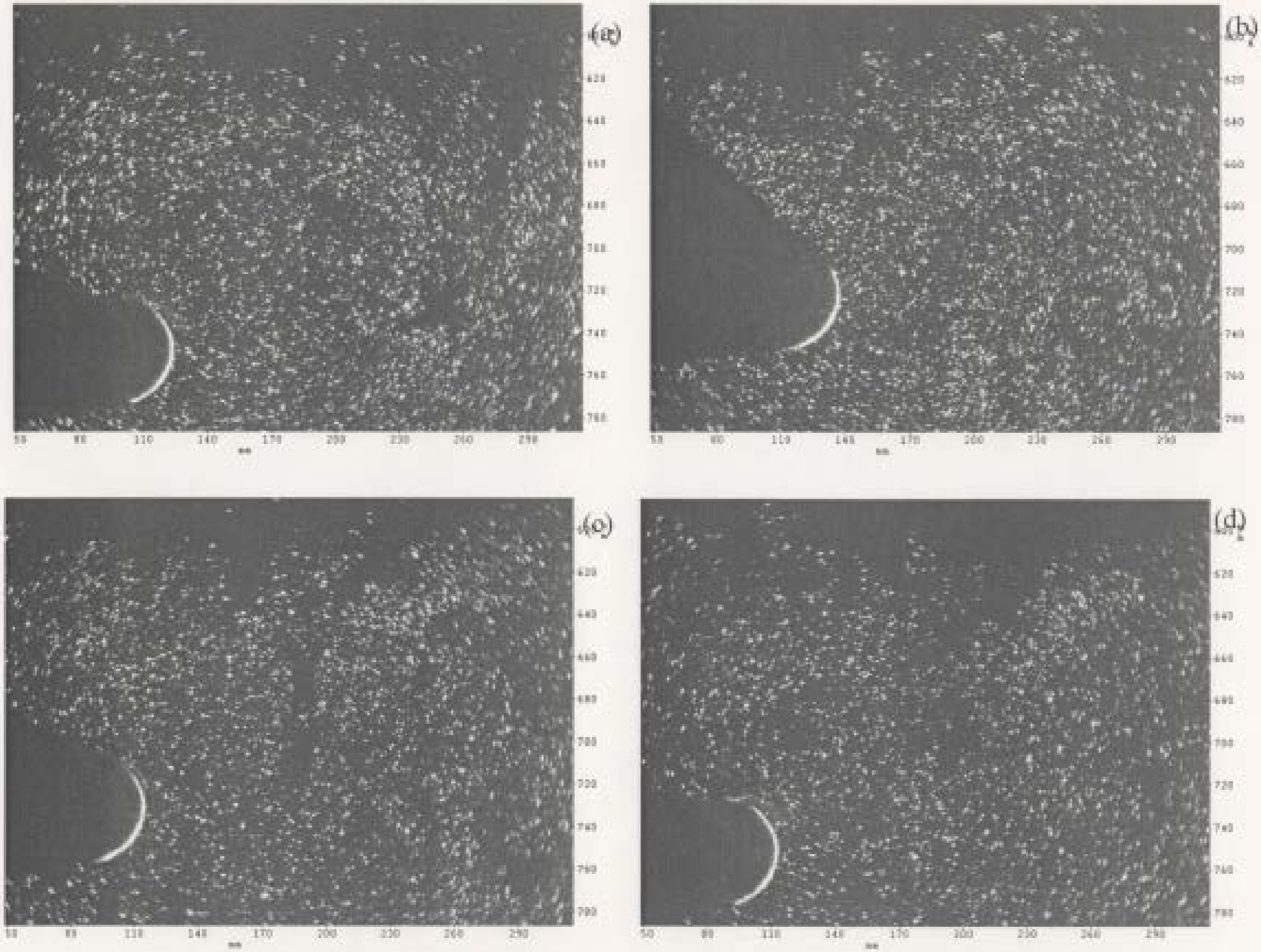

Figure 5-24 Particle images at four different instants at a carriage speed of 0.5 m/s (Image frame #2(a), #3(b), # 50(c), # 128(d))

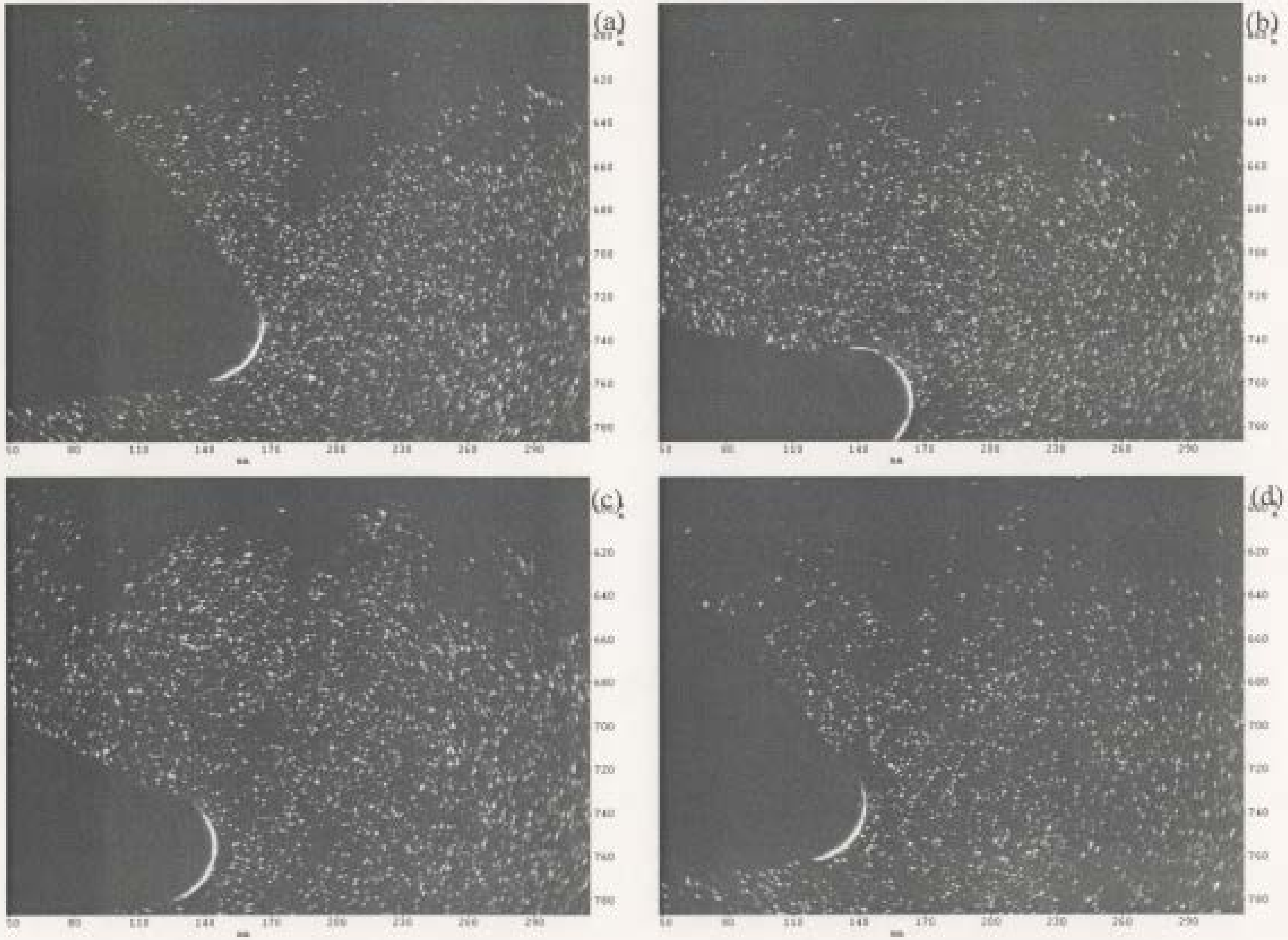

Figure 5-25 Particle images at four different instants at a carriage speed of 0.8 m/s (Image frame # 3(a), #2(b), #7(c), #104(d))

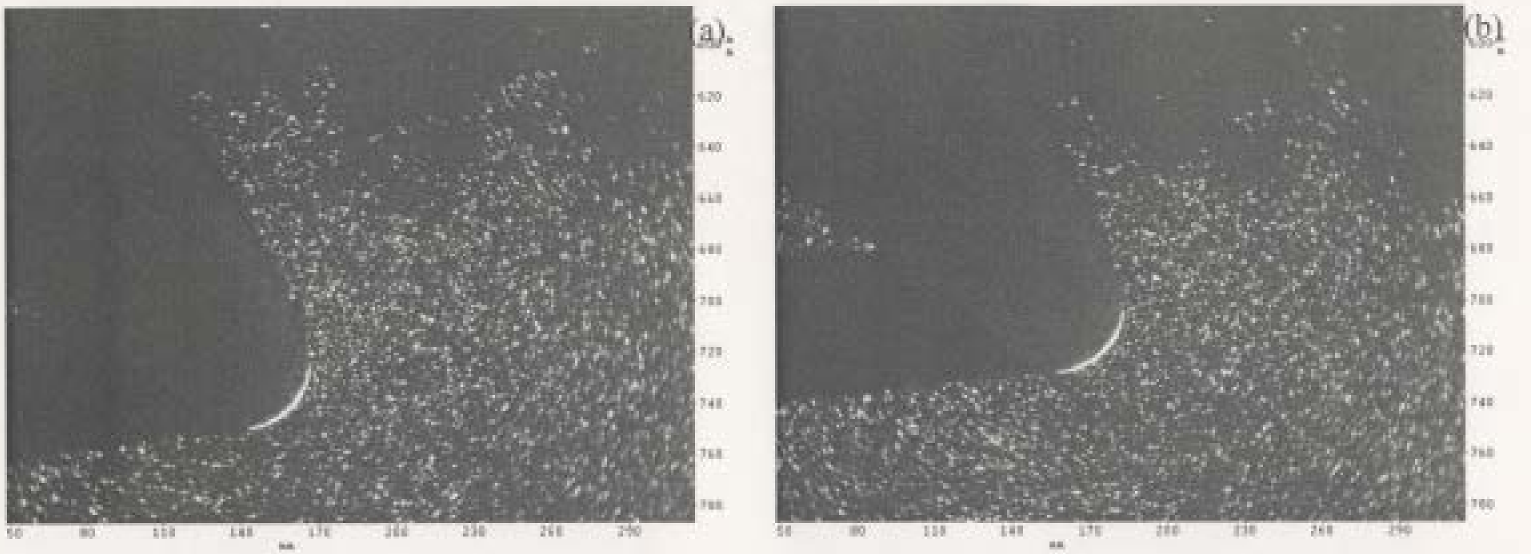

Figure 5-26 Particle images at two different instants at a carriage speed of 0.9 m/s (Image frame #15(a), #58(b))

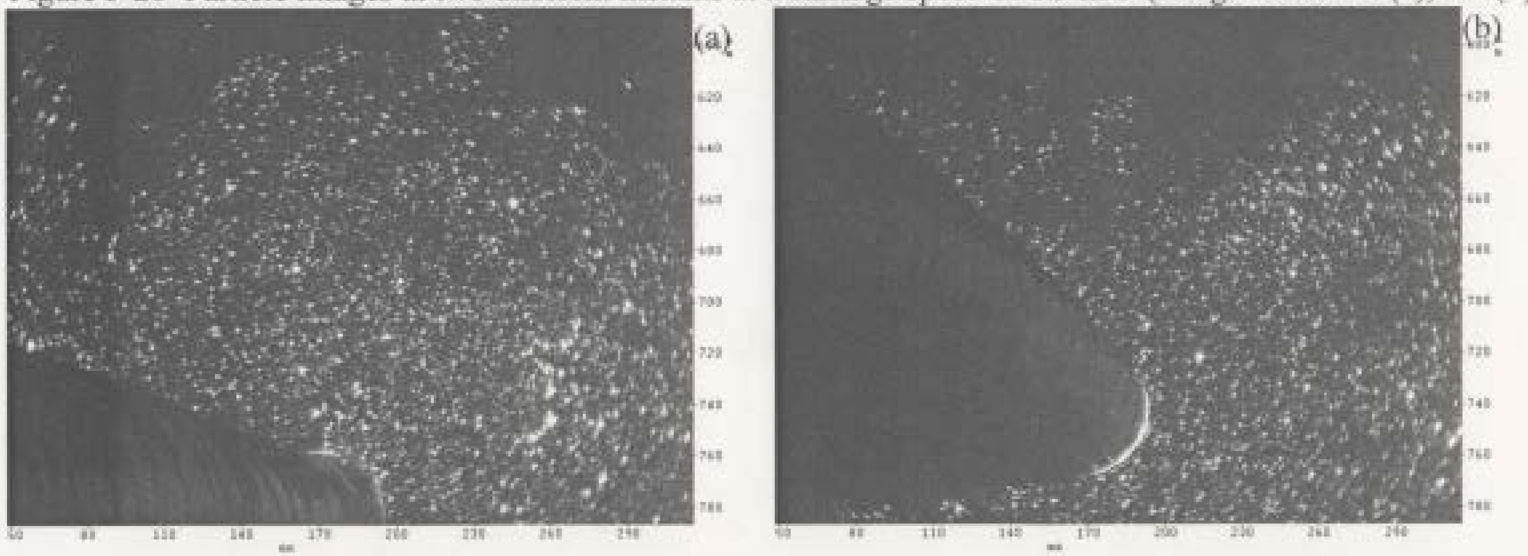

Figure 5-27 Particle images at two different instants at a carriage speed of 1.0 m/s (Image frame # 2(a), #3(b))

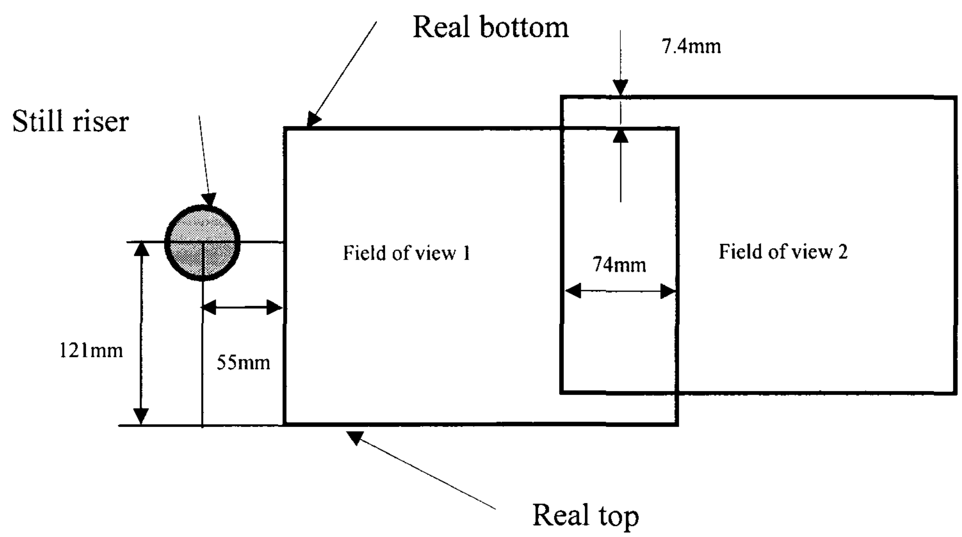

Figure 5-28 Sketch of the relative position for the riser and two fields of view

An initial shift of the riser caused by the drag of the water was observed after the carriage started moving. The riser section then moved to new equilibration position and vibrated around it. The initial shift can be obtained from the image and the coordinate of the riser center point provided the position of the riser over 150 images at each different speed. Figure 5-29 shows the mean position of the riser in the measurement plane against the speeds. The mean position in the in-line and cross-flow direction, $\bar{x}$ and $\bar{y}$, were obtained by averaging x and y for the 150 image at the same speed.

$$\bar{x} = \sum_{1}^{n} x \Big/ n$$
$$\bar{y} = \sum_{1}^{n} y \Big/ n$$

where n is the total number of the images. The x and y were the absolute coordinate of the riser in the image. Figure 5-30 is the plot of the dimensionless initial shift, S, divided by the diameter of the riser, against the speeds. Where, S was difference of the coordinates of the riser when it was stationary and moving. Both the initial shift of the riser in the x and y direction increases with the speed increased. For both in-line and cross-flow direction, the augment of the initial shift at the low speed is bigger than that at high speed, especially in cross-flow direction. It also can be seen that the shift along the flow direction is bigger than that in cross-flow direction. There is an obvious jump of the shift at the speed of 0.3 m/s in both in-line and cross-flow direction.

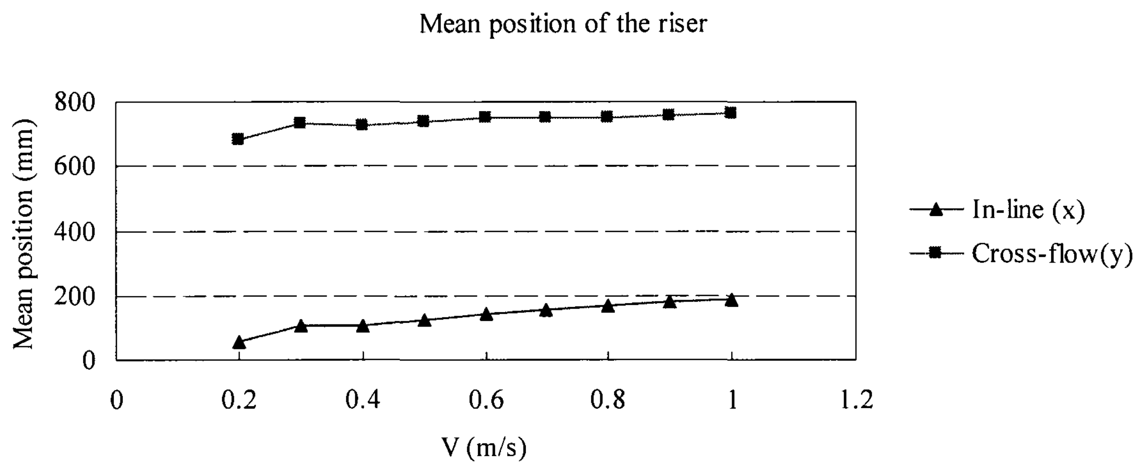

Figure 5-29 Riser mean position in the different speeds

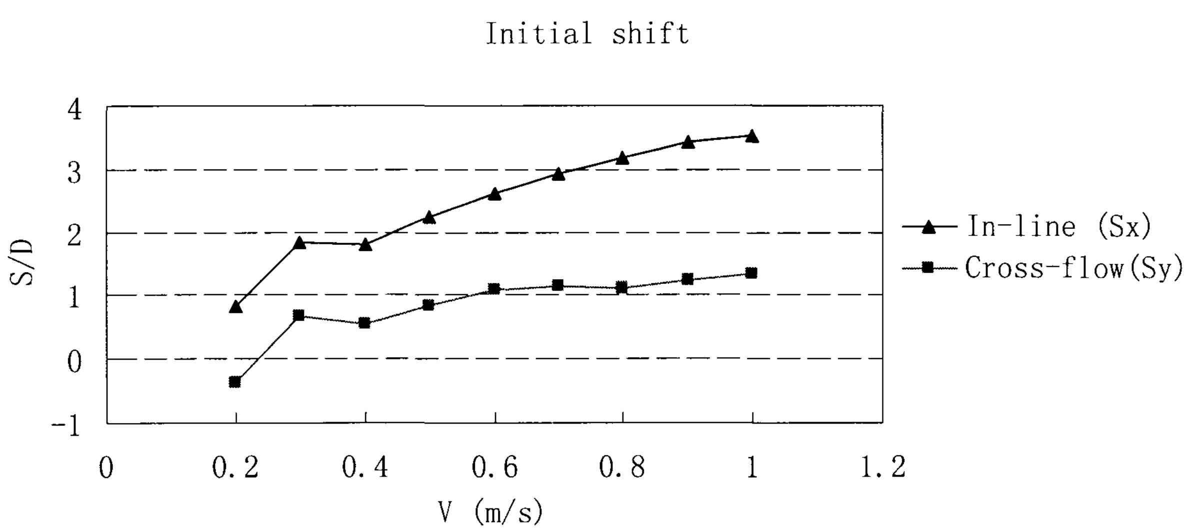

Figure 5-30 Initial shift to diameter ratio of the riser in the different speeds

5.4.6.2 Velocity field process

The velocity field of each image was obtained by calculating the cross-correlation function to the particle image from the experiment, as discussed in Chapter 3. The velocity field process was executed by the DaVis software. A high quality particle image is required to obtain accurate results.

For the evaluation of a velocity field, the corresponding complete image is divided into smaller interrogation windows. The size can be selected from 4, 6, 8, 12, 32, 64,128 or 256 pixels squared. Selection depends on the type of velocity field and the particle density. The window 64 by 64 or 32 by 32 pixels are typical values used for analyzing those experiments. Each correlation operates only on the intensities of the image inside the corresponding interrogation windows. For the interrogation window, the adaptive multi-pass method with decreasingly smaller sizes was selected with an initial interrogation window size of 64×64 pixels and a final interrogation window size of 32×32 pixels. This process helps to correlate the right particles and improves the signal-to-noise (LaVision, 2004). Figure 5-31 shows the multi-pass process. The evaluation starts with a first pass using the initial interrogation window size and calculates a reference vector field. In the next pass the window size is half the previous size and the vector calculated in the first pass is used as a best-choice window shift for the second pass. In this manner, the window shift is adaptively improved to compute the vectors in the following steps more accurately and more reliably as this ensures the same particles are correlated with each other even if small interrogation windows are used. This improves the spatial resolution of the vector field and produces less erroneous vectors.

The resolution of a whole particle image taken by the CCD camera in this system was 1376× 1040 pixels, which represents a real field of view of 258mm ×195mm. With the interrogation

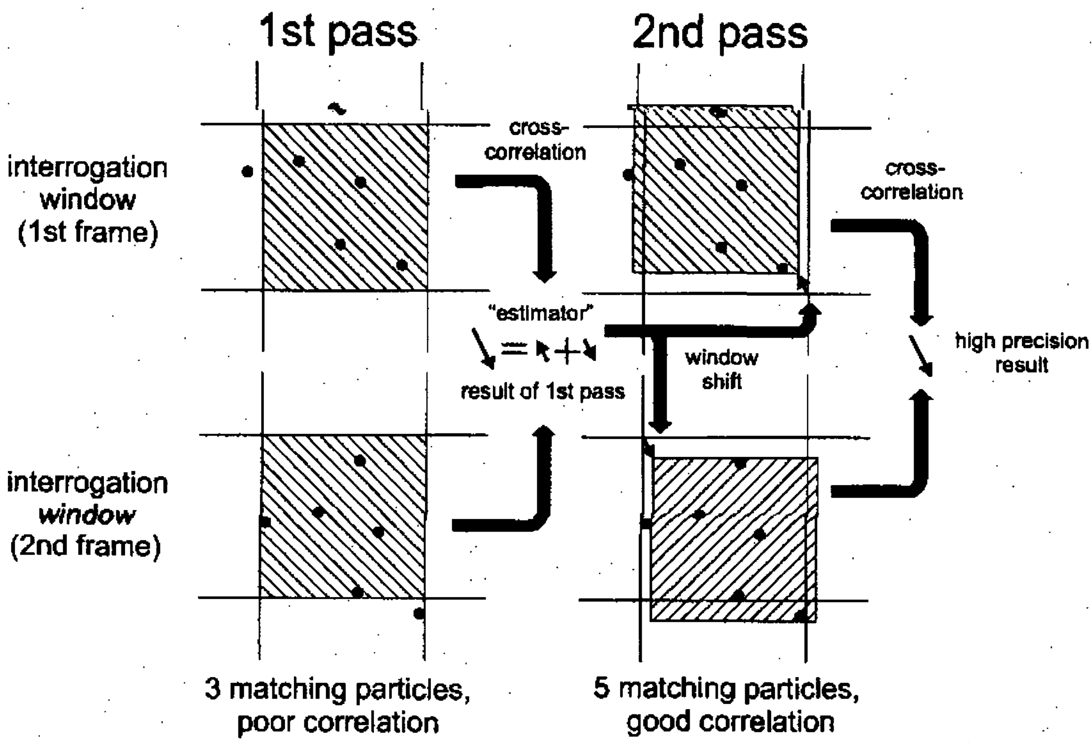

Figure 5-31 Adaptive multi-pass with constant interrogation window size

window size of 64×64 pixels for the initial interrogation window and 32×32 pixels for the final interrogation window, the 1376 ×1040 pixels for each camera was divided into 43 ×32 interrogation windows (without an overlap). A single vector represents the average velocity within an interrogation area of 6×6mm^2. By computing the cross-correlation function for each interrogation window, 43 ×32, or 1376 vectors were obtained to cover the whole measurement area for one camera. The velocity fields of two cameras were then combined since the relative position of the two fields of view was determined during the experiment. The total number of velocity vectors was 2336 in Vx and Vy, respectively. Figure 5-32 shows a typical combined velocity vector field and vorticity field of the particle image in Figure 5-21.

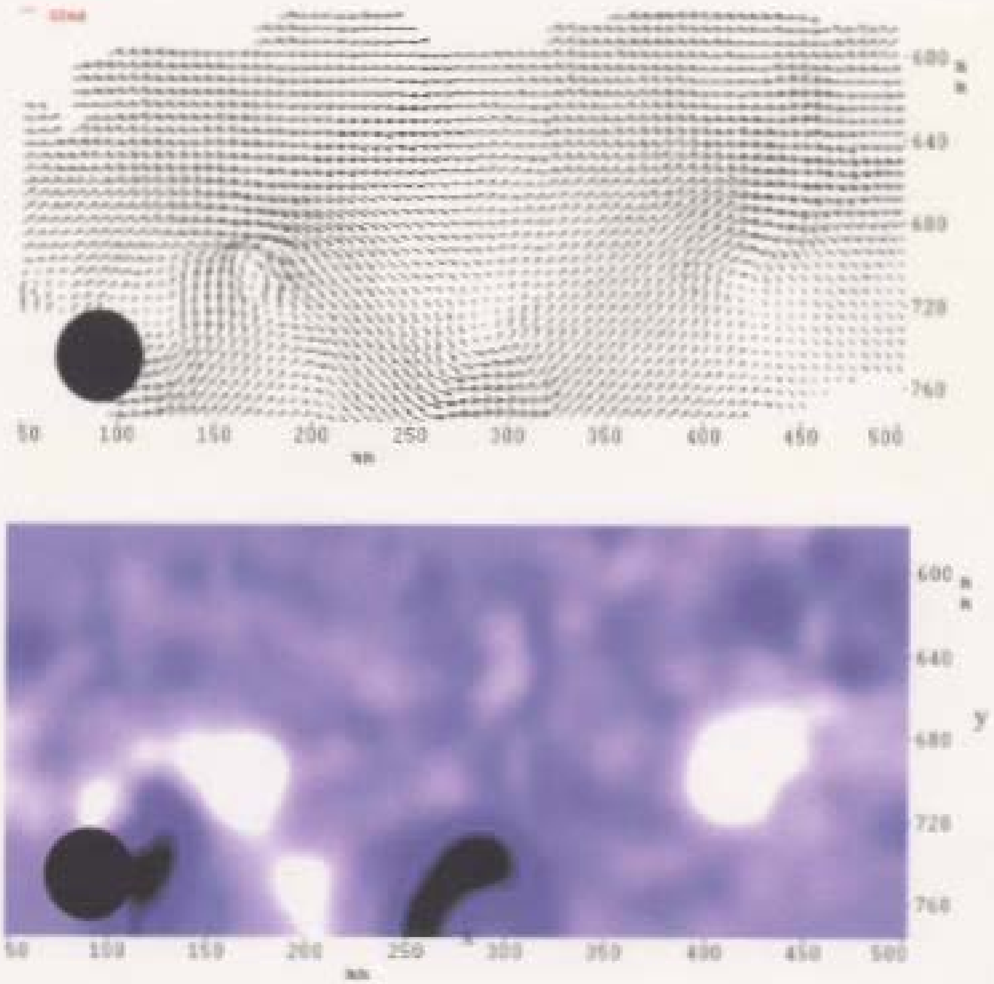

Figure 5-32 Velocity and Vorticity plots of wake field of VIV in Figure 5-21

Chapter 6 Results and Discussion

6.1 Introduction

In this chapter, the experiment results for both vortex-induced vibration measurement and wake field measurement are presented and analyzed. The vibration frequency spectra of the riser were obtained by Fast Fourier Transformation (FFT) from the acceleration data in the time domain. The displacement and the vibration amplitude of the riser were obtained from both the acceleration and the PIV images. The wake fields of the riser were obtained by calculating the cross-correlation function of the particle image. The different wake vortex patterns observed in this set of experiments are presented and the relationship between certain wake vortex patterns and the vibration response of the riser is discussed.

6.2 VIV Experiment Results

In this PIV-VIV experiment, there was only one measurement plane along the riser span direction, which was located at the position, z/L=0.43, close to the position of node 8 of the riser, as shown in Figure 5-13. The VIV response result for node 8, which was the closest the measurement plane, are presented and discussed below.

6.2.1 Vibration Frequency

The vibration frequencies of the riser varied in both in-line and cross-flow directions when moving, due to its length and flexibility, as shown by Li *et al.* 2005. In order to analyze the frequency characteristics of the long flexible riser vibration, the FFT technique was used to transform acceleration signals or displacement data from the time domain to the frequency domain and then the result is squared to convert to energy units. The FFT program used in the present work was adopted from the "Numerical Recipes" (Press *et al.* 1986). The energy spectrum, Power Spectral Density (PSD), was obtained by FFT as below:

$$S(\omega) = \frac{1}{T_s}\left[\sum_{n=1}^{N} \eta(n\Delta t) e^{i2\pi f(n\Delta t)} \Delta t\right]^2$$

where η(t) is the displacement data as a function of time, T_s is the total acquisition time of data, N is the number of data points and is a power of 2, Δt is the time increment of data. Frequency resolution, Δf and frequency range, or so-called Nyquist frequency, f_N, that have to be selected before an energy spectrum of a wave signal can be obtained by the FFT method are calculated as follows:

$$\Delta f = \frac{1}{N(\Delta t)}$$

$$f_N = \frac{1}{2(\Delta t)}$$

The vibration frequency spectra of the riser for both the in-line and cross-flow directions can be respectively produced by the FFT method. Here, the energy spectra for node 8 in both in-line and cross-flow directions, in the range of carriage speeds from 0.2 to 1.0 m/s, are presented in figure 6-1 to figure 6-9.

Figure 6-1 shows the VIV power spectrum in both in-line and cross-flow directions at the speed of 0.2 m/s. It is obvious that there is a dominant frequency of 0.64 Hz, with the higher peak in figure 6-1 (a), and a secondary dominant frequency of 1.28 Hz, with a lower peak, in the cross-flow direction. In the VIV power spectrum in the in-line direction at the same speed Figure 6-1 (b), three dominant frequencies are observed, which have dominant frequencies of 0.64 Hz, the secondary dominant frequency of 1.28 Hz, and the third dominant frequency of 1.89 Hz. The first two dominant frequencies are the same as that in cross-flow direction.

In Figure 6-2, 0.9 Hz is the first peak in the spectrum of the cross-flow direction, although there are a few much weaker peaks appearing at higher frequencies. In the power spectrum of the in-line direction, the first dominant frequency is also 0.9 Hz and the secondary frequency is 1.83 Hz. The first dominant frequencies for both cross-flow and in-line directions still are the same at this speed.

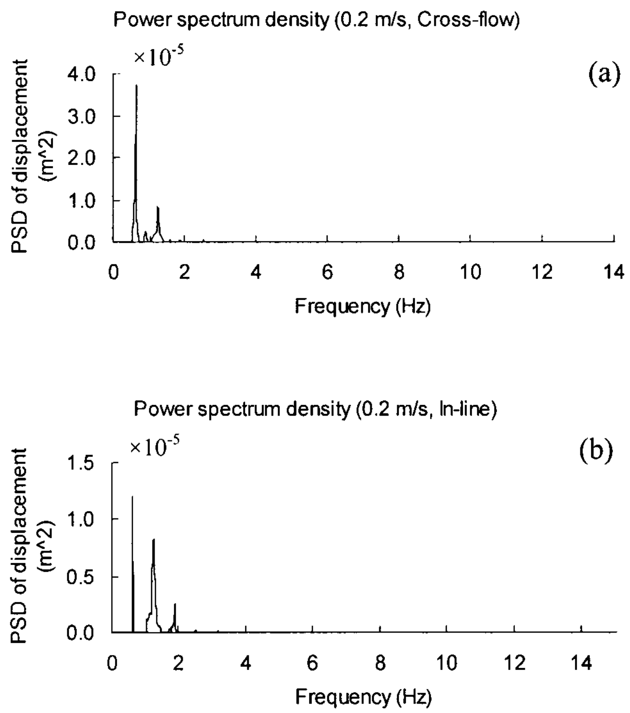

Figure 6-1 Power spectra for node 8 at speed of 0.2 m/s

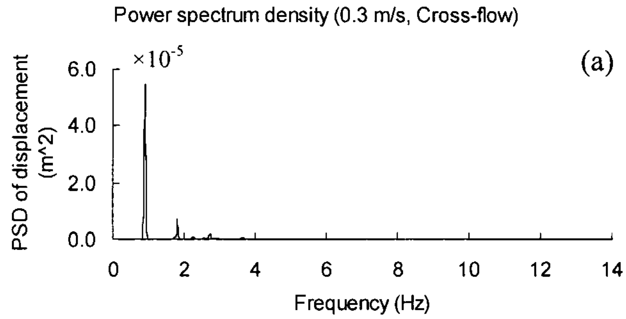

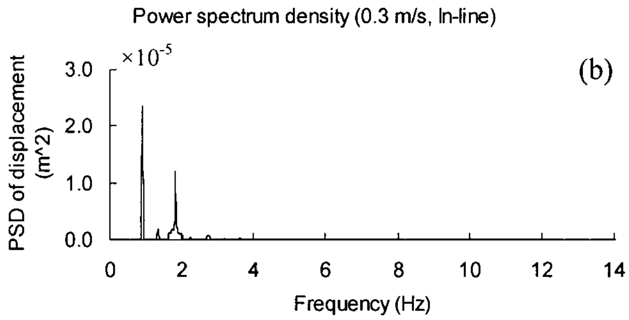

Figure 6-2 Power spectra for node 8 at speed of 0.3 m/s

In Figure 6-3, at a speed of 0.4 m/s, the first dominant frequency in the cross-flow direction is 1.34 Hz and two weaker frequencies are 2.68 Hz and 4.05 Hz. The peak at 1.34 Hz is much higher than those at 2.68 Hz and 4.05 Hz. There are two peaks at the frequencies of 1.34 Hz and 2.68 Hz in the in-line direction. The two peaks in energy are very close. The peak at 1.34 Hz is a little bit weaker than that at 2.68 Hz.

Figure 6-4 shows the VIV power spectrum in both in-line and cross-flow directions at the speed of 0.5 m/s. Again, the peak at the frequency of 1.59 Hz in the cross-flow direction is much higher than those at the frequencies of 3.2 Hz and 4.79 Hz. In the in-line direction, two peaks at the frequencies of 1.59 Hz and 3.2 Hz are very close in energy.

Figure 6-5 provides the VIV power spectrum in both in-line and cross-flow directions at the speed of 0.6 m/s. In the cross-flow direction, there is a strong peak at the frequency of 1.86 Hz and two very weak peaks at the frequencies of 3.72 Hz and 5.59 Hz. In the in-line direction, a strong peak is at the frequency of 1.86 Hz and a weaker peak is at the frequency of 3.72 Hz.

Figure 6-6 gives the VIV power spectrum in both in-line and cross-flow directions at the speed of 0.7 m/s. In Figure 6-6 (a), we can see a strong peak is at the frequency of 2.1 Hz in the cross-flow direction. Two small peaks are at the frequencies are 4.18 Hz and 6.29 Hz. In Figure 6-6 (b), for the in-line direction, a strong peak is at the frequency of 2.1 Hz; a weaker peak is at the frequency of 4.18 Hz; and a very weak peak is at the frequency of 6.29 Hz.

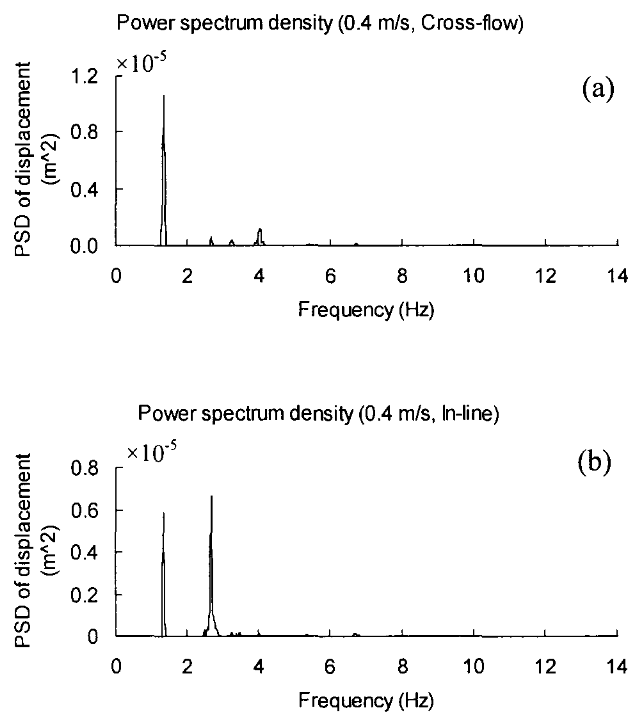

Figure 6-3 Power spectra for node 8 at speed of 0.4 m/s

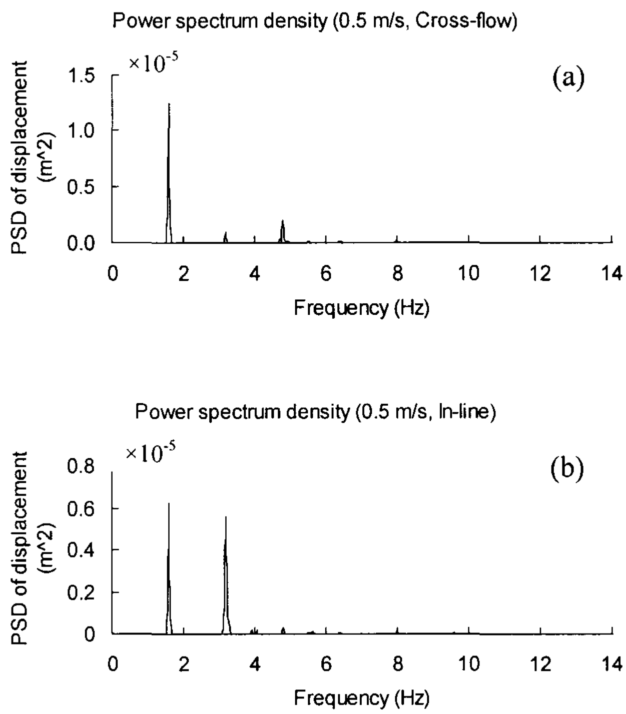

Figure 6-4 Power spectra for node 8 at speed of 0.5 m/s

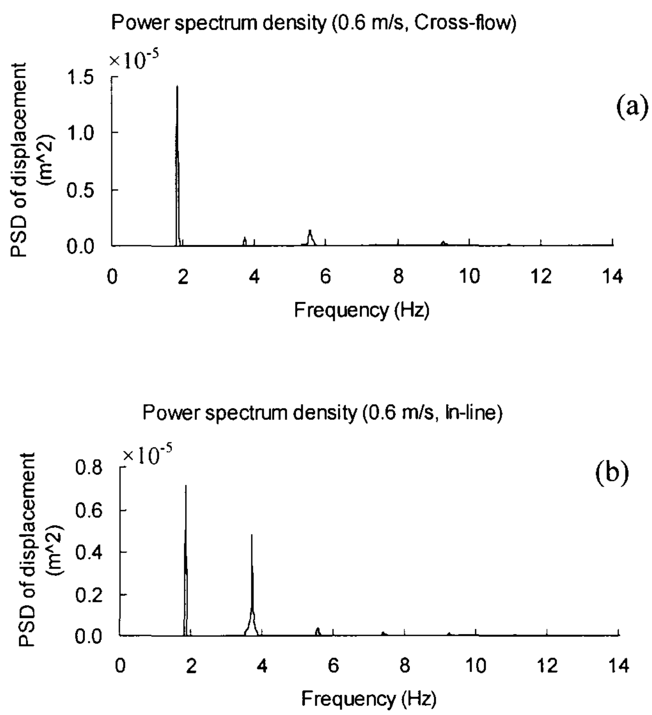

Figure 6-5 Power spectra for node 8 at speed of 0.6 m/s

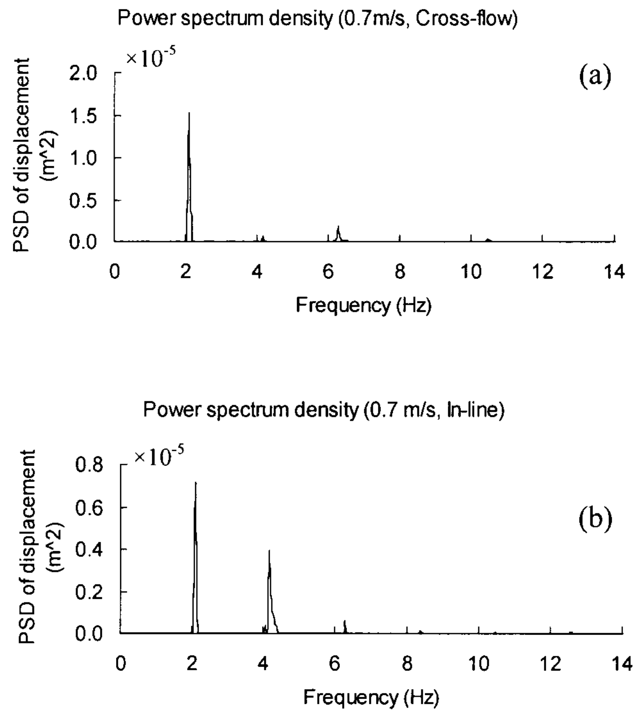

Figure 6-6 Power spectra for node 8 at speed of 0.7 m/s

Figure 6-7 shows the power spectrum in both in-line and cross-flow directions at the speed of 0.8 m/s. In Figure 6-7 (a), a strong peak is at the frequency of 2.41 Hz and two weaker peaks are at the frequencies of 2.44 Hz and 2.74 Hz, in cross-flow direction. Two very weak peaks lie at the frequencies of 4.88 Hz and 7.29 Hz. In the in-line direction as shown in Figure 6-7 (b), the VIV response contains a dominant frequency of 2.41 Hz, a weaker peak at frequency of 4.85 Hz and two very weak peak at frequencies of 5.22 Hz and 7.29 Hz.

Figure 6-8 is the power spectrum in both in-line and cross-flow directions at the speed of 0.9 m/s. In the cross-flow as shown in Figure 6-8 (a), a strong peak is at the frequency of 2.59 Hz and two very weak peaks are at the frequencies of 5.22 Hz and 7.78 Hz. In the in-line direction in Figure 6-8 (b), the dominant frequency is 2.59 Hz.

There are a weaker peak at the frequency of 5.16 Hz and two very weak peaks around the frequencies of 5.43 Hz and 5.8 Hz.

Figure 6-9 shows the power spectrum in both in-line and cross-flow directions at the speed of 1.0 m/s. In Figure 6-9 (a), we can see there are a dominant frequency of 3.45Hz in the cross-flow direction and two very weak frequencies of 6.96 Hz and 10.38Hz. In the in-line direction in Figure 6-9 (b), the strong peak is at the frequency of 3.45 Hz and the weaker peak is at the frequency of 6.92 Hz.

From the discussion above, we can summarize the results of the frequency domain analysis at node 8. The first four frequency peaks in both in-line and cross-flow direction are listed in Table 6-1. The VIV responses in both in-line and cross-flow directions consist of one or two strong frequency peaks and a few very weak frequency peaks. The first frequency peaks in the in-line and cross-flow directions are the same in all speeds, except in the speed of 0.4 m/s. The first frequency peak in the cross-flow direction is the largest at all flow speeds and occurs at the lowest frequency at the same speed. In the in-line direction, both the first and the second frequency peaks are obvious larger than other peaks, and the first frequency peak lies at the lowest frequency in all flow speeds, except the speed of 0.4 m/s. In the same flow speed, these higher frequencies usually are the second and the third harmonics of the first frequency. With the increase of the flow speed, frequencies become higher in both the in-line and cross-flow directions. Figure 6-10 shows the vibrating frequencies in both the in-line and cross-flow directions over the range of speeds.

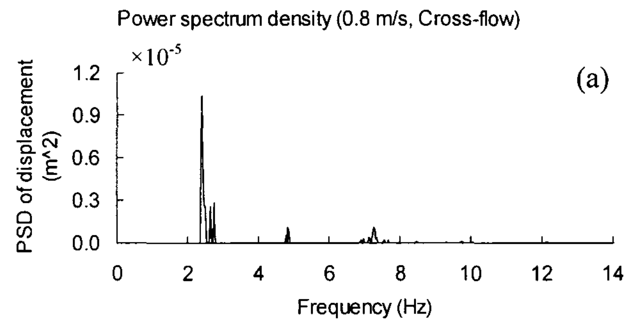

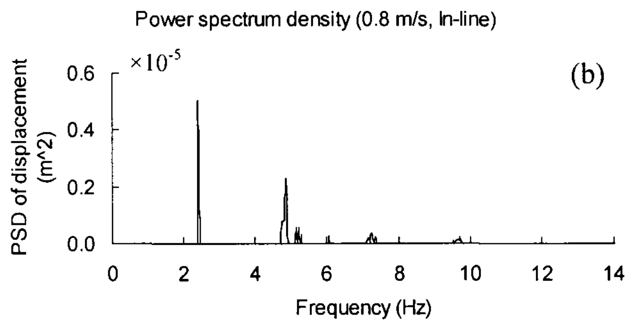

Figure 6-7 Power spectra for node 8 at speed of 0.8 m/s

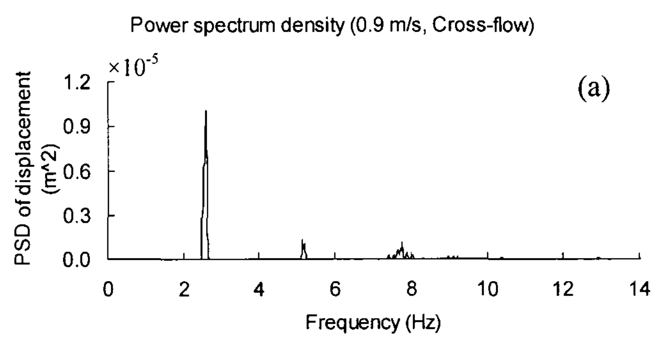

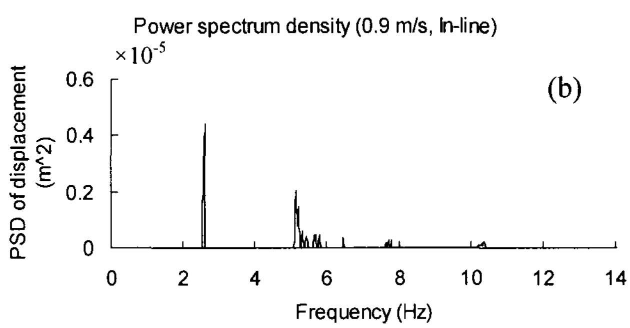

Figure 6-8 Power spectra for node 8 at speed of 0.9 m/s

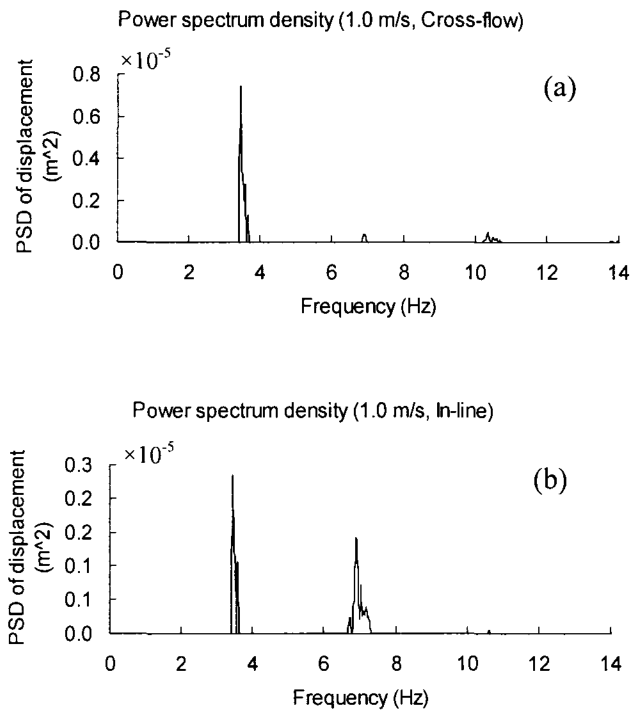

Figure 6-9 Power spectra for node 8 at speed of 1.0 m/s

Table 6-1 Vibration frequencies of VIV responses

U	Cross-flow direction				In-line direction			
	f_1	f_2	f_3	f_4	f_1	f_2	f_3	F_4
0.2	0.64	0.61	1.28	0.92	0.64	1.28	1.22	1.89
0.3	0.92	0.89	1.83	2.74	0.92	1.83	1.80	1.34
0.4	1.34	1.37	2.69	3.27	2.68	1.34	1.37	2.72
0.5	1.59	1.62	3.2	4.79	1.58	3.2	1.62	1.56
0.6	1.86	1.83	3.72	5.59	1.86	3.72	3.69	5.55
0.7	2.11	2.08	3.2	4.79	2.1	4.18	2.07	6.28
0.8	2.41	2.44	2.65	2.74	2.4	4.85	5.22	7.29
0.9	2.59	2.56	5.16	7.78	2.59	5.16	5.8	5.43
1.0	3.45	3.48	6.93	10.38	3.45	6.93	7.12	6.74

6.2.2 Displacement

The displacement of the riser vibration can be obtained by two methods based on this experimental design, one from the signal of the accelerometer and another from the images. The common method is to measure the motion of the pipe by the

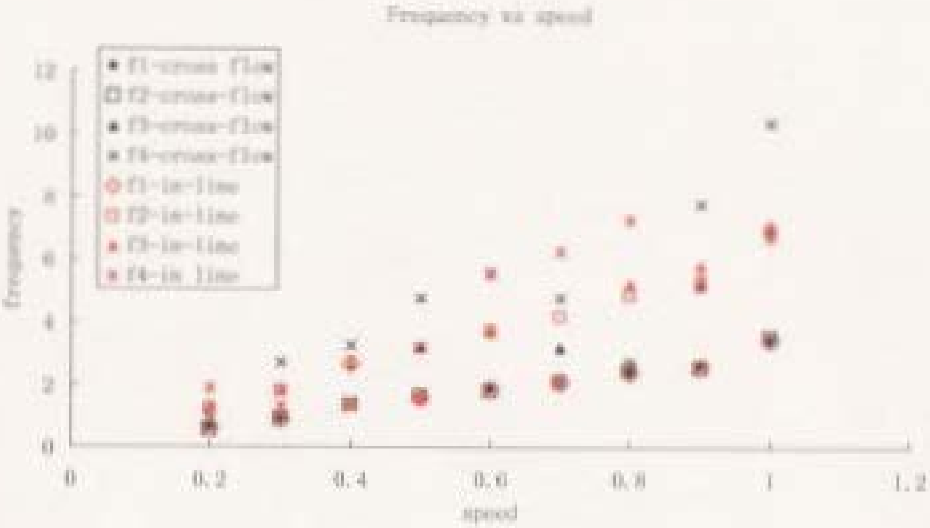

Figure 6-10 Vibrating frequencies over the range of speeds

accelerometers. Since acceleration is the second derivative of the position, a displacement time signal can be obtained by integrating the acceleration twice in the time domain.

$$\dot{x} = \iint a dt$$
$$x = \iint \dot{x} dt$$

where, x is the displacement , $\dot{x}$ is the velocity and a is the acceleration.

The displacement, velocity and acceleration of the riser can be expressed in the frequency domain as below (Lewis 1988):

$$x = \sum_{i=1}^{m} [A_i \sin(\omega_i t) + B_i \cos(\omega_i t)]$$

$$v = \sum_{i=1}^{m} [A_i \omega_i \cos(\omega_i t) - B_i \omega_i \sin(\omega_i t)]$$

$$a = \sum_{i=1}^{m} [-A_i \omega_i^2 \sin(\omega_i t) - B_i \omega_i^2 \cos(\omega_i t)]$$

where m is the sample size; the A_i and B_i are the real and imaginary magnitude of the FFT of displacement signal in frequency domain, respectively; ω_i is the corresponding frequency component of the FFT; x, v and a are the displacement, velocity and acceleration, respectively.

The acceleration data was transformed using FFT to obtain the magnitude of the acceleration in the frequency domain. Some very low frequencies were filtered in the frequency domain by the FFT program, to prevent low frequency noise expansion, but keep lower limits to the frequency range. The corresponding magnitude of the displacement and the velocity were calculated from the magnitude and the frequency of the acceleration by the above equation in the frequency domain. The displacement and the velocity in the time domain then were obtained by reverse FFT of the corresponding magnitude.

The displacement of the riser in in-line and cross-flow directions determined the position of the riser at any moment. By tracking the position of the transverse section of the riser for a period, the motion trajectories of the section can be obtained. Figure 6-11 shows the motion trajectories of the transverse section by the accelerometers at node 8 from the speed 0.2 m/s to 1.0 m/s. We can see that the motion trajectories vary with the flow speed. At the lower speeds of 0.2m/s and 0.3 m/s, the motion trajectories followed a figure of 8-pattern. With the increase of the speed, from 0.4 m/s to 0.7 m/s, the motions shifted to a C-shape. At higher speeds from 0.8 m/s to 1.0 m/s, the motions of the transverse section seem random, but within a limited region, as shown in Figure 6-11. These motions are characteristic of flexible cylinder vibration (Davis *et al.* 2000).

Another reliable method to obtain the displacement is to record the position of the

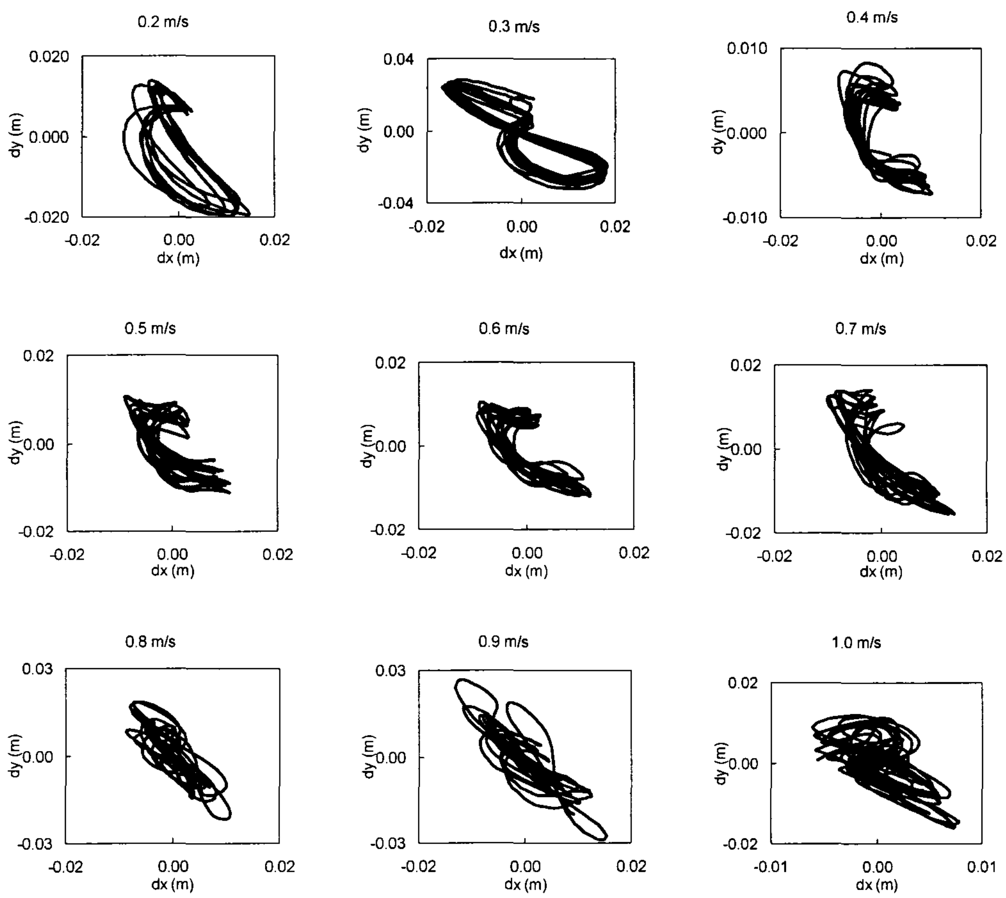

Figure 6-11 Vibration trajectory of the transverse section of the riser at z/L=0.43

riser from each particle image. The displacement determined from this method can exactly represent the motion of the transverse section in the measurement plane. As shown in previous chapter, the riser section at the measurement plane has been recorded in most particle images, except those images at the speed of 0.1 m/s and some images at the speed of 0.2 m/s. This is because the initial shift of the riser section was not big enough to move it into the measurement area at the lower speed. The coordinate of the riser section in each image can be acquired by the DaVis software. Defining x and y as the coordinate of the center point of the rear edge of the riser section, the values of x and y for the 150 images in the same run were averaged to obtain the mean position as below:

$$\bar{x} = \sum_{1}^{n} x \Big/ n$$

$$\bar{y} = \sum_{1}^{n} y \Big/ n$$

where n is the total number of the images. The x and y give the absolute coordinate of the riser in the image. The plot of the mean position against the flow speeds is shown in Figure 5-29. The displacement of the riser, d_x and d_y, at each moment for each images was determined by the deviation of x and y, where d_x is $(x-\bar{x})$ and d_y is $(y-\bar{y})$.

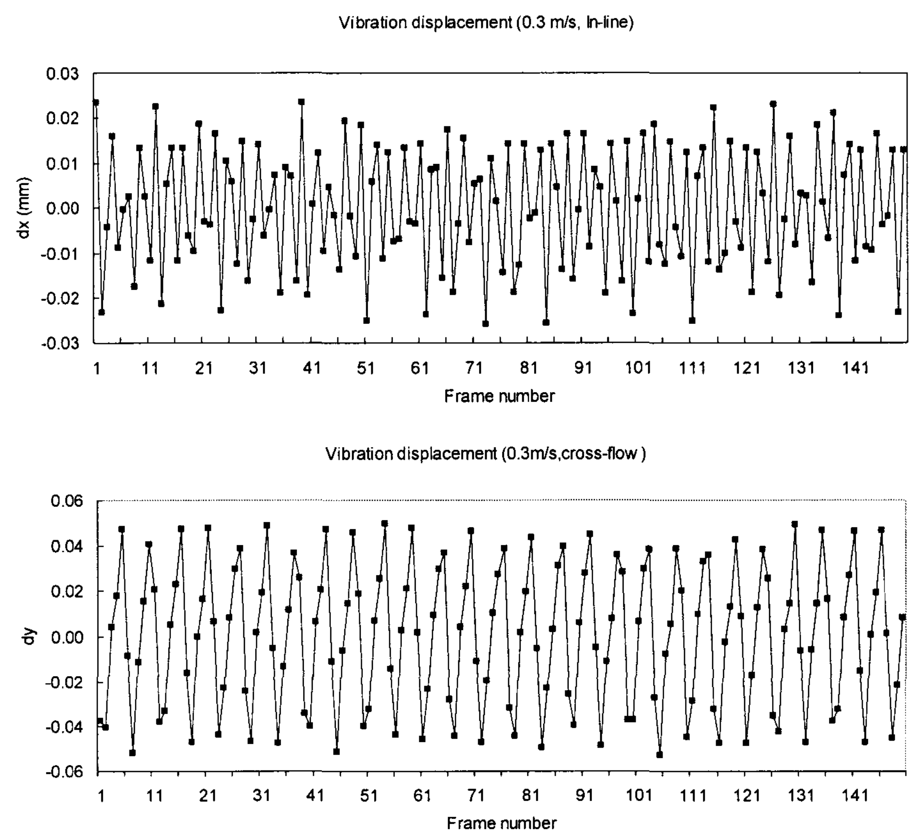

Figure 6-12 Displacement determined by images, z/L=0.44

Figure 6-12 shows the displacement in the in-line and cross-flow directions for 150 images which represent 150 different instants at the speed of 0.3 m/s. The duration for acquiring 150 images was about 30 seconds. The points represent the displacement of the riser at each image moment. The VIV response in the cross-flow shows a regular vibration pattern and the amplitude can be easily determined from the displacement peak. It can be seen from Figure 6-12 that the displacement in the cross-flow direction is obviously bigger than that in the in-line direction at this speed.

6.2.3 Amplitude

For steady-state periodic vibration, amplitude is the maximum repeating absolute value of the vibratory response, such as displacement, velocity or acceleration. For a freely vibrating riser, the amplitude is time dependent. The amplitude can be determined by the mean peak of the displacement (Chakrabarti 1987, Lewis 1988).

The amplitude also was assessed by two methods for this experiment. One is from the displacements computed from the accelerations, as discussed in 6.2.2, and another is from images. As discussed above, the location of node 8 was not exactly on the measurement plane, but away by a distance of 90 mm; hence the VIV responses at the two locations could not be the same for the multi-modal flexible riser. The result of the amplitude from the accelerations and from images is compared in Figure 6-13. The amplitude of the VIV response was assessed as the average of the highest one third displacement peaks in the same run. Figure 6-13 shows the curves of vibration amplitude against the current speed, where A*is the amplitude to diameter ratio, A/D. The symbols '■' and '□ ' represent the amplitudes of the cylinder at node 8, which were obtained from the accelerations, while symbols '▲' and ' Δ' are the amplitudes at the measurement plane, obtained from the images. It can be seen that the amplitude trends from both methods are similar, while the amplitudes in measurement plane are bigger than that at the location of the node 8. The amplitude in the cross-flow direction was bigger than that in the in-line direction for all speeds, except the speed of 0.4 m/s. The maximum amplitude was close to the diameter of the riser and appears at the speed of 0.3 m/s. The amplitudes for both in-line and cross-flow directions reached the highest value at this speed. As discussed above, the initial shift also showed a jump for both in-line and cross-flow at the speed of 0.3 m/s.

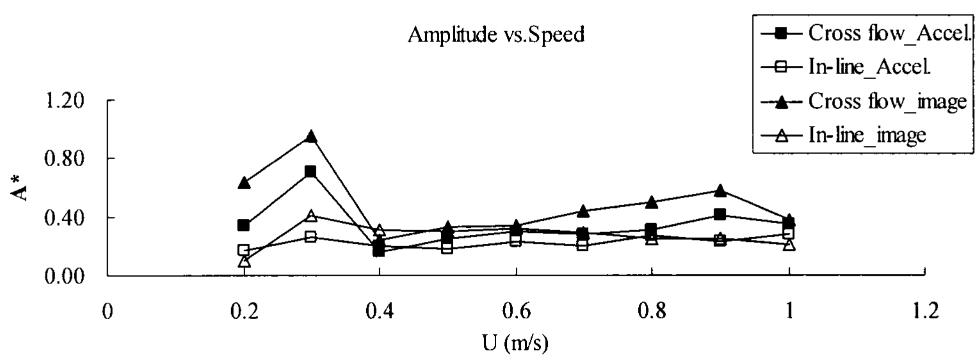

Figure 6-13 Vibration amplitude from both acceleration and images

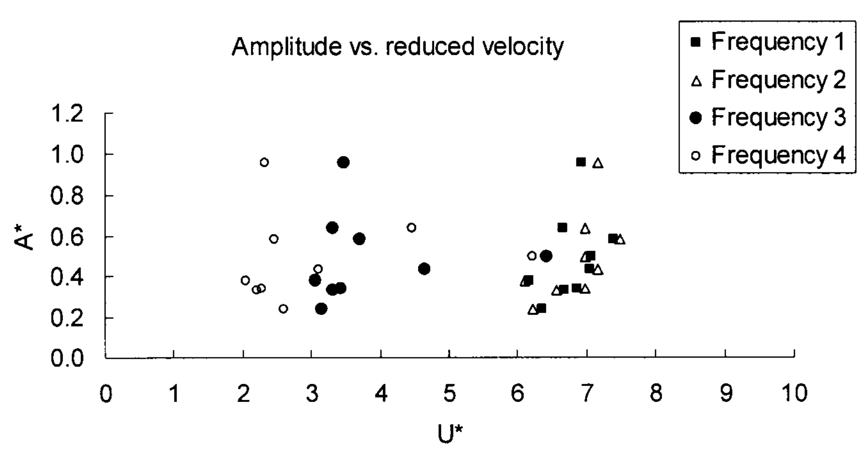

Figure 6-14 Vibration amplitude in cross-flow direction

Figure 6-14 provides the dimensionless amplitude, $A^*=A/D$, against the reduced velocity, $U^*= U/(fD)$, in the cross-flow direction. The reduced velocity is obtained from the free stream velocity, U, the first four vibration frequencies, f, and the diameter of the riser, D. In Figure 6-14, the symbols '■', '△', '•' and 'o' represente the reduced velocities computed from the first, second, third, and fourth dominant frequency, respectively. Figure 6-14 gives a combination range of amplitude to diameter ratio and reduced velocities in the set of experiments. In a later section, this will be discussed further with the wake vortex patterns.

6.3 Wake Field Results

The periodic wake of a smooth, circular cylinder is a function of Reynolds number for low Mach numbers (Blevins 1977). This means that Reynolds number plays a key role in the wake pattern of a cylinder. A regular pattern of vortices is formed in the wake that interacts with the cylinder motion and is the source of the effects of vortex-induced vibration.

It has also been found from the vortex map by Williamson & Roshko (1988) that the vortex patterns behind a rigid circular cylinder which is forced to oscillate harmonically transversely to an oncoming stream, vary significantly as the function of the amplitude and frequency. For a flexible circular cylinder, the vortex patterns have been shown to be associated with the change of the amplitudes and the reduced velocities by Ferguson (1965) and Brika & Laneville (1993). These previous studies have shown that the wake vortex patterns are relative to the vibration frequencies, amplitudes of the riser vibration and the flow speeds.

6.3.1 Velocity Field

The instantaneous velocity vector fields behind the vibrating riser at different speeds were obtained by calculating the cross-correlation function of the particle images, as discussed in previous chapters. The range of the current speeds in this set of experiments was from 0.1 to 0.2 m/s, which corresponded to the range of Reynolds number from 4700 to 47000.

Figure 6-15 (a) shows a velocity vector field, corresponding to Re=9400, i.e. the speed of 0.2 m/s. The displacement of the riser at the moment the image was taken was d_x=2.77mm and d_y= -22.08 mm, away from its average position $\bar{x}$=56.23 mm and $\bar{y}$=682.08mm. The color pattern shows the velocity along the flow direction, V_x. The contour with the velocity vector for the same velocity field is shown in Figure 6-15 (b). It can be seen that those velocity vectors on the top and the bottom are closer to the free stream. In the middle region, the velocity fluctuations caused by the growth of vortices are apparent. The velocity component normal to the flow, V_y, becomes much more dominant in this region.

Figure 6-16 to Figure 6-23 show the velocity vector fields in the different current speed from 0.3 to 1.0 m/s with an increment of 0.1 m/s, which correspond to the Reynolds number of 14100, 18800, 23500, 28200, 32900, 37600, 42300, and 47000, respectively.

As fluid flows toward the leading edge of the riser, the pressure in the fluid rises from the free stream pressure to the stagnation pressure. The high fluid pressure near the leading edge impels the developing boundary layers about both sides of the riser. The

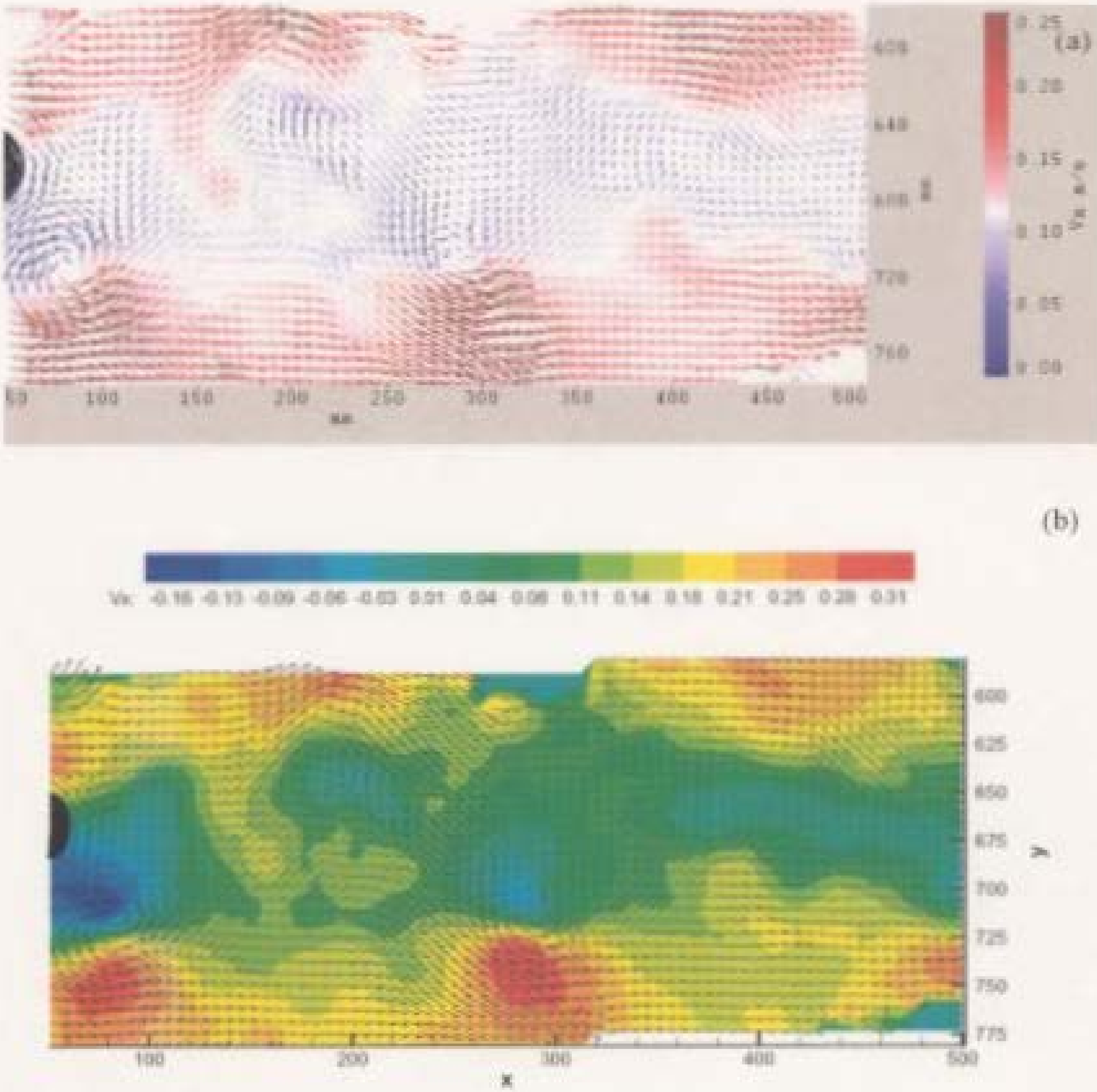

Figure 6-15 Velocity vector field and contour at Re=9400 (Image No 61)

pressure forces, however are not sufficient to force the boundary layers completely around the back side of bluff cylinders at high Reynolds numbers. This leads to the fact that the boundary layers separate from each side of the cylinder surface and form two free shear layers that trail aft in the flow. The two free shear layers bound the wake. With the increase of *Re*, the separation point moves backward around the riser section so that the wake region becomes narrow. Meanwhile, the wake becomes turbulent and unstable. Since the innermost portion of the free shear layers moves

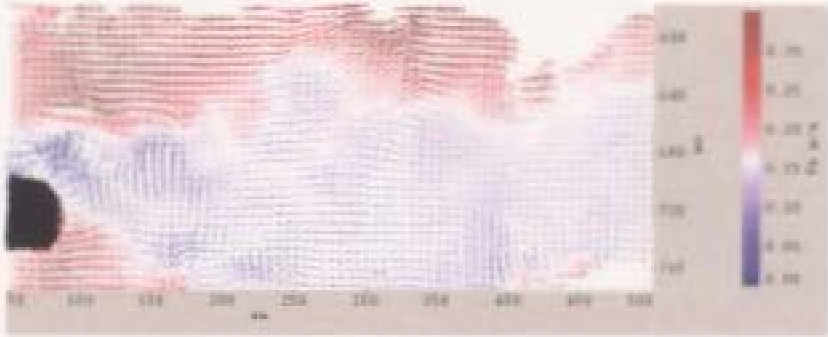

Figure 6-16 Velocity vector field at Re=14100 (No19, 36-03)

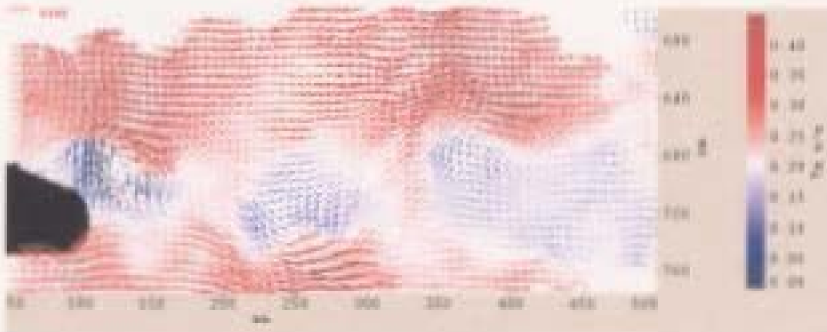

Figure 6-17 Velocity vector field at Re= 18800 (No.66, 46-04)

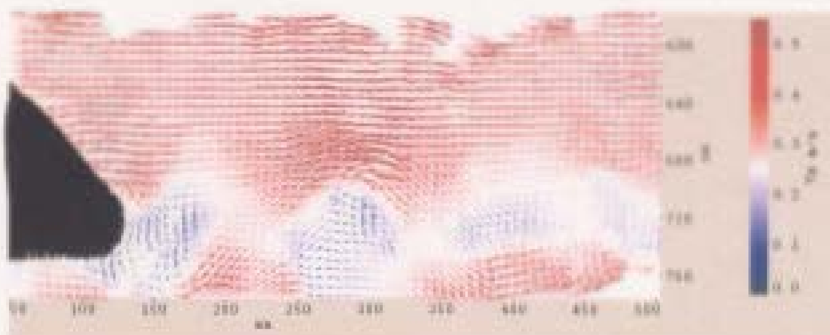

Figure 6-18 Velocity vector field at Re=23500 (No 40, 47-05)

Figure 6-19 Velocity vector field at Re=28200 (No 37, 48-06)

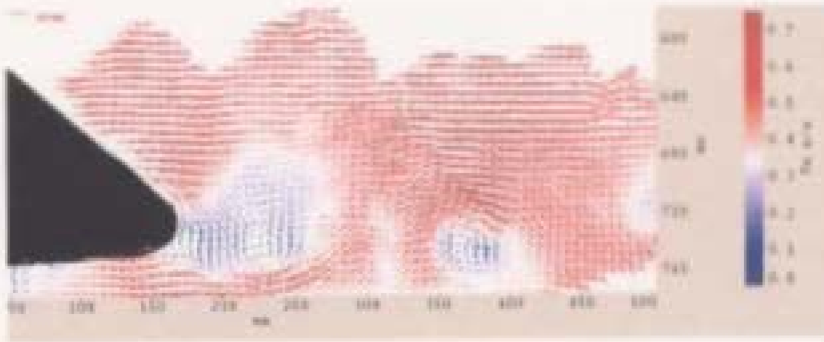

Figure 6-20 Velocity vector field at Re=32900 (No 29, 49-07)

Figure 6-21 Velocity vector field at Re=37600 (No 27, 50-08)

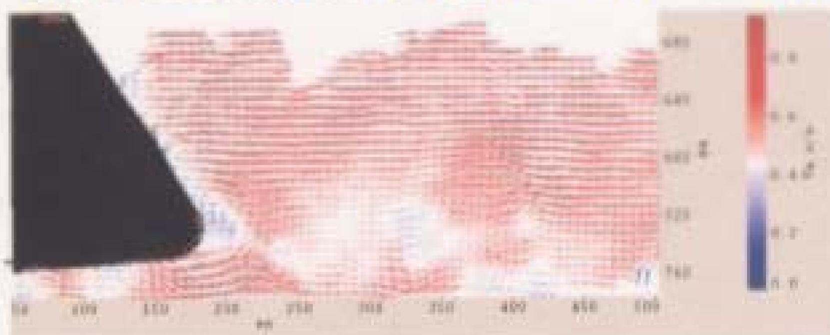

Figure 6-22 Velocity vector field at Re=42300 (No 42, 51-09)

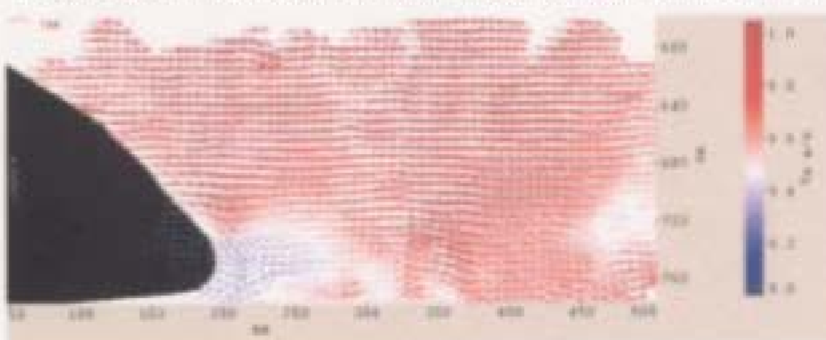

Figure 6-23 Velocity vector field at Re=47000 (No 120, 43-10)

much more slowly than the outermost portion of layers which are in contact with the free stream, finally, the free shear layers tend to roll up into discrete, swirling vortices.

6.3.2 Wake Vortex Pattern

The form of the patterns behind a uniform cylinder with forced harmonic oscillation transverse to an on coming stream has been mapped by Williamson & Roshko (1988) as shown in Figure 2-2. The vortex pattern has been found to vary significantly as a function of the amplitude and frequency. The major vortex patterns near the fundamental synchronization region are 2S, 2P and P+S. The vortex patterns 2S and 2P present a symmetric structure, while P+S pattern is asymmetric.

A long flexible riser vibrates freely in both in-line and cross-flow directions. The vortex patterns in the wake may not have the same formation as those of a rigid cylinder only vibrating transversely, because the vibration frequency and amplitude of the riser vary with time, as discussed above. In the discussion below, the first frequency and the average amplitude at each speed are used as the inputs to discuss the corresponding vortex patterns in the wake.

6.3.2.1 Vortex Pattern '2S'

For certain values of the frequency of vibration, *f*, the Reynolds number, *Re*, and the amplitude to diameter ratio, A/D, as the analysis above, '2S' vortex modes, i.e. two single vortices with opposite sign, using the nomenclature of Williamson & Roshko (1988) were observed in the experiments.

Figure 6-24 shows the velocity and vorticity field of a typical '2S' mode for a Reynolds number, Re=18800. According to the definition of '2S' vortex mode, in each half cycle, a single vortex is fed into the downstream wake and the two vortices

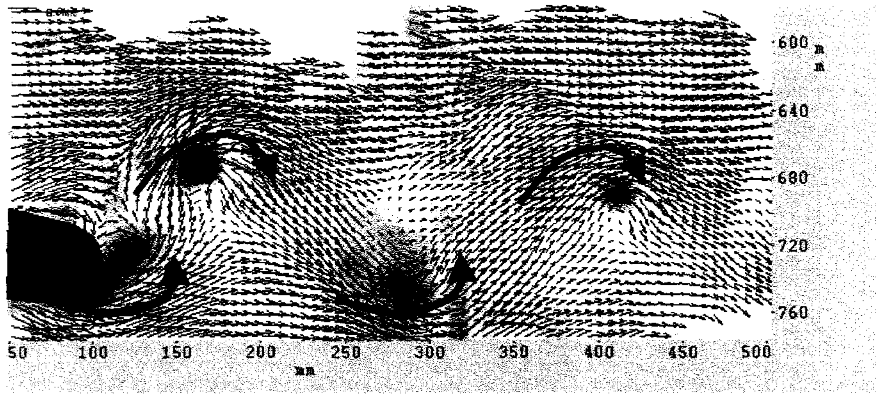

Figure 6-24 Velocity and vorticity field showing a '2S' pattern for Re= 18800, A_x/D=0.31 and A_y/D=0.24, f_x=f_y=1.34Hz (No 4,46-04)

shedding in each cycle rotate in different directions, like the natural Karman vortex shedding. In Figure 6-24, the red color represents positive vorticity, clockwise rotation of the fluid; and the blue spots show negative vorticity, counter-clockwise rotation of the flow.

In this figure, the amplitude to diameter ratios in in-line and cross-flow directions are A_x/D=0.31 and A_y/D=0.24 and the first dominant frequencies in both directions were f_x=f_y =1.34Hz. The area of the combined velocity field is about 9.5 diameters in length and 4 diameters in height. In Figure 6-24, the riser is moving at constant speed from right to left; a pair of vortices, clockwise and anticlockwise, was forming on the rear side of the cross section of the riser. At this moment, the displacement to diameter ratio of the riser in in-line and cross-flow direction were d_x/D=0.07 and d_y/D=0.16, from its mean position, $\bar{x}$ =103mm and $\bar{y}$ = 724mm, at this speed.

Figure 6-25 provides three velocity fields corresponding to the same Reynolds number, Re=9400, and with almost the same displacement, d_x/D=0 and d_y/D=-0.77, in in-line and cross-flow direction, respectively. The mean position in this speed was

$\bar{x}$ =56mm and $\bar{y}$ = 682 mm. The amplitude to diameter ratios in in-line and cross-flow direction are A_x/D=0.10 and A_y/D=0.64 and the dominant frequencies in both directions are f_x=f_y=0.64Hz, at this speed. The riser was on the maximum negative position in transverse direction and had the minimum oscillation in flow direction among all the images. From these figures, the identical vortex mode, '2S' mode is observed. These vortices are marked using A, B, C and D, as shown in Figure 6-25. The corresponding vortices in the three figures are marked with the number 1, 2 and 3. According to the definition of '2S' vortex mode, it can be seen that the clockwise vortex A was shed in the first half cycle and counter-clockwise vortex B followed in the next half cycle; while clockwise vortex C was shed in another first half cycle and counter-clockwise vortex D was shed in the second half cycle. The process of the formation of the '2S' vortex mode was explained by Williamson & Roshko (1988) to trace vortices convection downstream from a cylinder. They demonstrated the complete process of the motion of a vortex during a cycle of cylinder oscillation. They showed that each vortex of the '2S' mode was formed from two like-signed vortices amalgamating each half cycle. It was also shown that vortex position can be connected to the displacement and phase of the oscillating cylinder.

The coordinates of the vortex core, the vorticity and the accèleration of the riser at the moment are provided in Table 6-2. Although the vortex modes in the three figures look the same, we notice that the vibration accelerations of the riser at the three measurement instants were different, especially, the acceleration in the cross-flow direction for the flow field (c), and a_y, is at an opposite sign to the others. For a

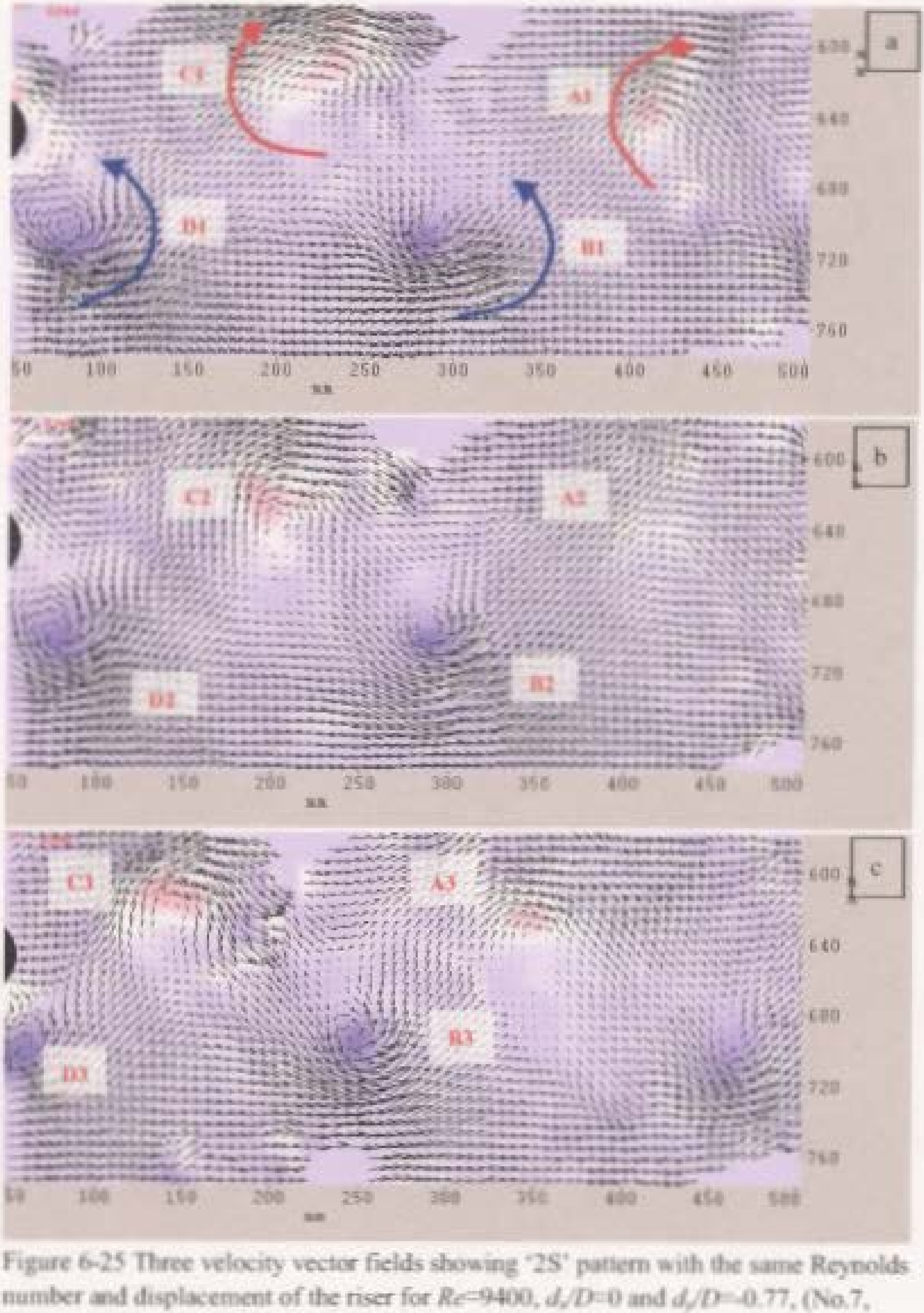

Figure 6-25 Three velocity vector fields showing '2S' pattern with the same Reynolds number and displacement of the riser for Re=9400, d_x/D=0 and d_y/D=-0.77, (No.7, No.124 and No 130, 44-02)

regular oscillating cylinder, the acceleration represents its movement characteristics, i.e. displacement and velocity. For the motion with the same displacements and different

accelerations, it means the velocities are different. This may be connected to the shedding phase of the vortices. From Figure 6-25, it can be seen that the relative positions of the individual vortices were slightly different. This implies instantaneous acceleration influenced the wake vortex structure.

Figure 6-26 provides two velocity fields corresponding to the same Reynolds number, Re=9400, and with the displacement, d_x/D=-0.05 and d_y/D=0.47 in Figure (a), and d_x/D=0, d_y/D=0.47 in Figure (b), respectively. At this moment of the two images, the riser was at its maximum positive position in the transverse direction, while the two positions of the riser along the flow direction were slightly different. The '2S' wake pattern can be clearly seen downstream of the riser. At the moment the image was taken, the counter-clockwise vortices D1 and D2 were shedding from the rear edge of the riser in both figures (a) and (b). The coordinate and the vorticity of the vortex core, as well as the acceleration of the riser at the moment are shown in Table 6-3.

The '2S' vortex patterns are also observed at a higher speed of 0.4 m/s. Figure 6-27 provides two velocity fields showing the formation of a "2S" mode for Re=18800, d_x/D=0.19 and d_y/D=-0.22. In the two figures, the amplitude to diameter ratios in the in-line and cross-flow directions were A_x/D=0.31 and A_y/D=0.24 and the dominant frequencies in both directions were f_x=f_y=1.34Hz. The accelerations of the riser at the two instants were close; where a_x=2.58 m/s^2 and a_y=-2.88 m/s^2 in figure (a), a_x=2.99 m/s^2 and a_y=-2.93 m/s^2 in figure (b). The position and the vorticity of the vortex core, as well as the acceleration of the riser at the moment are shown in Table 6-4.

With the same displacement and the close accelerations, two very similar vortex patterns are observed in figure (a) and figure (b). Here, it can be seen that the clockwise vortices D1 and D2 were shedding from the riser, while the anti-clockwise vortices C1 and C2 had just completely formed in both velocity fields. Another two different sign vortices A and B had convected further downstream. The locations of the corresponding vortices in the two figures are almost the same. This implies that vortices were shed at the same period and phase angle under the same Reynolds number, displacement and the acceleration.

By comparison of the two "2S" patterns in Figure 6-26 and Figure 6-27, it was noticed that the structures of the patterns were slightly different. The lateral distance between vortices obviously decreases, while the longitudinal distance between the vortices slightly increase, with the increase of Reynolds number. Williamson & Roshko (1988) have observed that the structure of vortex pattern 2S changed with an increase in imposed wavelength λ, or U/f. With the increase of the Reynolds number, the vorticity of the individual vortices also was increasing. This can be observed directly as the color of the vortices becomes darker with increasing Reynolds number, as shown in Figure 6-26 and 6-27.

Table 6-2 Coordinate, vorticity of the vortex core and the acceleration of the riser in figure 6-25

Frame #	Vortex A			Vortex B			Vortex C			Vortex D			Accel.	
	x	y	Vor.	x	y	Vor.	x	y	Vor.	x	y	Vor.	a_x	a_y
7	412.40	636.64	17.52	282.49	711.22	-35.33	231.93	611.78	17.24	80.24	717.43	-31.5	-1.97	1.66
124	431.85	602.45	10.9	287.94	705.00	-37.73	195.267	624.983	20.62	81.01	704.23	-32.67	-1.09	1.17
130	350.17	625.76	17.17	245.15	697.23	-35.33	139.358	611.776	23.93	56.90	703.45	-35.66	-0.05	-1.03

Mean position of the riser: $\bar{x}$ =56.23 mm, $\bar{y}$ =682.08mm; Vibration amplitude: Ax/D=0.10, Ay/D=0.41

Displacement of the riser: d_x=0, d_y=-36mm; Dominant vibration frequency: fx=fy=0.64 Hz

Table 6-3 Coordinate, vorticity of the vortex core and the acceleration of the riser in figure 6-26

Frame #	Vortex A			Vortex B			Vortex C			Vortex D			Accel.	
	x	y	Vor.	x	y	Vor.	x	y	Vor.	x	y	Vor.	a_x	a_y
20	428.74	710.44	-22.61	371.18	615.66	12.5	215.59	715.88	-20.62	130.02	642.98	28.13	0.52	-0.69
59	437.30	723.65	-27.58	335.39	627.31	14.8	224.15	705.78	-34.46	125.36	605.56	23.34	-0.21	-0.47

Mean position of the riser: $\bar{x}$ =56.23 mm, $\bar{y}$ =682.08mm; Vibration amplitude: Ax/D=0.1, Ay/D=0.41

Displacement of the riser: d_x=-2.23 (Figure a), d_x=-0.23 (Figure b), d_y=-36mm; Dominant vibration frequency: fx=fy=0.64 Hz

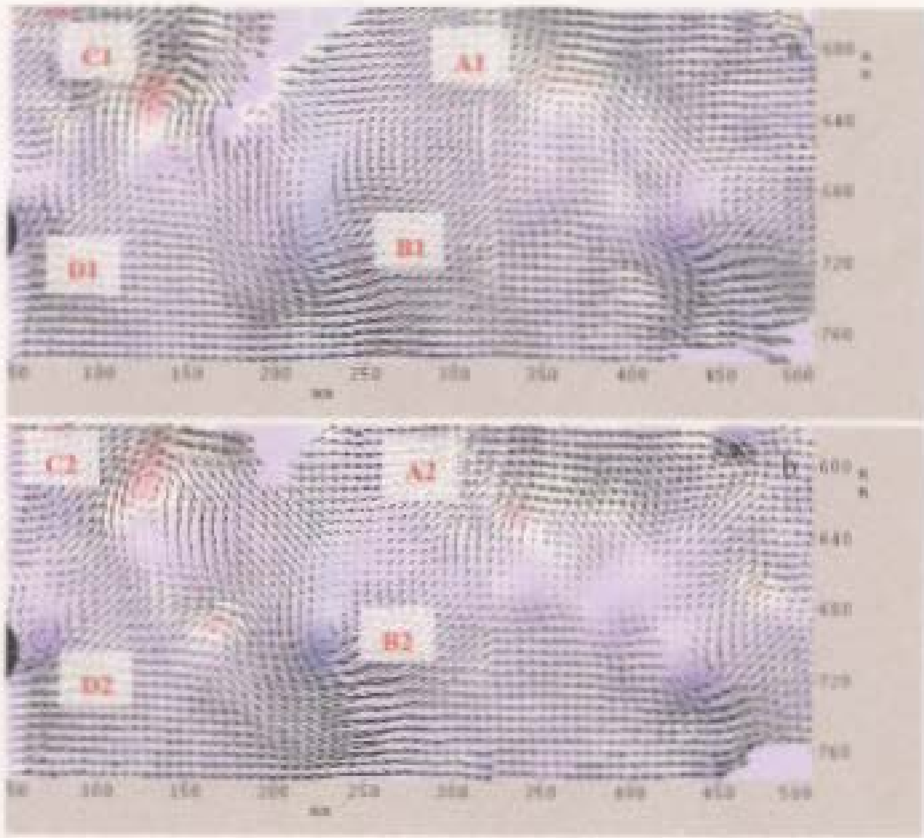

Figure 6-26 Two velocity vector fields showing '2S' for the same Reynolds number, Re=9400 and for the displacement, d_x/D=-0.05, d_y/D=0.47 in "a", and d_x/D=0, d_y/D=0.47 in "b" (No.20 and No.59, 44-02)

The formation and movement of the vortices can be demonstrated clearly from the successive image frames. Figure 6-28 provides nine successive flow fields of the '2S'vortex mode, at the speed of 0.4 m/s, corresponding to the Reynolds number 18800. The time interval between each two figures is about 0.2 s.

A vortex just shedding from the riser can stay in the field of view for several successive image frames. The numbers of the successive frames that involved the same vortex depended on the flow speed. At the speed of 0.4 m/s, the vortex E and the vortex F appeared in seven successive frames before leaving the field of view, as shown in Figure 6-28 a to i. The animated pictures clearly showed the same vortex moving from frame to frame. All plots in Figure 6-28 show obvious '2S' vortex

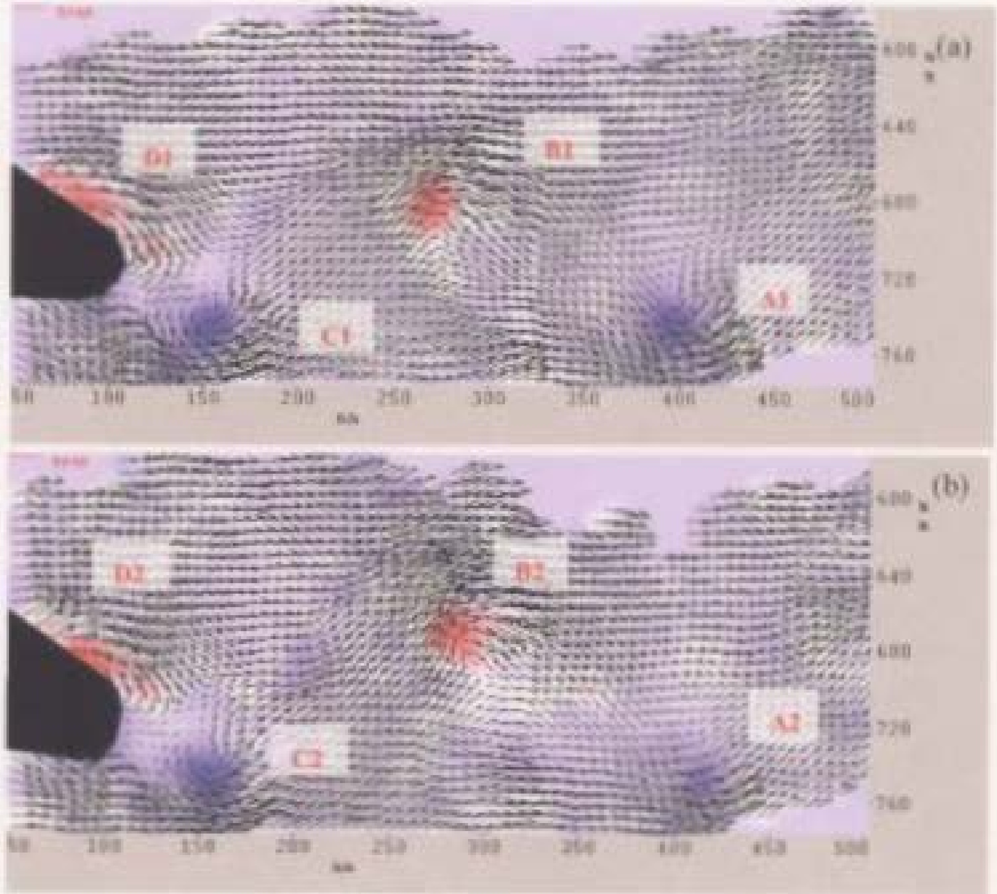

Figure 6-27 Two velocity vector fields showing '2S' pattern with the same Reynolds number, Re=18800, and the same displacement d_x/D=0.19, d_y/D=-0.22, the acceleration of the riser very close in "a" and "b" (#105, #138, 46_04)

patterns. Here, the movement of the vortex E and F is tracked in these successive frames to assess the vortex convection speed.

From the figure 6-28 a, the counter-clockwise vortex E was shed from the rear side of the riser, as the displacement of the riser was d_x/D=-0.28 and d_y/D=0.08. Figure 6-28 b, 0.2 s later, shows the vortex E has moved to a new position and has completely formed. From figure 6-27 c- g, the position of the vortex E moves downstream of the riser until it leaves the image. For the clockwise vortex F, it was generated on the rear side of the riser as vortex E shed away from the riser in figure 6-28a, and was shed 0.4 s (after two frames) after the vortex E. In figure 6-28 d, another 0.2 s later, the vortex F had completely formed downstream away from the riser. After then,

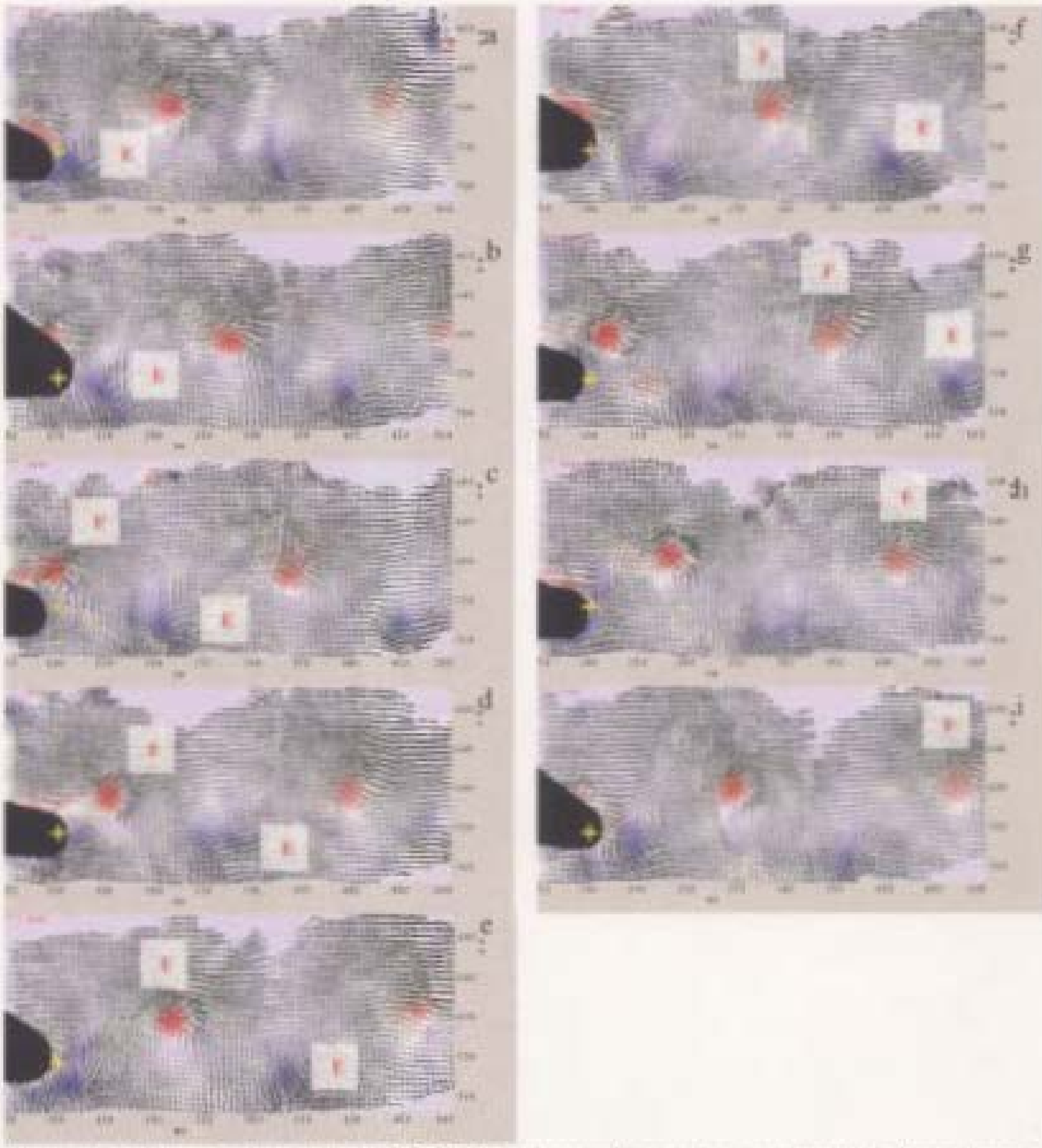

Figure 6-28 Successive velocity fields showing wake vortices convection downstream for Reynolds number, Re=18800, the symbol "+" indicates the mean position of the riser. (No.34-No.42, 46-04)

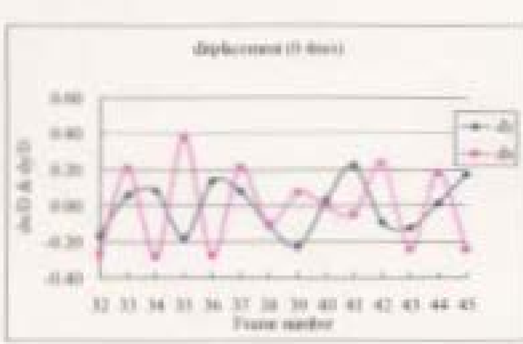

Figure 6-29 Displacement of the riser at each instant in figure 6-28

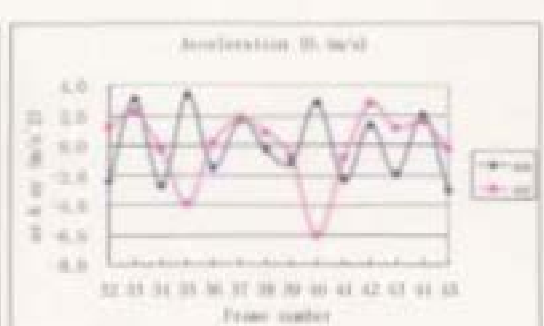

Figure 6-30 Acceleration of the riser at each instant in figure 6-28

similar to vortex E, it kept moving downstream until leaving the image, as shown in Figure 6-28 e to i. Figure 6-29 and Figure 6-30 provide the displacement and the acceleration of the riser corresponding to each frame. Table 6-5 provides the coordinates and the vorticity of the vortex core of the vortices E and F in each frame. The data for the displacement and the acceleration of the riser at each moment are also collected in the table.

Figure 6-31 shows the plot of the vorticity against position of the vortices E and F. The coordinate axis x is the non-dimensional position of the vortex, x^*/D, where $x^*=(x_v-\bar{x})$; x_v is the coordinate of the core of the vortex in x direction and $\bar{x}$ is the mean position of the riser at the corresponding speed; D is the diameter of the riser. The y axis is the vorticity of the core of the vortex. From Figure 6-31, it can be seen that the vorticity of vortex F is gradually decreasing as the vortex moves downstream. This is because the vortex gradually diffused due to viscous action and the vorticity of the core decreased. For the vorticity of the vortex E, it shows a decreasing trend at first, then rises from the locations of x^*/D=4.86 to x^*/D=6.47, after that, it falls down a little and gets out the field of view. This phenomenon is unusual because the vorticity of a vortex will gradually decrease without any external dynamics, like the trend of vortex F. Although this phenomenon could not be explained here, it may be linked to the temporary dispersion of the vortex E as shown in Figure 6-28d. It can be seen that the vortex E has an obvious dispersion around the position x*/D=3.65, which corresponds to the sharp decrease of the vorticity as shown in Figure 6-31. In the next frame, Figure 6-28 e, the vortex E gathers again. This leads to the obvious increase of the vorticity in Figure 6-31. In Figure 6-32, it can be seen that the speed of vortex E has a sharp increase around the same location. The average convection speed of the two vortices is about 0.6 U.

Table 6-4 Coordinate, vorticity of the vortex core and the acceleration of the riser in figure 6-27

Frame #	Vortex A			Vortex B			Vortex C			Accel.	
	x	y	Vor.	x	y	Vor.	x	y	Vor.	a_x	a_y
105	158. 03	747. 73	−58. 77	273. 16	680. 14	50. 81	399. 18	743. 84	−54. 05	2.58	-2.88
138	155. 69	750. 06	−55. 02	282. 49	669. 26	55. 63	416. 29	747. 73	−39. 47	2.98	-2.93

Re=18800
Mean position of the riser: $\bar{x}$=104 mm, $\bar{y}$=724mm
Displacement of the riser: $d_x/D=0.19$ $d_y/D=-0.22$
Vibration amplitude: $A_x/D=0.31$, $A_y/D=0.24$
Dominant vibration frequency: $f_y=f_y=1.34$ Hz

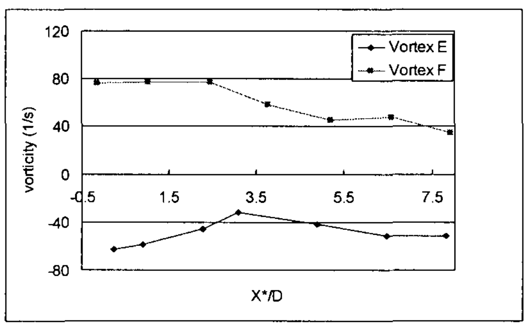

Figure 6-31 Vorticity of the vortices E and F along their position

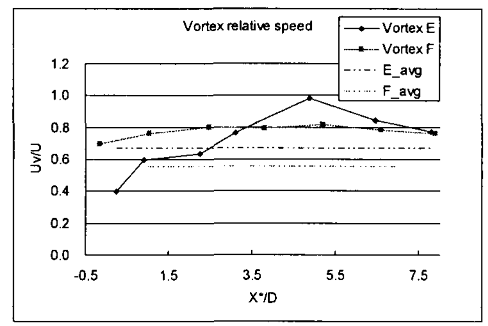

Figure 6-32 Convection speed of the Vortices E and F downstream

Table 6-5 Coordinate, vorticity of the vortex core and acceleration and displacement of the riser in figure 6-28

Frame#	Time	Vortex E			Vortex F			Acceleration		Displacement	
		x	y	Vor.	x	y	Vor.	a_x	a_y	d_x/D	d_y/D
34	43.156	113.687	736.856	-63.12				-2.73	-0.29	-0.28	0.08
35	43.358	145.58	737.63	-57.94				3.36	-3.96	0.38	-0.18
36	43.560	208.59	743.07	-45.43	95.79	689.47	76.29	-1.51	0.11	-0.27	0.14
37	43.762	248.27	729.09	-32.18	151.8	686.36	77.30	1.73	1.83	0.21	0.08
38	43.964	333.06	736.08	-41.50	218.71	681.70	76.59	-0.28	0.84	-0.10	-0.11
39	44.166	406.96	736.08	-51.50	280.94	681.70	58.04	-1.17	-0.78	0.07	-0.22
40	44.368	469.19	734.53	-51.27	347.06	676.26	45.30	2.87	-6.03	0.00	0.03
41	44.570				412.40	680.14	47.35	-2.33	-0.83	-0.05	0.22
42	44.772				473.86	678.59	34.68	1.35	2.81	0.24	-0.09
Mean speed		Vx=0.29m/s, Vy=0.003m/s			Vx=0.31 m/s, Vy=0.008m/s						
Mean position of the riser: $\bar{x}$ = 103mm, $\bar{y}$ =724mm Vibration amplitude: Ax/D=0.31, Ay/D=0.24 Dominant vibration frequency: fx=fy=1.34 Hz											

6.3.2.2 Vortex Pattern '2P'

From the velocity fields discussed above, it can be seen that the '2S' vortex patterns at lower Reynolds number were stable and repeatable, while the vortex pattern at higher Reynolds number and larger amplitude was instable as shown in this section. This phenomena were also found in the simulation results of Evangelinos & Karniadakis (1999). For certain values of the frequency of vibration, f, the Reynolds number, Re and the amplitude to diameter ratio, A/D, another kind of vortex pattern, '2P' mode, i.e. four vortices per cycle, was observed.

Figure 6-33 provides three velocity fields of the formation of a '2P' mode at Re=14100. In Figure 6-33, the amplitude to diameter ratios in the in-line and the cross-flow directions were A_x/D=0.41 and A_y/D=0.95 and the dominant frequencies in both directions were f_x=f_y=0.9 Hz. The displacement and the acceleration at the three moments were different, as shown in the Table 6-6. At this speed, the mean position of the riser was $\bar{x}$=104mm and $\bar{y}$=731mm.

Table 6-6 Displacement and acceleration of the riser at each moment in Figure 6-33

Frame	displacement		Acceleration	
	d_x (mm)	d_y (mm)	a_x(m/s^2)	a_y(m/s^2)
8	-17.4mm	-11.7 mm	1.28	-0.45
25	10.6	8.1	-0.36	-1.04
46	-13.5	-6.2	1.47	-1.62

From Figure 6-33, '2P' patterns are clearly seen downstream near the riser with the vorticity marked by color. Each pair consists of two opposite sign vortices which are close and just shed from the riser. The two vortex pairs are distributed asymmetrically around the riser due to the free vibration in both in-line and cross-flow directions. In Figure 6-33 (a), an anti-clockwise vortex, forming one of a pair of vortices together with the clockwise vortex above it, is shed from the rear side of the riser whose displacement in the in-line and the cross-flow direction at this moment is also shown in the plot of displacement in Figure 6-33 (a). The two vortices of each pair are adjacent. In Figure 6-33 (b), the '2P' pattern looks slightly different from the upper one. The two vortices of each pair are separate, and the anti-clockwise vortex in the downstream pair has almost convected out of the bottom of the field of view. The plot of displacement shows the position of the riser at this moment. Figure 6-33 (c) shows a '2P' pattern whose two clockwise vortices in two vortex pairs are very close. The formation of the '2P' has been demonstrated by Williamson & Roshko (1988): the acceleration of the riser causes a pair of trailing vortices, the two vortices form close to the riser; while earlier shed clockwise vortex is left behind to pair up with an earlier shed anti-clockwise vortex.

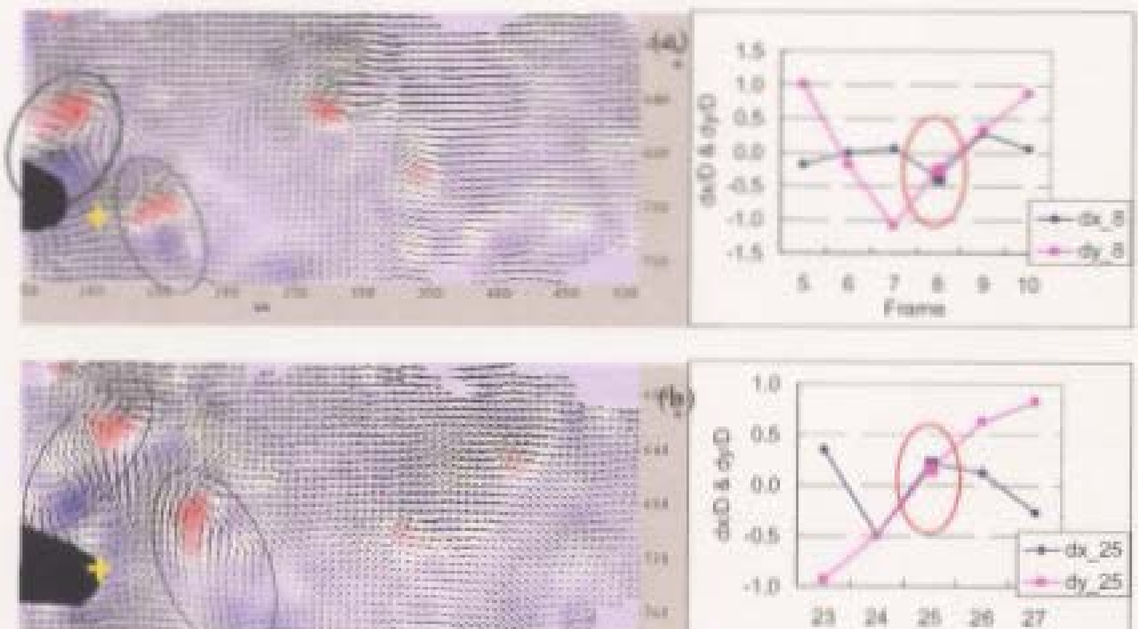

Figure 6-33 Three velocity vector fields showing '2P' pattern with the same Reynolds number, Re=14100. (No 8, No 25 and No 46, 36-03)

It can also be found, from some successive frames, that the '2P' pattern behind the flexible riser presented was very unstable. After shedding from the riser, the vorticity of the vortices decreased quickly downstream, and both lateral and longitudinal distance between vortices increased with the vortices convection downstream. The mode structure changed quickly due to the dispersal of the vortex. Although the reason which causes the pattern to be come unstable has not been completely understood, the phenomenon may be associated with the large amplitude of the riser at this speed, as shown in Figure 6-13. From the amplitude plot in Figure 6-13, the average amplitude at the speed of 0.3 m/s, corresponding to a Reynolds number of 14100, was the highest, i.e. A_x/D=0.41 and A_y/D=0.95, among the amplitudes at all speeds, especially, the amplitude in the cross-flow direction, close to the diameter of the riser. The larger amplitude may also be the reason the vortex mode was asymmetric. At a large amplitude of about A/D=1.0, normal to the flow, Blevins (1977) and Williamson (1988) found asymmetric vortex modes, which were associated with the coalescence of some small vortices into a large structure. From the movie of the velocity field, some vortices merged and some split in the wake of the riser.

With the increase of Reynolds number, other kinds of '2P'structures were observed. Figure 6-34 and Figure 6-35 provides two velocity fields of the formation of a '2P' mode for Re=18800 and Re=23500, respectively. In Figure 6-34, the amplitude to diameter ratios in in-line and cross-flow direction were A_x/D=0.31 and A_y/D=0.24 and the dominant frequencies in both directions were f_x=f_y=1.34 Hz in this speed. The displacements in the in-line and the cross-flow directions at this moment were, d_x/D=-0.14 and d_y/D=0.39, respectively. At this speed, the mean position of the riser was $\bar{x}$=103mm and $\bar{y}$=724mm.

In Figure 6-35, the amplitude to diameter ratios in the in-line and the cross-flow directions at this speed were A_x/D=0.29 and A_y/D=0.33 and the dominant frequencies in both directions were f_x=f_y=1.6 Hz. The displacements in the in-line and the cross-flow directions at this moment were, d_x/D=-0.24 and d_y/D=0.27. At this speed, the mean position of the riser was $\bar{x}$=123 mm, and $\bar{y}$=738 mm. From some successive frames, it can be seen that this type of '2P' vortex mode can keep its structure when convected downstream and the structure of the two vortex pairs was symmetric, unlike the asymmetric '2P' patterns shown in figure 6-33. This vortex mode may correspond to the smaller amplitude of the riser vibration.

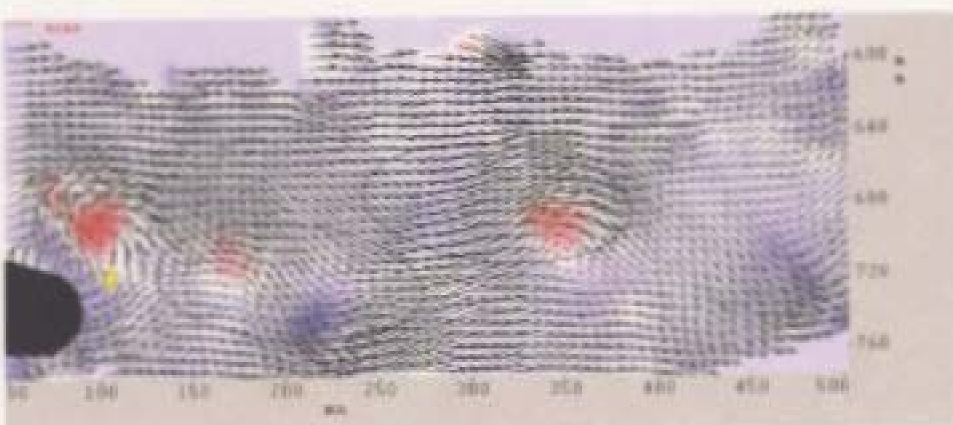

Figure 6-34 Velocity vector field of '2P' pattern for the Reynolds number, Re=18800, the displacement, d_x/D=-0.14 and d_y/D=0.39 (No.95, 46-04)

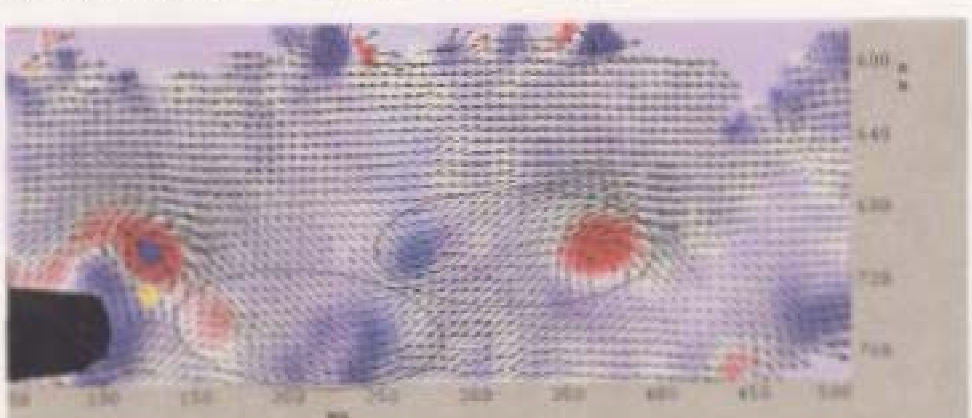

Figure 6-35 Velocity vector fields of '2P' pattern for the Reynolds number, Re=23500 the displacement, d_x/D=-0.24 and d_y/D=0.27 (No.134, 47-05)

Figure 6-36 to Figure 6-39 show the '2P' vortex mode at higher Reynolds numbers, 32900, 37600, 42300 and 47000, respectively. The average amplitudes of the in-line and the cross-flow directions corresponding to these different Reynolds numbers were A_x/D=0.28, 0.25, 0.24, 0.20 and A_y/D=0.43, 0.49, 0.58. 0.38. The first dominant frequencies corresponding to these different Reynolds were f_v/f_n=2.1, 2.42, 2.59 and 3.47. With the increase of the Reynolds number, the lateral distance between wake vortices decreases and the fluctuations in the wake are apparent.

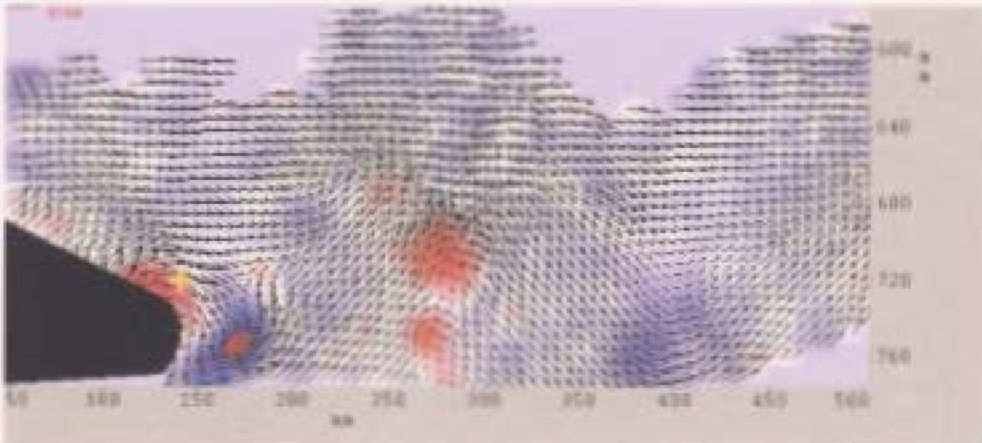

Figure 6-36 Velocity vector fields of '2P' pattern for the Reynolds number, Re=32900 the displacement, d_x/D=-0.25 and d_y/D=-0.05 (No. 40, 49-07)

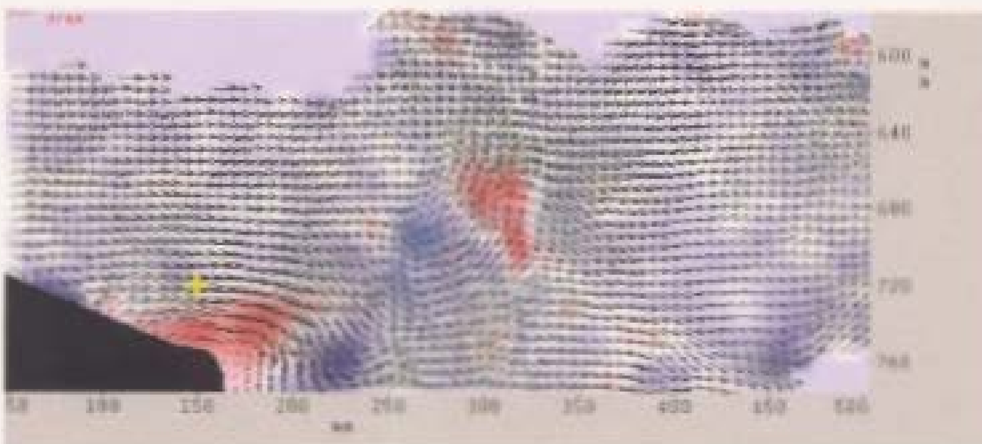

Figure 6-37 Velocity vector fields of '2P' pattern for the Reynolds number, Re=37600 the displacement, d_x/D=0.16 and d_y/D=0.58 (No.104, 50-08)

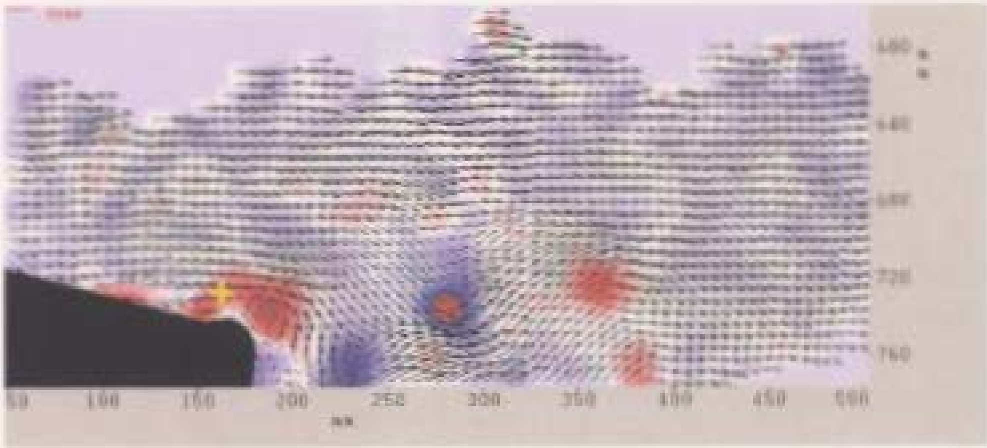

Figure 6-38 Velocity vector fields of '2P' pattern for the Reynolds number, Re=42300, the displacement, d_x/D=-0.02 and d_y/D=0.25 (No.47, 51-09)

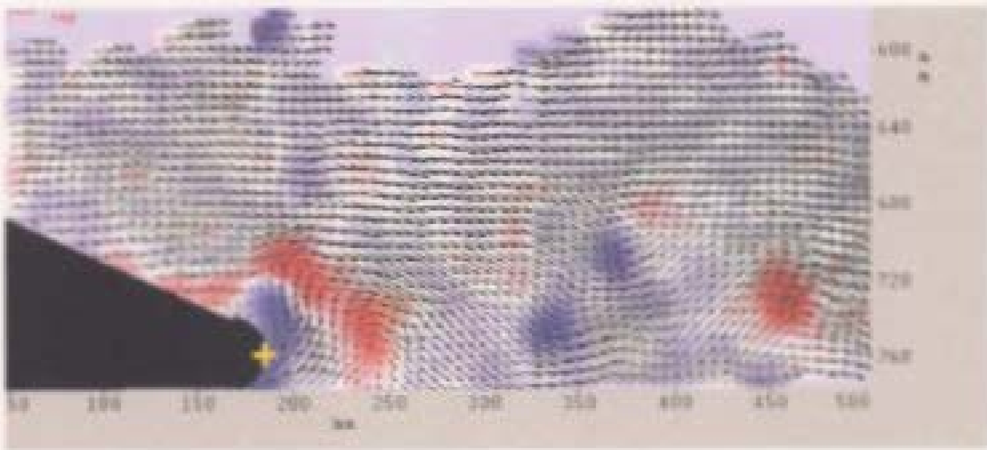

Figure 6-39 Velocity vector fields of '2P' pattern for the Reynolds number, Re=47000 the displacement, d_x/D=0.11 and d_y/D=0.01 (No.92, 43-10)

A vortex pattern 'P+S', a pair and a single vortex shedding in each cycle, was also observed at Reynolds number of 14100, as shown in Figure 6-40. The 'P+S' mode is one type of asymmetric version of the 2P mode. In Figure 6-40, the 'P+S' pattern is shown with a single clockwise vortex and a pair of clockwise and anticlockwise vortices. Similar to the asymmetric '2P' mode, the vortices present in 'P+S' mode diffused very quickly and disappeared or deformed almost immediately after shedding. The amplitude to diameter ratios in in-line and cross-flow direction are A_x/D=0.41 and A_y/D=0.95 and the dominant frequencies in both directions are f_x=f_y=0.9 Hz. The displacement of the cylinder at the moment was d_x/D=-0.49 and d_y/D=-0.86. The mean position of the riser was $\bar{x}$=104mm and $\bar{y}$=731mm. The acceleration of the cylinder at this moment is a_x=0.38 m/s^2 and a_y=3.38 m/s^2.

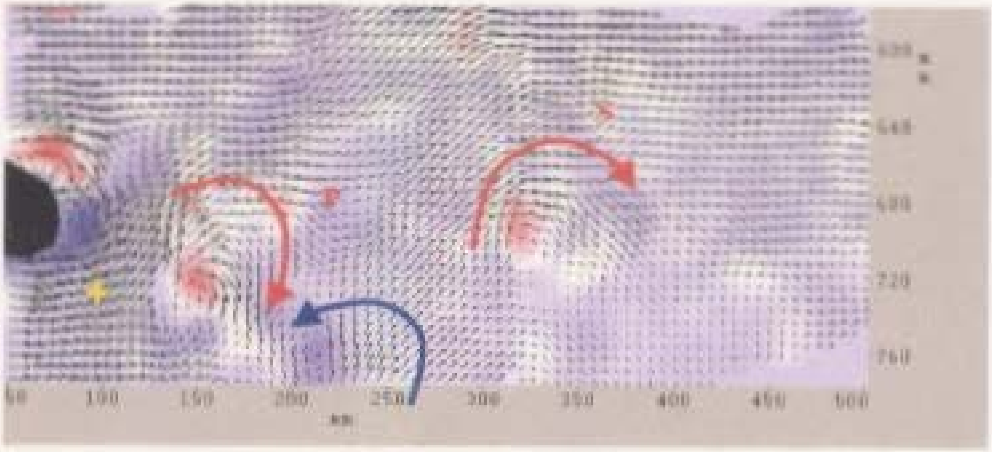

Figure 6-40 Velocity vector fields of 'P+S' pattern for the Reynolds number, Re=14100 the displacement, d_x/D=-0.49 and d_y/D=-0.86 (No.2, 36-03)

6.3.3 Comparison with Regime of Vortex Pattern

By flow visualization of the wake vortex patterns for a rigid cylinder, using controlled vibrations normal to the flow direction, Williamson & Roshko (1988) defined a whole set of different regimes for vortex wake modes in the plane of {λ/D, A/D}, as shown in Figure 2-2, where the wavelength ratio, $\lambda/D=UT/D=U/(fD)$, is the reduced velocity, and T is the vibration period. In their experiments, the rigid cylinder was forced to oscillate at given amplitudes and vibration frequencies, while the flow was relatively fixed with a certain speed U. Although the results from forced vibration may not be expected to be the same as those from free vibration in this set of experiments, these modes from controlled vibration provided a map of regimes within which certain branches of free vibration may also be observed.

The present results are provided with the combinations of A/D and $U/(fD)$ at each speed. Table 6-7 gives the range of the vibration frequencies and the reduced velocity for each speed. Where A^* is the average amplitude to diameter ratio, A/D, as shown in Figure 6-13, f_1-f_4 are the first to the fourth frequency peaks in the cross-flow direction at each speed, as shown in Figure 6-1-Figure 6-9, and U^*_1-U^*_4 are the reduced velocity corresponding to f_1-f_4.

Table 6-7 Amplitude, frequency and reduced velocity for each speed

U (m/s)	A^* A/D	f_1 (Hz)	U_1^* $U/(f_1D)$	f_2 (Hz)	U_2^* $U/(f_2D)$	f_3 (Hz)	U_3^* $U/(f_3D)$	f_4 (Hz)	U_4^* $U/(f_4D)$
0.2	0.64	0.64	6.65	0.61	6.98	1.28	3.32	0.95	4.48
0.3	0.95	0.92	6.94	0.89	7.17	1.83	3.49	2.74	2.33
0.4	0.24	1.34	6.35	1.37	6.21	2.69	3.16	3.27	2.60
0.5	0.33	1.59	6.69	1.62	6.57	3.2	3.32	4.79	2.22
0.6	0.34	1.86	6.86	1.83	6.98	3.72	3.43	5.59	2.28
0.7	0.43	2.11	7.06	2.08	7.16	3.2	4.65	4.79	3.11
0.8	0.49	2.41	7.06	2.44	6.98	2.65	6.42	2.74	6.21
0.9	0.58	2.59	7.39	2.56	7.48	5.16	3.71	7.78	2.46
1.0	0.38	3.45	6.17	3.48	6.11	6.93	3.07	10.38	2.05

Figure 6-43 gives a comparison between the vortex pattern results of the free oscillation riser undergoing multi-modal vibration, obtained from this set of experiments, and the results of the rigid forced vibration cylinder, adapted from the paper of Williamson & Roshko (1988). In Figure 6-43, the solid line gives the boundaries of the transitions between '2S', '2P' and 'P+S' modes obtained by Williamson & Roshko (1988). In Figure 6-43, the symbol '■', '△', '•' and 'o' are the data points in the cross-flow direction obtained in the current experiments. The '■' symbol expresses that the first dominant frequency at each speed is applied in obtaining the reduced velocity; the '△' symbol represented that the second high frequency peaks at each speed is used; the '•' and 'o' symbols indicated that the third and fourth frequencies at each speed are used, respectively.

When the long flexible cylinder was freely vibrating, the vibration frequencies varied with time at the same speed, as shown in Section 6.2.1. The first frequency peak, f_1, for the cross-flow vibration had an apparent dominance in the Power Spectral Density at all speeds, as shown in Figure 6-1 to Figure 6-9; however, it can be seen that those weaker frequency peaks also occurred at the same speed. The vibration frequencies in the time domain can not be determined for the free vibration cylinder because the FFT only provided the frequency distribution in the frequency domain. It means the frequency corresponding to each image moment was unknown.

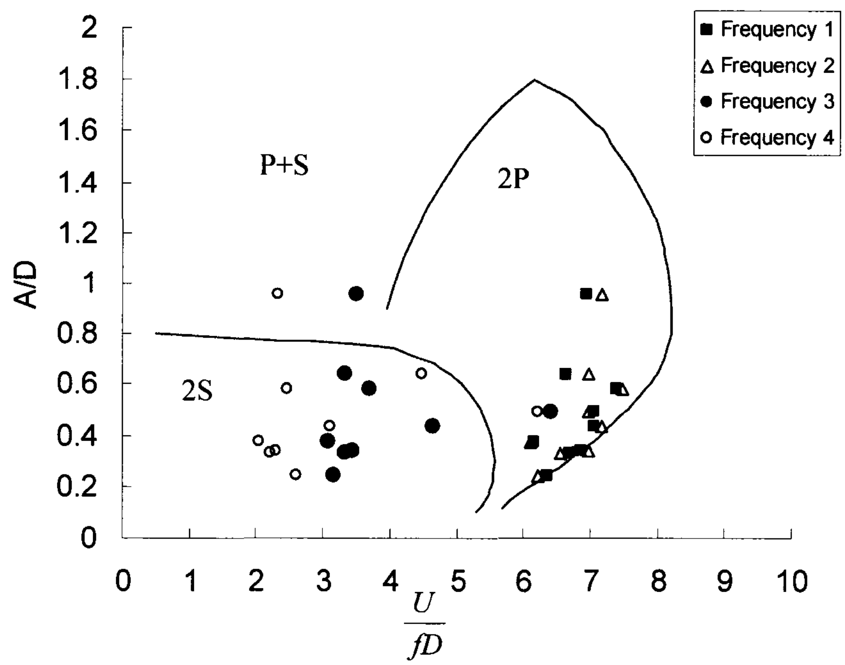

Figure 6-43 Range of reduced velocity versus amplitude to diameter ratio for the VIV wake experiments: ■indicates cross-flow with the first vibration frequency; △ the second vibration frequency; • the third vibration frequency; o the fourth vibration frequency. Lines mark the mode transitions obtained by Williamson & Roshko (1988).

In Figure 6-43, the results for the first and second frequencies, f_1 and f_2, were mainly concentrated between the reduced velocity, U*, of 6 and 8, which was the regime of vortex mode '2P', while for the higher frequencies, the third and fourth dominant frequencies, the results mostly appeared in the regime '2S' and less in the regime 'P+S'. The range of the U_1* and U_2* is the dominant regime because they corresponded to the dominant frequencies.

At the lower speed of 0.2 m/s, Re= 9400, for the average amplitude ratio, A*=0.64, the U_1*and U_2*, are in the region of '2P', while the U_3*and U_4* are in the region of '2S', as shown in Figure 6-43. From the Figure 6-1 (a), it can be seen that the first peak was very strong, while the third and fourth peaks were much weaker than the first one. This means that the first and second frequencies were dominant in the cross-flow direction at this speed. The vortex mode '2P' was the dominant mode in Williamson's vortex map. The present wake field measurement, however, showed different results. Very stable '2S' vortex modes were observed all the time at this speed. From the vortex map shown by the solid line in Figure 6-43, it can be seen that, at the same speed, the lower frequencies are corresponding to the '2P' pattern and the higher frequencies are in the region of '2S'. In Figure 6-43, only the results in the cross-flow direction are shown in order to compare them with the Williamson's vortex map. In fact, the cylinder also freely vibrated in the in-line direction. As shown in Figure 6-1(b), for the PDS in the in-line direction at a speed of 0.2 m/s, except the first peak of 0.64 Hz, the second peak of 1.27 Hz was also strong. The frequency of the second peak is the same as the frequency f_3 in Table 6-7, which is in the region of '2S'. This results indicates that it was the wake vortex mode '2S', not the mode '2P', that induced the vibration of the cylinder in both in-line and cross-flow directions at this speed.

At the speed of 0.3 m/s, Re=14100, for the average amplitude ratio, A*=0.95, the U_1* and U_2* are in the region of '2P', while the U_3*and U_4* are in the region of 'P+S' in Figure 6-43. The wake field measurement showed the same result, i.e. both '2P' and

'P+S' vortex pattern, as shown in the Figure 6-33 and Figure 6-40, were observed at different moments at the same speed,. Although the instantaneous frequency could not be determined as the vibration frequency changed with time, the f_1 and f_2 are obviously dominant at this speed. as shown in Figure 6-2. As a result, the '2P' vortex pattern was dominant at this speed and some images showed the 'P+S' pattern. A few images showed the '2S' vortex patterns at this speed, as showed in Appendix.

At the speed of 0.4 and 0.5 m/s, Re=18800 and Re=23500, for the lower average amplitude ratio, A^*=0.24 and A^*=0.33, the U_1^* and U_2^* fall into the region of '2P', while the U_3^* and U_4^* fall into the region of '2S', in Williamson's vortex map. Both vortex patterns '2S' and '2P', as shown in Figure 27, 28, 34 and 35, were observed in the wake at different moments at the two speeds. The wake field measurement showed that '2S' vortex is the dominant pattern at the two speeds, while the wake vortices in the range of the U_1^* and U_2^* were the '2P' pattern according to Williamson's vortex map. The difference between the present results and Williamson's vortex map is considered to be the effect of the vibration in the in-line direction. The vibration mode for Williamson & Roshko (1988) was constrained only in the cross-flow direction, while the free vibration of the long flexible cylinder in the present study has two degrees of freedom of vibration in both in-line and cross-flow directions. From the Figure 6-3 and Figure 6-4, it is noticed that strong frequency peaks in the in-line direction are at the frequencies of 2.68 Hz and 3.2 Hz, respectively. The reduced velocities for the two frequencies are 3.17 and 3.32, respectively, and correspond to the '2S' vortex pattern in Williamson's vortex map. Ongoren & Rockell (1988b) observed the '2S' and '2P' vortex modes from flow visualization behind a rigid cylinder vibrating in the in-line direction. Moreover, the multi-modal vibration also could affect the wake vortex patterns and lead to the present results being different from that of a forced rigid cylinder, although the response mechanism has not been fully understood.

With the increase of the speed, the vibration frequencies also go up. The U_1* and U_2* fall into the region of '2P', while the U_3* and U_4* fall into the region of '2S' in Figure 6-43. From the wake field results, it can be seen that both vortex modes '2S' and '2P' occurred at different moments. With more velocity fluctuation in the wake and quick diffusion of vortices, and the riser moving to the bottom of the image, the vortex patterns in some frames were not very clearly identified. It can be seen that the percentage of the '2P' vortex patterns increased at the higher speed as shown in Appendix.

Chapter 7 Conclusions and Recommendation

7.1 Conclusions

Since the PIV system was delivered in January 2004, substantial progress has been achieved at Memorial University of Newfoundland in using the PIV system. The PIV measurement techniques, such as 3D calibration, particle selection and seeding methods associated with PIV measurement, have be investigated and applied to sets of flow field measurement experiments. PIV flow field experiments in 2D and 3D have been carried out in small water tanks and two different towing tanks. Both steady and unsteady flow fields have been measured by the system. The results from different sets of experiments showed that the PIV system works well in performing the flow field measurement for different models. These experiments are essential in the development of experimental techniques for PIV measurements in a towing tank.

Vortex-induced vibration responses of a long flexible free vibrating cylinder in both in-line and cross-flow directions, with length to diameter ratio of 181, in a free stream, were investigated at moderate Reynolds numbers in the range of 9400-47000. The DPIV technique was employed to determine the wake velocity field and vorticity field behind a cylinder, simultaneously with acceleration measurement of the cylinder, for the first time, as far as is known, in such a free-vibration study.

VIV responses in both in-line and cross-flow directions at the span location, z/L=0.43, included a combination of frequencies and amplitudes. The VIV responses in both the in-line and cross-flow directions consisted of one or two strong frequency peaks and a few very weak frequency peaks. The vibration frequencies with the highest peak in the in-line and cross-flow directions are the same at the same speeds, except at the speed of

0.4 m/s. In the cross-flow direction, the highest peak at given speed was at the lowest frequency. In the in-line direction, the first and the second frequency peaks were larger than other peaks, and the first frequency peak lay at the lowest frequency at all flow speeds, except the speed of 0.4 m/s. At the same speed, those higher frequencies with lower peaks were usually the second and the third harmonics of the first frequency. With the increase of the flow speed, frequencies became higher in both in-line and cross-flow directions. The vibration frequencies of the cylinder were in a range of 0.64 Hz to 10.38 Hz over the range of the speeds. The average amplitude did not obviously increase with an increase of Reynolds number; however, there was an obvious amplitude peak at the speed of 0.3 m/s. The average amplitude to diameter ratios in the in-line and the cross-flow directions covered a range 0.10-0.41 and 0.24-0.95, respectively. Vibration amplitudes in the cross-flow direction were larger than those in the in-line direction, especially at lower speeds.

Instantaneous wake fields were obtained using MUN's DPIV system. The measurement results revealed that, within the range of Reynolds numbers, the vibration frequencies and amplitude to diameter ratios of the cylinder tested, as discussed above, three vortex modes '2S', '2P' and 'P+S' were formed in the near wake of the cylinder. At the lower Reynolds number, *Re*=9400 or the speed of 0.2 m/s, and with lower response frequencies from 0.61 Hz to 1.28 Hz, only '2S' vortex modes were observed in the experiments, and the '2S' vortex modes presented were stable in the wake at different moments of the same speed. At a higher Reynolds number, at *Re*=14100, or the speed of 0.3 m/s, and with frequencies from 0.95 Hz to 2.74 Hz, two vortex modes, '2P' and 'P+S', were observed in the near wake at different moments. The '2P' mode was dominant in the wake and occurred very close to the cylinder with the large average amplitude to diameter ratio of 0.95. Vortex modes '2S' and '2P' were observed at different moments when the Reynolds number further increased, to Re=18800 and 23500 or the speed of 0.4 m/s and 0.5 m/s, and with frequencies from 1.34 Hz to 4.79 Hz. The vortex pattern '2S' played a dominant role in the wake at the two speeds. At higher Reynolds number, Re>23500, and with frequencies from 1.86 Hz to 10.38 Hz, '2S' and '2P' vortex mode were also observed at different moments and the vortex patterns presented were unstable due to velocity fluctuation and quick diffusion of vortices in the wake. The percentage of the vortex pattern '2P' increases with the increase of the Reynolds numbers. The results also showed that the vortex modes '2S' and '2P' were repeatable with the similar vibration responses of displacements and accelerations. The analysis from the vorticity fields of the wake shows the period of vortex shedding and the location of the vortex in the near wake, at the same Reynolds number, was fixed relative to the vibration accelerations.

The ranges of the reduced velocity and the average amplitude to diameter ratio for the VIV response of forced vibration of a rigid cylinder, covered the regions of the '2S', '2P' and 'P+S' modes, as defined by Williamson & Roshko (1988). The results of the present study agreed partially with their results. The three kinds of vortex patterns, '2S', '2P' and 'P+S', were observed in the wake of the long flexible cylinder. In the '2P' vortex pattern region in Williamson & Roshko (1988), in addition to the '2P' vortex pattern, the '2S' pattern also was observed in the present study. The differences may arise from the different vibration modes, one degree of freedom vibration in the cross-flow direction in their experiments but two degrees of freedoms of vibration in both in-line and cross-flow direction in the present experiments. The vibration in the in-line direction may be the main reason which leads to the different vortex modes in the present free vibration experiments.

7.2 Recommendation

There are always some lessons to be learnt after an experiment. Some recommendations are made in order to improve the next round of testing. Recommendations include the following:

In these experiments, a large range of carriage speeds was covered and the riser was long, flexible and freely vibrating. The initial shifts of the cylinder, caused by the drag of water, changed with the carriage speeds and covered a large range from -0.36D to 1.32D in the cross-flow direction and from 0.82D to 3.53D in the in-line direction. This meant that the average position of the cylinder in the images varied significantly at different speeds. At relatively lower speeds, the cylinder average position was around the vertical center of the images, while at relatively higher speed, the cylinder moved up towards the top of the images. This led to a problem that only part of the interesting wake region was captured due to constriction of the field of view, therefore, it has brought some difficulties to the analysis of the wake vortex patterns because vortex patterns are not always symmetric. In the future experiments, an approach should be taken to make sure that the cylinder is always close to the vertical center in the field of view.

A flow field measurement of a uniform flow without a model may be useful to confirm the measurement results by comparing them with the known free stream. The results can also be used to check the effect of seeding conditions. In the future PIV experiments, it is recommended that the flow field measurement without a model should be carried out during the experiments, with the PIV system and the seeding rake set up in-situ.

In this set of experiments, the vibration frequency and amplitude of the long flexible cylinder varied with time and could not be exactly associated with each image moment. Hence, the corresponding relationship between the vibration responses and the wake vortex patterns of the cylinder cannot be fully determined from the present work. The wake vortex patterns have been proved to vary as a function of the amplitudes and frequencies by several previous investigations at lower Reynolds numbers. It is necessary that the experiments for forced vibration of a rigid cylinder with a large diameter are conducted to further understand the relationship between the vibration responses and the wake vortex patterns at higher Reynolds numbers.

References

Adrian, R. J. 1991, Particle Imaging Techniques for Experimental Fluid Mechanics, *Annual Review of Fluid Mechanics*, Vol.23, pp.261-304,

Adrian, R.J. 1986a, Image shifting technique to resolve directional ambiguity in double-pulsed velocimetry, *Applied Optics* 23, 1690-1691

Adrian, R.J. 1986b, Multi-point optical measurements of simultaneous vectors in unsteady flow---a review, *International Journal of Heat Fluid Flow* 7, 127-45

Adrian, R.J. & Yao, C.S. 1985, Pulsed laser technique application to liquid and gaseous flows and the scattering power of seed material, *Applied Optics* 24:44-52

Adrian, R. J. 1984, Scattering Particle characteristics and their effect on pulse laser measurements of fluid flow: speckle velocimetry vs. particle image velocimetry, *Applied Optics* 23 1690

Adrian, R.J. 1983, Laser velocimetry In Goldstein, R.J., editor, *Fluid Mechanics Measurement*, Springer, Berlin.

Allen, D.W & Henning, D.L. 2001, Prototype vortex-induce vibration tests for production risers, Offshore Technology Conference, Houston, Texas, 30 April-3 May 2001.

Allan, R.G.. & Molyneux, W. D., Escort Tug Design Alternatives and a Comparison of Their Hydrodynamic Performance, Paper A11, Maritime Technology Conference and Expo, S.N.A.M.E. Washington, D. C. September 30th to October 1st, 2004.

Bearman, P.M. 1984, Vortex shedding from oscillating bluff bodies, *Annual Review of Fluid Mechanics*. 16:195-222

Bishop R.E.D. & Hassan A.Y. 1964, The lift and drag forces on a circular cylinder oscillating in a flowing fluid, Proceedings of the Royal Society, London Series A 277:51-57

Blevins, R.D. 1990, *Flow-Induce Vibrations*. New York: Van Nostrand Reinhold

Brika, D. & Laneville, A. 1993, Vortex-induced vibrations of a long flexible circular cylinder, *Journal of Fluid Mechanics*, 250, 481-508

Brika, D. & Laneville, A. 1995, An experimental study of the aeolian vibrations of a flexible circular cylinder at different incidences. *Journal of Fluids Structures* 9:271-91

Chakrabarti, S.K. 1987, *Hydrodynamics of offshore structures*, Computational Mechanics Publications and Springer-Verlag

Chen, S.S. 1987, *Flow-induced vibration of circular cylinder structures*, Hemosphere Publishing Corporation, Springer, Washington, DC, USA

DiMarco, S. F., Reid, R. O., Jochens, A. E., Nowlin, W. D. J. & Howard, M. K. 2001 General Characteristics of Current in the Deepwater Gulf of Mexico, The Proceedings of Offshore Technology Conference, Vol. 1, Houston, U.S.A, pp..513-525

Ding, Z.J., Balasubramanian, S., Lokken, R.T. & Yung, T-W. ExxonMobil Upstream Research Company, 2004, Lift and Damping Characteristics of Bare and Straked Cylinders at Riser Scale Reynolds Numbers, OTC 16341

Davis, J. T., Hover, F. S. Landolt, A & Triantafyllou, M.S. 2000, Vortex induced vibrations of rigid and flexible cylinders. Proceedings of Workshop on Vortex-Induced Vibrations of Offshore Structures.

Dong, R., Chu, S. & Kaze, J. 1992, Quantitative Visualization of the flow within the volute of a Centrifugal Pump, Part A: Technique, *Journal of Fluids Engineering*, Vol.114, 390-395,

Dong, R. R., Katz, J. & Huang, T. T. 1997, On the structure of bow waves on a ship model, *Journal of Fluid Mechanics* Vol. 346, pp.77-115

Evangelinos, C. & Karniadakis, G. E, 1999, Dynamics and flow structures in the turbulent wake of rigid and flexible cylinders subject to vortex-induced vibrations, *Journal of Fluid Mechanics* Vol. 400, 91-124

Erf, R. K. 1980, application of laser speckle to measurement, *laser Applied* 4:1-69

Feng, C.C. 1968, The measurements of vortex-induced effects in flow past a stationary and oscillating circular and D-section cylinders, Master's thesis, University of British Columbia

Ferguson, N. 1965, The measurement of wake and surface effects in the subcritical flow past a circular cylinder at rest and in vortex-excited oscillation, MASc thesis, University of British Columbia

Fingerson, L.M. & Freymuth, P., 1983, Thermal anemometers, In Goldstein, R.J., editor, *Fluid Mechanics Measurement*, Springer, Berlin.

Gharib, M.R., Leonard, A., Gharib, M. & Roshko, A. 1998, The absence of lock-in and the role of mass ratio, In Paper Proceedings Conference on Bluff Body Wakes and Vortex-induced Vibrations, Washington, DC, 21-23 June 1998

Goldstein, R. J. 1983, Optical Systems for Flow Measurement: Shadowgraph, Schlieren, and Interferometric Techniques, *Fluid Mechanics Measurements*, Goldstein, R. J., Ed., Hemisphere, Washington, D. C. pp. 377-422.

Govardhan, R., & Williamson, C.H.K., 2000, Modes of vortex formation and frequency response of a freely vibrating cylinder, *Journal of Fluid Mechanics* 420, 85-130

Griffin, O.M. 1971, The unsteady wake of an oscillating cylinder at low Reynolds number, *Journal of Applied Mechanics*, 38, 729-738.

Griffin, O.M. & Ramberg, S.E. 1974, The vortex-street Wakes of Vibrating Cylinders, *Journal of Fluid Mechanics* 66, 553-576

Griffin, O.M. & Ramberg, S.E. 1976, Vortex shedding from a cylinder vibrating in line with an incident uniform flow, *Journal of Fluid Mechanics* 66:553-76

Griffin, O.M. & Ramberg, S.E. 1982, Some recent studies of vortex shedding with application to marine tubulars and risers, ASME Journal of Energy Resource Technology. 104, 2-13

Gu, W, Chyu, C. & Rockwell, D, 1994, Timing of Vortex formation from an oscillating cylinder, *Physics Fluids* 6 (11)

Hover, F. S. , Techet, A. H.& Triantafyllou, M. S. 1998, Forces on Oscillating uniform and taped cylinders in crossflow. J. Fluid Mech. 363, 97-114

Khalak, A. & Williamson, C.H.K. 1999, Motions, forces and mode transitions in vortex-induced vibrations at low mass-damping, *Journal of Fluid and Structures* 13, 813-851.

Khalak, A. & Williamson, C.H.K. 1997b, Fluid forces and dynamics of a hydroelastic structure with very low mass and damping, *Journal of Fluid and Structures* 11, 973-982

Krishnamoorthy S., Price S. J. & Paidoussis M. P. 2001, Cross-flow past an oscillating circular cylinder: Synchronization phenomena in the near wake, *Journal of Fluid and Structures* 15, 955-980

Kompenhans, J. & Reichmuth, J. 1987, Two-dimensional flow field measurements in wind tunnels by means of particle image velocimetry, In Proceedings of International Conference of Applied Lasers and Electro-Optics, San Diego, USA

Koopmann, G.H. 1967, the vortex wakes of vibrating cylinders at low Reynolds Numbers, *Journal of Fluid Mechanics* 51, 31-48

Landreth,C.C. and Adrian, R.J. 1988, Electrooptical image shifting for particle image velocimetry, *Applied Optics* 27, 4216 4220
LaVision Inc., *DaVis Flowmaster Software Manual for DaVis 6.2*, August 2002

Lewis, E. V. Editor, 1988, *Principles of naval architecture*. Volume Ⅱ Resistance, Propulsion and Vibration, SNAME

Lighthill, J. 1986, Fundamentals concerning wave loading on offshore structures, *Journal of Fluid Mechanics* 173: 667-81

Lourenco, L. M., Krothapalli, A., Buchlin, J. M. & Riethmuller, M. L. 1986, Noninvasive Experimental technique for the measurement of unsteady velocity fields, *AIAA Journal* 24, 1715-1717

Li, X., Bose, N., Zhu, L. & Spencer, D. 2005, Multi-modal Vortex-induce Vibration tests on a Flexible Model Riser, International symposium on technology of Ultra Deep Ocean Engineering 2005, Tokyo, Japan, 1st- 2nd February 2005

Lienhard, J. H., 1966, Synopsis of Lift, Drag and Vortex Frequency Data for Rigid Circular Cylinders, Washington State University, College of Engineering, Research Division Bulletin 300.

Lin, J.-C., & Rockwell, D. 1996, Force identification by vorticity fields: techniques based on flow imaging. *Journal of Fluids Structures*. 10:663-68

Marris, A.W. 1964, A review of vortex streets, periodic wakes and induced vibration phenomena, Transaction of the ASME: *Journal of Basic Engineering*. 86, 185-194

Moe, G. & Wu, Z.J. 1990, The lift force on a cylinder vibrating in a current, *ASME Journal of Offshore Mechanics Arctic Engineering* 112:297-303

Molyneux, W. D. & Xu, J. 2005a, Report on Preliminary Particle Image Velocimetry experiments, NRC-IOT, TR-2005-02, February 2005.

Molyneux, W. D. & Xu, J. 2005b, Report on Particle Image Velocimetry experiments to measure flow around an escort Tug, NRC-IOT, TR-2005-10, August 2005

Newman, D & Karniadakis, G. E. 1996, Simulations of flow over a flexible cable: A comparison of forced and flow-induced vibration, *Journal of Fluid Structures* 10,439-453

Olsen, M. G. & Adrian, R. J. 2000, Brownian motion and correlation in particle image velocimetry, *Optics & Laser Technology*, Volume 32, Issues 7-8, Pages 621-627

Ongoren, A. & Rockwell, D. 1988a, Flow structure from an oscillating cylinder, Part 1: Mechanisms of phase shift and recovery in the near wake. *Journal of Fluid Mechanics* 191:197-223

Ongoren, A. & Rockwell, D. 1988b, Flow structure from an oscillating cylinder, Part 2: Mode competition in the near wake, *Journal of Fluid Mechanics* 191:225-245

Panton, R. L. 1996, *Incompressible Flow*, New York: John Wiley & Sons, INC.

Paone, N., Riethmuller, M. L. & Van den Braembussche, R. A. 1989, Experimental investigation of the flow in the vaneless diffuser of a centrifugal pump by particle image displacement velocimetry, *Experimental Fluids* 7:371-78

Parkinson, G. 1989, Phenomena and modeling of flow-induced vibrations of bluff bodies, Progress in Aerospace Sciences. 26, 169-224

Press, W. H., Teukolsky, S. A., Vetterling, W. T. & Flannery, B. P. 1986, *Numerical Recipes*, Cambridge University Press

Price, S.J., Smith, J. G., Leong, K. & Paidoussis, M. P. 2000, Flow visualization around a circular cylinder near to a plane wall, Flow induced vibration, Proceedings of the 7th International Conference on Flow-Induced Vibration-FIV2000 /Lucerne / Switzerland/19-22 June 2000

Robinson, N. J. 2002, Faroes Gap to Offshore West Africa: Challenges for drilling risers in two radically different deepwater exploration areas, EnergyWise Workshop: Signposting deepwater technology requirements for Atlantic Canada, St. John's, Canada.

Roshko, A., 1961, Experiments on the flow past a cylinder at Very High Reynolds number, *Journal of Fluid Mechanics* 10, 345-356

Sarpkaya, T. 1995, Hydrodynamic damping, flow-induced oscillations, and biharmonic response. ASME Journal of Offshore Mechanics and Arctic Engineering 117, 232-238

Sarpkaya, T. 2004, A critical review of the intrinsic nature of Vortex-induced vibrations , *Journal of Fluid and Structures* 19 389-447

Sheridan, J., Carberry, J. Lin J.C. & Rockwell, D. 1998, On the near wake topology of an oscillating cylinder, *Journal of Fluid and Structures*, 12:215-220

Smits, A. J. & Lim, T. T. 2000, *Flow visualization*, Techniques and Examples, London: Imperial College Press

Sumer, B. M. & Fredsoze, J. 1997, *Hydrodynamics around Cylindrical Structures*, Singapore: World Scientific.

Techet, A. H., Hover, F. S. & Triantafyllou, M. S. 1998, Vortical patterns behind a tapered cylinder oscillating transversely to a uniform flow, *Journal of Fluid Mechanics* 363, 79-96

Toebea, G.H., 1968, The unsteady flow and wake near an oscillating cylinder, *Journal of Basic Engineering*, Trans. ASME. Series D, Vol. 91, pp.493-505.

Triantafyllou, M. S., Techet, A. H., Hover, F. S. & Yue, D.K.P., 2003, VIV of slender structures in shear flow, Presented at IUTAM Symposium on Flow-Structure Interactions, June 2003, Rutgers State University, USA.

Unal, M.F., Lin, J.-C. & Rockwell, D. 1997, Force Prediction by PIV imaging: A momentum-based approach, *Journal of Fluid Structures* 11, 965-971

Vandiver, J.K. & Marcollo, H. 2003, High mode number VIV experiments. IUTAM Symposium On Integrated Modeling of Fully Coupled Fluid-Structure Interactions Using Analysis, Computations, and Experiments, 1-6 June 2003, Kluwer Academic Publishers, Dordrecht.

Wernet, M.P. 1999, Fuzzy Logic Enhanced Digital PIV Processing Software, 18th International Congress on Instrumentation for use in Aerospace Simulation facilities (ICIASF), Toulouse, France, June 1999

Willamson, C.H.K. & Roshko, A., 1988, Vortex formation in the wake of an oscillating cylinder, *Journal of Fluids and Structures* 2, 355-381.

Williamson, C.H.K. & Govardhan, R. 2004, Vortex-Induced Vibrations Annual Review of Fluid Mechanics, 36:413-55

Willert, C. E. & Gharib, M. 1991, Digital particle image velocimetry. *Experiments Fluids* 10, 181-193.

Willis, N.R.T. & Thethi, K.S. 2H Offshore Engineering Ltd. 1999, Stride JIP: Steel Risers in Deepwater Environments-Prograss Summary, OTC 10974

Xu, J. Molyneux, W.D. and Bose, N. 2005 A Versatile Particle Image Velocimetry System for Flow Measurements in Water Tanks, 7th Canidian Marine Hydromechanics and Structures Conference, Halifax, Canada, 21-22 September 2005

Appendix

Data for velocity field and vorticity field

A list of velocity fields and vorticity fields is provided in Table A-1. All plots of velocity fields and vorticity fields are collected in the WORD file in an additional CD disk. The name of the file is expressed by the speed, i.e. 02, 03, 04, 05, 06, 07, 08, 09 and 10.doc. The plot number provides the number for all plots of the velocity fields and vorticity fields at different moments which images were taken. At each speed, 150 images were taken at different moments. A total of 1350 wake fields were obtained in the experiments, which are numbered from Figure A-1 to Figure A-1350. In Table A-1, the mean position and average vibration amplitude of the riser at each speed also are given.

The position, displacement and acceleration of the riser for each moment of the image taken are provided at a carriage speed of 0.2 m/s in Table A-2. In Table A-2, the time expresses the relative time in seconds for each image recorded, x and y are the coordinates of the riser in each image. The empty cells in the table mean that the riser did not appear in the images. The symbols d_x and d_y are the displacements of the riser relative to the mean position in motion in the in-line and cross-flow directions, a_x and a_y are the acceleration of the riser in the in-line and cross-flow directions, V is the carriage speed for each run. In the last column, the type of the vortex mode in the wake field is provided. In Table A-2 to A-9 is the information of the riser at the speeds of 0.3 m/s to 1.0 m/s. Table A-10 provides the list of the plots of velocity fields and vorticity fields.

Table A-1 Description of the file of the plots of velocity and vorticity fields in the CD disk

File name	Plot number	Speed m/s	Mean position of the riser		Average amplitude	
			x (mm)	y (mm)	A_x (mm)	A_y (mm)
02.doc	A1 to A150	0.2	56	682	4.77	29.98
03.doc	A151 to A300	0.3	104	731	19.21	44.82
04.doc	A301 to A450	0.4	103	724	14.39	11.42
05.doc	A451 to A600	0.5	123	738	13.75	15.54
06.doc	A601 to A750	0.6	140	750	14.72	15.95
07.doc	A751 to A900	0.7	155	753	13.29	20.26
08.doc	A901 to A1050	0.8	167	751	11.62	23.20
09.doc	A1051 to A1200	0.9	180	757	11.46	27.23
10.doc	A1201 to A1350	1.0	184	761	9.58	17.73

Table A-2 VIV responses of the riser and the wake vortex mode for each plot of velocity and vorticity fields at a speed of 0.2 m/s

Serial number	Plot number	time s	x mm	y mm	d_x mm	d_y mm	a_x m/s^2	a_y m/s^2	V m/s	Vortex mode
1	A1	24.311					0.917	0.224	0.2	2S
2	A2	24.513	50	694	-6.23	11.92	0.761	-0.209	0.2	2S
3	A 3	24.715	61	693	4.77	10.92	-0.573	0.218	0.2	2S
4	A 4	24.917	60	696	3.77	13.92	-0.849	0.179	0.2	2S
5	A 5	25.119	50	702	-6.23	19.92	0.430	-1.540	0.2	2S
6	A 6	25.321	52	675	-4.23	-7.08	0.368	-0.588	0.2	2S
7	A 7	25.523	56	646	-0.23	-36.08	-1.968	1.656	0.2	2S
8	A 8	25.725					0.846	0.554	0.2	2S
9	A 9	25.927					0.647	-0.268	0.2	2S
10	A1 0	26.129	58	696	1.77	13.92	0.227	0.102	0.2	2S
11	A11	26.331	61	696	4.77	13.92	-1.288	0.979	0.2	2S
12	A12	26.533	58	702	1.77	19.92	-0.463	0.011	0.2	2S
13	A13	26.735					0.472	-1.210	0.2	2S
14	A14	26.937	57	661	0.77	-21.08	-1.075	0.106	0.2	2S
15	A15	27.139	52	648	-4.23	-34.08	-1.024	1.071	0.2	2S
16	A16	27.341					0.952	0.066	0.2	2S
17	A17	27.543					0.258	-0.381	0.2	2S
18	A18	27.745	58	693	1.77	10.92	-0.612	0.110	0.2	2S
19	A19	27.947	60	695	3.77	12.92	-0.843	0.592	0.2	2S
20	A20	28.149	54	704	-2.23	21.92	0.516	-0.688	0.2	2S
21	A21	28.351					0.581	-1.462	0.2	2S
22	A22	28.553	57	660	0.77	-22.08	-0.524	1.051	0.2	2S
23	A23	28.755					-1.164	1.895	0.2	2S
24	A24	28.957					0.766	0.190	0.2	2S
25	A25	29.159					0.110	-0.193	0.2	2S
26	A26	29.361	60	695	3.77	12.92	-0.231	0.497	0.2	2S
27	A27	29.563	60	696	3.77	13.92	0.535	0.717	0.2	2S

28	A28	29.765	50	700	-6.23	17.92	0.365	-0.810	0.2	2S
29	A29	29.968					0.524	-0.141	0.2	2S
30	A30	30.170	58	651	1.77	-31.08	-1.978	0.887	0.2	2S
31	A31	30.372					-1.331	0.590	0.2	2S
32	A32	30.574					0.301	0.053	0.2	2S
33	A33	30.776					-0.184	-1.578	0.2	2S
34	A34	30.978	57	689	0.77	6.92	-0.496	0.361	0.2	2S
35	A35	31.180	56	694	-0.23	11.92	-0.005	-0.340	0.2	2S
36	A36	31.382					0.320	-1.332	0.2	2S
37	A37	31.584					0.567	0.278	0.2	2S
38	A38	31.786	57	647	0.77	-35.08	-2.010	1.267	0.2	2S
39	A39	31.988					0.081	0.423	0.2	2S
40	A40	32.190					0.563	0.012	0.2	2S
41	A41	32.392					0.291	-0.716	0.2	2S
42	A42	32.594	59	693	2.77	10.92	-0.456	0.513	0.2	2S
43	A43	32.796	58	697	1.77	14.92	-0.080	-0.335	0.2	2S
44	A44	32.998					0.855	-1.555	0.2	2S
45	A45	33.200	50	671	-6.23	-11.08	0.523	-0.185	0.2	2S
46	A46	33.402	57	647	0.77	-35.08	-1.814	1.912	0.2	2S
47	A47	33.604					0.317	1.265	0.2	2S
48	A48	33.806					0.250	-1.002	0.2	2S
49	A49	34.008	55	693	-1.23	10.92	-0.773	-0.737	0.2	2S
50	A50	34.210	60	694	3.77	11.92	-0.419	0.488	0.2	2S
51	A51	34.412	58	702	1.77	19.92	0.254	-0.647	0.2	2S
52	A52	34.614					0.723	-0.185	0.2	2S
53	A53	34.816	55	666	-1.23	-16.08	-1.329	0.723	0.2	2S
54	A54	35.018	54	648	-2.23	-34.08	-0.950	1.022	0.2	2S
55	A55	35.220					-0.033	0.320	0.2	2S
56	A56	35.422					0.172	-1.189	0.2	2S
57	A57	35.624	59	692	2.77	9.92	0.034	-0.276	0.2	2S
58	A58	35.826	62	696	5.77	13.92	-0.577	-0.137	0.2	2S
59	A59	36.028	56	704	-0.23	21.92	-0.207	-0.474	0.2	2S
60	A60	36.230					1.395	-1.453	0.2	2S
61	A61	36.432	59	660	2.77	-22.08	-1.327	0.915	0.2	2S
62	A62	36.634					-0.344	0.483	0.2	2S
63	A63	36.836					1.211	-0.241	0.2	2S
64	A64	37.038					-0.513	-0.911	0.2	2S
65	A65	37.240	60	695	3.77	12.92	-0.699	-0.831	0.2	2S
66	A66	37.442	60	698	3.77	15.92	-0.462	0.099	0.2	2S
67	A67	37.644	52	703	-4.23	20.92	-0.002	-0.163	0.2	2S
68	A68	37.846					1.280	-0.646	0.2	2S
69	A69	38.048	62	651	5.77	-31.08	-1.370	0.482	0.2	2S
70	A70	38.250					-0.195	0.428	0.2	2S
71	A71	38.452					0.174	-1.056	0.2	2S
72	A72	38.654					-0.398	-0.763	0.2	2S
73	A73	38.856	59	690	2.77	7.92	-0.769	-0.426	0.2	2S
74	A74	39.058	57	695	0.77	12.92	0.452	0.086	0.2	2S

75	A75	39.260					0.825	-0.983	0.2	2S
76	A76	39.462					0.839	0.051	0.2	2S
77	A77	39.664	57	649	0.77	-33.08	-1.671	1.413	0.2	2S
78	A78	39.866					0.240	1.093	0.2	2S
79	A79	40.068					0.329	-0.652	0.2	2S
80	A80	40.270	53	693	-3.23	10.92	-0.499	0.080	0.2	2S
81	A81	40.472	58	694	1.77	11.92	-0.362	-0.877	0.2	2S
82	A82	40.674	56	700	-0.23	17.92	-0.345	0.394	0.2	2S
83	A83	40.876					0.863	-0.964	0.2	2S
84	A84	41.078					-0.375	0.996	0.2	2S
85	A85	41.280	55	647	-1.23	-35.08	-1.143	0.643	0.2	2S
86	A86	41.482					0.571	0.559	0.2	2S
87	A87	41.684					0.096	-1.228	0.2	2S
88	A88	41.886	54	691	-2.23	8.92	-1.069	0.549	0.2	2S
89	A89	42.088	58	691	1.77	8.92	-0.683	0.426	0.2	2S
90	A90	42.290	55	698	-1.23	15.92	0.043	0.404	0.2	2S
91	A91	42.492					0.545	-1.348	0.2	2S
92	A92	42.695	52	662	-4.23	-20.08	0.165	1.142	0.2	2S
93	A93	42.897	52	648	-4.23	-34.08	-1.109	0.352	0.2	2S
94	A94	43.099					0.122	0.709	0.2	2S
95	A95	43.301					0.066	-0.700	0.2	2S
96	A96	43.503	56	695	-0.23	12.92	-0.285	-0.749	0.2	2S
97	A97	43.705	59	693	2.77	10.92	-0.387	0.094	0.2	2S
98	A98	43.907	53	699	-3.23	16.92	-0.055	-1.306	0.2	2S
99	A99	44.109					0.066	-0.700	0.2	2S
100	A100	44.311	55	658	-1.23	-24.08	-0.835	1.213	0.2	2S
101	A101	44.513					-0.880	0.617	0.2	2S
102	A102	44.715					1.447	-0.354	0.2	2S
103	A103	44.917					0.137	-0.986	0.2	2S
104	A104	45.119	58	693	1.77	10.92	-0.276	-0.069	0.2	2S
105	A105	45.321	60	695	3.77	12.92	-0.498	0.213	0.2	2S
106	A106	45.523	53	702	-3.23	19.92	-0.018	-1.375	0.2	2S
107	A107	45.725					0.401	-0.924	0.2	2S
108	A108	45.927	60	653	3.77	-29.08	-1.203	1.787	0.2	2S
109	A109	46.129					-0.711	1.086	0.2	2S
110	A110	46.331					1.179	0.198	0.2	2S
111	A111	46.533					-0.878	0.795	0.2	2S
112	A112	46.735	58	690	1.77	7.92	-0.351	-0.064	0.2	2S
113	A113	46.937	59	695	2.77	12.92	-0.553	-1.108	0.2	2S
114	A114	47.139	51	701	-5.23	18.92	-0.220	-1.508	0.2	2S
115	A115	47.341					0.642	-0.682	0.2	2S
116	A116	47.543	60	648	3.77	-34.08	-1.512	1.084	0.2	2S
117	A117	47.745					-0.108	1.280	0.2	2S
118	A118	47.947					1.243	-0.621	0.2	2S
119	A119	48.149					-0.504	-0.275	0.2	2S
120	A120	48.351	57	691	0.77	8.92	-0.618	-0.378	0.2	2S
121	A121	48.553	57	693	0.77	10.92	-1.483	0.468	0.2	2S

122	A122	48.755					0.242	-1.593	0.2	2S
123	A123	48.957					0.185	-0.243	0.2	2S
124	A124	49.159	56	646	-0.23	-36.08	-1.098	1.165	0.2	2S
125	A125	49.361					0.137	1.803	0.2	2S
126	A126	49.563					0.985	-0.270	0.2	2S
127	A127	49.765	51	690	-5.23	7.92	-0.570	0.455	0.2	2S
128	A128	49.967	56	690	-0.23	7.92	-0.306	0.547	0.2	2S
129	A129	50.169	55	693	-1.23	10.92	-0.288	-0.971	0.2	2S
130	A130	50.371	56	646	-0.23	-36.08	-0.051	-1.040	0.2	2S
131	A131	50.573					0.186	-0.154	0.2	2S
132	A132	50.775					-0.959	0.342	0.2	2S
133	A133	50.977					0.312	0.910	0.2	2S
134	A134	51.179					0.795	-0.456	0.2	2S
135	A135	51.381					-0.427	-0.103	0.2	2S
136	A136	51.583	57	690	0.77	7.92	-0.498	0.213	0.2	2S
137	A137	51.785	55	694	-1.23	11.92	-0.252	-1.040	0.2	2S
138	A138	51.987					-0.022	-1.641	0.2	2S
139	A139	52.189					-0.489	0.849	0.2	2S
140	A140	52.391	53	646	-3.23	-36.08	-0.792	0.648	0.2	2S
141	A141	52.593					0.957	0.480	0.2	2S
142	A142	52.795					0.342	0.338	0.2	2S
143	A143	52.997	51	689	-5.23	6.92	-0.758	0.387	0.2	2S
144	A144	53.199	55	688	-1.23	5.92	-0.697	-0.653	0.2	2S
145	A145	53.401	54	694	-2.23	11.92	-0.171	-0.632	0.2	2S
146	A146	53.603					-0.332	-1.434	0.2	2S
147	A147	53.805					-0.190	0.739	0.2	2S
148	A148	54.007	51	647	-5.23	-35.08	-0.997	0.322	0.2	2S
149	A149	54.209					0.126	0.990	0.2	2S
150	A150	54.411					0.147	-0.218	0.2	2S

Table A-3 VIV responses of the riser and the wake vortex mode for each plot of velocity and vorticity fields at a speed of 0.3 m/s

Serial number	Plot number	time s	x mm	y mm	d_x mm	d_y mm	a_x m/s^2	a_y m/s^2	V m/s	Vortex mode
1	A151	34.736	128	693	23.39	-37.71	-2.926	1.132	0.3	Unknown
2	A152	34.938	81	690	-23.22	-40.43	0.383	3.383	0.3	P+S
3	A153	35.140	100	735	-4.19	3.85	0.539	-1.821	0.3	Unknown
4	A154	35.342	120	749	16.01	17.83	-1.391	1.704	0.3	P+S
5	A155	35.544	95	778	-8.85	46.97	1.211	-3.001	0.3	2P
6	A156	35.746	104	722	-0.30	-8.58	0.625	1.805	0.3	2S
7	A157	35.948	107	679	2.42	-52.09	-1.121	2.299	0.3	Unknown
8	A158	36.150	87	719	-17.40	-11.69	1.283	-0.453	0.3	2P
9	A159	36.352	117	746	13.29	15.50	-1.105	0.648	0.3	P+S
10	A160	36.554	107	771	2.42	40.37	0.517	-0.673	0.3	Unknown
11	A161	36.756	93	751	-11.57	20.55	2.693	-0.709	0.3	Unknown
12	A162	36.958	127	693	22.61	-38.10	-3.242	0.837	0.3	Unknown

13	A163	37.160	83	697	-21.28	-33.44	2.176	2.738	0.3	2P
14	A164	37.362	110	736	5.52	5.02	0.400	-0.953	0.3	2P
15	A165	37.564	117	754	13.29	22.88	-0.786	1.121	0.3	Unknown
16	A166	37.766	93	778	-11.57	47.36	2.283	-3.387	0.3	Unknown
17	A167	37.968	117	714	13.29	-16.35	-1.437	1.093	0.3	Unknown
18	A168	38.170	98	684	-6.13	-47.04	-0.871	4.131	0.3	Unknown
19	A169	38.372	95	731	-9.63	-0.03	1.266	-1.754	0.3	2P
20	A170	38.574	123	747	18.73	16.28	-1.637	1.093	0.3	Unknown
21	A171	38.776	101	778	-3.02	47.75	0.773	-2.111	0.3	Unknown
22	A172	38.978	100	737	-3.80	6.18	0.968	1.263	0.3	2S
23	A173	39.180	121	687	16.40	-43.93	-1.720	0.507	0.3	Unknown
24	A174	39.382	81	708	-22.83	-22.95	2.291	0.111	0.3	2P
25	A175	39.584	115	739	10.57	8.12	-0.364	-1.040	0.3	2P
26	A176	39.786	110	761	5.91	29.88	0.406	-0.495	0.3	2P
27	A177	39.988	92	770	-12.35	38.81	2.823	-3.211	0.3	Unknown
28	A178	40.190	119	706	14.85	-24.51	-3.053	0.039	0.3	Unknown
29	A179	40.392	88	684	-16.23	-46.65	0.550	4.688	0.3	Unknown
30	A180	40.594	102	732	-2.64	1.52	0.899	-1.107	0.3	Unknown
31	A181	40.796	118	750	14.07	19.00	-1.494	2.459	0.3	P+S
32	A182	40.998	98	779	-6.13	48.52	2.174	-3.047	0.3	2P
33	A183	41.200	104	725	-0.30	-5.47	-0.665	1.756	0.3	Unknown
34	A184	41.402	112	683	7.47	-47.81	-1.240	1.827	0.3	2P
35	A185	41.604	85	717	-18.95	-13.63	2.069	-1.560	0.3	P+S
36	A186	41.806	113	742	9.02	11.62	-0.733	-0.510	0.3	P+S
37	A187	42.008	111	768	7.08	36.87	0.586	-1.077	0.3	P+S
38	A188	42.210	88	757	-16.23	25.99	3.449	-1.258	0.3	Unknown
39	A189	42.412	128	696	23.39	-34.61	-2.912	-0.696	0.3	Unknown
40	A190	42.614	85	691	-19.34	-40.05	1.868	3.078	0.3	Unknown
41	A191	42.816	105	737	0.86	6.18	-0.362	-0.847	0.3	Unknown
42	A192	43.018	116	751	12.13	20.55	-1.632	1.492	0.3	Unknown
43	A193	43.220	95	778	-9.63	46.97	1.967	-3.594	0.3	Unknown
44	A194	43.422	109	719	4.75	-11.30	-0.863	1.933	0.3	Unknown
45	A195	43.625	103	679	-1.47	-51.70	-1.476	3.804	0.3	Unknown
46	A196	43.827	91	724	-13.51	-6.25	1.468	-1.621	0.3	2P
47	A197	44.029	124	745	19.51	14.34	-1.482	0.527	0.3	2P
48	A198	44.231	102	776	-1.86	45.80	1.614	-1.897	0.3	2P
49	A199	44.433	93	749	-10.79	18.61	2.387	1.688	0.3	Unknown
50	A200	44.635	123	691	18.34	-40.05	-2.865	0.048	0.3	Unknown
51	A201	44.837	79	698	-25.17	-32.66	1.927	1.846	0.3	Unknown
52	A202	45.039	110	738	5.91	6.96	0.165	-1.750	0.3	Unknown
53	A203	45.241	118	756	14.07	25.60	-1.250	1.058	0.3	P+S
54	A204	45.443	93	780	-11.18	49.69	2.647	-4.183	0.3	2P
55	A205	45.645	117	716	12.52	-14.41	-0.978	1.741	0.3	Unknown
56	A206	45.847	97	687	-7.30	-43.93	0.389	3.842	0.3	Unknown
57	A207	46.049	97	733	-6.91	2.69	1.158	-1.414	0.3	2P

58	A208	46.251	117	752	13.29	20.94	-1.632	1.492	0.3	P+S
59	A209	46.453	101	778	-3.02	47.75	1.060	-3.123	0.3	2P
60	A210	46.655	101	732	-3.41	1.52	0.176	1.926	0.3	Unknown
61	A211	46.857	119	685	14.46	-45.87	-2.771	1.477	0.3	Unknown
62	A212	47.059	80	707	-23.83	-23.34	1.867	0.215	0.3	2P
63	A213	47.261	113	740	8.63	9.29	-0.213	-0.991	0.3	2P
64	A214	47.463	113	760	9.02	29.49	0.263	0.048	0.3	2P
65	A215	47.665	89	768	-15.45	36.87	3.206	-2.602	0.3	Unknown
66	A216	47.867	122	702	17.57	-28.39	-3.133	0.629	0.3	Unknown
67	A217	48.069	86	686	-18.56	-44.32	0.928	3.885	0.3	2P
68	A218	48.271	101	735	-3.41	4.10	0.130	-1.548	0.3	2P
69	A219	48.473	120	753	15.62	22.11	-1.145	0.496	0.3	2P
70	A220	48.675	97	777	-7.69	46.19	2.170	-3.357	0.3	Unknown
71	A221	48.877	110	719	5.52	-11.30	-0.809	2.225	0.3	Unknown
72	A222	49.079	110	684	6.30	-47.04	-0.916	0.790	0.3	Unknown
73	A223	49.281	78	711	-25.94	-19.46	1.909	0.545	0.3	2P
74	A224	49.483	115	741	10.96	10.07	-1.050	-0.850	0.3	2P
75	A225	49.685	106	758	1.64	27.16	0.531	0.421	0.3	2P
76	A226	49.887	90	770	-14.29	38.81	2.884	-4.251	0.3	Unknown
77	A227	50.089	119	699	14.46	-31.89	-3.002	1.005	0.3	Unknown
78	A228	50.291	86	686	-18.56	-44.32	0.261	2.689	0.3	Unknown
79	A229	50.493	91	732	-12.74	1.52	0.970	-1.378	0.3	Unknown
80	A230	50.695	119	750	14.46	19.78	-0.957	0.460	0.3	Unknown
81	A231	50.897	102	774	-2.25	43.47	1.968	-3.506	0.3	2S
82	A232	51.099	103	725	-1.08	-5.47	0.405	2.235	0.3	2S
83	A233	51.301	117	681	12.90	-49.37	-2.114	1.948	0.3	Unknown
84	A234	51.503	79	708	-25.55	-22.95	2.250	-0.189	0.3	2P
85	A235	51.705	119	734	14.46	3.07	-1.796	0.468	0.3	2P
86	A236	51.907	109	762	4.75	31.04	0.685	-0.278	0.3	P+S
87	A237	52.109	91	770	-13.51	39.59	2.584	-3.276	0.3	P+S
88	A238	52.311	121	705	16.40	-25.67	-2.438	1.076	0.3	Unknown
89	A239	52.513	88	691	-15.84	-39.66	-0.070	4.192	0.3	Unknown
90	A240	52.715	104	736	-0.30	5.79	0.129	-1.592	0.3	P+S
91	A241	52.917	121	758	16.40	27.55	-1.291	0.817	0.3	P+S
92	A242	53.119	96	775	-8.46	44.64	2.464	-3.881	0.3	Unknown
93	A243	53.321	113	726	8.63	-4.80	-0.780	1.609	0.3	Unknown
94	A244	53.523	109	682	4.75	-48.59	-0.869	1.445	0.3	Unknown
95	A245	53.725	85	720	-18.95	-10.91	1.615	-1.809	0.3	2P
96	A246	53.927	119	738	14.46	7.74	-0.719	0.525	0.3	2P
97	A247	54.129	106	766	1.64	35.70	0.906	-0.560	0.3	Unknown
98	A248	54.331	88	759	-16.23	28.32	2.568	-1.714	0.3	Unknown
99	A249	54.533	119	693	14.85	-37.33	-3.913	2.194	0.3	Unknown
100	A250	54.735	81	693	-23.61	-37.33	0.767	3.083	0.3	Unknown
101	A251	54.937	106	737	2.03	6.57	0.209	-1.228	0.3	Unknown
102	A252	55.139	121	760	16.40	29.49	-1.119	-0.431	0.3	Unknown
103	A253	55.341	92	769	-11.96	38.03	3.427	-2.929	0.3	2P

104	A254	55.543	123	703	18.73	-27.23	-1.477	0.896	0.3	2P
105	A255	55.745	96	678	-8.07	-52.86	-0.528	3.589	0.3	Unknown
106	A256	55.947	92	723	-12.35	-7.80	1.304	-1.690	0.3	2P
107	A257	56.149	119	736	14.85	5.40	-1.364	0.955	0.3	2P
108	A258	56.352	100	769	-4.19	38.42	1.428	-1.773	0.3	2P
109	A259	56.554	93	751	-10.79	20.17	1.475	-1.074	0.3	Unknown
110	A260	56.756	117	686	12.52	-44.71	-3.447	2.390	0.3	2P
111	A261	56.958	79	702	-25.17	-28.78	2.642	1.100	0.3	2P
112	A262	57.160	111	740	7.08	9.68	0.032	-0.394	0.3	2P
113	A263	57.362	117	764	13.29	32.98	-0.027	0.794	0.3	2P
114	A264	57.564	92	766	-11.96	35.70	3.502	-2.978	0.3	P+S
115	A265	57.766	126	698	22.23	-32.28	-2.450	0.218	0.3	2P
116	A266	57.968	91	683	-13.51	-47.81	0.106	2.345	0.3	Unknown
117	A267	58.170	94	728	-10.02	-2.75	0.698	-2.062	0.3	P+S
118	A268	58.372	119	744	14.85	13.17	-0.262	1.040	0.3	P+S
119	A269	58.574	101	773	-3.02	42.31	1.457	-2.434	0.3	P+S
120	A270	58.776	95	740	-8.85	8.90	1.947	0.565	0.3	P+S
121	A271	58.978	117	683	13.29	-47.81	-3.661	3.219	0.3	2P
122	A272	59.180	86	714	-18.56	-17.13	2.124	-1.194	0.3	Unknown
123	A273	59.382	117	743	12.52	12.40	-0.653	-0.205	0.3	2P
124	A274	59.584	107	769	3.19	38.03	0.749	-1.052	0.3	Unknown
125	A275	59.786	92	756	-11.96	25.22	2.674	-2.158	0.3	Unknown
126	A276	59.988	127	695	23.00	-35.38	-3.107	-0.253	0.3	Unknown
127	A277	60.190	85	688	-19.34	-42.38	1.221	3.331	0.3	Unknown
128	A278	60.392	102	734	-2.64	3.01	0.666	-1.682	0.3	2P
129	A279	60.594	120	745	16.01	14.34	-1.126	1.885	0.3	Unknown
130	A280	60.796	96	780	-8.07	48.91	1.713	-2.918	0.3	Unknown
131	A281	60.998	107	724	3.19	-6.25	-0.219	1.414	0.3	Unknown
132	A282	61.200	107	684	2.80	-47.04	-1.582	2.413	0.3	P+S
133	A283	61.402	88	725	-16.62	-5.86	1.623	-1.217	0.3	P+S
134	A284	61.604	123	745	18.34	14.34	-1.716	0.817	0.3	P+S
135	A285	61.806	105	777	1.25	46.58	1.866	-2.707	0.3	P+S
136	A286	62.008	98	747	-6.52	16.28	1.983	0.407	0.3	2P
137	A287	62.210	125	693	21.06	-37.71	-1.919	-0.315	0.3	Unknown
138	A288	62.412	80	698	-24.00	-32.66	1.631	2.193	0.3	Unknown
139	A289	62.614	112	739	7.47	8.51	-0.443	-1.300	0.3	2P
140	A290	62.816	118	757	14.07	26.77	-1.249	1.147	0.3	Unknown
141	A291	63.018	93	777	-11.57	46.19	2.278	-3.757	0.3	Unknown
142	A292	63.220	117	716	12.90	-15.18	-1.680	0.704	0.3	Unknown
143	A293	63.422	96	684	-8.46	-47.04	-0.179	4.400	0.3	P+S
144	A294	63.624	95	731	-9.24	0.74	1.303	-1.779	0.3	2P
145	A295	63.826	121	750	16.40	19.39	-0.833	0.422	0.3	2P
146	A296	64.028	100	777	-3.80	46.58	1.421	-2.276	0.3	P+S
147	A297	64.230	102	732	-1.86	1.13	0.427	1.072	0.3	Unknown
148	A298	64.432	117	686	12.90	-45.09	-2.435	1.297	0.3	Unknown
149	A299	64.634	81	709	-23.22	-21.40	1.601	-0.025	0.3	Unknown

150	A300	64.836	117	739	12.90	8.51	-1.200	-0.840	0.3	Unknown
2S: 4 frames; 2P: 41 frames; P+S: 24 frames										

Table A-4 VIV responses of the riser and the wake vortex mode for each plot of velocity and vorticity fields at a speed of 0.4 m/s

Serial number	Plot number	Time s	x mm	y mm	d_x mm	d_y mm	a_x m/s^2	a_y m/s^2	V m/s	Vortex mode
1	A301	36.489	98	736	-4.759	11.60	-0.466	0.699	0.4	2S
2	A302	36.691	106	739	3.403	14.70	0.438	0.006	0.4	2S
3	A303	36.893	94	727	-9.027	3.05	-0.096	-2.516	0.4	2P
4	A304	37.095	106	731	3.399	7.32	-0.610	-0.667	0.4	2S
5	A305	37.297	106	714	3.010	-10.55	-0.352	3.665	0.4	2S
6	A306	37.499	96	712	-7.090	-12.49	-1.195	0.455	0.4	2S
7	A307	37.701	108	727	4.952	2.66	3.794	-2.651	0.4	2S
8	A308	37.903	94	738	-8.643	13.93	-3.606	0.781	0.4	2S
9	A309	38.105	121	715	18.160	-9.38	4.485	-2.427	0.4	2S
10	A310	38.307	89	723	-14.082	-1.22	-1.961	0.235	0.4	2S
11	A311	38.509	113	726	10.002	2.27	2.949	2.506	0.4	2S
12	A312	38.711	91	725	-12.139	1.11	-1.252	-1.014	0.4	2S
13	A313	38.913	118	719	15.052	-5.50	1.042	-0.681	0.4	2S
14	A314	39.115	91	728	-11.363	3.83	-0.820	-2.346	0.4	2S
15	A315	39.317	108	725	4.953	1.10	0.280	-0.575	0.4	2P
16	A316	39.519	100	716	-3.207	-8.62	0.406	3.249	0.4	2S
17	A317	39.721	104	710	0.683	-13.66	-1.128	-0.098	0.4	2P
18	A318	39.923	103	728	-0.097	4.21	3.883	-5.395	0.4	2S
19	A319	40.125	97	740	-5.537	15.87	-3.684	0.565	0.4	2S
20	A320	40.327	119	720	16.603	-3.95	3.650	0.636	0.4	2S
21	A321	40.529	90	717	-13.307	-7.05	-2.073	1.264	0.4	2S
22	A322	40.731	112	723	9.614	-1.23	1.861	3.515	0.4	2S
23	A323	40.933	91	727	-12.137	3.05	-3.390	-0.855	0.4	2S
24	A324	41.135	118	716	15.443	-7.83	2.851	-2.067	0.4	2S
25	A325	41.337	93	727	-10.197	3.05	-1.616	0.781	0.4	2S
26	A326	41.539	111	728	8.060	4.22	0.781	0.403	0.4	2S
27	A327	41.741	100	719	-2.982	-4.72	0.500	1.873	0.4	2S
28	A328	41.943	107	715	4.564	-8.99	-0.849	1.089	0.4	2S
29	A329	42.146	102	726	-0.874	1.88	1.857	-5.266	0.4	2S
30	A330	42.348	97	729	-5.924	5.38	-2.966	-0.004	0.4	2S
31	A331	42.550	115	711	11.944	-13.27	1.784	3.328	0.4	2S
32	A332	42.752	90	716	-12.528	-7.83	-2.412	1.177	0.4	2S
33	A333	42.954	112	727	9.614	2.66	3.058	2.254	0.4	2S
34	A334	43.156	90	728	-13.307	3.82	-2.732	-0.295	0.4	2S
35	A335	43.358	121	716	17.771	-8.60	3.364	-3.960	0.4	2S
36	A336	43.560	90	731	-12.916	6.55	-1.513	0.115	0.4	2S
37	A337	43.762	113	728	10.002	3.83	1.726	1.831	0.4	2S

38	A338	43.964	98	719	-4.759	-5.11	-0.277	0.841	0.4	2S
39	A339	44.166	106	714	3.399	-10.55	-1.174	-0.782	0.4	2S
40	A340	44.368	103	726	-0.098	1.50	2.873	-6.033	0.4	2S
41	A341	44.570	100	735	-2.428	10.43	-2.326	-0.834	0.4	2S
42	A342	44.772	114	720	11.168	-4.33	1.351	2.812	0.4	2S
43	A343	44.974	91	718	-11.362	-5.89	-1.987	1.162	0.4	2P
44	A344	45.176	111	725	8.448	0.72	2.061	1.607	0.4	2S
45	A345	45.378	91	732	-11.362	8.10	-3.044	-0.265	0.4	2P
46	A346	45.580	123	718	20.490	-5.89	4.363	-3.121	0.4	2S
47	A347	45.782	88	725	-14.859	1.11	-2.192	0.747	0.4	2S
48	A348	45.984	111	725	8.448	0.72	0.121	2.529	0.4	2S
49	A349	46.186	95	716	-7.478	-8.60	-0.955	1.562	0.4	2S
50	A350	46.388	107	712	4.175	-12.49	-1.084	0.380	0.4	2S
51	A351	46.590	101	734	-2.040	9.65	1.800	-3.916	0.4	2S
52	A352	46.792	102	735	-0.486	10.82	-2.169	-0.312	0.4	2S
53	A353	46.994	114	718	10.779	-6.27	0.824	3.655	0.4	2S
54	A354	47.196	93	723	-10.197	-0.84	-1.192	0.676	0.4	2S
55	A355	47.398	110	731	7.283	7.32	4.361	-0.479	0.4	2S
56	A356	47.600	92	725	-10.586	0.72	-3.997	-0.405	0.4	2S
57	A357	47.802	120	714	16.994	-10.55	4.559	-2.476	0.4	2S
58	A358	48.004	88	731	-14.858	6.55	-1.932	-0.381	0.4	2S
59	A359	48.206	116	729	13.498	5.38	1.454	2.102	0.4	2S
60	A360	48.408	91	721	-11.362	-2.78	-1.035	1.213	0.4	2P
61	A361	48.610	113	714	10.002	-10.55	0.680	-1.572	0.4	2P
62	A362	48.812	94	733	-8.643	8.88	1.456	-3.462	0.4	2S
63	A363	49.014	108	733	4.952	8.49	-1.805	0.683	0.4	2S
64	A364	49.216	106	719	3.399	-4.72	1.767	2.116	0.4	2S
65	A365	49.418	95	717	-7.867	-6.66	-1.397	0.365	0.4	2S
66	A366	49.620	110	728	6.895	4.22	2.875	-0.219	0.4	2S
67	A367	49.822	92	728	-10.586	4.22	-3.493	-0.100	0.4	2S
68	A368	50.024	118	714	15.441	-9.77	4.382	-4.550	0.4	2S
69	A369	50.226	88	733	-14.912	8.88	-2.283	-0.415	0.4	2P
70	A370	50.428	116	731	13.110	7.32	2.393	1.192	0.4	2P
71	A371	50.630	91	721	-11.362	-3.55	-1.287	-0.767	0.4	2S
72	A372	50.832	114	714	11.556	-10.16	2.041	0.070	0.4	2S
73	A373	51.034	92	733	-10.586	8.88	-0.799	-0.765	0.4	2S
74	A374	51.236	109	730	5.729	5.77	0.108	-1.280	0.4	2S
75	A375	51.438	103	717	0.291	-7.44	-0.104	2.501	0.4	2P
76	A376	51.640	97	717	-5.924	-7.44	-1.887	0.186	0.4	2S
77	A377	51.842	108	732	4.952	7.71	2.736	-2.214	0.4	2S
78	A378	52.044	96	734	-7.089	10.04	-2.689	0.124	0.4	2S
79	A379	52.246	118	713	15.441	-10.94	5.054	-2.940	0.4	2S
80	A380	52.448	86	725	-16.412	1.11	-1.554	-0.171	0.4	2S
81	A381	52.650	116	725	13.498	1.11	3.030	2.959	0.4	2S
82	A382	52.852	90	712	-12.917	-11.65	-2.612	0.267	0.4	2S
83	A383	53.054	109	717	6.506	-7.44	1.603	-0.861	0.4	2S
84	A384	53.256	94	738	-9.032	14.32	-0.776	-1.869	0.4	2S
85	A385	53.458	110	733	6.895	8.49	0.959	-1.252	0.4	2S

86	A386	53.660	104	712	1.456	-11.71	0.162	2.785	0.4	2P
87	A387	53.862	97	715	-5.924	-8.99	-1.093	-0.344	0.4	2S
88	A388	54.064	108	733	5.341	8.88	3.602	-2.971	0.4	2S
89	A389	54.266	95	732	-7.478	8.10	-3.433	1.575	0.4	2S
90	A390	54.468	118	717	15.441	-7.05	4.017	-0.892	0.4	2S
91	A391	54.670	86	731	-17.189	6.93	-1.760	-1.584	0.4	2S
92	A392	54.873	117	725	14.275	1.11	2.018	3.992	0.4	2S
93	A393	55.075	91	712	-11.362	-11.71	-1.585	0.297	0.4	2S
94	A394	55.277	107	714	4.563	-10.16	1.891	-2.694	0.4	2S
95	A395	55.479	96	742	-6.701	18.20	-0.380	-1.312	0.4	2P
96	A396	55.681	110	739	6.895	15.09	1.309	-0.352	0.4	2S
97	A397	55.883	104	714	1.456	-10.16	1.003	2.030	0.4	2P
98	A398	56.085	97	718	-6.317	-6.28	-0.999	1.099	0.4	2S
99	A399	56.287	102	738	-0.486	14.32	2.472	-2.306	0.4	2S
100	A400	56.489	98	733	-4.370	8.88	-4.633	0.706	0.4	2S
101	A401	56.691	115	719	11.944	-5.11	3.007	-1.575	0.4	2S
102	A402	56.893	87	729	-16.024	4.99	-3.159	-0.427	0.4	2S
103	A403	57.095	118	725	15.052	1.11	1.480	4.038	0.4	2S
104	A404	57.297	90	720	-13.307	-3.94	-1.800	1.082	0.4	2S
105	A405	57.499	112	714	8.837	-10.16	2.577	-2.883	0.4	2S
106	A406	57.701	93	737	-9.809	12.76	0.188	-1.841	0.4	2S
107	A407	57.903	112	736	8.837	11.60	0.391	-0.694	0.4	2S
108	A408	58.105	103	721	-0.098	-3.17	0.537	1.804	0.4	2S
109	A409	58.307	98	716	-4.759	-7.83	-0.505	0.591	0.4	2S
110	A410	58.509	105	728	2.622	4.22	2.552	-1.912	0.4	2S
111	A411	58.711	98	731	-4.701	6.55	-2.581	-0.261	0.4	2S
112	A412	58.913	117	718	13.887	-6.27	3.159	0.412	0.4	2S
113	A413	59.115	88	727	-15.247	3.05	-2.830	1.725	0.4	2S
114	A414	59.317	116	726	12.721	1.88	1.755	4.033	0.4	2S
115	A415	59.519	91	718	-12.139	-6.45	-1.870	1.457	0.4	2S
116	A416	59.721	114	709	11.168	-15.60	2.914	-2.929	0.4	2S
117	A417	59.923	92	734	-10.974	9.65	-1.905	-1.160	0.4	2S
118	A418	60.125	114	734	10.779	10.04	0.584	-0.330	0.4	2S
119	A419	60.327	100	718	-2.428	-6.27	-0.607	2.388	0.4	2S
120	A420	60.529	99	720	-3.593	-3.94	-1.089	0.011	0.4	2S
121	A421	60.731	105	728	2.622	3.83	2.920	-2.471	0.4	2S
122	A422	60.933	97	724	-5.924	-0.45	-2.856	-0.212	0.4	2S
123	A423	61.135	116	710	12.721	-14.43	3.382	0.219	0.4	2P
124	A424	61.337	86	726	-16.412	1.50	-3.062	1.238	0.4	2P
125	A425	61.539	118	729	15.052	4.99	1.162	2.699	0.4	2P
126	A426	61.741	90	720	-12.528	-4.01	-2.602	1.021	0.4	2P
127	A427	61.943	113	713	10.391	-10.94	2.432	-2.518	0.4	2S
128	A428	62.145	92	733	-10.974	8.49	-1.558	-0.437	0.4	2S
129	A429	62.347	112	729	9.225	4.99	0.989	0.951	0.4	2P
130	A430	62.549	102	715	-0.874	-9.38	0.031	1.367	0.4	2P
131	A431	62.751	96	719	-6.701	-5.50	-1.613	1.047	0.4	2S
132	A432	62.953	108	729	4.952	4.60	2.926	-2.072	0.4	2S

133	A433	63.155	95	731	-8.255	7.32	-2.783	-0.350	0.4	2S
134	A434	63.357	116	715	13.498	-9.38	3.297	-0.456	0.4	2P
135	A435	63.559	88	732	-14.858	7.71	-2.861	-0.581	0.4	2S
136	A436	63.761	118	731	15.441	6.93	1.691	2.987	0.4	2S
137	A437	63.963	91	718	-11.751	-6.27	-2.300	1.103	0.4	2S
138	A438	64.165	112	714	8.837	-10.16	2.989	-2.935	0.4	2P
139	A439	64.367	93	737	-9.809	12.76	-0.954	-1.168	0.4	2S
140	A440	64.569	111	734	8.060	9.65	1.421	-0.382	0.4	2S
141	A441	64.771	104	717	1.456	-6.66	0.229	1.234	0.4	2S
142	A442	64.973	95	722	-7.866	-2.39	-1.808	0.491	0.4	2S
143	A443	65.175	109	733	6.506	8.49	2.771	-2.372	0.4	2S
144	A444	65.377	95	728	-7.866	3.83	-2.693	-0.231	0.4	2S
145	A445	65.579	117	713	13.887	-10.94	3.317	-1.782	0.4	2S
146	A446	65.781	86	731	-17.189	7.32	-2.497	0.414	0.4	2P
147	A447	65.983	119	732	16.606	8.10	2.240	3.755	0.4	2S
148	A448	66.185	91	718	-11.751	-6.27	-2.166	-0.076	0.4	2S
149	A449	66.387	110	713	7.671	-11.32	2.734	-2.391	0.4	2S
150	A450	66.589	93	729	-9.809	4.99	-1.428	-2.029	0.4	2S
2S:128 frames; 2P: 22 frames										

Table A-5 VIV responses of the riser and the wake vortex mode for each plot of velocity and vorticity fields at a speed of 0.5 m/s

Serial number	Plot number	time s	x mm	y mm	d_x mm	d_y mm	a_x m/s^2	a_y m/s^2	V m/s	Vortex mode
1	A451	40.051	112	750	-11.44	12.55	5.220	-5.497	0.5	2P
2	A452	40.253	124	747	0.99	9.05	1.174	-5.839	0.5	2P
3	A453	40.455	137	721	14.20	-16.59	-5.377	1.217	0.5	2S
4	A454	40.657	110	748	-12.99	9.83	3.732	-5.414	0.5	2S
5	A455	40.859	131	750	7.60	11.77	-1.662	-3.589	0.5	2S
6	A456	41.061	132	720	8.76	-17.75	-2.543	-1.137	0.5	2S
7	A457	41.263	109	745	-13.77	7.50	2.884	-3.341	0.5	2S
8	A458	41.465	133	752	10.32	14.10	-2.679	-2.910	0.5	2S
9	A459	41.667	128	724	4.88	-13.48	0.463	-1.919	0.5	2S
10	A460	41.869	110	745	-12.99	7.50	3.838	-1.204	0.5	2S
11	A461	42.071	135	749	11.48	10.99	-1.774	-0.695	0.5	2S
12	A462	42.273	126	725	3.32	-13.09	1.203	-0.818	0.5	2S
13	A463	42.475	112	739	-10.66	1.28	1.414	3.784	0.5	2S
14	A464	42.677	137	752	13.42	14.49	-2.950	0.268	0.5	2S
15	A465	42.879	119	725	-3.67	-13.09	-0.006	3.315	0.5	2S
16	A466	43.081	116	731	-7.17	-6.88	-0.337	3.804	0.5	2S
17	A467	43.283	134	747	11.09	8.66	-2.999	2.225	0.5	2S
18	A468	43.485	113	724	-9.88	-14.26	0.692	6.861	0.5	2P
19	A469	43.687	119	726	-3.67	-11.54	0.055	5.093	0.5	2S
20	A470	43.889	132	745	8.93	7.11	-4.321	3.465	0.5	unknown
21	A471	44.091	110	730	-12.99	-8.04	2.499	7.280	0.5	2P

22	A472	44.293	126	727	3.32	-10.76	-1.048	2.101	0.5	2S
23	A473	44.495	124	750	1.38	12.16	-1.309	3.230	0.5	2S
24	A474	44.697	111	732	-11.83	-5.71	4.429	3.725	0.5	2S
25	A475	44.899	132	726	9.15	-11.93	-1.918	-0.271	0.5	2S
26	A476	45.101	127	747	3.71	9.44	-0.358	-0.552	0.5	2S
27	A477	45.303	109	743	-14.55	5.56	6.914	-2.303	0.5	2S
28	A478	45.505	138	726	14.98	-12.31	-4.367	0.036	0.5	2S
29	A479	45.707	114	753	-8.72	15.27	3.232	-0.710	0.5	2S
30	A480	45.909	117	742	-6.39	3.61	4.725	-6.032	0.5	2S
31	A481	46.111	136	724	13.03	-14.26	-5.150	-1.484	0.5	2S
32	A482	46.313	116	752	-6.78	13.71	4.826	-6.875	0.5	2S
33	A483	46.515	121	753	-2.12	15.27	4.273	-8.056	0.5	2S
34	A484	46.717	138	722	14.98	-16.20	-4.964	4.073	0.5	2S
35	A485	46.919	112	753	-11.05	15.27	4.883	-8.270	0.5	2S
36	A486	47.121	127	750	4.10	12.55	-0.681	-4.154	0.5	2S
37	A487	47.323	135	726	11.87	-11.93	-3.784	0.557	0.5	2S
38	A488	47.525	110	746	-12.99	7.89	5.145	-5.536	0.5	2S
39	A489	47.727	130	751	7.21	12.94	0.450	-5.684	0.5	2S
40	A490	47.929	133	722	9.54	-16.20	-1.478	-1.027	0.5	unknown
41	A491	48.131	113	752	-10.27	14.49	3.871	-4.373	0.5	unknown
42	A492	48.333	136	757	13.03	18.76	-3.065	-2.742	0.5	unknown
43	A493	48.535	126	730	2.93	-8.04	0.030	-2.436	0.5	2S
44	A494	48.737	109	739	-14.16	0.89	3.061	1.536	0.5	2S
45	A495	48.939	134	745	10.70	6.72	-2.669	0.633	0.5	2S
46	A496	49.141	123	731	0.22	-7.26	0.061	-0.101	0.5	2S
47	A497	49.343	114	744	-8.72	5.94	2.206	3.121	0.5	2S
48	A498	49.545	135	757	11.48	19.54	-2.032	-0.389	0.5	2P
49	A499	49.747	120	730	-3.28	-7.65	0.181	3.279	0.5	2P
50	A500	49.949	115	731	-7.94	-6.49	0.805	4.101	0.5	2S
51	A501	50.151	137	744	13.81	5.94	-5.066	2.009	0.5	2S
52	A502	50.353	114	723	-9.11	-15.03	-0.973	7.778	0.5	2S
53	A503	50.555	121	726	-2.12	-11.54	-0.901	4.688	0.5	2S
54	A504	50.757	133	754	9.54	15.65	-2.851	2.022	0.5	2S
55	A505	50.959	110	729	-12.60	-8.82	2.343	7.757	0.5	2S
56	A506	51.161	128	723	4.49	-15.03	-1.444	1.545	0.5	2S
57	A507	51.363	124	744	0.60	5.94	-0.582	3.252	0.5	2S
58	A508	51.565	109	735	-14.55	-2.60	4.802	2.611	0.5	2S
59	A509	51.767	131	727	7.60	-11.15	-2.690	-0.949	0.5	unknown
60	A510	51.970	121	745	-1.73	6.72	0.834	0.622	0.5	2S
61	A511	52.172	111	739	-12.22	1.28	6.020	-3.704	0.5	2S
62	A512	52.374	138	721	14.98	-16.98	-4.020	-0.240	0.5	2S
63	A513	52.576	117	750	-6.00	12.55	2.576	-1.093	0.5	unknown
64	A514	52.778	116	743	-6.78	5.17	4.696	-5.416	0.5	2S
65	A515	52.980	140	719	17.31	-18.53	-5.035	1.570	0.5	unknown
66	A516	53.182	114	753	-8.72	15.27	5.055	-6.654	0.5	2S
67	A517	53.384	122	750	-0.95	12.16	1.365	-5.564	0.5	2P
68	A518	53.586	140	727	16.53	-11.15	-5.326	2.227	0.5	2S

69	A519	53.788	112	756	-11.44	18.37	4.597	-7.169	0.5	2S
70	A520	53.990	128	752	5.27	14.10	-1.089	-3.792	0.5	2S
71	A521	54.192	135	722	12.26	-16.20	-2.802	0.080	0.5	2S
72	A522	54.394	108	745	-15.32	6.72	5.393	-4.703	0.5	2S
73	A523	54.596	133	750	9.93	12.55	-3.160	-4.274	0.5	2S
74	A524	54.798	128	728	4.88	-10.37	-0.661	-2.661	0.5	2S
75	A525	55.000	108	741	-15.32	3.22	3.373	-1.401	0.5	2S
76	A526	55.202	136	749	12.65	10.60	-3.269	-1.159	0.5	2S
77	A527	55.404	121	723	-2.12	-15.42	0.246	1.595	0.5	2S
78	A528	55.606	109	729	-14.36	-9.21	1.464	4.705	0.5	2S
79	A529	55.808	135	739	12.26	0.89	-2.713	2.989	0.5	2S
80	A530	56.010	114	727	-9.11	-11.15	1.146	3.411	0.5	2S
81	A531	56.212	120	733	-3.28	-5.32	-0.291	4.460	0.5	unknown
82	A532	56.414	130	750	7.21	11.77	-2.217	0.779	0.5	2S
83	A533	56.616	110	728	-12.60	-9.60	1.405	5.922	0.5	2P
84	A534	56.818	122	729	-1.34	-8.43	-1.487	3.945	0.5	2P
85	A535	57.020	130	744	7.21	5.94	-4.667	2.876	0.5	2S
86	A536	57.222	111	724	-11.83	-13.48	1.148	9.151	0.5	2S
87	A537	57.424	126	724	3.32	-14.26	-0.812	2.943	0.5	2S
88	A538	57.626	123	756	0.22	17.99	1.358	2.360	0.5	2S
89	A539	57.828	112	737	-11.05	-1.05	4.715	1.715	0.5	2S
90	A540	58.030	133	725	9.93	-13.09	-3.212	0.265	0.5	2S
91	A541	58.232	121	753	-2.50	15.27	1.524	-2.076	0.5	2S
92	A542	58.434	114	747	-9.50	9.44	4.733	-5.440	0.5	2S
93	A543	58.636	140	727	16.53	-11.15	-4.214	-0.752	0.5	2S
94	A544	58.838	113	751	-9.88	12.94	3.739	-2.048	0.5	2S
95	A545	59.040	120	745	-3.28	6.72	1.956	-4.407	0.5	2S
96	A546	59.242	138	724	14.81	-14.26	-3.940	0.109	0.5	unknown
97	A547	59.444	113	744	-10.27	5.94	5.111	-5.245	0.5	unknown
98	A548	59.646	119	746	-3.67	8.27	2.614	-6.711	0.5	2P
99	A549	59.848	137	720	13.42	-18.14	-5.958	3.604	0.5	2S
100	A550	60.050	109	750	-13.77	12.16	5.032	-8.325	0.5	2S
101	A551	60.252	133	751	9.93	12.94	-2.453	-2.881	0.5	2S
102	A552	60.454	131	727	7.98	-11.15	-1.934	-1.453	0.5	unknown
103	A553	60.656	109	741	-14.16	3.22	4.829	-3.820	0.5	2P
104	A554	60.858	133	746	10.32	7.89	-1.801	-2.721	0.5	2S
105	A555	61.060	126	723	3.32	-14.65	0.114	-1.776	0.5	2P
106	A556	61.262	110	745	-12.99	6.72	3.362	-2.214	0.5	2S
107	A557	61.464	138	753	14.98	15.27	-3.516	-2.813	0.5	2S
108	A558	61.666	124	721	0.60	-16.59	0.507	-1.397	0.5	2S
109	A559	61.868	112	736	-11.05	-1.93	2.585	2.406	0.5	2S
110	A560	62.070	135	747	11.48	9.05	-2.212	1.148	0.5	2S
111	A561	62.272	119	725	-4.06	-12.70	1.254	3.026	0.5	2S
112	A562	62.474	114	733	-8.72	-4.55	2.797	4.263	0.5	2S
113	A563	62.676	133	748	9.54	9.83	-2.891	1.825	0.5	2S
114	A564	62.878	116	724	-7.55	-13.87	0.187	6.512	0.5	unknown
115	A565	63.080	120	726	-2.89	-11.54	0.187	3.738	0.5	unknown

116	A566	63.282	130	745	6.98	7.11	-4.071	1.569	0.5	2S
117	A567	63.484	110	728	-13.38	-9.98	2.574	7.230	0.5	2S
118	A568	63.686	126	728	2.55	-10.37	-1.126	1.929	0.5	2P
119	A569	63.888	128	745	5.27	7.11	-2.727	1.939	0.5	2P
120	A570	64.090	109	729	-13.77	-8.43	4.316	6.485	0.5	2S
121	A571	64.292	131	724	7.98	-14.26	-2.782	1.573	0.5	2S
122	A572	64.494	121	749	-2.12	11.38	1.164	1.937	0.5	2S
123	A573	64.697	111	737	-12.22	-1.05	6.057	-0.911	0.5	2S
124	A574	64.899	135	723	11.48	-14.65	-3.909	-0.359	0.5	2S
125	A575	65.101	119	750	-4.45	11.77	2.944	-1.607	0.5	2S
126	A576	65.303	114	742	-8.72	4.00	6.216	-5.893	0.5	2S
127	A577	65.505	138	720	14.59	-18.14	-4.425	1.298	0.5	2S
128	A578	65.707	113	750	-9.88	12.55	4.067	-3.773	0.5	2S
129	A579	65.909	123	748	-0.56	10.22	1.894	-6.230	0.5	2S
130	A580	66.111	138	727	14.98	-10.76	-5.447	1.578	0.5	2S
131	A581	66.313	111	747	-11.83	9.05	4.343	-5.598	0.5	2S
132	A582	66.515	124	745	0.99	7.50	0.566	-5.433	0.5	2S
133	A583	66.717	137	721	14.20	-16.98	-4.605	1.880	0.5	2S
134	A584	66.919	112	750	-11.44	12.55	4.222	-6.247	0.5	2P
135	A585	67.121	130	751	6.43	12.94	-1.279	-3.934	0.5	2P
136	A586	67.323	136	724	13.03	-13.48	-2.574	-0.653	0.5	2S
137	A587	67.525	109	746	-14.55	8.27	4.699	-5.194	0.5	2S
138	A588	67.727	133	747	10.32	9.05	-2.403	-4.735	0.5	2P
139	A589	67.929	130	721	6.43	-17.36	-0.731	-2.256	0.5	2P
140	A590	68.131	110	743	-13.38	4.78	3.685	-3.339	0.5	2P
141	A591	68.333	137	751	14.20	13.32	-3.373	-0.538	0.5	2S
142	A592	68.535	126	726	2.93	-11.54	0.268	-2.460	0.5	2S
143	A593	68.737	114	745	-9.50	6.72	2.637	0.730	0.5	2S
144	A594	68.939	130	754	6.82	16.43	-1.775	-0.828	0.5	2S
145	A595	69.141	122	723	-0.95	-15.03	1.229	1.119	0.5	2S
146	A596	69.343	110	729	-13.38	-9.21	1.324	5.484	0.5	2P
147	A597	69.545	136	735	13.03	-2.99	-4.368	2.722	0.5	2S
148	A598	69.747	114	723	-8.72	-15.03	1.928	1.979	0.5	2S
149	A599	69.949	118	733	-4.83	-5.32	0.728	3.958	0.5	2P
150	A600	70.151	130	757	6.82	18.94	-1.858	1.463	0.5	2P
2S: 115 frames: 2P: 22 frames										

Table A-6 VIV responses of the riser and the wake vortex mode for each plot of velocity and vorticity fields at a speed of 0.6 m/s

Serial number	Plot number	time s	x mm	y mm	d_x mm	d_y mm	a_x m/s^2	a_y m/s^2	V m/s	Vortex mode
1	A601	33.706	156	734	15.50	-16.04	-4.370	4.527	0.6	2P
2	A602	33.908	136	759	-4.70	8.82	1.258	2.367	0.6	2P
3	A603	34.110	125	749	-15.19	-0.89	5.807	2.880	0.6	2S
4	A604	34.312	142	738	1.13	-11.38	-0.874	2.970	0.6	2S

5	A605	34.514	152	758	12.00	8.43	-4.856	-0.980	0.6	unknown
6	A606	34.716	141	740	0.35	-9.44	0.367	-1.587	0.6	2P
7	A607	34.918	125	755	-15.19	4.94	7.853	-7.001	0.6	2P
8	A608	35.120	142	757	1.52	7.27	1.625	-6.707	0.6	Unknown
9	A609	35.322	154	764	13.17	13.87	-7.095	6.570	0.6	2S
10	A610	35.524	142	742	1.13	-7.88	0.272	3.517	0.6	2S
11	A611	35.726	125	763	-15.19	13.48	4.477	6.407	0.6	Unknown
12	A612	35.928	144	762	3.07	12.32	-1.236	4.897	0.6	Unknown
13	A613	36.130	157	735	16.28	-15.26	-5.648	-0.361	0.6	Unknown
14	A614	36.332	139	763	-1.20	13.48	2.271	-4.230	0.6	Unknown
15	A615	36.534	130	744	-10.92	-5.94	8.997	-10.404	0.6	2S
16	A616	36.736	140	734	-0.04	-16.04	-0.259	-5.404	0.6	2S
17	A617	36.938	154	758	13.95	8.43	-7.425	4.329	0.6	2S
18	A618	37.140	140	738	-0.04	-11.38	0.151	2.867	0.6	2S
19	A619	37.342	127	764	-13.25	14.65	3.590	5.538	0.6	2S
20	A620	37.544	144	766	3.07	16.59	-0.448	3.953	0.6	Unknown
21	A621	37.746	156	733	15.50	-16.82	-5.457	-0.072	0.6	2S
22	A622	37.948	139	756	-1.20	6.49	-0.971	1.304	0.6	2S
23	A623	38.150	124	748	-15.97	-1.67	7.607	-8.566	0.6	2S
24	A624	38.352	143	738	2.29	-11.77	0.609	-5.984	0.6	2S
25	A625	38.554	150	761	9.67	11.54	-7.425	4.374	0.6	Unknown
26	A626	38.756	141	738	0.35	-11.38	0.434	3.498	0.6	2S
27	A627	38.958	126	755	-14.41	4.94	6.344	2.790	0.6	2S
28	A628	39.160	142	761	1.52	10.76	-0.882	2.378	0.6	2P
29	A629	39.362	158	735	17.44	-14.88	-3.357	-0.295	0.6	2P
30	A630	39.564	136	762	-4.70	11.93	-1.081	1.556	0.6	Unknown
31	A631	39.766	126	750	-14.02	-0.11	7.782	-3.896	0.6	2P
32	A632	39.968	144	734	3.07	-15.65	0.163	-4.687	0.6	2S
33	A633	40.170	150	759	9.28	9.60	-6.919	4.767	0.6	2P
34	A634	40.372	140	736	-0.82	-14.10	-0.634	1.258	0.6	2P
35	A635	40.574	124	756	-16.74	6.49	6.011	1.327	0.6	Unknown
36	A636	40.776	145	758	4.23	8.04	-1.956	5.377	0.6	2P
37	A637	40.978	154	731	13.17	-18.37	-3.070	-1.262	0.6	2S
38	A638	41.180	136	762	-4.31	12.48	0.822	1.555	0.6	2S
39	A639	41.382	127	750	-13.25	0.27	6.592	-3.922	0.6	2P
40	A640	41.584	144	737	3.46	-12.55	0.300	-3.824	0.6	2P
41	A641	41.786	151	760	10.84	10.37	-6.507	4.715	0.6	2P
42	A642	41.988	139	738	-1.20	-11.38	-0.065	0.789	0.6	2P
43	A643	42.191	126	755	-14.80	5.32	5.365	1.624	0.6	Unknown
44	A644	42.393	146	763	5.79	13.48	-2.128	3.717	0.6	2P
45	A645	42.595	157	736	16.67	-14.10	-3.476	0.202	0.6	2S
46	A646	42.797	135	762	-5.48	11.93	-0.494	3.342	0.6	Unknown
47	A647	42.999	128	750	-12.86	-0.11	6.981	-3.869	0.6	2S
48	A648	43.201	146	736	5.40	-13.71	-1.263	-3.691	0.6	2S
49	A649	43.403	151	766	10.45	15.81	-6.177	3.138	0.6	2S
50	A650	43.605	140	739	-0.82	-10.99	1.283	-1.393	0.6	Unknown
51	A651	43.807	124	752	-16.35	2.22	6.197	0.249	0.6	2S

52	A652	44.009	147	761	6.95	11.15	-2.718	5.423	0.6	2S
53	A653	44.211	156	740	15.11	-9.83	-3.811	0.381	0.6	2S
54	A654	44.413	133	759	-7.81	8.82	0.198	3.567	0.6	2S
55	A655	44.615	127	746	-13.25	-3.61	7.315	-1.362	0.6	2P
56	A656	44.817	143	733	2.29	-16.82	-1.562	-2.671	0.6	Unknown
57	A657	45.019	152	760	11.62	9.99	-5.697	2.550	0.6	2P
58	A658	45.221	138	736	-2.37	-13.32	-0.150	0.025	0.6	2S
59	A659	45.423	125	756	-15.19	6.10	5.940	1.598	0.6	2P
60	A660	45.625	145	762	5.01	12.32	-1.757	5.244	0.6	2P
61	A661	45.827	155	732	14.33	-17.98	-5.002	0.266	0.6	2S
62	A662	46.029	138	769	-1.98	18.92	0.861	1.722	0.6	2S
63	A663	46.231	128	752	-12.47	2.67	7.775	-4.398	0.6	2S
64	A664	46.433	145	735	4.23	-14.88	-1.190	-3.874	0.6	Unknown
65	A665	46.635	151	761	10.06	11.54	-5.446	3.560	0.6	2S
66	A666	46.837	138	737	-2.37	-12.93	1.155	0.288	0.6	2S
67	A667	47.039	126	756	-14.02	6.10	5.363	1.491	0.6	2S
68	A668	47.241	143	764	2.29	14.65	-1.994	2.524	0.6	2P
69	A669	47.443	154	735	13.95	-15.26	-4.201	0.224	0.6	2S
70	A670	47.645	136	764	-4.31	14.65	-1.090	3.695	0.6	2S
71	A671	47.847	127	753	-13.64	2.99	7.887	-4.429	0.6	Unknown
72	A672	48.049	144	739	3.46	-10.99	0.157	-5.145	0.6	unknown
73	A673	48.251	150	759	9.67	9.66	-6.240	4.046	0.6	Unknown
74	A674	48.453	138	736	-1.98	-13.32	0.807	0.431	0.6	2S
75	A675	48.655	125	756	-15.19	6.10	7.027	-0.439	0.6	2S
76	A676	48.857	145	761	4.62	11.15	-1.895	3.367	0.6	2P
77	A677	49.059	156	732	15.50	-17.59	-4.316	0.077	0.6	2P
78	A678	49.261	136	769	-4.70	18.92	-1.004	4.458	0.6	2P
79	A679	49.463	127	756	-13.25	6.10	6.481	-1.029	0.6	2P
80	A680	49.665	148	739	7.73	-10.99	-1.378	-2.972	0.6	2S
81	A681	49.867	151	764	10.84	14.65	-5.564	3.132	0.6	2S
82	A682	50.069	139	738	-1.59	-11.38	1.739	-1.877	0.6	2S
83	A683	50.271	126	755	-14.80	4.94	6.292	-1.083	0.6	2S
84	A684	50.473	149	766	8.90	16.20	-4.095	4.478	0.6	Unknown
85	A685	50.675	155	731	14.72	-18.37	-4.212	-0.589	0.6	2S
86	A686	50.877	135	760	-5.87	9.99	-1.615	4.687	0.6	2P
87	A687	51.079	128	751	-12.86	1.05	6.731	-1.972	0.6	2S
88	A688	51.281	145	736	5.01	-13.71	-2.451	-3.673	0.6	Unknown
89	A689	51.483	151	764	10.84	14.26	-3.729	0.908	0.6	Unknown
90	A690	51.685	139	744	-1.20	-5.94	1.807	-2.414	0.6	2S
91	A691	51.887	126	757	-14.80	7.22	6.219	-0.944	0.6	2S
92	A692	52.089	147	766	6.18	16.20	-2.276	3.861	0.6	2P
93	A693	52.291	153	735	12.78	-14.88	-4.140	1.048	0.6	unknown
94	A694	52.493	136	756	-4.70	6.49	-0.783	4.176	0.6	2S
95	A695	52.695	126	750	-14.02	-0.11	5.981	-0.979	0.6	2S
96	A696	52.897	141	733	0.74	-17.21	-0.749	-4.586	0.6	2S
97	A697	53.099	150	758	9.67	8.43	-4.781	1.848	0.6	2S
98	A698	53.301	142	734	1.13	-15.65	0.097	1.636	0.6	2S

99	A699	53.503	128	756	-12.08	5.71	6.464	0.533	0.6	2P
100	A700	53.705	145	766	5.01	16.59	-0.678	3.614	0.6	2P
101	A701	53.907	156	737	15.11	-12.93	-3.506	0.759	0.6	2S
102	A702	54.109	135	761	-5.09	11.54	-2.453	4.650	0.6	2P
103	A703	54.311	127	750	-13.25	0.66	5.123	-2.450	0.6	2P
104	A704	54.513	143	738	2.68	-12.16	-0.886	-3.584	0.6	2S
105	A705	54.716	149	764	8.51	14.65	-3.065	1.926	0.6	2S
106	A706	54.918	140	736	-0.43	-14.10	1.590	-0.867	0.6	2P
107	A707	55.120	125	753	-15.58	3.38	6.754	-0.257	0.6	Unknown
108	A708	55.322	148	764	7.34	14.26	-1.843	4.481	0.6	2S
109	A709	55.524	154	733	13.56	-16.82	-3.930	-0.047	0.6	2S
110	A710	55.726	134	764	-6.25	13.87	-1.016	3.601	0.6	2S
111	A711	55.928	129	753	-11.69	3.38	7.080	-2.071	0.6	2P
112	A712	56.130	142	736	1.90	-13.32	-1.085	-4.451	0.6	2P
113	A713	56.332	150	758	9.67	8.43	-4.730	2.814	0.6	2S
114	A714	56.534	138	732	-2.37	-17.59	1.678	0.118	0.6	2S
115	A715	56.736	124	752	-15.97	2.22	6.270	0.066	0.6	2S
116	A716	56.938	144	759	3.07	8.82	-1.712	2.977	0.6	2P
117	A717	57.140	153	729	12.78	-20.31	-3.573	-1.463	0.6	2P
118	A718	57.342	137	760	-3.54	10.37	0.385	2.621	0.6	2S
119	A719	57.544	127	754	-13.25	4.16	6.610	-2.577	0.6	2S
120	A720	57.746	145	738	4.62	-11.77	-0.020	-4.341	0.6	2S
121	A721	57.948	153	756	12.39	5.71	-4.353	2.965	0.6	2S
122	A722	58.150	139	742	-1.59	-7.61	0.621	0.600	0.6	2S
123	A723	58.352	125	756	-15.19	6.10	5.994	-0.018	0.6	unknown
124	A724	58.554	143	761	2.68	10.76	-1.337	0.176	0.6	2P
125	A725	58.756	156	730	15.11	-19.93	-6.834	-0.107	0.6	2S
126	A726	58.958	137	759	-3.54	9.21	0.870	-0.476	0.6	2S
127	A727	59.160	126	743	-14.41	-7.11	7.413	-5.290	0.6	2P
128	A728	59.362	139	735	-1.20	-14.88	1.553	-6.524	0.6	2S
129	A729	59.564	151	762	10.45	11.93	-7.673	5.493	0.6	2S
130	A730	59.766	143	742	2.68	-7.88	0.713	1.866	0.6	2S
131	A731	59.968	125	759	-15.58	9.21	4.819	5.762	0.6	2P
132	A732	60.170	142	761	1.13	11.15	-0.899	3.940	0.6	2P
133	A733	60.372	156	733	15.89	-17.21	-3.628	0.065	0.6	Unknown
134	A734	60.574	142	757	1.13	6.88	1.666	-3.647	0.6	2S
135	A735	60.776	125	743	-15.19	-6.72	10.091	-10.910	0.6	2S
136	A736	60.978	136	737	-4.70	-12.93	1.881	-5.342	0.6	2P
137	A737	61.180	152	760	12.00	9.99	-9.408	4.832	0.6	2P
138	A738	61.382	144	738	3.46	-11.77	-0.592	4.422	0.6	2P
139	A739	61.584	124	764	-15.97	14.65	4.835	6.989	0.6	2P
140	A740	61.786	139	758	-1.20	8.43	0.108	5.267	0.6	2P
141	A741	61.988	155	731	14.72	-18.76	-4.705	-0.946	0.6	2P
142	A742	62.190	141	759	0.35	9.21	1.203	-7.424	0.6	2P
143	A743	62.392	127	742	-13.25	-7.50	9.938	-13.940	0.6	2S
144	A744	62.594	135	737	-5.87	-12.55	4.290	-7.710	0.6	2P
145	A745	62.796	153	760	12.39	10.37	-10.101	7.308	0.6	Unknown

146	A746	62.998	145	736	4.62	-13.81	-1.418	5.331	0.6	2P
147	A747	63.200	128	764	-12.86	13.87	2.906	8.723	0.6	2P
148	A748	63.402	139	761	-1.59	11.15	-0.022	6.860	0.6	2S
149	A749	63.604	154	728	13.56	-21.87	-4.587	-0.563	0.6	2P
150	A750	63.806	142	764	1.90	14.26	0.457	-6.121	0.6	2S
2S: 75 frames; 2P: 49 frames										

Table A-7 VIV responses of the riser and the wake vortex mode for each plot of velocity and vorticity fields at a speed of 0.7 m/s

Serial number	Plot number	time s	x mm	y mm	d_x mm	d_y mm	a_x m/s^2	a_y m/s^2	V m/s	Vortex mode
1	A751	25.087	156	742	0.88	-11.50	-0.434	4.048	0.7	unknown
2	A752	25.289	165	770	10.21	16.47	-3.636	-4.314	0.7	2P
3	A753	25.491	167	732	12.54	-21.21	-5.845	4.617	0.7	2P
4	A754	25.693	158	774	2.83	20.74	-0.770	4.183	0.7	unknown
5	A755	25.895	153	736	-1.45	-16.55	0.790	3.917	0.7	2P
6	A756	26.097	141	771	-13.49	17.63	11.909	-16.284	0.7	2P
7	A757	26.299	145	755	-9.61	2.09	6.382	-3.767	0.7	2P
8	A758	26.501	157	739	2.05	-13.83	-3.340	5.719	0.7	2S
9	A759	26.703	164	768	9.04	14.52	-3.360	-4.230	0.7	2S
10	A760	26.905	163	728	8.65	-25.10	-3.085	2.313	0.7	2S
11	A761	27.107	160	770	5.54	16.47	-2.905	7.427	0.7	2S
12	A762	27.309	148	736	-6.50	-16.94	0.856	8.839	0.7	2S
13	A763	27.511	143	766	-11.94	12.58	10.854	-11.896	0.7	Unknown
14	A764	27.713	148	762	-6.89	8.70	7.689	-9.009	0.7	2P
15	A765	27.915	162	739	7.10	-14.22	-5.754	2.961	0.7	2S
16	A766	28.117	167	763	12.15	9.86	-6.306	-1.817	0.7	unknown
17	A767	28.319	164	737	9.04	-15.78	-0.864	-2.854	0.7	2P
18	A768	28.521	152	767	-3.00	14.14	-0.115	4.565	0.7	2P
19	A769	28.723	144	738	-10.38	-15.00	1.782	15.498	0.7	2S
20	A770	28.925	140	757	-14.66	3.65	8.174	-0.728	0.7	2S
21	A771	29.127	151	761	-3.39	7.53	3.651	-7.731	0.7	2P
22	A772	29.329	165	735	10.59	-17.72	-8.504	5.123	0.7	Unknown
23	A773	29.531	165	764	10.59	10.64	-6.653	-1.585	0.7	2S
24	A774	29.733	163	738	8.26	-15.00	-1.055	-5.947	0.7	2S
25	A775	29.935	150	769	-4.94	15.69	3.099	-3.127	0.7	Unknown
26	A776	30.137	141	740	-13.49	-12.67	3.277	13.099	0.7	2S
27	A777	30.339	144	752	-10.38	-0.63	4.672	6.024	0.7	2P
28	A778	30.541	158	766	2.83	12.97	0.695	-6.071	0.7	2S
29	A779	30.743	169	731	14.09	-22.38	-11.145	7.841	0.7	2S
30	A780	30.945	167	767	12.15	13.75	-4.470	-1.177	0.7	2S
31	A781	31.147	159	740	3.99	-12.67	0.112	-6.681	0.7	Unknown
32	A782	31.349	145	770	-9.61	17.24	7.991	-14.534	0.7	2P
33	A783	31.551	142	747	-13.10	-6.45	6.563	4.255	0.7	2P
34	A784	31.753	150	745	-4.94	-8.01	1.269	7.922	0.7	2P
35	A785	31.955	164	765	9.43	12.19	-3.088	-3.591	0.7	2P

36	A786	32.157	169	733	14.09	-19.66	-8.073	6.461	0.7	2S
37	A787	32.359	163	771	7.88	18.02	-1.286	3.080	0.7	2S
38	A788	32.561	153	737	-1.45	-16.16	1.237	-0.154	0.7	2S
39	A789	32.763	141	767	-13.49	14.14	12.926	-16.963	0.7	2S
40	A790	32.965	143	751	-11.94	-2.18	6.699	-2.487	0.7	2P
41	A791	33.167	153	742	-1.45	-11.50	0.328	6.776	0.7	2P
42	A792	33.369	161	764	6.71	10.64	-2.245	-3.200	0.7	Unknown
43	A793	33.571	166	731	11.37	-22.38	-5.358	3.561	0.7	2S
44	A794	33.773	160	771	5.16	17.63	-0.989	7.520	0.7	2S
45	A795	33.975	147	737	-7.66	-15.78	1.870	7.029	0.7	2S
46	A796	34.177	137	763	-18.15	9.86	12.330	-10.019	0.7	2P
47	A797	34.379	147	755	-8.05	2.09	6.304	-6.772	0.7	2P
48	A798	34.581	158	733	3.21	-20.05	-5.721	5.488	0.7	Unknown
49	A799	34.783	165	764	10.59	11.42	-4.522	-2.232	0.7	2P
50	A800	34.985	167	731	12.54	-22.38	-2.625	-0.724	0.7	2S
51	A801	35.187	151	771	-3.78	18.41	1.473	3.506	0.7	2S
52	A802	35.389	144	737	-10.38	-16.16	1.633	12.735	0.7	2S
53	A803	35.591	142	764	-13.10	11.03	7.370	-0.967	0.7	Unknown
54	A804	35.793	152	768	-2.61	14.91	4.162	-9.757	0.7	2S
55	A805	35.995	168	731	13.31	-21.99	-11.044	6.998	0.7	2S
56	A806	36.197	163	771	8.65	18.41	-3.227	-2.679	0.7	2S
57	A807	36.399	159	739	4.38	-14.22	-1.178	-6.686	0.7	2S
58	A808	36.601	147	772	-8.05	18.80	5.266	-6.765	0.7	2S
59	A809	36.803	142	741	-12.71	-12.28	1.524	13.031	0.7	2S
60	A810	37.005	146	752	-8.83	-0.63	5.708	5.780	0.7	2P
61	A811	37.207	159	772	3.99	18.80	1.151	-6.599	0.7	2S
62	A812	37.409	171	730	16.42	-23.16	-10.788	9.288	0.7	2S
63	A813	37.611	166	762	10.98	8.70	-2.948	1.312	0.7	2S
64	A814	37.814	153	749	-1.45	-3.73	0.310	-3.950	0.7	2S
65	A815	38.016	140	763	-15.04	9.86	10.159	-15.206	0.7	2S
66	A816	38.218	141	748	-13.49	-4.90	7.256	-1.084	0.7	2S
67	A817	38.420	152	736	-2.61	-17.33	0.460	7.328	0.7	2P
68	A818	38.622	164	757	9.04	4.04	-2.739	0.083	0.7	2P
69	A819	38.824	169	737	14.48	-15.88	-6.832	4.768	0.7	2S
70	A820	39.026	155	770	0.11	16.85	-1.281	3.435	0.7	2P
71	A821	39.228	149	743	-6.11	-9.56	1.149	4.542	0.7	2S
72	A822	39.430	140	763	-15.04	9.86	14.971	-15.643	0.7	2P
73	A823	39.632	144	756	-10.38	3.26	8.869	-8.663	0.7	2P
74	A824	39.834	157	736	2.44	-16.55	-2.722	7.036	0.7	2P
75	A825	40.036	166	771	10.98	17.63	-4.037	-3.420	0.7	2P
76	A826	40.238	164	732	9.82	-20.83	-0.814	-1.888	0.7	2P
77	A827	40.440	154	766	-0.28	13.36	-0.236	3.916	0.7	2S
78	A828	40.642	142	742	-12.71	-10.73	2.936	12.820	0.7	2P
79	A829	40.844	140	761	-14.27	8.31	6.849	-2.483	0.7	2P
80	A830	41.046	154	764	-0.67	11.42	3.021	-8.996	0.7	Unknown
81	A831	41.248	167	732	12.54	-20.83	-7.806	6.790	0.7	2S
82	A832	41.450	166	770	11.37	17.24	-5.607	-3.819	0.7	unknown

83	A833	41.652	163	736	7.88	-16.55	0.021	-5.040	0.7	2S
84	A834	41.854	149	778	-5.72	24.62	4.885	-7.138	0.7	2P
85	A835	42.056	143	744	-11.55	-9.17	-0.046	15.362	0.7	2P
86	A836	42.258	145	753	-9.99	-0.24	3.216	8.487	0.7	2P
87	A837	42.460	160	770	5.54	16.85	1.030	-7.249	0.7	2P
88	A838	42.662	168	730	13.31	-23.16	-10.992	8.096	0.7	2S
89	A839	42.864	167	761	12.15	8.31	-2.309	0.482	0.7	2S
90	A840	43.066	153	731	-1.45	-21.60	-0.384	-1.623	0.7	2S
91	A841	43.268	144	773	-10.77	19.96	9.473	-17.850	0.7	2S
92	A842	43.470	143	749	-11.94	-3.73	6.854	0.735	0.7	2S
93	A843	43.672	154	743	-0.28	-10.34	-0.217	5.364	0.7	2S
94	A844	43.874	162	771	7.10	18.41	-3.356	-1.101	0.7	2S
95	A845	44.076	174	738	19.53	-15.39	-8.888	5.380	0.7	Unknown
96	A846	44.278	157	774	2.05	21.13	-3.894	7.371	0.7	2P
97	A847	44.480	151	735	-3.39	-17.72	-0.451	5.655	0.7	2S
98	A848	44.682	144	775	-11.16	21.90	11.931	-17.447	0.7	2P
99	A849	44.884	146	759	-8.66	5.98	6.609	-6.424	0.7	2S
100	A850	45.086	161	736	5.93	-17.33	-5.531	4.720	0.7	2S
101	A851	45.288	169	770	14.48	17.24	-7.402	-0.533	0.7	2S
102	A852	45.490	167	745	12.15	-8.40	-0.918	-4.085	0.7	2S
103	A853	45.692	151	767	-3.39	14.14	-0.693	4.325	0.7	2P
104	A854	45.894	144	736	-11.16	-16.94	2.258	16.463	0.7	2P
105	A855	46.096	144	762	-10.38	8.70	8.195	0.884	0.7	2S
106	A856	46.298	151	766	-3.78	12.58	6.572	-9.262	0.7	Unknown
107	A857	46.500	169	726	14.09	-27.43	-11.035	10.496	0.7	Unknown
108	A858	46.702	163	783	8.26	29.67	-2.530	-2.055	0.7	2S
109	A859	46.904	162	746	7.49	-7.23	-1.276	-8.440	0.7	Unknown
110	A860	47.106	145	770	-9.22	16.47	7.989	-11.804	0.7	2S
111	A861	47.308	140	747	-15.04	-6.06	6.068	7.449	0.7	Unknown
112	A862	47.510	146	738	-8.83	-14.61	0.017	11.666	0.7	Unknown
113	A863	47.712	164	763	9.43	9.47	-2.643	-4.932	0.7	Unknown
114	A864	47.914	166	729	10.98	-24.32	-9.759	5.767	0.7	2S
115	A865	48.116	158	771	3.60	18.41	0.818	0.349	0.7	2S
116	A866	48.318	154	739	-0.28	-14.22	-0.948	2.124	0.7	2S
117	A867	48.520	140	768	-14.27	15.30	14.673	-17.353	0.7	2P
118	A868	48.722	142	757	-13.10	4.42	8.811	-7.446	0.7	2P
119	A869	48.924	156	742	1.27	-10.73	-0.343	4.360	0.7	2P
120	A870	49.126	164	766	9.26	12.58	-3.399	-4.338	0.7	2P
121	A871	49.328	167	731	12.54	-22.38	-5.537	4.232	0.7	2S
122	A872	49.530	159	768	3.99	14.91	-2.383	6.169	0.7	2P
123	A873	49.732	147	740	-7.28	-13.45	0.997	8.149	0.7	Unknown
124	A874	49.934	143	769	-11.55	16.08	9.307	-10.596	0.7	2P
125	A875	50.136	149	766	-6.11	13.36	7.112	-9.086	0.7	Unknown
126	A876	50.339	166	736	10.98	-16.55	-8.153	6.112	0.7	Unknown
127	A877	50.541	166	767	11.37	14.14	-4.833	-3.023	0.7	2S
128	A878	50.743	166	743	11.37	-9.95	0.417	-4.380	0.7	2P
129	A879	50.945	152	770	-3.00	17.24	-0.185	4.940	0.7	2P

130	A880	51.147	143	742	-11.94	-11.11	3.406	13.371	0.7	Unknown
131	A881	51.349	142	759	-12.33	6.37	6.097	3.969	0.7	2P
132	A882	51.551	152	767	-3.00	13.75	5.017	-8.553	0.7	2P
133	A883	51.753	167	732	12.15	-20.83	-10.738	10.209	0.7	2P
134	A884	51.955	163	775	8.65	22.29	-3.984	0.601	0.7	2P
135	A885	52.157	161	740	6.32	-12.67	0.674	-7.697	0.7	Unknown
136	A886	52.359	146	767	-8.83	14.14	7.626	-10.920	0.7	2P
137	A887	52.561	140	747	-15.04	-6.45	5.521	9.633	0.7	2P
138	A888	52.763	145	746	-9.22	-6.84	2.481	7.799	0.7	2P
139	A889	52.965	159	768	4.77	14.91	1.224	-6.797	0.7	2P
140	A890	53.167	167	731	12.15	-22.38	-10.214	9.217	0.7	Unknown
141	A891	53.369	162	772	7.49	19.19	-1.376	-0.916	0.7	2P
142	A892	53.571	156	741	1.27	-11.89	-0.885	1.173	0.7	2S
143	A893	53.773	143	773	-11.94	20.35	12.214	-18.725	0.7	2P
144	A894	53.975	142	754	-13.10	0.54	10.199	-3.720	0.7	2P
145	A895	54.177	154	742	-0.28	-11.11	0.244	6.101	0.7	2S
146	A896	54.379	163	770	8.65	16.47	-2.546	-6.100	0.7	2P
147	A897	54.581	168	732	13.31	-21.21	-7.696	2.810	0.7	Unknown
148	A898	54.783	162	760	7.10	7.14	-5.078	7.743	0.7	2P
149	A899	54.985	147	735	-7.28	-17.72	1.553	3.870	0.7	2P
150	A900	55.187	143	769	-11.94	15.69	8.633	-12.368	0.7	unknown
2S: 63 frames: 2P: 60 frames										

Table A-8 VIV responses of the riser and the wake vortex mode for each plot of velocity and vorticity fields at a speed of 0.8 m/s

Serial number	Plot number	time s	x mm	y mm	d_x mm	d_y mm	a_x m/s^2	a_y m/s^2	V m/s	Vortex mode
1	A901	32.493	161	753	-5.90	2.18	5.238	0.546	0.8	unknown
2	A902	32.695	158	755	-9.39	4.12	8.563	-2.494	0.8	2P
3	A903	32.897	160	760	-7.06	9.17	6.205	4.628	0.8	2P
4	A904	33.099	156	755	-10.95	4.12	7.800	-5.355	0.8	2P
5	A905	33.301	161	752	-6.28	0.63	5.720	7.680	0.8	2P
6	A906	33.503	158	770	-9.39	18.49	8.402	-17.493	0.8	2P
7	A907	33.705	160	744	-6.67	-7.14	2.864	14.001	0.8	2P
8	A908	33.907	159	773	-7.84	21.99	4.395	-11.091	0.8	P+S
9	A909	34.109	166	745	-0.85	-6.37	-7.390	18.339	0.8	P+S
10	A910	34.311	164	783	-2.79	32.09	2.946	-13.718	0.8	2P
11	A911	34.513	174	731	6.92	-20.35	-9.771	11.428	0.8	2P
12	A912	34.715	161	768	-5.90	16.94	-0.146	-2.512	0.8	Unknown
13	A913	34.917	169	742	2.26	-9.48	-5.968	4.744	0.8	2P
14	A914	35.119	171	752	4.59	1.40	-2.024	-2.572	0.8	2P
15	A915	35.321	181	731	13.92	-20.35	-10.434	7.724	0.8	2S
16	A916	35.523	167	760	-0.07	9.17	-0.738	-3.758	0.8	2S
17	A917	35.725	181	747	14.30	-3.65	-11.045	5.030	0.8	2P
18	A918	35.927	174	763	6.92	12.28	-4.960	-2.252	0.8	Unknown
19	A919	36.129	186	742	18.97	-9.48	-16.190	8.613	0.8	2S

20	A920	36.331	165	771	-2.01	20.44	-0.168	1.514	0.8	2P
21	A921	36.533	173	743	5.76	-7.53	1.360	-6.888	0.8	2S
22	A922	36.735	173	750	6.15	-1.32	-2.773	6.936	0.8	2P
23	A923	36.937	180	733	12.75	-17.63	-1.941	-1.956	0.8	2S
24	A924	37.139	173	766	5.76	15.00	-5.734	8.226	0.8	2P
25	A925	37.341	173	761	6.15	9.56	1.879	-5.504	0.8	Unknown
26	A926	37.543	170	755	3.04	3.73	-5.037	6.076	0.8	2S
27	A927	37.745	174	730	7.48	-21.13	3.248	-8.864	0.8	2S
28	A928	37.947	177	763	10.42	11.50	-7.053	6.974	0.8	2S
29	A929	38.149	174	746	6.92	-5.20	0.075	0.024	0.8	2S
30	A930	38.351	166	757	-0.85	5.68	-3.391	6.618	0.8	2S
31	A931	38.553	161	744	-6.28	-7.14	-0.744	1.481	0.8	2S
32	A932	38.755	163	771	-3.57	20.05	-2.120	-1.329	0.8	2P
33	A933	38.957	168	743	0.71	-7.53	-5.369	3.747	0.8	2P
34	A934	39.159	161	751	-5.90	-0.15	-0.872	-2.564	0.8	2P
35	A935	39.361	155	754	-12.11	2.96	5.317	-1.968	0.8	2S
36	A936	39.563	154	747	-13.28	-4.04	6.348	-5.340	0.8	2P
37	A937	39.765	151	756	-16.00	4.51	0.763	8.483	0.8	unknown
38	A938	39.967	157	742	-9.78	-8.70	6.051	-4.143	0.8	unknown
39	A939	40.169	164	778	-2.79	27.43	4.586	-5.164	0.8	Unknown
40	A940	40.371	164	740	-3.18	-11.03	1.965	0.956	0.8	2P
41	A941	40.573	159	780	-8.23	28.98	12.092	-10.039	0.8	P+S
42	A942	40.775	166	731	-1.24	-20.35	1.638	14.044	0.8	2P
43	A943	40.977	167	758	-0.07	6.84	-1.242	1.634	0.8	2S
44	A944	41.179	165	750	-2.01	-1.32	-4.113	1.268	0.8	2P
45	A945	41.381	164	777	-3.18	25.87	6.829	-11.581	0.8	P+S
46	A946	41.583	166	745	-0.46	-6.37	-0.704	-4.004	0.8	2P
47	A947	41.785	174	763	6.92	12.28	-5.467	-0.870	0.8	Unknown
48	A948	41.987	168	742	1.10	-9.48	-6.463	-0.430	0.8	Unknown
49	A949	42.190	176	766	8.87	15.39	-6.698	-6.834	0.8	Unknown
50	A950	42.392	168	729	0.71	-21.52	-10.073	6.574	0.8	Unknown
51	A951	42.594	173	769	5.76	17.72	-3.775	-5.370	0.8	Unknown
52	A952	42.796	170	738	3.43	-12.58	-7.390	4.186	0.8	2P
53	A953	42.998	173	766	5.76	15.00	-5.284	1.603	0.8	Unknown
54	A954	43.200	170	738	3.43	-13.36	-5.769	-0.027	0.8	2P
55	A955	43.402	175	764	8.48	13.06	-4.254	1.915	0.8	2P
56	A956	43.604	173	735	5.76	-16.47	-2.518	2.620	0.8	Unknown
57	A957	43.806	172	752	5.37	1.40	-2.280	-2.087	0.8	Unknown
58	A958	44.008	170	732	3.43	-18.80	-2.846	-1.352	0.8	2P
59	A959	44.210	182	763	15.08	12.28	-5.464	-3.423	0.8	Unknown
60	A960	44.412	181	718	14.30	-33.17	-6.031	2.832	0.8	P+S
61	A961	44.614	182	776	15.47	24.71	-3.301	1.100	0.8	2P
62	A962	44.816	182	716	15.47	-35.11	-5.422	2.515	0.8	Unknown
63	A963	45.018	179	771	11.97	20.05	-3.342	1.813	0.8	Unknown
64	A964	45.220	170	721	2.65	-30.45	-2.291	-0.082	0.8	2S
65	A965	45.422	161	752	-6.28	0.63	0.384	6.291	0.8	2S
66	A966	45.624	163	741	-3.57	-10.25	1.743	-3.505	0.8	2P

67	A967	45.826	177	756	10.03	5.29	-8.636	5.480	0.8	Unknown
68	A968	46.028	168	737	1.49	-13.75	-3.750	-3.433	0.8	Unknown
69	A969	46.230	166	755	-0.46	4.40	-6.411	-2.238	0.8	2P
70	A970	46.432	166	754	-0.46	2.96	0.750	-3.797	0.8	2S
71	A971	46.634	177	747	10.03	-4.43	-6.526	3.252	0.8	2S
72	A972	46.836	175	737	8.48	-14.14	-2.785	-2.392	0.8	2P
73	A973	47.038	177	754	9.64	3.34	-4.851	3.133	0.8	2P
74	A974	47.240	163	748	-3.95	-2.87	3.855	0.097	0.8	Unknown
75	A975	47.442	166	753	-0.85	2.18	1.929	-4.583	0.8	2P
76	A976	47.644	169	730	2.26	-20.74	-5.859	10.129	0.8	Unknown
77	A977	47.846	167	747	-0.07	-3.65	-0.986	-2.593	0.8	Unknown
78	A978	48.048	158	752	-8.62	0.63	1.188	12.211	0.8	2S
79	A979	48.250	161	745	-5.51	-6.37	10.869	-15.456	0.8	2S
80	A980	48.452	156	726	-10.56	-25.01	-0.729	13.894	0.8	2P
81	A981	48.654	158	758	-9.39	6.84	13.565	-14.079	0.8	2S
82	A982	48.856	153	769	-13.67	18.11	11.859	4.449	0.8	Unknown
83	A983	49.058	159	737	-7.45	-13.75	19.537	-7.223	0.8	2P
84	A984	49.260	164	770	-2.79	18.88	13.219	-2.469	0.8	Unknown
85	A985	49.462	166	741	-0.46	-10.25	6.665	-6.924	0.8	Unknown
86	A986	49.664	163	774	-4.34	23.16	5.267	-0.070	0.8	2P
87	A987	49.866	162	746	-5.12	-4.81	6.115	-7.824	0.8	2P
88	A988	50.068	160	751	-7.06	-0.15	9.738	-5.426	0.8	Unknown
89	A989	50.270	167	743	-0.07	-8.31	4.666	-1.996	0.8	2P
90	A990	50.472	163	782	-3.57	31.31	10.851	-22.453	0.8	Unknown
91	A991	50.674	164	739	-2.40	-11.81	-0.242	11.018	0.8	2S
92	A992	50.876	157	752	-9.78	1.01	6.912	-11.861	0.8	Unknown
93	A993	51.078	170	749	3.04	-2.09	-7.843	7.769	0.8	2S
94	A994	51.280	166	763	-0.85	11.50	-2.026	-8.357	0.8	2S
95	A995	51.482	174	738	7.31	-12.58	-8.527	10.866	0.8	Unknown
96	A996	51.684	163	774	-4.34	23.16	3.288	-11.545	0.8	Unknown
97	A997	51.886	166	736	-0.85	-14.53	-1.647	5.096	0.8	2S
98	A998	52.088	174	779	6.92	27.82	0.194	-17.399	0.8	2P
99	A999	52.290	171	726	4.20	-25.01	-10.168	24.891	0.8	2P
100	A1000	52.492	167	787	-0.07	35.59	7.663	-15.687	0.8	Unknown
101	A1001	52.694	173	720	6.15	-30.84	-3.431	17.710	0.8	Unknown
102	A1002	52.896	171	783	4.20	31.70	5.123	-10.891	0.8	Unknown
103	A1003	53.098	176	714	8.87	-36.67	-2.378	7.537	0.8	Unknown
104	A1004	53.300	174	778	7.31	27.43	-0.815	-6.748	0.8	2P
105	A1005	53.502	173	721	5.76	-29.67	-1.880	-3.995	0.8	2P
106	A1006	53.704	175	747	8.48	-3.65	-10.416	6.206	0.8	Unknown
107	A1007	53.906	159	730	-7.45	-21.13	0.682	2.349	0.8	Unknown
108	A1008	54.108	166	732	-0.46	-18.80	-6.654	10.615	0.8	2S
109	A1009	54.310	165	738	-1.62	-12.58	0.725	-2.914	0.8	2S
110	A1010	54.512	168	759	1.49	7.62	-2.651	7.675	0.8	2P
111	A1011	54.715	172	746	5.37	-5.20	-4.125	-2.497	0.8	2S
112	A1012	54.917	178	751	10.81	-0.15	-5.725	6.088	0.8	2P
113	A1013	55.119	173	739	6.53	-12.19	-0.862	-4.585	0.8	Unknown

114	A1014	55.321	182	744	14.69	-6.76	-6.785	6.378	0.8	2P
115	A1015	55.523	173	740	6.15	-11.03	-0.795	-2.392	0.8	Unknown
116	A1016	55.725	179	752	12.36	1.01	-7.040	13.557	0.8	Unknown
117	A1017	55.927	173	743	5.76	-8.31	1.580	-4.484	0.8	2P
118	A1018	56.129	172	757	5.37	6.45	-3.494	4.465	0.8	2P
119	A1019	56.331	171	741	4.20	-10.25	-0.279	-1.231	0.8	2P
120	A1020	56.533	174	753	7.31	2.18	-5.322	1.628	0.8	Unknown
121	A1021	56.735	170	729	3.04	-21.52	-3.789	2.067	0.8	2S
122	A1022	56.937	175	755	8.24	4.12	-6.291	4.005	0.8	Unknown
123	A1023	57.139	166	735	-0.85	-15.69	-4.392	5.690	0.8	2S
124	A1024	57.341	173	751	6.53	0.24	-5.504	2.018	0.8	Unknown
125	A1025	57.543	165	733	-2.01	-18.41	-2.436	3.117	0.8	Unknown
126	A1026	57.745	169	754	2.26	2.57	-6.649	-0.305	0.8	Unknown
127	A1027	57.947	158	749	-9.00	-2.48	-4.584	17.614	0.8	2P
128	A1028	58.149	168	761	0.71	9.56	0.020	-9.811	0.8	Unknown
129	A1029	58.351	160	733	-7.06	-18.02	-3.429	12.235	0.8	Unknown
130	A1030	58.553	164	763	-3.18	11.50	2.748	-14.495	0.8	Unknown
131	A1031	58.755	158	750	-9.00	-0.54	-3.065	18.912	0.8	Unknown
132	A1032	58.957	164	765	-2.40	14.22	6.194	-14.155	0.8	2S
133	A1033	59.159	160	750	-7.06	-1.32	-3.985	13.710	0.8	2S
134	A1034	59.361	163	762	-4.34	10.73	5.411	-15.646	0.8	2S
135	A1035	59.563	154	751	-13.28	0.24	-0.018	12.793	0.8	2P
136	A1036	59.765	156	766	-11.33	15.00	22.148	-34.870	0.8	2S
137	A1037	59.967	152	752	-15.22	0.63	6.539	8.998	0.8	2S
138	A1038	60.169	154	763	-13.28	11.89	19.986	-15.814	0.8	Unknown
139	A1039	60.371	149	756	-17.55	4.51	14.931	-2.598	0.8	Unknown
140	A1040	60.573	151	759	-16.00	8.01	26.120	-20.355	0.8	2S
141	A1041	60.775	149	758	-17.94	7.23	19.174	-2.566	0.8	2S
142	A1042	60.977	155	756	-11.72	4.51	17.121	-4.521	0.8	Unknown
143	A1043	61.179	154	776	-12.50	25.10	14.468	-17.679	0.8	2S
144	A1044	61.381	163	747	-4.34	-3.65	4.794	10.491	0.8	2S
145	A1045	61.583	158	763	-8.62	11.89	11.641	-11.975	0.8	Unknown
146	A1046	61.785	162	750	-4.73	-0.93	-2.074	7.782	0.8	Unknown
147	A1047	61.987	163	756	-4.34	4.90	1.459	-13.590	0.8	Unknown
148	A1048	62.189	173	732	6.53	-18.80	-14.481	25.219	0.8	Unknown
149	A1049	62.391	167	773	-0.07	21.99	3.130	-17.807	0.8	Unknown
150	A1050	62.593	170	742	3.43	-8.70	-7.207	12.311	0.8	Unknown
2S: 38 frames; 2P: 49 frames; P+S: 4 frames										

Table A-9 VIV responses of the riser and the wake vortex mode for each plot of velocity and vorticity fields at a speed of 0.9 m/s

Serial number	Plot number	time s	x mm	y mm	d_x mm	d_y mm	a_x m/s^2	a_y m/s^2	V m/s	Vortex mode
1	A1051	29.290	183	768	3.51	11.59	-6.172	6.342	0.9	2P
2	A1052	29.492	186	744	6.22	-12.49	-0.658	-3.393	0.9	2S

3	A1053	29.694	178	767	-1.16	10.37	-0.865	0.831	0.9	2P
4	A1054	29.896	187	732	7.39	-24.54	-16.753	15.267	0.9	2P
5	A1055	30.098	178	777	-1.55	20.14	0.788	-3.777	0.9	2P
6	A1056	30.300	181	750	1.56	-6.28	-3.604	-0.936	0.9	unknown
7	A1057	30.502	188	749	8.55	-7.83	-6.594	-7.485	0.9	2P
8	A1058	30.704	186	740	6.61	-16.38	-9.604	18.370	0.9	2P
9	A1059	30.906	166	777	-13.59	20.52	9.768	-12.589	0.9	2S
10	A1060	31.108	170	742	-9.31	-15.21	2.381	18.156	0.9	2S
11	A1061	31.310	162	768	-17.47	11.59	23.358	-12.547	0.9	unknown
12	A1062	31.512	171	787	-8.93	29.85	19.742	-28.566	0.9	Unknown
13	A1063	31.714	166	761	-13.59	4.21	9.355	-0.338	0.9	Unknown
14	A1064	31.916	167	768	-12.42	10.81	23.008	-24.751	0.9	Unknown
15	A1065	32.118	167	726	-12.42	-30.75	-2.011	29.454	0.9	Unknown
16	A1066	32.320	177	779	-2.71	22.47	1.089	-13.164	0.9	Unknown
17	A1067	32.522	178	755	-1.16	-1.62	-14.086	11.623	0.9	Unknown
18	A1068	32.724	187	763	7.00	6.15	-9.214	-6.885	0.9	2P
19	A1069	32.926	178	744	-1.16	-12.49	-3.734	6.206	0.9	Unknown
20	A1070	33.128	178	785	-1.93	27.90	0.430	-2.479	0.9	Unknown
21	A1071	33.330	180	749	0.01	-8.22	-2.168	9.172	0.9	2P
22	A1072	33.532	189	762	9.72	4.99	-6.123	10.081	0.9	Unknown
23	A1073	33.734	196	738	16.32	-19.10	-1.378	-5.776	0.9	Unknown
24	A1074	33.936	182	769	2.73	12.37	-2.616	7.473	0.9	2S
25	A1075	34.138	183	747	3.51	-9.39	2.959	-7.090	0.9	2S
26	A1076	34.340	194	761	14.38	4.60	-7.968	6.809	0.9	2P
27	A1077	34.542	197	739	17.10	-17.54	-12.647	10.662	0.9	Unknown
28	A1078	34.744	176	777	-3.49	20.14	-4.320	2.600	0.9	2S
29	A1079	34.946	185	736	5.84	-20.65	-20.353	23.083	0.9	2S
30	A1080	35.148	170	771	-9.31	13.92	8.665	-20.264	0.9	2P
31	A1081	35.350	177	741	-2.71	-15.99	-4.481	10.253	0.9	2S
32	A1082	35.552	173	787	-6.60	29.85	6.707	-21.686	0.9	2P
33	A1083	35.754	171	746	-8.15	-10.55	-0.557	15.509	0.9	2S
34	A1084	35.956	175	787	-4.65	29.85	15.233	-20.367	0.9	Unknown
35	A1085	36.158	178	749	-1.55	-8.22	1.358	4.269	0.9	Unknown
36	A1086	36.360	173	786	-6.60	29.46	1.726	-11.397	0.9	Unknown
37	A1087	36.562	176	702	-3.49	-54.84	-4.598	22.217	0.9	2S
38	A1088	36.764	175	787	-4.26	29.85	9.375	-12.997	0.9	Unknown
39	A1089	36.967	183	733	3.51	-24.15	-8.223	4.563	0.9	2P
40	A1090	37.169	174	763	-5.43	5.76	2.059	-8.935	0.9	Unknown
41	A1091	37.371	170	770	-10.09	13.14	3.784	-8.088	0.9	Unknown
42	A1092	37.573	186	731	6.22	-25.70	-6.091	3.961	0.9	Unknown
43	A1093	37.775	175	786	-5.04	29.07	8.920	-12.381	0.9	P+S
44	A1094	37.977	170	741	-10.09	-15.99	10.097	3.671	0.9	Unknown
45	A1095	38.179	186	774	6.22	17.03	0.706	-10.000	0.9	2P
46	A1096	38.381	178	762	-1.16	5.37	-4.629	1.985	0.9	Unknown
47	A1097	38.583	179	769	-0.77	11.98	-2.059	-2.369	0.9	2P
48	A1098	38.785	178	747	-1.55	-9.78	-3.636	5.096	0.9	Unknown

49	A1099	38.987	186	767	6.22	10.04	-5.016	2.020	0.9	2P
50	A1100	39.189	174	738	-5.43	-18.71	-1.347	10.712	0.9	Unknown
51	A1101	39.391	173	771	-6.21	14.31	6.377	-8.820	0.9	Unknown
52	A1102	39.593	177	762	-3.10	5.37	1.521	-0.389	0.9	Unknown
53	A1103	39.795	178	763	-1.55	5.76	-0.506	-3.227	0.9	2P
54	A1104	39.997	176	732	-3.88	-24.94	1.344	3.190	0.9	2P
55	A1105	40.199	178	766	-1.55	9.65	3.278	-3.843	0.9	Unknown
56	A1106	40.401	181	721	1.17	-36.19	-4.369	7.405	0.9	Unknown
57	A1107	40.603	179	787	-0.77	29.85	2.712	-8.745	0.9	Unknown
58	A1108	40.805	184	703	4.67	-53.28	-4.343	17.856	0.9	Unknown
59	A1109	41.007	180	772	0.79	15.09	-0.778	4.516	0.9	2P
60	A1110	41.209	182	759	1.95	2.66	-4.130	5.605	0.9	Unknown
61	A1111	41.411	170	767	-9.70	10.42	4.510	3.209	0.9	Unknown
62	A1112	41.613	173	743	-6.60	-14.05	-2.080	7.338	0.9	2P
63	A1113	41.815	175	773	-5.04	16.64	-1.294	-2.239	0.9	Unknown
64	A1114	42.017	179	733	-0.77	-24.15	-0.406	12.813	0.9	Unknown
65	A1115	42.219	168	770	-11.65	13.14	9.029	-4.177	0.9	Unknown
66	A1116	42.421	176	740	-3.88	-16.38	0.326	7.553	0.9	Unknown
67	A1117	42.623	169	757	-10.48	-0.06	9.950	-4.553	0.9	Unknown
68	A1118	42.825	173	748	-6.21	-9.00	14.813	-8.663	0.9	2P
69	A1119	43.027	175	747	-5.04	-9.78	0.916	11.528	0.9	Unknown
70	A1120	43.229	184	758	3.89	1.49	2.124	-4.027	0.9	Unknown
71	A1121	43.431	182	749	2.34	-7.83	-2.288	8.611	0.9	Unknown
72	A1122	43.633	186	761	6.22	3.82	-5.713	4.171	0.9	2S
73	A1123	43.835	186	731	6.22	-25.31	-0.611	5.851	0.9	2P
74	A1124	44.037	188	767	8.55	10.42	-3.795	10.079	0.9	Unknown
75	A1125	44.239	196	752	15.94	-5.11	-4.268	-7.635	0.9	2S
76	A1126	44.441	187	774	7.00	17.42	-4.539	11.530	0.9	Unknown
77	A1127	44.643	196	749	15.94	-7.83	-4.421	-7.802	0.9	2P
78	A1128	44.845	190	774	10.33	17.42	-6.085	1.630	0.9	Unknown
79	A1129	45.047	192	737	12.44	-19.49	-11.774	7.575	0.9	Unknown
80	A1130	45.249	178	776	-1.16	18.97	-0.637	-13.101	0.9	Unknown
81	A1131	45.451	185	731	5.84	-25.29	-14.070	18.428	0.9	2P
82	A1132	45.653	177	778	-2.71	21.69	5.170	-25.269	0.9	2S
83	A1133	45.855	170	750	-10.09	-6.67	6.485	19.056	0.9	2S
84	A1134	46.057	162	786	-17.47	29.46	17.352	-21.930	0.9	unknown
85	A1135	46.259	171	746	-8.15	-10.55	16.802	11.082	0.9	2S
86	A1136	46.461	161	773	-18.25	16.25	22.989	-8.303	0.9	Unknown
87	A1137	46.663	169	768	-10.48	11.20	22.699	-27.318	0.9	2P
88	A1138	46.865	163	753	-17.08	-3.56	5.763	8.025	0.9	Unknown
89	A1139	47.067	176	766	-3.49	9.65	15.549	-37.146	0.9	2P
90	A1140	47.269	175	754	-4.65	-2.40	-7.845	27.426	0.9	Unknown
91	A1141	47.471	181	766	1.17	9.26	-7.163	-4.197	0.9	2S
92	A1142	47.673	181	743	1.17	-14.05	-10.423	17.008	0.9	2S
93	A1143	47.875	189	754	9.33	-3.17	-8.500	10.072	0.9	2S

94	A1144	48.077	189	738	9.72	-18.71	-5.007	2.730	0.9	Unknown
95	A1145	48.279	184	775	3.89	18.19	1.508	1.395	0.9	2P
96	A1146	48.481	184	739	3.89	-17.54	3.168	3.016	0.9	2P
97	A1147	48.683	187	778	7.00	20.91	6.164	1.523	0.9	2P
98	A1148	48.885	188	736	8.17	-20.26	2.861	-3.192	0.9	Unknown
99	A1149	49.087	187	760	7.39	3.04	0.417	2.212	0.9	Unknown
100	A1150	49.289	185	744	5.45	-12.88	-3.116	-1.932	0.9	Unknown
101	A1151	49.491	185	757	5.84	0.32	-3.464	1.074	0.9	Unknown
102	A1152	49.694	182	745	1.95	-11.72	-4.073	9.936	0.9	Unknown
103	A1153	49.896	178	787	-1.93	29.84	5.514	-16.341	0.9	Unknown
104	A1154	50.098	184	739	4.28	-17.54	-0.279	13.876	0.9	Unknown
105	A1155	50.300	182	786	2.73	29.46	6.818	-18.942	0.9	Unknown
106	A1156	50.502	182	748	2.73	-8.61	-4.295	-1.190	0.9	Unknown
107	A1157	50.704	175	759	-4.26	1.88	16.832	-26.221	0.9	2P
108	A1158	50.906	169	762	-10.87	5.37	17.774	-12.787	0.9	Unknown
109	A1159	51.108	168	731	-12.03	-26.09	11.446	8.229	0.9	2P
110	A1160	51.310	178	786	-1.16	29.46	13.153	-15.892	0.9	P
111	A1161	51.512	175	738	-4.26	-19.10	-3.031	18.666	0.9	unknown
112	A1162	51.714	191	777	10.89	20.52	-8.664	0.578	0.9	2P
113	A1163	51.916	184	741	4.67	-15.60	-2.879	13.106	0.9	2P
114	A1164	52.118	191	771	11.27	14.70	-11.017	18.448	0.9	Unknown
115	A1165	52.320	187	735	7.00	-21.82	-1.462	-0.814	0.9	Unknown
116	A1166	52.522	181	772	1.56	15.09	0.591	12.476	0.9	Unknown
117	A1167	52.724	191	743	10.89	-13.27	-4.994	-4.780	0.9	Unknown
118	A1168	52.926	177	756	-2.32	-1.23	-3.893	11.188	0.9	2P
119	A1169	53.128	194	745	13.99	-11.33	-4.874	-8.051	0.9	2P
120	A1170	53.330	185	770	5.45	12.76	-4.909	-4.061	0.9	Unknown
121	A1171	53.532	188	746	8.17	-10.55	-4.168	2.722	0.9	2S
122	A1172	53.734	170	779	-9.70	22.08	3.553	-14.212	0.9	2S
123	A1173	53.936	183	723	3.12	-33.86	-14.337	27.539	0.9	2P
124	A1174	54.138	173	787	-6.60	29.85	7.326	-25.976	0.9	Unknown
125	A1175	54.340	173	743	-6.98	-14.05	-2.258	16.510	0.9	Unknown
126	A1176	54.542	174	773	-5.82	16.64	10.592	-13.676	0.9	2P
127	A1177	54.744	185	742	5.45	-14.83	0.622	3.492	0.9	2S
128	A1178	54.946	175	778	-5.04	20.91	15.843	-20.640	0.9	Unknown
129	A1179	55.148	174	750	-5.43	-6.28	9.179	1.465	0.9	Unknown
130	A1180	55.350	164	746	-15.53	-10.94	9.227	13.587	0.9	Unknown
131	A1181	55.552	174	765	-5.43	8.48	14.163	-2.950	0.9	Unknown
132	A1182	55.754	171	772	-8.54	15.47	5.280	0.876	0.9	2P
133	A1183	55.956	188	787	8.55	29.85	-12.282	4.185	0.9	Unknown
134	A1184	56.158	187	749	7.39	-7.83	-3.218	1.730	0.9	Unknown
135	A1185	56.360	193	786	13.22	29.46	-2.545	0.550	0.9	2P
136	A1186	56.562	185	737	5.84	-19.49	-1.596	14.576	0.9	Unknown
137	A1187	56.764	189	776	9.72	18.97	3.513	-8.727	0.9	2P
138	A1188	56.966	186	733	6.22	-24.15	-5.647	6.349	0.9	Unknown

139	A1189	57.168	185	750	5.06	-7.06	0.807	-2.373	0.9	Unknown
140	A1190	57.370	181	732	1.56	-24.54	-3.947	-1.377	0.9	2P
141	A1191	57.572	192	773	12.05	16.64	-3.947	-1.377	0.9	2P
142	A1192	57.774	187	719	7.00	-38.13	-7.539	19.304	0.9	Unknown
143	A1193	57.976	179	787	-0.77	29.85	11.370	-23.933	0.9	Unknown
144	A1194	58.178	177	724	-2.71	-32.31	6.497	17.139	0.9	Unknown
145	A1195	58.380	173	787	-6.60	29.85	12.318	-12.785	0.9	Unknown
146	A1196	58.582	181	742	1.56	-14.44	-0.461	5.796	0.9	2P
147	A1197	58.784	180	736	0.79	-20.26	2.144	-5.309	0.9	2S
148	A1198	58.986	185	770	5.06	13.53	-0.991	-5.856	0.9	2P
149	A1199	59.188	178	747	-1.49	-9.39	6.779	-6.806	0.9	Unknown
150	A1200	59.390	178	750	-1.93	-6.67	-1.373	5.912	0.9	Unknown
2S:22 frames ; 2P: 42 frames; P+S: 1 frame; P: 1 frame										

Table A-10 VIV responses of the riser and the wake vortex mode for each plot of velocity and vorticity fields at a speed of 1. 0 m/s

Serial number	Plot number	time s	x mm	y mm	d_x mm	d_y mm	a_x m/s^2	a_y m/s^2	V m/s	Vortex mode
1	A1201	19.474	176	766	-7.60	4.65	21.022	-15.059	1.0	unknown
2	A1202	19.676	196	787	12.40	25.65	-8.099	-20.022	1.0	unknown
3	A1203	19.878	176	753	-7.60	-8.35	15.955	-2.759	1.0	unknown
4	A1204	20.080	194	742	10.40	-19.35	-18.889	16.498	1.0	unknown
5	A1205	20.282	175	777	-8.60	15.65	16.371	-6.303	1.0	unknown
6	A1206	20.484	193	753	9.40	-8.35	-10.936	17.007	1.0	2P
7	A1207	20.686	183	742	-0.60	-19.35	4.419	0.167	1.0	2S
8	A1208	20.888	176	761	-7.60	-0.35	12.401	-14.078	1.0	Unknown
9	A1209	21.090	197	773	13.40	11.65	-6.863	-23.979	1.0	2P
10	A1210	21.292	175	753	-8.60	-8.35	17.748	-5.313	1.0	2S
11	A1211	21.494	192	748	8.40	-13.35	-8.929	1.336	1.0	unknown
12	A1212	21.696	180	775	-3.60	13.65	7.522	-1.769	1.0	Unknown
13	A1213	21.898	185	759	1.40	-2.35	3.211	3.434	1.0	2S
14	A1214	22.100	190	732	6.40	-29.35	-15.484	19.371	1.0	2S
15	A1215	22.302	175	766	-8.60	4.65	16.658	1.142	1.0	2S
16	A1216	22.504	194	776	10.40	14.65	-10.267	7.105	1.0	2S
17	A1217	22.706	180	754	-3.60	-7.35	4.932	3.867	1.0	2S
18	A1218	22.908	182	759	-1.60	-2.35	3.628	-7.641	1.0	2S
19	A1219	23.110	192	777	8.40	15.65	-5.880	-19.728	1.0	2S
20	A1220	23.312	175	763	-8.60	1.65	15.734	-10.933	1.0	2S
21	A1221	23.514	189	754	5.40	-7.35	-6.317	-0.810	1.0	2P
22	A1222	23.716	182	771	-1.60	9.65	3.719	-0.737	1.0	Unknown
23	A1223	23.918	182	756	-1.60	-5.35	5.020	2.034	1.0	2S
24	A1224	24.120	185	744	1.40	-17.35	-14.882	21.415	1.0	2P
25	A1225	24.322	176	769	-7.60	7.65	11.208	5.331	1.0	2S

26	A1226	24.524	187	759	3.40	-2.35	-1.923	8.814	1.0	2S
27	A1227	24.726	185	743	1.40	-18.35	-4.209	3.465	1.0	2P
28	A1228	24.928	181	761	-2.60	-0.35	7.013	-0.520	1.0	2S
29	A1229	25.130	193	777	9.40	15.65	-8.471	-4.652	1.0	unknown
30	A1230	25.332	184	749	0.40	-12.35	-0.114	6.474	1.0	unknown
31	A1231	25.534	182	750	-1.60	-11.35	4.027	-3.940	1.0	unknown
32	A1232	25.736	192	770	8.40	8.65	-8.358	-7.471	1.0	unknown
33	A1233	25.938	178	766	-5.60	4.65	10.351	-1.659	1.0	unknown
34	A1234	26.140	189	751	5.40	-10.35	-6.076	3.205	1.0	2S
35	A1235	26.342	184	771	0.40	9.65	5.454	-2.939	1.0	Unknown
36	A1236	26.544	181	771	-2.60	9.65	5.391	0.742	1.0	2S
37	A1237	26.746	189	757	5.40	-4.35	-11.883	11.688	1.0	2S
38	A1238	26.948	176	763	-7.60	1.65	15.324	1.495	1.0	Unknown
39	A1239	27.150	192	776	8.40	14.65	-4.931	-0.065	1.0	2P
40	A1240	27.352	183	747	-0.60	-14.35	-2.126	7.623	1.0	2S
41	A1241	27.554	177	763	-6.60	1.65	6.779	-6.821	1.0	2P
42	A1242	27.756	195	787	11.40	25.65	-6.964	-17.498	1.0	2P
43	A1243	27.958	176	760	-7.60	-1.35	13.193	-6.285	1.0	2S
44	A1244	28.160	184	746	0.40	-15.35	-4.862	-0.513	1.0	2S
45	A1245	28.362	178	778	-5.60	16.65	7.193	-6.739	1.0	2S
46	A1246	28.564	182	762	-1.60	0.65	4.945	2.083	1.0	2S
47	A1247	28.766	188	744	4.40	-17.35	-14.695	21.335	1.0	Unknown
48	A1248	28.968	172	771	-11.60	9.65	14.022	-1.335	1.0	Unknown
49	A1249	29.170	192	775	8.40	13.65	-6.727	-5.234	1.0	Unknown
50	A1250	29.372	177	747	-6.60	-14.35	10.052	1.270	1.0	2S
51	A1251	29.574	184	757	0.40	-4.35	-3.732	-3.997	1.0	2S
52	A1252	29.776	187	787	3.40	25.65	4.606	-23.490	1.0	2P
53	A1253	29.978	177	749	-6.60	-12.35	14.925	-11.586	1.0	2P
54	A1254	30.180	191	749	7.40	-12.35	-17.783	21.532	1.0	Unknown
55	A1255	30.382	176	771	-7.60	9.65	10.168	4.295	1.0	Unknown
56	A1256	30.585	186	756	2.40	-5.35	-2.744	12.956	1.0	Unknown
57	A1257	30.787	186	740	2.40	-21.35	-9.429	12.691	1.0	2P
58	A1258	30.989	177	766	-6.60	4.65	10.854	1.287	1.0	Unknown
59	A1259	31.191	193	762	9.40	0.65	-5.926	3.239	1.0	2P
60	A1260	31.393	182	761	-1.60	-0.35	1.551	5.587	1.0	2S
61	A1261	31.595	184	763	0.40	1.65	4.225	-6.026	1.0	2S
62	A1262	31.797	192	768	8.40	6.65	-5.909	-12.461	1.0	2S
63	A1263	31.999	180	758	-3.60	-3.35	6.478	-5.949	1.0	2P
64	A1264	32.201	187	761	3.40	-0.35	-1.286	-1.677	1.0	2P
65	A1265	32.403	186	787	2.40	25.65	1.918	-10.138	1.0	Unknown
66	A1266	32.605	184	754	0.40	-7.35	5.776	1.529	1.0	Unknown
67	A1267	32.807	186	746	2.40	-15.35	-3.975	11.631	1.0	2P
68	A1268	33.009	178	772	-5.60	10.65	10.944	-3.232	1.0	2S
69	A1269	33.211	185	768	1.40	6.65	2.853	2.809	1.0	Unknown
70	A1270	33.413	184	745	0.40	-16.35	-1.556	4.379	1.0	Unknown
71	A1271	33.615	177	747	-6.60	-14.35	7.507	2.745	1.0	Unknown

72	A1272	33.817	177	747	-6.60	-14.35	-1.209	-10.005	1.0	2S
73	A1273	34.019	178	753	-5.60	-8.35	5.503	0.712	1.0	Unknown
74	A1274	34.221	179	760	-4.35	-1.55	2.719	-7.302	1.0	Unknown
75	A1275	34.423	194	773	10.41	11.26	-4.606	-23.665	1.0	Unknown
76	A1276	34.625	175	759	-8.62	-2.33	15.468	-13.038	1.0	Unknown
77	A1277	34.827	187	752	3.42	-8.93	-7.451	6.181	1.0	2S
78	A1278	35.029	176	774	-7.85	12.82	10.331	-3.196	1.0	2P
79	A1279	35.231	185	766	1.48	5.05	1.675	9.321	1.0	2S
80	A1280	35.433	187	742	3.81	-19.81	-12.624	18.954	1.0	Unknown
81	A1281	35.635	173	773	-10.95	11.65	16.562	-3.254	1.0	2P
82	A1282	35.837	195	774	11.19	12.43	-8.799	-5.849	1.0	2S
83	A1283	36.039	179	752	-4.74	-8.93	5.988	3.311	1.0	2S
84	A1284	36.241	181	763	-2.41	1.55	3.386	-8.837	1.0	2S
85	A1285	36.443	193	778	9.25	16.31	-3.318	-16.159	1.0	Unknown
86	A1286	36.645	179	754	-4.74	-7.77	13.422	-9.807	1.0	2P
87	A1287	36.847	186	754	2.64	-7.77	-5.414	4.090	1.0	2P
88	A1288	37.049	184	772	-0.08	10.49	4.772	-5.303	1.0	2S
89	A1289	37.251	182	756	-1.63	-5.44	5.046	1.196	1.0	2S
90	A1290	37.453	189	748	5.36	-13.60	-8.086	10.198	1.0	2P
91	A1291	37.655	178	759	-5.51	-2.72	13.174	3.601	1.0	2P
92	A1292	37.857	189	762	5.36	0.39	-0.995	6.093	1.0	2P
93	A1293	38.059	185	753	1.48	-8.55	-5.427	5.919	1.0	Unknown
94	A1294	38.261	180	767	-3.18	5.44	7.630	-5.853	1.0	Unknown
95	A1295	38.463	197	775	13.13	13.60	-11.555	-7.022	1.0	2S
96	A1296	38.665	177	759	-6.68	-2.72	5.949	0.370	1.0	Unknown
97	A1297	38.867	180	752	-3.18	-9.71	-0.734	-2.493	1.0	2S
98	A1298	39.069	185	778	1.87	17.09	0.116	-16.720	1.0	Unknown
99	A1299	39.271	175	765	-9.01	3.50	13.613	-9.562	1.0	Unknown
100	A1300	39.473	189	745	5.75	-15.93	-11.237	11.302	1.0	Unknown
101	A1301	39.675	174	762	-9.40	0.78	11.787	2.796	1.0	Unknown
102	A1302	39.877	188	768	4.20	6.21	-5.169	11.249	1.0	2P
103	A1303	40.079	181	745	-2.41	-16.32	-3.693	13.038	1.0	Unknown
104	A1304	40.281	173	761	-10.56	0.00	13.102	-4.673	1.0	Unknown
105	A1305	40.483	195	779	11.58	17.87	-11.355	-17.387	1.0	2S
106	A1306	40.685	176	752	-7.46	-9.32	16.236	-7.077	1.0	2S
107	A1307	40.887	187	757	3.42	-4.66	-2.836	-9.054	1.0	Unknown
108	A1308	41.089	181	780	-2.41	18.65	7.111	-15.781	1.0	Unknown
109	A1309	41.291	182	763	-2.02	1.55	6.111	0.306	1.0	2P
110	A1310	41.493	189	744	5.36	-17.48	-19.840	27.781	1.0	Unknown
111	A1311	41.695	172	777	-11.73	15.54	17.929	-1.153	1.0	Unknown
112	A1312	41.897	190	775	6.53	13.21	-6.335	3.512	1.0	Unknown
113	A1313	42.099	180	760	-3.57	-1.17	1.566	3.891	1.0	Unknown
114	A1314	42.301	182	766	-1.63	4.66	6.292	-8.643	1.0	2P
115	A1315	42.503	194	787	10.02	25.25	-7.573	-17.181	1.0	Unknown
116	A1316	42.705	173	759	-10.18	-2.33	14.914	-12.399	1.0	2P
117	A1317	42.907	187	747	3.03	-14.37	-5.272	3.444	1.0	Unknown

118	A1318	43.109	179	776	-4.74	14.76	8.191	-6.078	1.0	2P
119	A1319	43.312	182	762	-1.63	0.39	4.485	2.257	1.0	2S
120	A1320	43.514	192	745	8.86	-16.70	-18.197	19.542	1.0	unknown
121	A1321	43.716	173	768	-10.95	6.99	17.577	-4.110	1.0	2P
122	A1322	43.918	192	767	8.47	5.44	-7.037	8.171	1.0	Unknown
123	A1323	44.120	181	754	-2.41	-7.38	4.428	0.803	1.0	2S
124	A1324	44.322	180	768	-3.96	6.99	8.086	-13.927	1.0	2S
125	A1325	44.524	193	773	9.63	11.65	-7.912	-17.268	1.0	2P
126	A1326	44.726	177	756	-6.68	-5.44	11.810	-9.641	1.0	2S
127	A1327	44.928	184	761	0.31	0.00	2.665	-8.490	1.0	2S
128	A1328	45.130	188	763	4.20	1.17	0.726	-10.387	1.0	Unknown
129	A1329	45.332	179	758	-4.35	-3.11	11.388	-7.496	1.0	Unknown
130	A1330	45.534	190	749	6.53	-12.04	-7.993	11.494	1.0	2S
131	A1331	45.736	182	763	-2.02	1.17	6.501	1.462	1.0	Unknown
132	A1332	45.938	185	756	1.09	-5.44	3.548	3.344	1.0	2S
133	A1333	46.140	186	750	2.64	-11.27	-4.203	6.697	1.0	2P
134	A1334	46.342	178	770	-5.51	8.55	15.081	-2.623	1.0	2S
135	A1335	46.544	194	782	10.80	20.98	-8.955	-6.297	1.0	unknown
136	A1336	46.746	180	745	-3.57	-15.93	0.940	5.770	1.0	2S
137	A1337	46.948	177	760	-7.07	-1.17	6.317	-12.433	1.0	Unknown
138	A1338	47.150	193	775	9.25	13.98	-6.132	-17.964	1.0	Unknown
139	A1339	47.352	176	761	-7.46	-0.39	14.250	-10.539	1.0	Unknown
140	A1340	47.554	192	743	8.47	-17.87	-12.583	7.965	1.0	2S
141	A1341	47.756	175	771	-8.62	10.10	11.401	-0.853	1.0	Unknown
142	A1342	47.958	187	756	3.03	-5.05	-3.321	15.624	1.0	2P
143	A1343	48.160	187	746	3.81	-15.54	-10.083	18.123	1.0	2S
144	A1344	48.362	171	765	-12.51	3.50	17.559	-5.425	1.0	Unknown
145	A1345	48.564	194	787	10.41	25.25	-10.302	-6.845	1.0	2S
146	A1346	48.766	177	756	-7.07	-5.05	8.429	-0.376	1.0	2S
147	A1347	48.968	182	761	-1.63	-0.39	-1.151	-8.493	1.0	2S
148	A1348	49.170	191	786	6.92	24.86	-2.818	-19.043	1.0	unknown
149	A1349	49.372	175	758	-8.23	-3.50	12.261	-10.480	1.0	2S
150	A1350	49.574	192	745	8.08	-15.93	-19.702	24.006	1.0	2S
2S: 56 frames; 2P: 31 frames;										